UNIVERSITY OF OKLAHOMA

GRADUATE COLLEGE

COHERENT CONTROL AND GEOMETRIC PHASE

A DISSERTATION

SUBMITTED TO THE GRADUATE FACULTY

in partial fulfillment of the requirements for the

Degree of

DOCTOR OF PHILOSOPHY

BY

XUAN LI

Norman, Oklahoma

2008

COHERENT CONTROL AND GEOMETRIC PHASE

A DISSERTATION APPROVED FOR THE
HOMER L. DODGE DEPARTMENT OF PHYSICS AND ASTRONOMY

BY

Dr. Gregory A. Parker

Dr. Michael A. Morrison

Dr. James P. Shaffer

Dr. Kimball A. Milton

Dr. Ralph A. Wheeler

Acknowledgments

It is a pleasure to thank the many people who made this thesis possible.

It is difficult to overstate my gratitude to my Ph.D. supervisor, Prof. Gregory A. Parker. With his enthusiasm, his inspiration, and his great efforts to explain things clearly and simply, he helped to make AMO physics fun for me. Throughout my thesis-writing period, he provided encouragement, sound advice, good teaching, good company, and lots of good ideas. I would have been lost without him.

I would like to thank my awesome advisor committee members, Michael Morrison, James Shaffer, Kim Milton and Ralph Wheeler. They have given me all the support I needed. I can't ask for more because they have given me more than enough. I am grateful for my collaborator and future supervisor, Moshe Shapiro, for all of his help in science and life. I also need to thank Dr. Brian Kendrick and Prof. Kieran Mullen for all the useful discussion and help on the geometric phase issues.

I owe my thank to the many people who have taught me physics and chemistry: my undergraduate teachers at NJU (Nanjing University, Department of Intensive Instruction for sciences and arts), my graduate school teachers (Michael Morrison, Kim Milton, Deborah Watson, Eric Abraham, Phil Gutierrez, Ron Kantowski, Michael Santos, Pat Skubic and Roger Frech).

I am indebted to my many student colleagues for providing a stimulating and fun environment in which to learn and grow. I am especially grateful to Daniel Brue who had a lot of discussion with me on the potential energy surfaces and the geometric phase effect. I thank particularly Richard Overstreet who helped me with experimental information and thesis work, Jeff Crawford for all the interesting discussion, and Blake Laing who gave me this great thesis template. I am also grateful to Arne Schwettmann, Jonathan Tallant, James Dizikes, Stephane

Contents

V Epilogue

List Of Tables

List Of Figures

Abstract

We present the ability to coherently control triatomic chemical reactions with pulsed-laser techniques. We show that one can control the final state probability distribution of triatomic chemical reactions with nearly 100% selectivity. We develop the population transfer by adiabatic passage theory to coherently control the chemical reaction with the ability of choosing the translational energies of the final reaction products. We also show a new way to achieve the creation of both homonuclear and heteronuclear diatomic molecules at an ultracold temperature using laser catalysis.

We also generalize the treatment of the geometric phase effect in a triatomic system which includes a seam of conical intersections. We derive generally how to include the geometric phase effect with nonlinear conical intersections in the c_{2v} geometries with the Numerov propagation method. We develop a Mixed-Odd-Even-State method to simplify the conventional treatment of the generally complex Hamiltonian. We are the first group to develop the theoretical derivation of how to include geometric phase in a triatomic system where the seam of conical intersection are located in the collinear geometries. We show that the vector potential, for the collinear conical intersections, not only depends on the three internal coordinates but also on one of the Euler angles. The resultant Hamiltonian in the internal coordinates, after the integration of the three Euler angles, is a real Hamiltonian when the nuclear total angular momentum J is assumed to be zero.

Part I

Prologue

Chapter 1

Introduction

1.1 Reactive Scattering

Triatomic collision processes are essential in developing a thorough understanding of chemical reaction dynamics. This reaction can be thought of as the key part of chemistry and it can be expressed as

$$A + BC \rightleftharpoons \begin{cases} B^* + AC^* \\ C^* + AB^* \\ A^* + B^* + C^* \end{cases}. \tag{1.1}$$
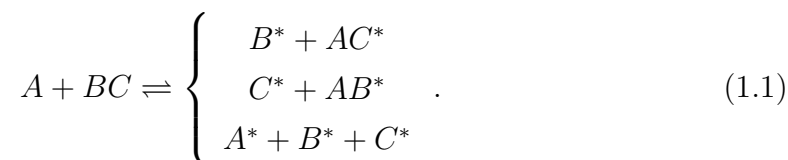
where A, B and C are atoms and the $*$ superscripts represent possible electronic, vibrational and rotational excitations. Accurate computation of the reactive scattering process enables us to truly understand the chemical activities. The branching ratios and the selective transitions are two of the most studied subjects of the reactive scattering processes. These studies help to accurately predict and explain experimental observations and possible quantum control of chemical reactions.

The recent development of ultracold techniques, e.g. BEC (Bose-Einstein Condensation) of different atoms and formation of ultracold diatomic molecules, has created a "coherent" system for researchers to study the chemical reaction on a new level. At ultracold temperatures, even collisions of large molecules exhibit significant quantum effects due to a large de Broglie wavelength. Also, the dominant reaction pathway depends heavily on the details of the electronic potential energy surfaces at ultracold temperatures. Quantum tunneling through barriers

and scattering resonances should be greatly enhanced in the ultracold regime. Understanding these chemical reactions at a microscopic level will thus be one of the most important tasks for both physicists and chemists.

In this thesis, we study two of the most interesting aspects of chemical reactive collisions: quantum control of reactive scattering processes and the geometric phase effect.

1.2   Coherent Control

Instead of passively observing the chemical-physical process, the maturation of quantum mechanics has enabled physicists and chemists to actively control these processes. Shapiro and Brumer pointed out in Ref. (1)

> "...the development of new laser devices that afford extraordinary facility in manipulating light, and the recognition that coherent laser light can be used to imprint information on atoms and molecules in a manner such that their subsequent dynamics leads to desirable goals".

Controlling chemical reactions with tunable external fields has long been a sought-after goal of AMO (Atomic, Molecular and Optical) physicists. Quantum control of chemical reactions will not only allow us to selectively obtain favored products, but also reveal fundamental mechanisms of various chemical reactions. Possible applications of quantum control over chemical reactions can be, but are not limited to, quantum information devices, examination of reactive scattering theories, revelation of molecular structures, and accurate description of inter-molecular potentials.

Different types of external fields may influence chemical reactions at different temperatures. The translational energies of the target molecules should be no larger than the perturbation due to system-field interactions, so the controllability is non-trivial compared to the relatively wide range of scattering possibilities. Strong field control can be applied to chemical reactions at cold (10^{-3}K to 1K) or hot (above 1K) temperatures, and quantization of the external electric-magnetic fields is usually necessary. Moderate and weak field controls are usually applied

to chemical reactions at cold or ultracold (10^{-9}K to 10^{-3}K) temperatures and the perturbation theory is still valid for the system-field interactions.

With the creation of BECs of atoms and possibly molecules, the ultracold temperature has opened a new world for us to be more actively involved in chemical reactions. Ultracold molecules usually display a nuclear angular momentum of zero in the asymptotic region, which greatly simplifies the theoretical calculation of these processes. Also, the ultracold collision processes depend heavily on the interaction potentials and translational energies of the initial reactants or final products. Any slight change in the effective potential, due to an external field, may lead to a drastic change in the final reaction. This external field can then be applied at ultracold temperatures to greatly enhance the controllability and it is even possible to completely enhance or suppress reaction. Recently, there have been a large number of successful experimental realizations of creating ultracold atoms or molecules. This ability to achieve coherence in the prepared ensemble of ultracold reactants has also enabled us to obtain more controllability over the chemical reactions.

On the other hand, the ability to use the quantum control techniques in the chemical reactions at cold/ultracold temperatures may lead to one way of generating ultracold molecules which may be hard to generate via other means. Recent development of the formation methods of ultracold molecules are: Stark Deceleration (2), sympathetic cooling (3), photoassociation (4) and Feshbach resonances (5; 6). The precise control of chemical reactions to achieve the formation of ultracold molecules is at least comparable to these methods. The quantum control method has its merits because it is not constrained to specific systems or apparatus, and it should be applicable to most of the triatomic systems.

Most quantum control scenarios involve the interaction between systems and external fields, e.g. lasers. In the context of a coherent control process, quantum interference effects are used to either constructively or destructively alter the final results. With the help of the laser techniques, one can (1)

> "coherently drive a state with phase coherence through multiple, coherent, indistinguishable routes... to the same final state allows for the possibility of control".

The scenario has an analogy to Young's double slit experiment. In this experiment a beam of particles can pass through both of the double slits. Particles can pass through either slit and form two indistinguishable routes and thus these two routes produce interference patterns. The possible realization of a coherent control process lies in the ability to remain coherent, which includes both the initial preparations of the system and the external laser fields. If the initial preparation of the system is not coherent the unwanted quantum processes or products occur and thus weaken the controllability. Laser fields, in a coherent control process, are usually required to have a narrow energy bandwidth compared to the translational energies of the colliding systems. This usually leads to the use of pulsed laser fields with a $ms - \mu s$ temporal width. Both techniques, the coherent preparation of the system and pulsed laser fields with moderate intensities, are now achievable in the labs and the realization of these processes are optimistically expected.

In chapter 2 we develop different ways to coherently control chemical reactions. We show that, by using one pulsed laser, the complete range of reaction yield at cold and ultracold temperatures can be achieved. We develop a new technique, the population transfer by adiabatic passage theory, to achieve quantum control of exchange reactions. This technique uses two pulsed lasers with moderate intensities and it is able to tune the final products' final translational energies. We also show the ability to create ultracold homonuclear and heteronuclear diatomic molecules using the laser catalysis techniques.

1.3   Geometric Phase

To describe a multi-particle quantum mechanical system which involves both electrons and nuclei, one can use a Born-Oppenheimer expansion to separate the nuclear and electronic motions as

$$\Psi^{tot} = \sum_i \psi_N^i(\vec{\mathbf{R}})\phi_e^i(\vec{\mathbf{R}}, \vec{\mathbf{r}}), \tag{1.2}$$

where the nuclear wavefunction ψ_N depends on the nuclear coordinates $\vec{\mathbf{R}}$ and the electronic wavefunction ϕ_e depends on both the nuclear coordinates $\vec{\mathbf{R}}$ and the electronic coordinates $\vec{\mathbf{r}}$. This total wavefunction Ψ^{tot} is then taken to be the

sum of an infinite number of basis functions which are complete. Note, the Born-Oppenheimer expansion is an exact method. To simplify the total wavefunction, the Born-Oppenheimer approximation is often used, and has been assumed to be a good approximation for over half a century (7). This approximation not only separates the nuclear and electronic motions, but also assumes the electrons move much faster than the slow nuclei. This approximation then treats these two motions, with different "speeds", separately and ignores the influence on each other. If so, the influence of other electronic adiabatic potential energy surfaces (PESs) on a single electronic PES is ignored and one can truncate the summation in Eq.(1.2) to a simple product form

$$\Psi^{tot} = \psi_N(\vec{\mathbf{R}})\phi_e(\vec{\mathbf{R}}, \vec{\mathbf{r}}). \tag{1.3}$$

The Born-Oppenheimer approximation is not valid when multiple electronic PESs heavily interfere with each other, e.g. those which cross to form conical intersections. Two electronic adiabatic PESs can intersect, in a polyatomic system, even if the corresponding electronic states have the same symmetry and spin. These intersections usually take a double-cone shape and thus are named conical intersections. Because the electronic wavefunction's dependence on the nuclear motion couples different electronic adiabatic states heavily especially near the conical intersection regions, the Born-Oppenheimer approximation breaks down. There are, in general, two kinds of conical intersections: symmetry allowed and accidental-degenerate. The first kind, the symmetry allowed ones, usually refers to the PESs which have the same irreducible representations in the general nuclear configuration, e.g. the C_s symmetry group for a triatomic molecular system. They also have different irreducible representations of a higher symmetry group for a special nuclear configuration, e.g. the $C_{\infty v}$ symmetry group for a triatomic molecular system in the collinear geometry. The second kind of conical intersections, the accidental-degenerate ones, are sometimes referred to as diabolic conical intersections. This results when such polyatomic systems have more than one independent nuclear coordinate. Two independent relations between electronic Hamiltonian matrix elements are sufficient for the existence of doubly degenerate electronic energy eigenvalues. Therefore, these relations are easily satisfied for systems with three

or more internal nuclear degrees of freedom. As pointed by Kuppermann in Ref. (8):

> "Conical intersections between electronically adiabatic potential energy surfaces are not only possible but actually quite frequent, if not prevalent, in polyatomic system."

Many systems display conical intersections such as H_3 and its isotopomers (isotopic isomers, as DH_2, HD_2, HDT, etc.), triatomic alkali systems such as Na_3 (9), Li_3 (10) and its isotopomers, HO_2 (11), NO_2 (12), NH_2 and other kinds.

Note, a triatomic system has three internal degrees of freedom and two independent relations need to be satisfied as we mentioned above. Therefore, there are usually a seam (line) of conical intersections in the three-dimensional internal coordinates. To be more general, the number of dimensions of the conical intersections can be expressed as $3N - 8$ where N is the number of atoms in this polyatomic system.

Since Berry's introduction of the geometric phase associated with the conical intersections between PESs (13), a lot of research has been done on this subject. Let us assume that in a triatomic system all spin terms (electronic and nuclear) and relativist effects in the Hamiltonian can be neglected , that two adiabatic electronic PESs display a seam of conical intersections, and that the electronic adiabatic wavefunctions are real and continuous in the nuclear coordinates. When the nuclear coordinates move on a closed loop and returns to its original position, the electronic wavefunction is different from its initial wavefunction only by a phase factor. This phase factor contains not only the conventional dynamic phase but also a purely geometric phase which depends solely on the loop that the electronic wavefunction took (14). This effect causes the electronic wavefunction to change sign when this closed loop encircles the seam of conical intersections an odd number of times (15). Equivalently, if an adiabatic electronic wavefunction changes sign as it is transported along a closed loop there must exist at least one conical intersection encircled by this loop. This purely quantum mechanical effect can be related to the well-known Y. Aharonov and D. Bohm effect (16). In this effect, though a vector potential produces a zero electric or magnetic field in the

configuration space of the free electrons, this vector potential can influence the phase of the electrons and thus produces interference patterns.

Herzberg and Longuet-Higgins (17) and Longuet-Higgins and his coworkers (18) were the first to notice that the electronic wavefunction, if taken to be real, can behave as a double-valued function. This function changes sign when it transversed via a closed loop which encircles a seam of conical intersections of electronic PESs. This problem was referred to as the well-known Jahn-Teller problem. In 1978, Mead and Truhlar did the theoretical derivation of the geometric phase effect in the H_3 scattering problem (14). The H_3 system is a typical Jahn-Teller system (19) and the conical intersections are located in the D_{3h} geometries where three Hydrogen nuclei form an equilateral triangular geometry. It is the first explicit derivation in a real system to show that the electronic wavefunction changes sign as it transverses completely around the conical intersection seams in the D_{3h} geometries. The Jahn-Teller theorem (19) states: if an electronic adiabatic state is degenerate because of symmetry of a non-linear molecule, then the degenerate high-symmetry configuration is unstable with respect to spontaneous distortions that lift the degeneracy to a low-symmetry configuration. Such degeneracy causes symmetry related conical intersections, whose effects will be studied in this thesis.

We need to specify whether the electronic wavefunction is real or complex because a complex electronic wavefunction can be obtained as a single-valued function (14). Note, if we multiply this real double-valued electronic wavefunction by a complex double-valued phase factor, we can form a complex single-valued electronic wavefunction. This double-valued phase factor depends on the nuclear coordinates and it leads to vector potential terms in the Hamiltonian. Thus this procedure is often referred as the vector potential method (14). The two major difference in using a real double-valued electronic wavefunction and complex single-valued electronic wavefunction will be shown in Chapter 3. The generally complex corrections to the Hamiltonian in the vector potential terms needs to be treated carefully because it usually complicates the computational process. Since most of the scattering computer codes are written to treat real Hamiltonians, we wish to minimize the computational effort caused by the complex terms. For example, we will show in chapter 4 that we can obtain real overlap matrices so

that the propagation in the hyperradius remains real and thus effectively minimize the computational effort. This is particularly true when one wishes to perform a large number of scattering calculations with different kinetic energies, where the calculation time can be long (hours to days).

The sign change of the real adiabatic electronic wavefunctions has nontrivial consequences for molecular structures and dynamics on these crossing electronic PESs. This sign change leads to a double-valued real electronic wavefunction and, in order to maintain the entire wavefunction of the system to be single-valued, the nuclear wavefunction needs to be double-valued as well. The double-valued nuclear wavefunction needs to undergo a sign-change around a conical intersection in order to cancel the sign-change of the electronic wavefunction at the same time. This change of sign greatly affects the nature of the solutions of the corresponding nuclear motion Schrodinger equation.

Even though the geometric phase was discovered over three decades ago, it was not generally included in molecular scattering calculations. With current computing technologies and numerical techniques, it is now possible to compare theoretical results to experimental results to examine the effect of geometric phase. More and more agreements between theoretical calculations and accurate experiments show that the geometric phase effect can be significant in molecular scattering processes (20; 21; 22). Accurate quantum mechanical reactive scattering calculations for the $H+H_2$ system and its isotopic variants ($D+H_2$ and $H+D_2$) have been performed by Kuppermann and his coworkers (23; 24; 25; 26; 27). They calculated accurate differential and integral cross sections of reactive scattering processes with and without the geometric phase effect. They showed that the cross sections with the inclusion of the geometric phase were in much better agreement with the experimental results (28; 29; 30) than those obtained without the geometric phase effect.

The simplest cases of conical intersections between different electronic PES's are in a triatomic system where the three internal coordinates have enough freedom to satisfy two conditions on the electronic Hamiltonian matrix elements: equal diagonal elements and zero off-diagonal couplings. The triatomic lithium system is of particular interest because it displays a seam of conical intersections between

the spin-aligned $1^4A'$ and $2^4A''$ electronic PESs in the collinear geometry. We choose the zero of energy to be the triatomic dissociation limit of $^2S + {}^2S + {}^2S$. Though the energy of the lowest conical intersection point is slightly above zero, the minimum energy for the nuclear wavefunction to circumvent this seam of conical intersections is lower than the ground vibrational energy level of the diatomic molecule (10). This means that, even at an ultracold temperature for the Li + Li$_2$ collision process, the nuclear wavefunction is able to completely traverse the conical intersections and thus the geometric phase effect may be non-trivial. Therefore, the nuclear wavefunctions need to be double-valued when real double-valued electronic wavefunctions are used. One alternative way to include the geometric phase effect is to follow Mead and Truhlar's work (14) in which the sign change can be accounted for by introducing a vector potential into the nuclear Schrodinger equation. In this approach, the real double-valued electronic adiabatic wavefunction is multiplied by a complex phase factor which also changes sign when the enclosed loop encircles the seam of conical intersections. This results in a complex single-valued electronic adiabatic wavefunction. Either procedure listed above is equivalent to the other. No geometric phase effects were considered in the recent reactive scattering calculations on the ground spin-aligned electronic PES of the triatomic lithium system (31; 32). It is then necessary to investigate the effect of geometric phase on the dynamics of this particular system.

In chapter 3 we briefly discuss the conventional treatment of the geometric phase in a triatomic system. In chapter 4 we use the vector potential procedure to treat the geometric phase with conical intersections in the C_{2v} geometries. We derive the Hamiltonian and nuclear wavefunctions with the inclusion of vector potentials. We then develop a new method to expand the nuclear wavefunctions so that the general complex problem can be treated in a simple fashion. With this new method, all the overlap matrices between different propagation sectors are real and thus need no further special treatment. In chapter 5 we derive the treatment of the geometric phase effect with conical intersections in the $C_{\infty v}$ geometries. We fully develop the geometric phase angle and the associated vector potential terms. We find that the resulting Hamiltonian in the internal coordinates, with certain approximations, is real. The complex components of the Hamiltonian are

zero when the total nuclear angular momentum is assumed to be zero, and the resulting real vector potential terms are easy to compute. The Hamiltonian with the inclusion of the geometric phase effect thus requires no special treatment and can be easily applied to the reactive scattering calculations.

Part II

Coherent Control

Chapter 2

Coherent Control

In this chapter we focus on various ways to achieve quantum control of triatomic reactive scattering dynamics. In chemical reactions, the triatomic reaction has become one of the most important systems because it is fundamental and non-trivial. In triatomic reactions, an atom and diatom collide to produce new products. With the help of external laser fields, one can control the direction of the chemical reactions and produce desired species

$$A + BC \longrightarrow \begin{cases} B + AC & \text{Reactive} \\ C + AB & \text{Reactive} \\ A + BC & \text{Non-reactive} \end{cases} . \qquad (2.1)$$
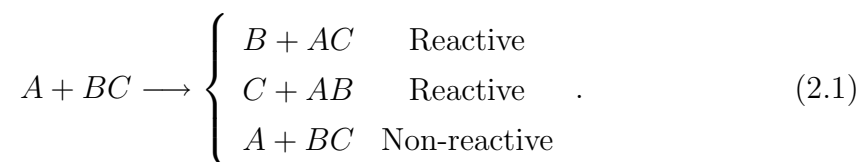
One way of controlling this triatomic reaction is to pump the reactants $A + BC$ on the ground electronic PES to form an electronically excited complex $(ABC)^*$ and then dump the complex to another chemical arrangement channel on the ground PES. The experimental parameters such as laser pulses' temporal durations, carrier frequencies, intensities, and effective operating times, as well as the different intermediate states give us enough freedom to interfere different quantum routes in this process. We can then achieve either constructive or destructive interferences to control the direction of the chemical reactions. We will discuss four major aspects of the coherent control project in this chapter: laser catalysis of chemical reaction at cold temperatures, population transfer by adiabatic passage theory, controlled formation of ultracold homonuclear molecules, and controlled formation of ultracold heteronuclear molecules.

2.1 Laser Catalysis at Cold Temperatures

The possibility of enhancing or suppressing atomic and molecular reactions by external lasers fields has attracted the attention of many researchers (33; 34; 35; 36; 37; 38; 39; 40; 41; 42; 43; 44; 45; 46; 47; 48; 49; 50; 51; 52; 53; 54; 55; 56; 57; 58; 59). Some of the most studied scenarios use light to modify the PESs of the colliding systems, which leads to "light induced potentials" (LIP) (46). The laser parameters are tuned so that LIPs possess lower reaction barriers along the reaction pathways leading to the desired final products. The main difficulty in realizing these scenarios is the requirement for high laser intensities (in the TW/cm^2 range). These high laser intensities are needed in these processes because of the relatively small *continuum-continuum* transition dipole moments, which are at the heart of the mechanism leading to the formation of LIP. In order to compensate for the weak transition dipole moments and still have a moderate Rabi transition frequency, one needs to tune up the laser intensity to a magnitude of TW/cm^2.

The necessity of using intense laser fields can be reduced when (quasi) bound states are used as the transition bridge. The Rabi transition frequency is proportional to the product of the transition dipole moment and the electric field strength. The presence of a much stronger *bound-continuum* transition dipole moments (than the weak *continuum-continuum* transition dipole moments) is expected to lower the laser intensity requirements to the order of MW/cm^2 to GW/cm^2 regime (46; 47; 60; 61; 62). We also show that a laser intensity of kW/cm^2 is big enough to achieve quantum control at ultracold temperature (63). This use of strong *bound-continuum* transition dipole moments is the situation in the "laser catalysis" (LC) scenario (46; 47; 60; 61; 62), so called because it involves no net absorption of photons. Rather, colliding partners, which cannot react due to the existence of a high reaction barrier, are made to "hop" over this barrier. This system first absorbs a photon to an excited bound state which straddles both sides of the reaction barrier. The system is then de-excited, by stimulated emission of a photon identical to the one just absorbed, to the products' side of the original reaction barrier. The process can occur on-resonance or off-resonance (64) with respect to the continuum-bound transition frequencies. It has also been shown (60)

that for a coherent process, as the laser power increases, the population of the intermediate bound state decreases. Eventually, the intermediate state becomes unpopulated, in great similarity to the simple three-state adiabatic passage process (65; 66). By not populating the intermediate states, one can significantly reduce the spontaneuous emission loss and thus increase the final reaction yield.

The use of ultracold reactants, e.g., hydrogen (67), lithium (68), sodium (69), rubidium (70) and cesium (71), is expected to greatly enhance the ability to quantum mechanically control reactive scattering. The coherence in the well-prepared initial state can drastically reduce the unwanted quantum routes and thus lead to a broader control range. Of special interest are reactions between spin-aligned atoms and molecules. Spin-aligned states have relatively large magnetic moments, making them easier to capture in magnetic traps. Using this technique one may consider reactions between cold/ultracold bosons and fermions, resulting in a large variety of molecular interactions. For example, isotopic mixtures of fermionic ^{6}Li and bosonic ^{7}Li result in the formation of either heteronuclear (^{6}Li^{7}Li) or homonuclear (^{6}Li$_2$ or ^{7}Li$_2$) diatomic molecules (32; 72; 73; 74).

It is thus of great interest to examine the use of laser fields to coherently control the reactive scattering process in cold and ultracold mixtures of spin aligned ^{6}Li $+^7$Li$_2$ or its isotopomers (^{7}Li $+^7$Li$_2$, ^{7}Li $+^6$Li$_2$ and ^{6}Li $+^6$Li$_2$). In addition to the light induced interaction between the two low-lying spin-aligned ($^4A'$) states, this system displays a variety of interesting features, including conical intersections between the two PESs in the collinear (C$_{\infty v}$) geometries (10; 31; 32; 75).

We present a non-perturbative time-dependent quantum mechanical theory of the laser catalysis. We apply this theory to control a bifurcating $A + BC \overset{\hbar\omega_0}{\longleftrightarrow} ABC^*(v) \overset{\hbar\omega_0}{\longleftrightarrow} AB + C$ reaction, with $ABC^*(v)$ denoting an intermediate, electronically excited, bound state of ABC in the v-th vibrational state (76). We apply this theory to the low collision energy fermion-boson light-induced exchange reaction, ^{6}Li$(^2S)+$ ^{7}Li$_2(^3\Sigma_u^+) \overset{\hbar\omega_0}{\longleftrightarrow} (^6$Li^{7}Li^{7}Li$)^* \overset{\hbar\omega_0}{\longleftrightarrow} {}^6$Li^{7}Li$(^3\Sigma^+) +^7$ Li(^2S).

We first consider low collision energies and energetically narrow (~ 0.01 cm^{-1}) initial reactant wave packets. We show that it is possible to tune the reaction yield from 0 to near 100% (yield $\geq$ 99%). We control the laser-assisted reactive probability in the ^{7}Li$+^6$Li^{7}Li product channel by varying the following parameters:
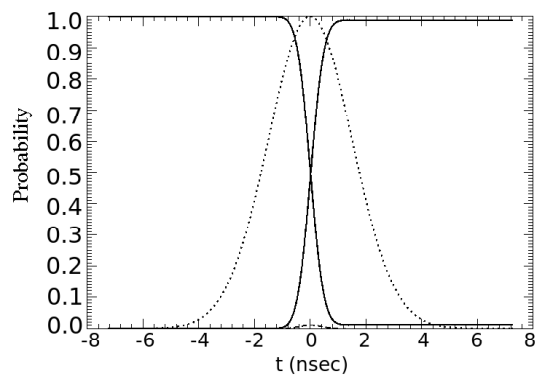
Figure 2.1: The integrated populations of the continuum and intermediate states. The dashed line is the intensity profile of the Gaussian pulse whose maximum intensity is 20 GW/cm^{-1}, the laser's temporal width is $\delta_t = 3$ nsec. The laser's carrier frequency ω_0 is chosen such that the laser is on resonance with the $|E_1\rangle$ state. The initial wave packet has a center energy of $E_o = -270.7$ cm^{-1}, and an energy band width of $\delta_E = 0.01$ cm^{-1}.

the laser intensity (P), the laser's temporal width (δ_t), the laser's carrier frequency (ω_0). We perform simulation with different energy bandwidths (δ_E) and center (average) energies (E_o) of the initial wave packet. The range of control obtained is truly impressive: Figure 2.1 shows that one can maximize the reaction probability to near 100%. By varying the above parameters we are in fact able to change the reaction probability from 0 to 99.9%. Thus we are able to suppress the naturally occurring reaction, as well as enhance it.

The reaction yield results are sensitive to the the center energy E_o of the wave packet. We find that the optimal reaction yield depends on the ratio of two *bound-continuum* dipole moments, $|\mu^-(E_o; i = 1, q = 1)|$ and $|\mu^-(E_o; i = 1, q = 2)|$, where $q = 1$ is the reactant arrangement and $q = 2$ is the product arrangement. This ratio of energy-dependent *bound-continuum* dipole moments is a function of E_o. Figure 2.2 describes the behavior of the optimized reactive yield versus the ratio of dipole moments for different chemical arrangements. It is clear that this ratio $|\mu(E_o; i = 1, q = 1, n = 0)/\mu(E_o; i = 1, q = 2, n = 0)|$ should be near unity in order to maximize the reaction yield. This phenomenon is analogous to Young's two slits

16
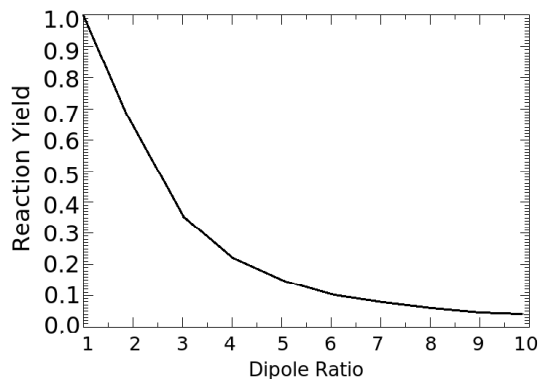
Figure 2.2: Reactive yield versus the ratio of two dipole moments in different channels. All experimental parameters have been optimized and we are using the $|E_1 >$ state to be the intermediate state.

experiment for which the highest fringe contrast is obtained when the slits widths are the same.

Controllability is somewhat reduced at collisions involving energetically wider (~ 1 cm^{-1}) initial reactant wave packets. At these energetic bandwidths the radiative reactive control, though still impressive, is limited to the range of $0 - 76\%$. However, we find that using the interference between the two intermediate states as an additional control mechanism can improve the controllability. This additional interference compensates for the relatively weakened interference between the optical route and the scattering route. With an equivalent range of experimental parameters, the reactive yield with one intermediate state is found to vary over a much smaller range than with two intermediate states.

More detailed information can be found in Appendix A or equivalently Ref. (76).

2.2 Population Transfer by Adiabatic Passage

The ability to completely transfer population from one chemical arrangement to another is very attractive to many researchers. But the need to use high laser intensities, up to TW/cm^2, has been a major stumbling block. Two possible

17

procedures for population transfers that require lower intensities are laser catalysis and adiabatic passage (AP).

Laser catalysis involves no net absorption of photons and usually requires a laser intensity of MW/cm^2 (60; 61; 62). The schematic process of laser catalysis has been described in the previous section. The conventional laser catalysis scenario uses a single laser pulse with a narrow energy bandwidth. No net photon absorption predicts different translational energies for the reactants and products when the diatoms have distinct energy levels. When a system consists of different atoms or isotopes, a single laser is not able to tune the product's translational energy for a fixed reactants translational energy. In a laser catalysis process conservation of the total energy of the molecular system enforces a relationship between the translational energies of the reactants and of the products when no net photon is absorbed. The ability to tune the reactants and products' translational energies requires a new theory.

Conventional AP (77; 78), on the other hand, involves three bound states and two slowly varying laser fields. The population is transferred from the initial bound state to the final bound state without populating the intermediate bound state. It is shown that the process follows the laser fields adiabatically to completely transfer the population to the desired final state. Vardi *et al.* (79) extends conventional AP theory to the photoassociation adiabatic passage (PAP). PAP involves one initial continuum state, one intermediate bound state, and one final bound state. In this process, the population of the intermediate state is suppressed to avoid spontaneous emission losses, and the process is assumed to be adiabatic when the lasers are varying slowly. Both conventional AP and PAP require a pump laser and a Stokes laser in a 'counter-intuitive' sequence, i.e. the Stokes pulse comes before the pump pulse ($t_p > t_s$). For conventional AP this mechanism can be understood in terms of *dark states* (80), and the intermediate state is not populated and thus the spontaneous decay lost can be minimized. But dark states do not formally exist in the PAP mechanism, and total suppression of the population of the intermediate state with a moderate laser intensity may be difficult (79).

Our goal is to derive a new control scenario which can be related to both laser catalysis and AP theories. We use two slowly varying laser pulses in a reactive

Intermediate bound state
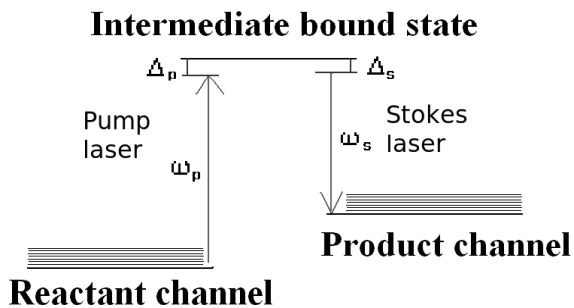
Figure 2.3: Schematic plot of population transfer by adiabatic passage with two pulsed lasers; ω_p and ω_s denote carrier frequencies of the pump laser and the Stokes laser, respectively, and Δ_p and Δ_s denote the detunings of the pump laser and the Stokes (dump) laser, respectively.

scattering process so as to keep the process adiabatic. We want to be able to tune the translational energies of continuum reactant and product states, and to minimize the population in the intermediate bound state. Fig. 2.3 shows a schematic of population transfer by adiabatic passage (PTAP) from the reactant channel to the product channel using two pulsed lasers. This PTAP theory can be applied to control the exchange process, in which one wishes to replace an atom attached to a molecule with another atom. PTAP can also be applied to control tuning of a vibrational mode, which uses two lasers to change the vibrational quantum number of the diatoms in an ensemble of cold or ultracold atom-diatom mixtures. In PTAP we can tune the carrier frequency of the Stokes (dump) laser to tune the translational energies of the final product.

We have derived a non-perturbative theory of PTAP using two laser pulses, for which more detailed information can be found in Section II of Ref. (81) or Appendix B. To apply this new theory, we thus envision a collinear collision between counter-propagating ^{6}Li and ^{6}Li^{7}Li beams, which can lead to either ^{6}Li^{6}Li+^{7}Li or ^{6}Li+^{6}Li^{7}Li. Note, PTAP can lead to the creation of four resultant wavepackets, with two associated centers energies E_o and $E_o + \omega_p - \omega_s$ for both of the chemical arrangements. We use q to denote the chemical arrangements, where $q = 1$ is for the reactants and $q = 2$ is for the products. Because we focus on collisions with

19
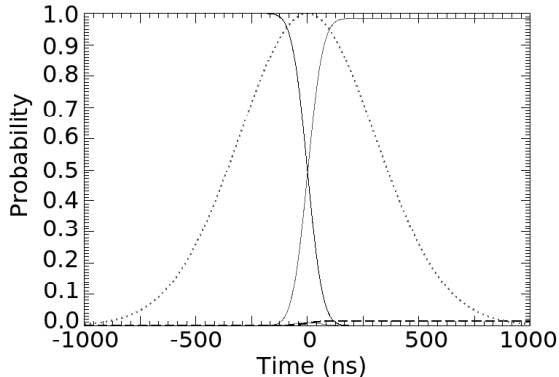
Figure 2.4: Integrated population of the reactant wavepacket centered at $|E = E_j - \omega_p, q = 1, n = 0>$, product wavepacket centered at $|E = E_j - \omega_s, q = 2, n = 0>$(solid lines), and reactant wavepacket centered at $|E = E_j - \omega_s, q = q, n = 0>$ (dashed lines) vs time; laser profile (dotted line) vs time; $T_p = T_r = 1$ mK, $\delta_E = 0.1$ mK, $\Delta_{ts} = \Delta_{tp} = 431$ ns, $t_p = t_s = 0$ and $I_p = 2.45$ GW/cm^2 and $I_s = 1$ MW/cm^2.

low translational energies, and $\omega_p > \omega_s$ for this study, the wavepacket with a center energy of E_o does not exist in the product arrangement, $q = 2$.

The two lasers do not have to be applied at the same time, and the sequence of these two lasers affect the dynamics of this process. We first study the coincident sequence when $t_p = t_s = 0$, where t_p and t_s denote the time to apply the pump laser and Stokes laser, respectively. Using two lasers with intensities $I_p = 2.45$ GW/cm^2 and $I_s = 1$ MW/cm^2 in the coincident sequence, we obtain a population transfer into the ^{6}Li^{6}Li+^{7}Li chemical arrangement with a probability of 98.44%. Here, I_p denotes the intensity of the pump laser, and I_s denotes the intensity of the Stokes laser. Fig. 2.4 shows the time dependence of the probabilities of the reactant, product, and intermediate states. Wavepackets centered at $|E = E_j - \omega_p, q = 1, n = 0>$ and $|E = E_j - \omega_s, q = 1, n = 0>$ contribute to the reactant probabilities, which are both minimized. Here, E_j denotes the energy of the jth bound intermediate state, ω_p denotes the pump laser carrier frequency, ω_s denotes the Stoke laser carrier frequency, q denotes the chemical arrangement, and n denotes quantum numbers associated with each arrangement. The total probability of the reactant wavepacket centered at $|E = E_j - \omega_s, q = 1, n = 0>$
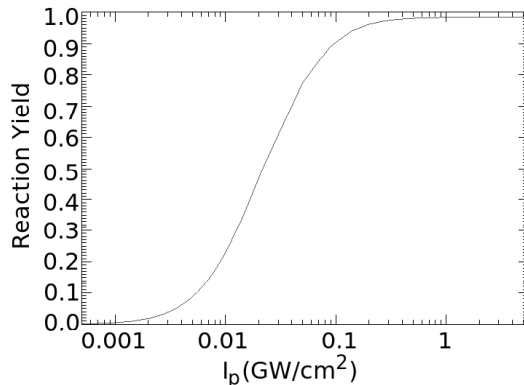
Figure 2.5: Reaction Yield versus laser intensity I_p. Here, $T = 1mK$, $\delta_E = 0.1$ mK, $t_p = t_s = 0$, $\Delta_{ts} = \Delta_{tp} = 431$ ns and I_s/I_p satisfies the relation in Eq. (27) in Ref. (81).

is 1.55%, and the probability that the system will stay in the initial reactant wavepacket centered at $|E = E_j - \omega_p, q = 1, n = 0 >$ is 0.01%.

When $t_p = t_s = 0$, the two-pulse PTAP theory is very similar to the laser catalysis theory, which uses only one pulsed laser. For population transfer, the triatomic system absorbs a photon from the pump laser and, simultaneously, the Stoke laser stimulates a photon emission while minimizing the population of the intermediate state; in laser catalysis, the system absorbs a photon and simultaneously emits the same photon into the field. The reaction yield of PTAP monotonically increases with increasing laser intensities, as shown in Fig. 2.5. This behavior is very similar to Fig. 9 of Vardi and Shapiro's laser catalysis paper (61).

We also need to study the intuitive sequence of the two lasers. When $t_p < t_s$, the pump pulse precedes the Stokes pulse, and the maximum reaction yield requires the pulses to overlap appreciably. Because the optimized reaction yield with an intuitive sequence is very close to the reaction yield obtained with a coincident sequence, we do not show the time-dependent probabilities of all possible states. But the relationship between laser intensities and the reaction yield in the intuitive sequence with the ratio I_s/I_p fixed, as shown in Fig. 2.6, differs from that in the coincident sequence. The reaction yield has a clear maximum with respect to laser intensities; merely increasing the pulse intensity does not improve the transfer
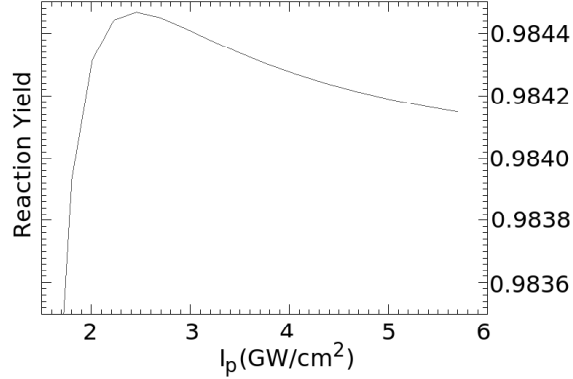
Figure 2.6: Reaction Yield versus laser intensity I_p. Here, $T = 1mK$, $\delta_E = 0.1$ mK, $t_p = -t_s = 12$ ns, $\Delta_{ts} = \Delta_{tp} = 431$ ns and I_s/I_p satisfies the relation in Eq. (27) in Ref. (81).

yield. This feature is similar to the radiative recombination studies by Vardi *et al.* (79), where the system has two bound states and one continuum state. In PTAP, if one decreases $|t_p - t_s|$, thereby increasing the overlap of the pulses, then the maxima occurs at a higher intensity. In the $t_p - t_s = 0$ limit, the location of the maximum approaches positive infinity, where a PTAP with the intuitive sequence becomes one with the coincident sequence and the reaction yield monotonically increases with increasing laser intensity.

When $t_p > t_s$ the Stokes pulse precedes the pump pulse, which leads to a "counter-intuitive" sequence. However, the reaction yield obtained with an counter-intuitive sequence is far smaller than that with an intuitive sequence or coincident sequence. This result is surprising because the conventional AP process favors the counter-intuitive sequence as promising greater reaction yield (77; 78). The underlying mechanism of this surprising result is still unclear and is currently under investigation.

To summarize, we develop a new theory, PTAP, which connects the laser catalysis theory with the AP theory. This PTAP theory uses two pulsed lasers with distinct carrier frequencies to control an exchange reaction. The merit of this theory is in the ability to choose the final products' translational energy. We apply this theory to control the collisions of the time-dependent ultracold mixtures of the

22

$^6\text{Li}^6\text{Li}^7\text{Li}$ system. We show that to obtain the maximum reaction yield ($\geq 98\%$) one should apply the pump laser and the Stokes laser either in an intuitive sequence or a coincident sequence instead of the counter-intuitive sequence.

2.3 Formation of Ultracold Molecules

The existence of Bose-Einstein Condensates (BEC) of various atoms (82), and the possibility of the production of their molecular analogues (83; 84; 85; 86; 87; 4) has spurred great interest in reactions between ultracold, bosonic or fermionic (spin-aligned) molecules. In recent years, several molecular schemes such as buffer-gas cooling (3) and Stark deceleration (2) have produced electronic ground state molecules at cold temperatures (1 mK), while Feshbach resonances (5; 6) have produced ground state molecules at ultracold temperatures (< 1 μK). However, more general schemes of producing homonuclear or heteronuclear molecules are still being pursued. In the following two studies, we advocate an alternative way of producing diatomic molecules with a fast rate.

2.3.1 Homonuclear Molecules

In this study we show that the involvement of pulsed lasers of moderate intensities in the reactions between *cold* reactants can lead to the production of *ultracold* diatomic molecules. We propose achieving this goal via the "laser catalysis" scenario (60; 61; 62; 88; 76; 63). In this scenario the pulsed laser assists the A+BC $\rightarrow$ AB+C reaction by first forcing a (virtual) transition of the A+BC reactants to the (ABC)* excited state complex (ESC). The ESC then undergoes a stimulated emission process to the AB+C ground state products, emitting a photon identical to the photon just absorbed. Therefore, no net photons are absorbed in this process, which justifies the name "laser catalysis". When the process is done coherently and the intensity of the laser is high enough, the system would change smoothly from reactants to products, with the ESC "stepping stone" remaining unpopulated even in a transient way (60), thus minimize the spontaneous emission loss.

As an illustration of this concept we apply this technique to the A=$^6\text{Li}(^2S)$, B=$^6\text{Li}(^2S)$ and C=$^7\text{Li}(^2S)$ triatomic system. The diatomic molecules AB = $^6\text{Li}_2$

Intermediate State (^{6}Li^{6}Li^{7}Li)*
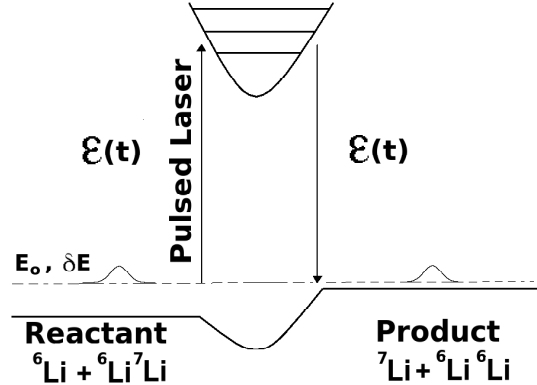
Figure 2.7: Schematic energy levels of ^{6}Li^{6}Li^{7}Li system in the laser catalysis scheme

($^3\Sigma_u^+$) and BC = ^{7}Li^{6}Li ($^3\Sigma^+$) are taken to be in their lowest spin-aligned electronic states. The triatomic states are the $1^4A'$ states for the reactants and products, and the $1^4A''$ states for the ESC (ABC)*. The zero energy is chosen to be at the three-body break up limit ($^2S + {}^2S + {}^2S$). There is no natural barrier in the reaction path between chemical arrangements of the quartet ^{6}Li^{6}Li^{7}Li system. We note, however, that the lowest vibrational energy of the triplet ^{6}Li^{7}Li state is calculated to be $E(q = 1, v = 0) = -300.51194$ cm^{-1}, while the lowest vibrational energy of the triplet ^{6}Li^{6}Li state is calculated to be slightly higher, at $E(q = 2, v = 0) = -299.29412$ cm^{-1}. Fig. 2.7 shows the schematic energy levels of the current ^{6}Li^{6}Li^{7}Li in a laser catalysis scenario.

We thus envision a collinear collision between counter propagating ^{6}Li and ^{6}Li^{7}Li beams, having zero center of mass velocity. Each beam is prepared with translational temperatures of $T_r \approx 1.75$ K. By tuning the laser center-frequency to be on exact resonance with a transition to one of the bound states of the ESC, we can make use of the energetic difference between the reactant and product diatoms' vibrational levels to produce the ^{6}Li^{6}Li at *ultracold* temperatures. These temperatures range between 0.01 mK and 1 mK, depending on the band-width of the laser used. The intervention of the laser is necessary because at translational temperatures of 1.75 K the non-radiative reaction probability is negligible ($< 1\%$).
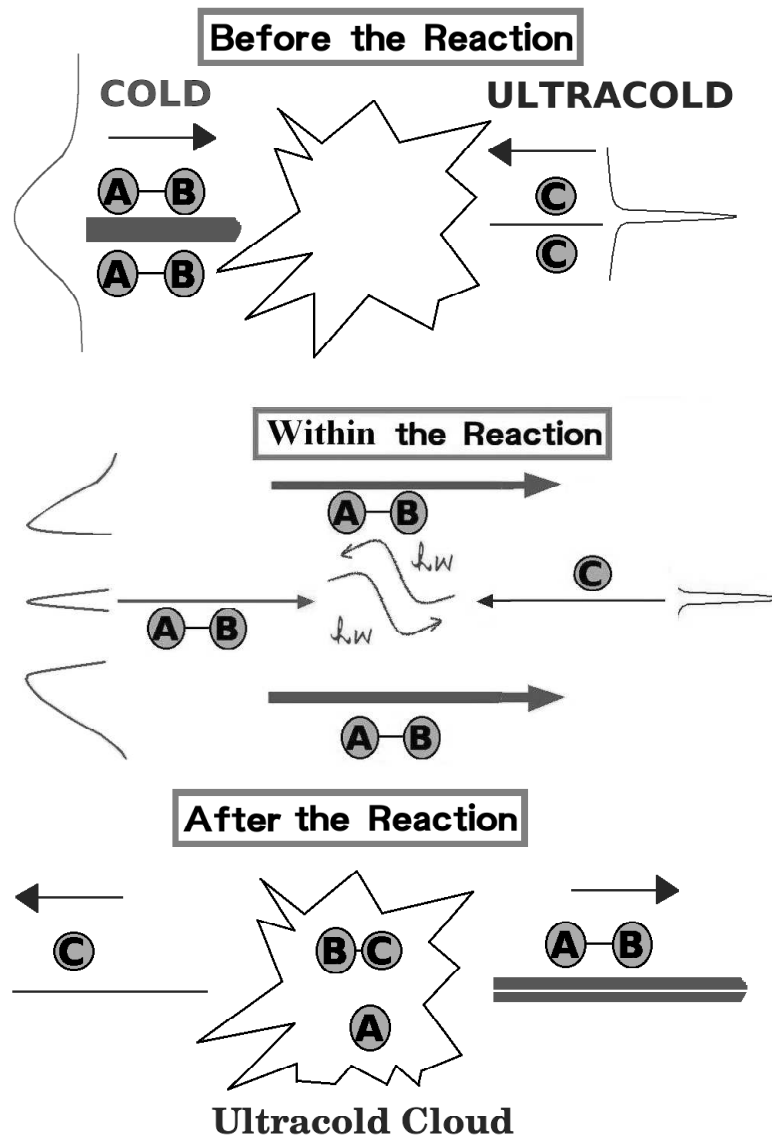
Figure 2.8: Schematic plot of the control process

In order to achieve the desired ultracold product temperature, we choose the resonance condition in which the detuning parameter defined as $\Delta \equiv \omega_o - E_j + E_o$ is equal to zero. Here, ω_o is defined as the laser's carrier frequency, E_j is energy of the jth bound state of the ESC, and E_o is the center energy of the initial wavepacket. In this way a energetically narrow (e.g. $\Delta_t = 431$ ns -43.1 μs) transform-limited laser pulse carves out of the $T_r = 1.75$ K initial reactant distribution a narrow energetic component whose band-width is ~ 0.01 mK-1 mK and transforms it into products of roughly ~ 0.01 mK-1 mK. Therefore, the molecular reactants, ^{6}Li^{7}Li, can be prepared with a Maxwell-Boltzmann distribution at $T_r \approx 1.75$ K. The atomic beam can be prepared with a narrow energy bandwidth ($\delta_E \approx 0.01$mK ~ 1 mK) to enhance the final reaction. With a typical experimental error (10% to 20%) in preparing the translational energies of the initial atomic species, the narrow energy bandwidth (δ_E) of the atomic species ^{6}Li and a narrow laser pulse will filter out the ultracold portion of the initial molecular beam of ^{6}Li^{7}Li reacting with ^{6}Li to form an ultracold cloud of ^{6}Li^{6}Li and ^{7}Li. Depending on the experimental error in beam preparation, the product cloud will then move uniformly in one direction with a known center of mass (CM) velocity. This slow CM motion can be calculated and is expected to be at least three to four times slower than the reactants and thus can be removed by a molecular optical lattice. Fig. 2.8 shows the schematic plot of this control process.

Figure 2.9 shows the time dependence of the probabilities in each state using a laser with an intensity of $I = 13.7$ MW/cm^2 and a temporal width of $\Delta_t = 431$ ns. The reaction yield of the ultracold ($T_p = 1$ mK) product is shown to be 99.3% when the non-radiative reaction probability at this temperature is negligible ($< 1\%$). It then clearly shows that the laser enhances the naturally suppressed chemical reactions. The probability of the intermediate state $|E_{j=27}\rangle$ (dashed line in Fig. 2.9) remains very small compared to that of the reactant or product so that spontaneous emission is negligible. Note, the decay rate of the intermediate state is taken to have a typical value of $1/\Gamma(= 30ns)$ and the spontaneous emission loss is clearly shown in Fig. 2.9 to be minimal.

To illustrate the effect of the laser intensity, Fig. 2.10 shows the reaction yield as a function of the laser intensity with other parameters being fixed as they are
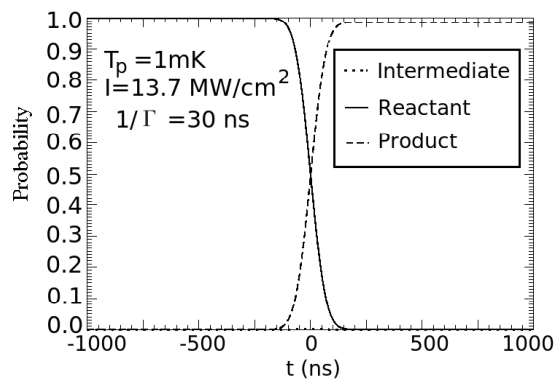
Figure 2.9: Population of the reactant (red solid lines), product (blue solid line), and intermediate (dashed line of near zero value) states, and laser profile (dotted line) vs. time; $T_p = 1$ mK
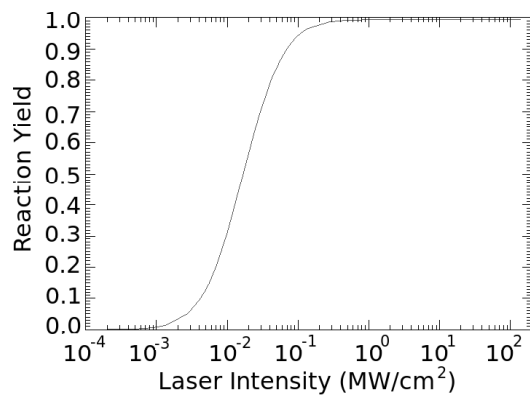
Figure 2.10: Reaction yield vs laser intensity; $T_p = 1$ mK
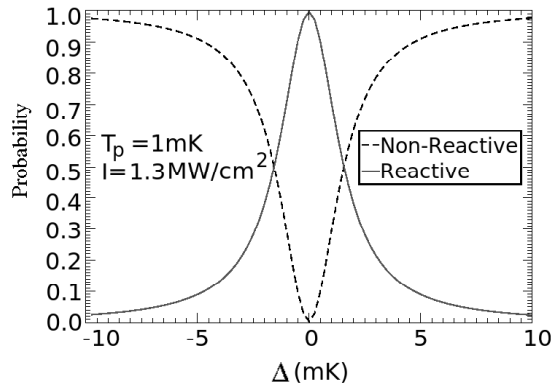
Figure 2.11: Reaction yield vs laser detuning; $T_p = 1$ mK

in Fig. 2.9. Before reaching saturation at $I \sim 2$ MW/cm^2, the reaction yield increases monotonically with increasing laser intensity. However, it is necessary to use a much higher intensity of $I \geq 10$ MW/cm^2 in order to avoid spontaneous emission loss from the intermediate bound state. The intense laser pulse couples the material state with the field state to form two dressed states, and more details about these two dressed states can be found in Ref. (60). In this way the population follows adiabatically from the reactants to the products on the ground dressed state without populating the intermediate state significantly (60).

Total suppression of the reaction scattering process can also be achieved which enables the selectivity of the procedure. For instance, if we use a detuning of $\Delta = 3 \times 10^{-3}$ cm^{-1} with the other parameters take as in Fig. 2.9, total suppression results, which is shown in Fig. 2.11. This total suppression is due to destructive interference between the optical and the non-radiative reactive process. This total suppression leads to the precise filtering of the ultracold piece of the reaction.

The production rate of the ultracold ^{6}Li^{6}Li diatoms, for the $T_p = 1$ mK case, is estimated to be 4×10^5 /s. This estimate is based on the temporal width of the pulse, the percentage of the carved portion of the broadly distributed initial molecular beam, and a typical molecular beam density of 10^{12} cm^{-3}.

We conclude that by using laser catalysis we can employ translationally cold ($T_r \approx 1.75$ K) collisions to produce *ultracold* (0.01 mK $< T_p <$ 1 mK) (homonuclear) molecules (63). We illustrate this approach by studying the laser catalysis

Intermediate State (^{6}L$_i$^{7}L$_i$^{7}L$_i$)*
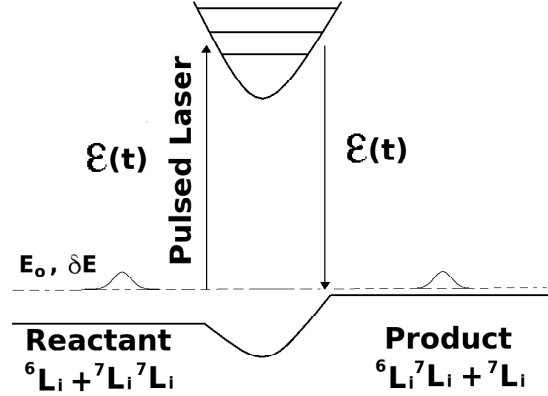
Figure 2.12: Schematic energy levels of ^{6}Li^{7}Li^{7}Li system in the laser catalysis scenario

of the ^{6}Li+^{6}Li^{7}Li $\xrightarrow{\hbar\omega}$ $\left(^6\text{Li}^6\text{Li}^7\text{Li}\right)^*(1^4A'')$ $\xrightarrow{\hbar\omega}$ ^{6}Li^{6}Li+^{7}Li reaction in the collinear approximation. Ultracold ^{6}Li^{6}Li product molecules are shown to be produced at an extraordinary yield of up to 99.97%, using moderate laser intensities of $I = 100$ kW/cm^2 $- 10$ MW/cm^2. The production rate of the ultracold ^{6}Li^{6}Li diatoms, for the $T_p = 1$ mK case, is estimated to be 4×10^5 /s.

More detailed information can be found in Appendix C or equivalently Ref. (63).

2.3.2   Heteronuclear Molecules

Heteronuclear molecules in low-lying vibrational states are particularly interesting since they exhibit a permanent electric dipole moment. Large induced dipole moments of the polar heteronuclear molecules can enable many fundamental studies of ultracold molecules such as quantum information devices (89), experimental searches of the electron dipole moment (90), and creation of dipolar superfluids (91). Different groups have shown theoretically and experimentally the possibility of creating different heteronuclear alkali molecules such as RbCs (92), KRb (93) and NaCs (94).

We consider quantum control of the reactive scattering process where the atoms are A=^{6}Li(^2S), B=^{7}Li(^2S) and C=^{7}Li(^2S) in the ultracold regime. The diatomic

molecules AB=^{6}Li^{7}Li($^3\Sigma^+$) and BC=^{7}Li$_2$($^3\Sigma_u^+$) are taken to be in their lowest spin-aligned electronic states. The triatomic states are the $1^4A'$ states for the reactants and products, and the $1^4A''$ states for the ESC (A-B-C)*. The zero of energy is chosen to be at the three-body break up limit ($^2S +^2 S +^2 S$). There is no natural barrier in the reaction path between chemical arrangements of the quartet ^{6}Li^{7}Li^{7}Li system. However, the lowest vibrational energy of the triplet ^{7}Li^{7}Li state is calculated to be $E(q = 1, v = 0) = -1.37501101 \times 10^{-3}$ Hartree, while the lowest vibrational energy of the triplet ^{6}Li^{7}Li state is calculated to be $E(q = 2, v = 0) = -1.36923315 \times 10^{-3}$ Hartree. Note, Hartree is the atomic unit for energy and it is usually denoted as Ha.. Therefore, the initial reactant ^{6}Li+^{7}Li^{7}Li is prepared at a cold temperature of $T_r \approx 1.8$ K, then is subjected to a moderate laser field ($I = 1 \sim 100$ MW/cm^2) and transferred to the product arrangement ^{6}Li+^{7}Li^{7}Li with an ultracold temperature of 0.01 mK $\leq T_p \leq 1$ mK. Here, T_r and T_p denote the temperatures in the reactant arrangement and the product arrangement respectively, and are thus defined as $T_r = [E - E(q = 1, v = 0)]/K_B$ and $T_r = [E - E(q = 2, v = 0)]/K_B$, where K_B is the Boltzmann constant. Fig. 2.12 shows schematic energy levels of the current ^{6}Li^{7}Li^{7}Li in a laser catalysis scenario. At the ultracold temperature, T_p, the non-radiative tunneling probability is negligible ($< 1\%$) and thus a laser catalysis scenario is useful to achieve the optimum controllability.

We show that the cold ($T_r \approx 1.8$ K) reactant ^{6}Li+^{7}Li^{7}Li, when optically coupled to the intermediate bound states on the $1^4A''$ electronic PES, can be transferred to the ultracold (0.01 mK $\leq T_p \leq 1$ mK) product arrangement ^{7}Li+^{7}Li^{6}Li with a reactive yield of up to 99.8% with a laser intensity of $I = 1 \sim 100$ MW/cm^2. For the $T_p = 0.01$ mK case, shown in Fig. 2.13, the reactive yield is optimized to be 99.8% with an intensity of $I = 1.37$ MW/cm^2. The probability of the intermediate state $|E_j>$ (dashed line in Fig. D.2) is negligible compared to that of the reactant or product so that spontaneous emission is essentially nonexistent. The production rate of the ultracold ^{6}Li^{6}Li diatoms, for the $T_p = 1$ mK case, is estimated to be 4×10^5 /s.

More detailed information can be found in Appendix D.
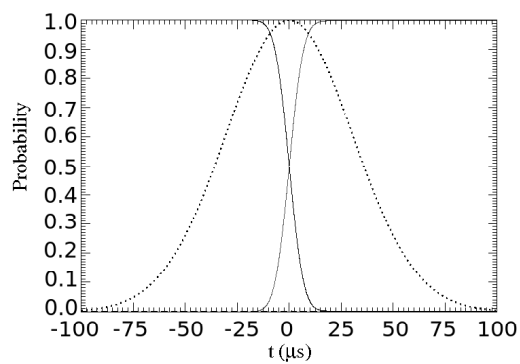
Figure 2.13: Integrated population of the reactant, product (solid lines) and intermediate state (dashed lines) vs time; laser profile (dotted line) vs time; $T_p = 0.01$ mK

Part III

Geometric Phase

Chapter 3

Conventional Geometric Phase Theory

3.1   Introduction

We mentioned in Chapter 1 that the geometric phase effect may lead to nontrivial consequences for molecular structures and dynamics on these crossing electronic PESs. There are in general three ways to treat the geometric phase problem:

- Use a double-valued basis set in both the electronic and nuclear wavefunctions (101).

- Use an electronic diabatic representation   (8; 102; 103; 104).

- Use the vector potential method (14).

The first procedure uses a real double-valued basis set in both the electronic and nuclear wavefunctions. This procedure has been applied to the H_3 system and its isotopomers (isotopic isomers). The simplicity of using this procedure results when the double-valuedness is easy to add explicitly in the nuclear wavefunctions. However, this double-valuedness is difficult to add in "manually" for the general case, in which the geometric phase angle can be a complicated function of all nuclear coordinates. Take the triatomic spin-aligned lithium system. The seams of conical intersections between the lowest two PESs are located in the collinear geometries and there are three seams of these conical intersections. Also, the angle η, which describes the rotation about the seam of conical intersections, can have a complicated dependence on nuclear coordinates. Thus, the construction of a real double-valued basis set of the nuclear wavefunctions is not trivial.

The second procedure uses an electronic diabatic representation, which does not explicitly depend on the nuclear coordinates and thus the nonadiabatic couplings do not exist. This procedure has the merit of using a single-valued basis set of nuclear wavefunctions. The double-valuedness is carried in the electronically adiabatic-to-diabatic transformation, and the resultant Hamiltonian in this diabatic representations is free of the double-valuedness problem. The difficulty of using the diabatic representation lies mainly in the adiabatic-to-diabatic transformation. One needs to be able to keep track of phases of the adiabatic-to-diabatic transformation matrix so that it carries the double-valuedness so that the diabatic representations is single-valued.

The third procedure, which uses a vector potential to treat the geometric phase, is a more general way to include geometric phase effects. In this procedure, we multiply the real double-valued electronic adiabatic wavefunction by a complex double-valued phase factor to cancel the double-valuedness. This phase factor results in vector potential terms in the Hamiltonian (14), and more detailed information will be provided in the next section. Kendrick and Pack has applied this vector potential method to H+O$_2$ (105), Na$_3$ (106) and H+D$_2$ (107).

In this study we focus on the use of vector potential techniques to treat the geometric phase effect in a triatomic system. We will briefly review the conventional derivation of the vector potentials for a Jahn-Teller system in which the conical intersections are nonlinear.

3.2 Vector Potential

The molecular Schrodinger equation is given by

$$\hat{H}\Psi_{tot}(\vec{R},\vec{r}) = E\Psi_{tot}(\vec{R},\vec{r}), \tag{3.1}$$

where $\Psi_{tot}(\vec{R},\vec{r})$ is the total molecular wavefunction of the nuclear coordinate $\vec{R}$ and the electronic coordinate $\vec{r}$, $\hat{H}$ is the total molecular Hamiltonian, and E is the total energy. In this thesis we focus on the triatomic system. Thus, we choose to use the adiabatically adjusting, principal axes hyperspherical (APH) coordinates $(\rho,\theta,\chi,\alpha_Q,\beta_q,\gamma_Q)$ formulated in Pack and Parker's work (108), which

is similar to Smith-Johnson's coordinates (109; 110) except for $2\chi = \phi$. More detailed information on this APH coordinates can be found in Appendix E.3. We distinguish two types of nuclear coordinates by expressing $\vec{R} = (R, \hat{R})$ in which $R = (\rho, \theta, \chi)$ for the three internal coordinates and $\hat{R} = (\alpha_Q, \beta_q, \gamma_Q)$ for the three Euler angles. In this study, we concentrate on the geometric phase effect at ultracold temperatures, where the the angular momentum are negligible. Therefore, we ignore all the spin-orbit couplings and consider only the Coulomb interactions. The inclusion of spin-orbit couplings would not change the qualitative results of the geometric effect. We also ignore the relativistic effects which is negligible for an ultracold reactive scattering process.

We can express $\hat{H}$ in space-frame(SF) coordinates as

$$\hat{H} = -\frac{\hbar^2}{2\mu}\nabla^2 + \hat{H}_e(R), \tag{3.2}$$

where ∇^2 is the six-dimensional Laplacian with respect to $\vec{R}$, μ is the three-body reduced mass, and $\hat{H}_e$ is the electronic Hamiltonian which depends on the three internal coordinates, R, parametrically. We choose to use the adiabatic representation of the electronic wavefunction, φ_n. φ_n is an eigenvector of the electronic Hamiltonian $\hat{H}_e$

$$\hat{H}_e\varphi_n(\vec{r}; R) = V_n(R)\varphi_n(\vec{r}, R), \tag{3.3}$$

where $n = 0$ denotes the ground state. The electronic Hamiltonian and the eigenvalues are real and we can choose the electronic wavefunctions to be real.

We use the Born-Oppenheimer expansion of the total molecular wavefunction in Eq. (3.1)

$$\Psi_{tot}(\vec{R}, \vec{r}) = \sum_{n=0} \Psi_n(\vec{R})\varphi_n(\vec{r}, R), \tag{3.4}$$

where the expansion coefficients $\Psi_n(\vec{R})$ are the nuclear wavefunctions. At a low collision energy with non-degenerate ground electronic PES, we can ignore the coupling to the excited electronic states $\varphi_{n \neq 0}$ and use a one-state approximation (8),

$$\Psi_{tot}(\vec{R}, \vec{r}) \approx \Psi_0(\vec{R})\varphi_0(\vec{r}, R). \tag{3.5}$$

For simplicity, we drop the subscript 0 from now on.

We substitute Eq. (3.5) into Eq. (3.1), multiply it on the left by $\varphi(\vec{r}, R)$, integrate over $\vec{r}$ and we obtain

$$\left\{ -\frac{\hbar^2}{2\mu} \nabla^2 + V(R) \right\} \Psi(\vec{R}) = E\Psi(\vec{R}), \qquad (3.6)$$

where the electronic wavefunction is real double-valued. Because the total wavefunction Ψ_{tot} needs to be single-valued, the associated nuclear wavefunction $\Psi(\vec{R})$ is double-valued. Both of the electronic and nuclear wavefunctions change sign when the nuclear motion encircles a conical intersection between the ground and excited electronic PESs. It is, in general, complicated to put in a mechanism to make the nuclear wavefunction double-valued and thus change sign as it completely transverses the conical intersections. We multiply the real double-valued electronic wavefunction by a complex phase (14)

$$\bar{\varphi}(\vec{r}, R) = \exp\left(i\frac{l}{2}\eta(R) \right) \varphi(\vec{r}, R), \qquad (3.7)$$

where l is an odd integer and $\eta(R)$ is a "rotating" angle which is defined to change by 2π for any nuclear motion which encircles a conical intersection an odd number of times. With the inclusion of the phase factor, the $\bar{\varphi}(\vec{r}, R)$ electronic wavefunction is complex single-valued. And, therefore, the nuclear wavefunction is single-valued.

The adiabatic electronic functions defined in Eq. (3.3) are body-frame (BF) electronic wavefunctions, which are needed to rotate to the SF electronic wavefunctions

$$\bar{\varphi}(\vec{r}, \vec{R})(SF) = U(\alpha_Q, \beta_Q, \gamma_Q)\bar{\varphi}(\vec{r}, R)(BF) \qquad (3.8)$$

where U is the rotation operator. It is explicitly defined as (105; 111)

$$U(\alpha_Q, \beta_Q, \gamma_Q) \equiv e^{-l_{ex}\alpha_Q} e^{-l_{ey}\beta_Q} e^{-l_{ez}\gamma_Q} \qquad (3.9)$$

where $l_{ei}, i = x, y, z$ are the components of the total electronic angular momentum in the BF.

Using Eq. (3.7) and Eq. (3.8), we derive the new Schrodinger equation for the molecular system

$$\left\{ \frac{\hbar^2}{2\mu}(-i\nabla - \mathbf{A}(\vec{R}))^2 + \varepsilon(\vec{R}) \right\} \bar{\Psi}(\vec{R}) = E\bar{\Psi}(\vec{R}), \qquad (3.10)$$

36

where $\mathbf{A}(\vec{R})$ is the vector potential defined as

$$\mathbf{A}(\vec{R}) \equiv i \left\langle \bar{\varphi}(\vec{r}, \vec{R}) | \nabla | \bar{\varphi}(\vec{r}, \vec{R}) \right\rangle \tag{3.11}$$

and $\varepsilon(\vec{R})$ is the effective scalar potential defined as (112)

$$\begin{aligned} \varepsilon(\vec{R}) &\equiv V(R) \quad -\frac{\hbar^2}{2\mu} \sum_{m=0} \left\langle \bar{\varphi}_0(\vec{r}, \vec{R}) | \nabla | \bar{\varphi}_m(\vec{r}, \vec{R}) \right\rangle \\ &\times \left\langle \bar{\varphi}_m(\vec{r}, \vec{R}) | \nabla | \bar{\varphi}_0(\vec{r}, \vec{R}) \right\rangle. \end{aligned} \tag{3.12}$$

We can separate the Laplacian operator as $\nabla = \nabla_R + \nabla_{\hat{R}}$, and we express the vector potential $\mathbf{A}(\vec{R})$ as (105)

$$\mathbf{A}(\vec{R}) = \mathbf{A}(R) + \mathbf{A}(R, \hat{R}) \tag{3.13}$$

where

$$\mathbf{A}(R) = -\frac{l}{2} \nabla_R \eta(R), \tag{3.14}$$

$$\mathbf{A}(R, \hat{R}) \equiv i \left\langle \bar{\varphi}_0(\vec{r}, \vec{R}) | U^{-1}(\hat{R}) \left(\nabla_{\hat{R}} U(\hat{R}) \right) | \bar{\varphi}_0(\vec{r}, \vec{R}) \right\rangle \tag{3.15}$$

However, there are two things to be noticed for the special system we study:

- We are interested in chemical reactions with very low scattering energies and, therefore, the effect of the excited electronic PESs can be neglected.

- For collisions at ultracold temperatures, the three chemical arrangements are assumed to have low electronic orbital angular momentum. Thus, for low energy collisions, the total electronic angular momentum l_e is small.

Based on these two arguments, we can neglect $\mathbf{A}(R, \hat{R})$ and the second term in Eq. (3.12). Therefore, Eq. (3.10) can be rewritten as

$$\left\{ \frac{\hbar^2}{2\mu} (-i\nabla - \mathbf{A}(R))^2 + V(R) \right\} \bar{\Psi}(\vec{R}) = E \bar{\Psi}(\vec{R}). \tag{3.16}$$

Following the derivation in Ref. (105), we obtain the molecular kinetic energy operator in Eq. (3.16) in terms of the one-form components $\mathbf{A}(R) = (A_\rho, A_\theta, A_\chi)$

$$
\begin{aligned}
\frac{\hbar^2}{2\mu}(-i\nabla - \mathbf{A}(R))^2 = \ &- \frac{\hbar^2}{2\mu}\left(\frac{\partial}{\partial\rho}\rho^5\frac{\partial}{\partial\rho} + \frac{4}{\rho^2\sin 2\theta}\frac{\partial}{\partial\theta}\sin 2\theta\frac{\partial}{\partial\theta} + \frac{1}{\rho^2\sin^2\theta}\frac{\partial^2}{\partial\chi^2}\right) \\
&+ \frac{J_x^2}{\mu\rho^2(1+\sin\theta)} + \frac{J_y^2}{\mu\rho^2\sin^2\theta} + \frac{J_z^2}{\mu\rho^2(1-\sin\theta)} \\
&+ i\frac{\hbar^2}{2\mu}\left[\frac{5}{\rho}A_\rho + \frac{\partial A_\rho}{\partial\rho} + \frac{8\cot 2\theta}{\rho^2}A_\theta + \frac{4}{\rho^2}\frac{\partial A_\theta}{\partial\theta}\right. \\
&+ \left.\frac{1}{\rho^2\sin^2\theta}\frac{\partial A_\chi}{\partial\chi} + 2A_\rho\frac{\partial}{\partial\rho} + \frac{8}{\rho^2}A_\theta\frac{\partial}{\partial\theta} + \frac{2}{\rho^2\sin^2\theta}A_\chi\frac{\partial}{\partial\chi}\right] \\
&+ \frac{\hbar^2}{2\mu}\left[A_\rho^2 + \frac{4}{\rho^2}A_\theta^2 + \frac{1}{\rho^2\sin^2\theta}A_\chi^2\right] - \frac{i\hbar\cos\theta}{\mu\rho^2\sin^2\theta}J_y\frac{\partial}{\partial\chi} \quad (3.17)
\end{aligned}
$$

It should be noticed that this kinetic energy operator includes complex terms and thus needs special treatment. We divide the problem into two categories: conical intersections in the C_{2v} geometries and conical intersections in the $C_{\infty v}$ geometries. Here, C_{2v} and $C_{\infty v}$ are different symmetry groups the molecular system belongs to. In a AB$_2$ system, when R_{AB_1} and R_{AB_2} are equal to the other, this system belongs to the C_{2v} symmetry group; when the three atoms are collinear, the system belongs to the $C_{\infty v}$ group. We will show in chapter 4 that the conical intersections in the C_{2v} geometries would lead to a complex Hamiltonian in the internal coordinates, (ρ, θ, χ). We will develop a Mixed-Odd-Even-States (MOES) method to create real interaction matrices and overlap matrices to be used in the propagation in the hyperradius ρ. We will show in chapter 5 that conical intersections in the $C_{\infty v}$ geometries would lead to a real Hamiltonian (the $J = 0$ case) in the internal coordinates, (ρ, θ, χ).

Chapter 4

The C_{2v} conical intersections

4.1 Introduction

The HD$_2$ and HO$_2$ systems have conical intersections in the C_{2v} geometries for the lowest doublet states. If one chooses the chemical arrangements B and C to be identical in these cases, the potential energy surfaces are then symmetric with respect to the $\phi \rightarrow -\phi$ operation where ϕ is one of the symmetric spherical internal coordinates (109; 110). The geometric phase angle η, which describes the rotation around the seam of conical intersections, is then antisymmetric with respect to the $\phi \rightarrow -\phi$ operation (101; 105). We will use this section to describe the solution to problems of this category.

If we want to solve for cross-sections or reaction probabilities in the time independent picture, we can use propagation methods, e.g. the Log-derivative method (113) and the Numerov method (114). Both methods propagate the nuclear wavefunction from the inner region with a small hyperradius to the asymptotic region with a large hyperradius, where the proper boundary conditions are applied to match onto the asymptotic behaviors of the nuclear wavefunction. Both propagation methods, the Log-derivative method and the Numerov method change the differential equation to a difference equation so that we can propagate the nuclear wavefunction from one hyperradius sector to the next hyperradius sector. The effective potential terms and the overlap matrices, which are used in these propagation methods, are obtained by first solving (diagonalizing) the two-dimensional

surface Hamiltonian which only parametrically depends on the hyperradius ρ. Details of the effective potential terms and the overlap matrices will be provided in the next subsection. However, Eq. (3.17) shows that the kinetic energy operator in the SF, in general, contains the first derivative terms $\partial/\partial\rho$ and complex terms. These two aspects pose problems when one wishes to use the Log-derivative propagator. On the contrary, using the Numerov propagator one can circumvent this theoretical obstacle because it does not include the first derivative terms $\partial/\partial\rho$ in the propagation.

We now derive some symmetry properties of the A_θ and A_χ vector components and their first derivatives. We know that the geometric phase angle η is antisymmetric under the symmetry operation $\eta(-\chi) \rightarrow -\eta(\chi)$ (101; 105). Therefore, using the definition of A_θ and A_χ in Eq. (3.14), we have

$$
\begin{aligned}
A_\theta(\rho,\theta,-\chi) &= -A_\theta(\rho,\theta,\chi) \\
\left(\frac{\partial A_\theta}{\partial\theta}\right)(\rho,\theta,-\chi) &= -\left(\frac{\partial A_\theta}{\partial\theta}\right)(\rho,\theta,\chi)
\end{aligned}
\tag{4.1}
$$

and

$$
\begin{aligned}
A_\chi(\rho,\theta,-\chi) &= +A_\chi(\rho,\theta,\chi) \\
\left(\frac{\partial A_\chi}{\partial\chi}\right)(\rho,\theta,-\chi) &= -\left(\frac{\partial A_\chi}{\partial\chi}\right)(\rho,\theta,\chi).
\end{aligned}
\tag{4.2}
$$

4.2 SVD treatment of Geometric phase

In this section, we use a combination of a smooth variable discretization (SVD) with an enhanced renormalized Numerov propagator (115). The purpose of this method is to eliminate the first derivative $\partial/\partial\rho$ and complex parts so that the propagation is kept real. Note that, this does not change the total complex form the molecular Hamiltonian, which then needs a special treatment to obtain real overlap matrices.

We start from the molecular Hamiltonian for the nuclear and electronic motions

$$
H = \frac{\hbar^2}{2\mu\rho^5}\frac{\partial}{\partial\rho}\rho^5\frac{\partial}{\partial\rho} + h_{int}(\rho,\hat{\Omega},\vec{r})
\tag{4.3}
$$

where h_{int} contains the Laplacian operator of the five angular coordinates $\hat{\Omega} \equiv (\theta, \chi, \alpha_Q, \beta_Q, \gamma_Q)$ and the electronic Hamiltonian $H_e(\vec{r}; R)$. We can express the time-independent Schrodinger equation as

$$(H - E)\Psi^{JMi} = 0 \tag{4.4}$$

where i denotes initial.

If we write the total molecular wavefunction Ψ^{JMi} as

$$\Psi^{JMi} = \frac{1}{\rho^{5/2}}\psi^{JMi}, \tag{4.5}$$

we can rewrite Eq. (4.3) as

$$H = \frac{\hbar^2}{2\mu}\frac{\partial^2}{\partial\rho^2} + H_{int}(\rho, \hat{\Omega}, \vec{r}) \equiv \frac{\hbar^2}{2\mu}\frac{\partial^2}{\partial\rho^2} + \frac{15\hbar^2}{2\mu\rho^2} + h_{int}(\rho, \hat{\Omega}, \vec{r}). \tag{4.6}$$

We then rewrite Eq. (4.4) as

$$\frac{\partial^2}{\partial\rho^2}\psi^{JM} = W\psi^{JM} \tag{4.7}$$

where

$$W(\hat{\Omega}, \vec{r}; \rho) = \frac{2\mu}{\hbar^2}(H_{int} - E) \tag{4.8}$$

is a differential operator in all coordinates but ρ, and it parametrically depends on ρ.

Following the standard SVD-Numerov algorithm (115), we obtain the recursion relation

$$(1 - \mathcal{T}_{n+1})\psi_{n+1} + (1 - \mathcal{T}_{n-1})\psi_{n-1} = (2 + 10\mathcal{T}_n)\psi_n - \mathcal{O}(h^6) \tag{4.9}$$

where $\mathcal{T}$ is defined as

$$\mathcal{T} = \frac{h^2}{12}W_n, \tag{4.10}$$

n denotes the nth ρ point in the propagation, and h is the equal spacing between ρ_n and ρ_{n+1}. Neglect the term of $\mathcal{O}(h^6)$ and higher order terms in Eq. (4.9) gives the ordinary Numerov propagator.

At this point we expand the total wavefunction ψ

$$\psi_n(\rho, \hat{\Omega}, \vec{r}) = \mathbf{\Phi}_n(\hat{\Omega}, \vec{r}; \rho)\mathbf{G}_n(\rho) \tag{4.11}$$

41

in the adiabatic basis $\mathbf{\Phi}(\hat{\Omega}, \vec{r}; \rho)$ defined as

$$H_{int}(\hat{\Omega}, \vec{r}; \rho)\Phi_q(\hat{\Omega}, \vec{r}; \rho) = \mathcal{E}_q(\rho)\Phi(\hat{\Omega}, \vec{r}; \rho). \tag{4.12}$$

We now substitute Eq. (4.11) in Eq. (4.9) and project the basis function $\mathbf{\Phi}_n$ on the left. Assuming this basis set $\mathbf{\Phi}_n$ is complete, we get terms such as

$$\begin{aligned}
\langle \mathbf{\Phi}_n \left| \mathcal{T}_{n+1} \right| \mathbf{\Phi}_{n+1} \rangle &= \langle \mathbf{\Phi}_n \mid \mathbf{\Phi}_{n+1} \rangle \langle \mathbf{\Phi}_{n+1} \left| \mathcal{T}_{n+1} \right| \mathbf{\Phi}_{n+1} \rangle \\
&= \mathbf{O}_{n,n+1}\mathbf{T}_{n+1}, \tag{4.13}
\end{aligned}$$

where the overlap matrices $\mathbf{O}_{n,n+1}$ are defined as

$$[\mathbf{O}_{n,n+1}]_{p,q} \equiv \int d\hat{\Omega} \; d\vec{r} \; \Phi_p^*(\hat{\Omega}, \vec{r}; \rho)\Phi_q(\hat{\Omega}, \vec{r}; \rho). \tag{4.14}$$

Note that, the basis set $\mathbf{\Phi}_n$ is not orthogonal to $\mathbf{\Phi}_{n+1}$ because they are eigenvectors of different internal Hamiltonians $H_{int}(\rho_n)$. Now let us assume the basis functions $\mathbf{\Phi}_n$ are truly adiabatic, which at each ρ_n point diagonalize H_{int} and thus $\mathcal{T}$. Therefore, we get a diagonal matrix $\mathbf{T}_n$

$$\mathbf{T}_n = \tau_n = \frac{h^2}{12}\frac{2\mu}{\hbar^2}(\mathcal{E}_n - E\mathbf{I}). \tag{4.15}$$

Thus, we can rewrite Eq. (4.9) as

$$\mathbf{O}_{n,n+1}(\mathbf{I} - \tau_{n+1})\mathbf{G}_{n+1} - (2\mathbf{I} + 10\tau_n) + \mathbf{O}_{n,n-1}(\mathbf{I} - \tau_{n-1})\mathbf{G}_{n-1} = \mathcal{O}(h^6). \tag{4.16}$$

4.3 $\quad H_{int}$ and the adiabatic basis $\Phi_q(\hat{\Omega}, \vec{r}; \rho)$

Let us investigate the properties of Eq. (4.12). For the $J = 0$ case, H_{int} can be expressed as

$$H_{int} = -\frac{\hbar^2}{2\mu}\left(\frac{4}{\rho^2 \sin 2\theta}\frac{\partial}{\partial\theta}\sin 2\theta\frac{\partial}{\partial\theta} + \frac{1}{\rho^2 \sin^2\theta}\frac{\partial^2}{\partial\chi^2}\right) + \frac{15\hbar^2}{2\mu\rho^2} + H_e. \tag{4.17}$$

We express $\Phi_q(\hat{\Omega}, \vec{r}; \rho)$ as

$$\Phi_q(\hat{\Omega}, \vec{r}; \rho) = \phi_q(\hat{\Omega}; \rho)\exp\left(i\frac{l}{2}\eta(R)\right)\varphi(\vec{r}; R) \tag{4.18}$$

where l is an odd number with the geometric phase and an even number without the geometric phase, and $\varphi(\vec{r}; R)$ is the adiabatic real-double valued electronic wavefunction defined as

$$H_e(\vec{r}; R)\varphi(\vec{r}; R) = V(R)\varphi(\vec{r}; R). \tag{4.19}$$

We left-multiply $\varphi(\vec{r}; R)$ onto Eq. (4.12) and integrate over all electronic coordinates $\vec{r}$. We then get a two-dimensional equation for surface wavefunctions $\phi_q(\theta, \chi; \rho_n)$ at the ρ_n point

$$\left\{ -\frac{\hbar^2}{2\mu} \left(\frac{4}{\rho_n^2 \sin 2\theta} \frac{\partial}{\partial \theta} \sin 2\theta \frac{\partial}{\partial \theta} + \frac{1}{\rho_n^2 \sin^2 \theta} \frac{\partial^2}{\partial \chi^2} \right) \right.$$
$$+ \frac{15}{8\mu\rho_n^2} + V(\theta, \chi; \rho_n) + \frac{\hbar^2}{2\mu\rho_n^2} \left[4A_\theta^2 + \frac{1}{\sin^2 \theta} A_\chi^2 \right.$$
$$+ i \left(8A_\theta \cot 2\theta + \frac{4\partial A_\theta}{\partial \theta} + 8A_\theta \frac{\partial}{\partial \theta} + \frac{1}{\sin^2 \theta} \frac{\partial A_\chi}{\partial \chi} \right.$$
$$\left. \left. \left. + \frac{2}{\sin^2 \theta} A_\chi \frac{\partial}{\partial \chi} \right) \right] \right\} \phi_q(\theta, \chi; \rho_n) = \mathcal{E}_q(\rho_n)\phi_q(\theta, \chi; \rho_n), \tag{4.20}$$

where A_θ and A_χ are defined in Eq. (3.14). Note that, this Hamiltonian is complex and Hermitian so the eigenvalues $\mathcal{E}_q(\rho_n)$ are real. Though the general solution $\phi_q(\theta, \chi; \rho_n)$ is complex, one way to construct real interaction and overlap matrices is to use the permutation symmetry, as in Ref. (105). An alternative and simpler way will be fully developed later on, which is named the MOES methods and will be used in the analytic basis method (ABM) (116) and DVR (117) method.

4.4 Numerov Propagator

4.4.1 The SVD-renormalized Numerov method

In order to avoid the unstable solutions of $\mathbf{G}$ in the classically forbidden region, we use the renormalized Numerov procedure developed by Johnson (114).

To simplify Eq. (4.16), we follow Johnson (114) and introduce

$$\mathbf{U}_n = (\mathbf{I} - \tau_n)\mathbf{G}_n \tag{4.21}$$

to define the ratio $\mathbf{R}$ matrix as

$$\mathbf{R}_n = \mathbf{O}_{n,n+1}\mathbf{U}_{n+1}\mathbf{U}_n^{-1}. \tag{4.22}$$

We then can rewrite the propagation function Eq. (4.9) as

$$\mathbf{R}_n = \mathbf{Q}_n - \mathbf{O}_{n,n-1}\mathbf{R}_{n-1}^{-1}\mathbf{O}_{n-1,n} \tag{4.23}$$

where we define $\mathbf{Q}_n$ as

$$\mathbf{Q}_n = (2\mathbf{I} + 10\tau_n)(\mathbf{I} - \tau_n)^{-1}. \tag{4.24}$$

Because τ_n is diagonal, the inverse of the matrix $(\mathbf{I} - \tau_n)^{-1}$ is also diagonal and can be easily calculated.

4.4.2 The SVD-enhanced renormalized Numerov method

Given an initial $\overline{\mathbf{R}}_1$ at ρ_1, we can propagate to large distance ρ_n. Here we follow Pack and Parker's work (115), and we use

$$[\overline{\mathbf{Q}}_n']_i = \cosh\left(\sqrt{12[\tau_n]_i}\right), \text{if } [\tau_n]_i > 0 \tag{4.25}$$

and:

$$[\overline{\mathbf{Q}}_n']_i = \cos\left(\sqrt{12[\tau_n]_i}\right), \text{if } [\tau_n]_i < 0 \tag{4.26}$$

to improve the divergence problem of $\mathbf{Q}$. More details on this improvement are explained in Ref. (115).

We start with $\mathbf{G}_0 = 0$ where $\rho = 0$, for it can be chosen arbitrarily and does not affect the dynamics. And we assume that $\mathbf{R}_0^{-1} = 0$ is also valid for this process, which gives:

$$\mathbf{R}_1 = \overline{\mathbf{Q}}_1' \tag{4.27}$$

And we take a further approximation of $\overline{\mathbf{Q}}_1'$ as:

$$[\mathbf{R}_1']_i = \exp\left(\sqrt{12[\tau_1]_i}\right) \tag{4.28}$$

to solve the numerical problems in the propagation. It has been shown in Ref. (115) that this approximation made little difference in the scattering results.

4.5 Boundary conditions and matching

4.5.1 Numerov matching

When the propagation reaches the asymptotic region at $\rho = \rho_M$, we can rewrite Eq. (4.22) to connect the $\mathbf{R}_M$ matrix to the radial wavefunction $\mathbf{G}$

$$\mathbf{R}_M(\mathbf{I} - \tau_M)\mathbf{G}_M = \mathbf{O}_{M,M+1}(\mathbf{I} - \tau_{M+1})\mathbf{G}_{M+1}. \tag{4.29}$$

One can then relate $\mathbf{G}_M$ and $\mathbf{G}_{M+1}$ to the asymptotic solutions to get the reactance matrix $\mathbf{K}$ (108; 115). Note that, in the asymptotic region, the geometric phase terms die off as $1/\rho^2$ and the conical intersections are located in the regions where the PES is extremely repulsive. Therefore, we can ignore the geometric phase factors in the asymptotic region.

Before we start to apply the boundary condition, we transform the $\mathbf{\Phi}$ wavefunction from APH coordinates to Delves coordinate. More information on the definition of Delves coordinates can be found in Appendix E.2. This is because we need to use a primitive basis set of rovibrational functions so the reactance matrix is labeled by the primitive indices. One can transform the adiabatic basis to a primitive basis $\mathbf{\Upsilon}$, by:

$$\mathbf{\Phi}_n = \mathbf{\Upsilon}_n \mathbf{D}_n. \tag{4.30}$$

Here the $\mathbf{\Phi}_n$ is obtained through diagonalizing h_{int}, as well as $\mathbf{D}_n$.

The wavefunction ψ can be expressed as

$$\psi_n = \mathbf{\Upsilon}_n \mathbf{D}_n \mathbf{G}_n. \tag{4.31}$$

We then right-multiply Eq. (4.31) by $\mathbf{D}_n^T$ to get

$$\begin{aligned}
\psi_n^{prim} &\equiv \psi_n \mathbf{D}_n^T \\
&= \mathbf{\Upsilon}_n \mathbf{\Gamma}_n,
\end{aligned} \tag{4.32}$$

where $\mathbf{\Gamma}_n$ is defined in the primitive basis as

$$\mathbf{\Gamma}_n \equiv \mathbf{D}_n \mathbf{G}_n \mathbf{D}_n^T. \tag{4.33}$$

The inversion of Eq. (4.33) can give

$$\mathbf{G}_n = \mathbf{D}_n^T \mathbf{\Gamma}_n \mathbf{D}_n. \tag{4.34}$$

45

We then substitute Eq. (4.34) to Eq. (4.29) to get the asymptotic form of the propagation in the well-labeled primitive basis

$$\mathbf{R}_M(\mathbf{I} - \tau_M)\mathbf{D}_M^T\boldsymbol{\Gamma}_M\mathbf{D}_M = \mathbf{O}_{M,M+1}(\mathbf{I} - \tau_{M+1})\mathbf{D}_{M+1}^T\boldsymbol{\Gamma}_{M+1}\mathbf{D}_{M+1}. \qquad (4.35)$$

We then can right-multiply Eq. (4.35) by $\mathbf{D}_{M+1}^T$ and assume $\mathbf{D}_M\mathbf{D}_{M+1}^T \sim \mathbf{I}$, where $\mathbf{I}$ is an identity matrix, in the asymptotic region. This leads to

$$\mathbf{R}_M(\mathbf{I} - \tau_M)\mathbf{D}_M^T\boldsymbol{\Gamma}_M = \mathbf{O}_{M,M+1}(\mathbf{I} - \tau_{M+1})\mathbf{D}_{M+1}^T\boldsymbol{\Gamma}_{M+1}. \qquad (4.36)$$

In order to relate the ratio $\mathbf{R}$ matrix to the reactance matrix $\mathbf{K}$, we also need to express the entire wavefunction in the mass-scaled Jacobi coordinates as

$$\rho^{5/2}\Psi^{JMi} = \sum_m \frac{2\rho^{1/2}}{\sin(2\theta_{D_m})} F_{mi}^J(S_m)\Theta_m(s)\mathcal{Y}_m(\hat{S}, \hat{s}), \qquad (4.37)$$

where $\theta_{D_m} \equiv \tan^{-1}(s_\tau/S_\tau)$ is the Delves angle for a chemical arrangement τ_m. Here, definitions of the Jacobi coordinates can be found in Appendix E.1. Note that, the ratio $\mathbf{R}$ matrix in the Numerov propagator is different from the Wigner $\mathbf{R}$ matrix in the Log-derivative propagator, and more information on how to relate these two $\mathbf{R}$ matrices will be provided in the next section. The asymptotic wavefunction $\mathbf{F}(S)$ can be written as

$$\mathbf{F}(\rho) = \mathbf{a} - \mathbf{b}\mathbf{K} \qquad (4.38)$$

where

$$[\mathbf{a}]_{fi} = \delta_{fi}\sqrt{k_f}S j_{l_f}(k_f S), \qquad (4.39)$$

and

$$[\mathbf{b}]_{fi} = \delta_{fi}\sqrt{k_f}S y_{l_f}(k_f S). \qquad (4.40)$$

Here, $k_f^2 = 2\mu(E - \epsilon_{\nu_f,j_f,\alpha_f}^{BS})/\hbar^2$, j_n is the spherical Bessel function of an integer order n, and y_n is the spherical irregular Bessel function of an integer order n. For the closed channels we replace j_n by i_n and y_n by k_n, which are modified spherical Bessel functions of an integer order n.

The entire wavefunction can also be written in terms of Delves coordinates

$$\rho^{5/2}\Psi^{JMi} = \sum_m \frac{2}{\sin(2\theta_{D_m})}\Gamma_{mi}(\rho)\Upsilon_m(\theta_{D_m})\mathcal{Y}_m(\hat{S}, \hat{s}). \qquad (4.41)$$

Using Eq. (4.37) and Eq. (4.41)we then can write $\Gamma_{fi}(\rho)$ as

$$\Gamma_{fi}(\rho) = \rho^{1/2} \sum_m \delta_{j_f j_m} \delta_{l_f l_m} \int d\theta \Upsilon_f(\theta; \rho) F_{mi}(S) \Theta_m(s). \qquad (4.42)$$

After substituting the boundary condition, Eq. (4.38), into Eq. (4.42), we obtain Γ at large distance in terms of the reactance matrix as $\Gamma = \mathbf{A} - \mathbf{BK}$. These matrix elements for the open channels are given as

$$[\mathbf{A}]_{fi} = \sqrt{k_f} \int \rho \cos\theta d\theta \Upsilon_n(\theta; \rho) \Theta_i(\rho \sin\theta) j_{l_f}(k_f \rho \cos\theta), \qquad (4.43)$$

and

$$[\mathbf{B}]_{fi} = \sqrt{k_f} \int \rho \cos\theta d\theta \Upsilon_n(\theta; \rho) \Theta_i(\rho \sin\theta) y_{l_f}(k_f \rho \cos\theta). \qquad (4.44)$$

For the elements of $\mathbf{A}$ and $\mathbf{B}$ in the closed channels we use the modified Bessel functions i_n and k_n, instead of j_n and y_n. At point ρ_M, we define $\mathbf{A}_M = \mathbf{A}(\rho_M)$ and

$$\mathbf{Z}_n = (\mathbf{I} - \tau_n)\mathbf{D}_n^T. \qquad (4.45)$$

We, therefore, can rewrite Eq. (4.36) as

$$\mathbf{R}_M \mathbf{Z}_M (\mathbf{A}_M - \mathbf{B}_M \mathbf{K}) = \mathbf{O}_{M,M+1} \mathbf{Z}_{M+1} (\mathbf{A}_{M+1} - \mathbf{B}_{M+1} \mathbf{K}). \qquad (4.46)$$

We can solve for the reactance $\mathbf{K}$ matrix

$$\mathbf{K}_M = [\mathbf{R}_M \mathbf{Z}_M \mathbf{B}_M - \mathbf{B}'_M]^{-1} [\mathbf{R}_M \mathbf{Z}_M \mathbf{A}_M - \mathbf{A}'_M], \qquad (4.47)$$

where we define

$$\mathbf{A}'_M = \mathbf{O}_{M,M+1} \mathbf{Z}_{M+1} \mathbf{A}_{M+1} \qquad (4.48)$$

and

$$\mathbf{B}'_M = \mathbf{O}_{M,M+1} \mathbf{Z}_{M+1} \mathbf{B}_{M+1}. \qquad (4.49)$$

We can get the scattering $\mathbf{S}$ matrix from the reactance $\mathbf{K}$ matrix by the Caley transformation:

$$\mathbf{S} = [\mathbf{I} + i\mathbf{K}][\mathbf{I} - i\mathbf{K}]^{-1}, \qquad (4.50)$$

and observable properties are calculated from $\mathbf{S}$.

4.5.2 Log-derivative matching

Two major approximations, $D_M^T D_{M+1} \approx 1$ and $D_M^T D_M = 1$, are used in the Numerov matching. The first assumes the matching is done in the asymptotic region and the change of the surface energy, $\mathcal{E}$, is negligible compared with the translational energy. The second approximation assumes both the primitive basis set and the adiabatic basis set are complete. However, this is not always true and it can be sometimes very difficult to get converged results. As an alternative, we can relate the Wigner matrix R^W in the Log-derivative propagator with the ratio matrix R_N used in the Numerov method. In this way we can convert R_N to the Wigner matrix and apply the associated Log-derivative matching.

The Wigner matrix R^W is defined as $R^W = \mathbf{G}(\partial \mathbf{G}/\partial \rho)^{-1}$ in the APH coordinates. The first derivative term can be defined as

$$\frac{\partial \mathbf{G}}{\partial \rho} = \lim_{h \to 0} \frac{\mathbf{G}(\rho + h) - \mathbf{G}(\rho)}{h}. \tag{4.51}$$

And thus the inverse of the Wigner matrix R^W can be expressed as

$$\begin{aligned}
[R^W]_n^{-1} &= \lim_{h \to 0} \frac{\mathbf{G}(\rho + h) - \mathbf{G}(\rho)}{h} \mathbf{G}^{-1}(\rho) \\
&= \lim_{h \to 0} \frac{1}{h} \left[\frac{\mathbf{G}(\rho + h)}{\mathbf{G}(\rho)} - \mathbf{I} \right]. \tag{4.52}
\end{aligned}$$

Note that, this expression has an $O(h^2)$ error where h is the step size. However, in the asymptotic region, the step size h is much smaller than the local wavelength and thus this $O(h^2)$ error is negligible here. We can then approximate this equation as

$$[R^W]_n^{-1} h = \left[\frac{\mathbf{G}_{n+1}}{\mathbf{G}_n} - \mathbf{I} \right]. \tag{4.53}$$

Using Eq. (4.22) we obtain

$$[R^W]_n^{-1} = \frac{1}{h} \left[(\mathbf{I} - \tau_{n+1})^{-1} \mathbf{O}_{n,n+1} \mathbf{R}^N (\mathbf{I} - \tau_n) - \mathbf{I} \right]. \tag{4.54}$$

Therefore, the Wigner matrix $\mathbf{R}$ can be calculated via the Numerov ratio $\mathbf{R}$ matrix as

$$[R^W]_n = h \left[(\mathbf{I} - \tau_{n+1})^{-1} \mathbf{O}_{n,n+1} \mathbf{R}^N (\mathbf{I} - \tau_n) - \mathbf{I} \right]^{-1}. \tag{4.55}$$

4.5.2.1 APH to Delve transformation

Before we apply the boundary conditions, we need to transform the Wigner matrix $\mathbf{R}^W(APH)$ to $\mathbf{R}^W(Delves)$. We define the SF wavefunction in Delves coordinates as:

$$
\begin{aligned}
\Psi^{JMn} &= 2 \sum_{\tau_f \nu_f j_f \Lambda_f} \frac{\Gamma^{Jn}_{\tau_f \nu_f j_f \Lambda_f}(\rho)}{\rho^{5/2}} \frac{\Upsilon_{\nu_f j_f}(\theta_{D_f}; \rho_n)}{\sin(2\theta_D)} \\
&\times \quad \hat{P}_{j_f \Lambda_f}(\Theta_f) \hat{D}^J_{\Lambda_f M}(\alpha_f, \beta_f, \gamma_f)
\end{aligned}
\tag{4.56}
$$

and the SF wavefunction in the APH coordinates as

$$
\Psi^{JMpn} = 4 \sum_{t,\Lambda} \rho^{-5/2} \psi^{Jpn}_{t\Lambda}(\rho) \Phi^{Jp}_{t\Lambda}(\theta, \chi_i; \rho_n) \hat{D}^{Jp}_{\Lambda M}(\alpha_Q, \beta_Q, \gamma_Q),
\tag{4.57}
$$

where J is the total angular momentum quantum number, M is the quantum number for the projection of J along the space frame z-axis, Λ is the quantum number for the projection of J along the body frame z-axis, p is the parity, t indicates the tth surface function, and n indicates the nth solution for Ψ^{JMpn} functions. Here ρ is the APH hyperradius, θ and χ are the APH hyperangles, and ρ_n is the center of the nth ρ sector in which the nonadiabatic surface basis $\Phi^{Jp}_{t\Lambda}$ is expanded. The $\hat{D}^{Jp}_{\Lambda M}(\alpha_Q, \beta_Q, \gamma_Q)$ are normalized Wigner rotation matrix elements of good parity p (108). The expansion coefficients, $\psi^{Jpn}_{t\Lambda}(\rho)$, are functions of ρ and labeled by the good quantum numbers J (total nuclear angular momentum) and p (parity).

We then can obtain the transformation matrix $U^J_{\tau_f \nu_f j_f \Sigma_f, t\Gamma}$ as

$$
\begin{aligned}
U^J_{\tau_f \nu_f j_f \Lambda_f, t\Lambda} &= 2 \int_0^{\pi/2} \sin(2\theta_{D_f}) d\theta_{D_f} \\
&\times \quad \int \hat{s}_f d\hat{S}_f \Upsilon_f \hat{P}_f \hat{D}^{J*}_{\Lambda_f M}(\alpha_f, \beta_f, \gamma_f) \\
&\times \quad \phi^{Jp}_{t\Lambda} \hat{D}^{Jp}_{\Lambda_f M}(\alpha_Q, \beta_Q, \gamma_Q).
\end{aligned}
\tag{4.58}
$$

More details of the transformation matrix can be found in Ref. (108). The Delves Wigner matrix is then obtained as

$$
\mathbf{R}(Delves) = \mathbf{U}\mathbf{R}(APH)\mathbf{U}^T.
\tag{4.59}
$$

4.5.2.2 Boundary conditions of the Delves coordinates wave functions

Once the Wigner $\mathbf{R}$ matrix is obtained in the Delves coordinates, we can apply boundary conditions. First, we define the wavefunction in the mass-scaled Jacobi coordinates $(S_f, s_f, \hat{S}_f, \hat{s}_f)$ as

$$
\begin{aligned}
\Psi^{JM\tau_i\nu_ij_il_i} &= \sum_{\tau_i\nu_ij_il_i} \frac{1}{s_fS_f} G^{J\tau_i\nu_ij_il_i}_{\tau_f\nu_if_il_f} \\
&\times\ \Xi_{\nu_fj_f}(s_f)\mathcal{Y}(\hat{S}_f, \hat{s}_f).
\end{aligned} \tag{4.60}
$$

The reactance matrix $\mathbf{K}$ is obtained by calculating

$$
\mathbf{K} = (\mathbf{R}\mathcal{F} - \mathcal{B})^{-1}(\mathbf{R}\mathcal{E} - \mathcal{A}) \tag{4.61}
$$

where $\mathbf{R} = \Gamma(\partial\Gamma/\partial\rho)^{-1}$ is the Wigner R matrix we obtained from section 4.5.2.1. The four matrices $\mathcal{A}$, $\mathcal{B}$, $\mathcal{E}$ and $\mathcal{F}$ are defined as

$$
\mathcal{A}_{fi} = \delta_{\tau_f\tau_i}\delta_{j_fj_i}\delta_{l_fl_i}\rho^{1/2}\int_0^{\pi/2} d\theta_{D_f}\Upsilon_f^*(\theta_{D_f}, \rho_n)a_{ii}(S_f)\Xi_i(s_f), \tag{4.62}
$$

$$
\mathcal{A}_{fi} = \delta_{\tau_f\tau_i}\delta_{j_fj_i}\delta_{l_fl_i}\rho^{1/2}\int_0^{\pi/2} d\theta_{D_f}\Upsilon_f^*(\theta_{D_f}, \rho_n)b_{ii}(S_f)\Xi_i(s_f), \tag{4.63}
$$

$$
\mathcal{E} = \frac{1}{2\rho}\mathcal{A} + \mathcal{C}, \tag{4.64}
$$

and

$$
\mathcal{F} = \frac{1}{2\rho}\mathcal{B} + \mathcal{D}. \tag{4.65}
$$

The $\mathcal{C}$ and $\mathcal{D}$ matrices are defined as

$$
\begin{aligned}
\mathcal{C}_{fi} &= \delta_{\tau_f\tau_i}\delta_{j_fj_i}\delta_{l_fl_i}\rho^{1/2}\int_0^{\pi/2} d\theta_{D_f}\Upsilon_f^*(\theta_{D_f}, \rho_n) \\
&\times\ \left[\cos\theta_{D_f}\Xi_i(s_f)\frac{\partial a_{ii}}{\partial S_f} + \sin\theta_{D_f}a_{ii}\frac{\partial\Xi_i}{\partial S_f}\right]
\end{aligned} \tag{4.66}
$$

and

$$
\begin{aligned}
\mathcal{D}_{fi} &= \delta_{\tau_f\tau_i}\delta_{j_fj_i}\delta_{l_fl_i}\rho^{1/2}\int_0^{\pi/2} d\theta_{D_f}\Upsilon_f^*(\theta_{D_f}, \rho_n) \\
&\times\ \left[\cos\theta_{D_f}\Xi_i(s_f)\frac{\partial b_{ii}}{\partial S_f} + \sin\theta_{D_f}b_{ii}\frac{\partial\Xi_i}{\partial S_f}\right]
\end{aligned} \tag{4.67}
$$

50

where a_{ii} and b_{ii} are proportional to the spherical Riccati-Bessel functions,

$$a_{fi} = \delta_{fi} k_f^{1/2} S_f j_{l_f}(k_f S_f) \tag{4.68}$$

and

$$b_{fi} = \delta_{fi} k_f^{1/2} S_f y_{l_f}(k_f S_f). \tag{4.69}$$

The scattering matrix $\mathbf{S}$ is then obtained from open-open parts of the reactance matrix

$$\mathbf{S} = (\mathbf{I} + i\mathbf{K})(\mathbf{I} - i\mathbf{K})^{-1}. \tag{4.70}$$

4.6 ABM treatment

The discrete variable representation (DVR) calculations of the surface functions and energies are very expensive at a large hyperradii. The analytic basis method (ABM) (116) has some similarities to the Delves hyperspherical methods of Schatz (118), Kuppermann and coworkers (119), and Kendrick (120) in that the ABM uses both functions, which are centered in the chemical arrangement channels, and diatomic rotational functions of Θ_τ. These functions are centered in each chemical arrangement channels where we pack more points near the equilibrium point of the diatomic potential curve.

Because the ABM uses primitive basis functions centered in the chemical arrangements, it describes the surface functions very well at large hyperradius. Because the ABM is less effective than the DVR at a small hyperradius, one can then use the DVR at a small ρ and use the ABM at a large ρ. We perform a DVR-to-ABM transformation to connect the methods so that the Wigner matrix $\mathbf{R}$(DVR) can be transformed to $\mathbf{R}$(ABM).

4.6.1 The Mixed-Odd-Even-State (MOES) method in the ABM

The surface Hamiltonian, H_{int}, is given in Eq. (4.20) and we only consider the $J = 0$ case in this study. In order to define the basis functions correctly, we need to discuss some of the symmetry properties of this surface Hamiltonian. We define

an operator $\mathcal{P}$ as $\mathcal{P}f(\chi) \rightarrow f(-\chi)$. The surface Hamiltonian can be proved to be Hermitian, and from Eq. (4.1) and Eq. (4.2) we can derive

$$\mathcal{P}H_{int} = H_{int}(-\chi) = H_{int}^*. \tag{4.71}$$

From Eq. (4.71), the surface functions $\phi_q(\theta, \chi; \rho_n)$ must have specific symmetry properties with respect to the operation $\mathcal{P}$. We choose

$$\phi_q(\theta, -\chi; \rho_n) = \phi_q^*(\theta, \chi; \rho_n), \tag{4.72}$$

which means ϕ_q is neither even nor odd with respect to $\mathcal{P}$. We then express the surface functions as a basis set expansion of the form

$$\phi_q(\theta, \chi; \rho_n) = \sum_{f_e} \mathcal{F}_f^e B_{fq}^e + i \sum_{f_o} \mathcal{F}_t^o B_{fq}^o \tag{4.73}$$

where the superscripts e and o denotes even and odd symmetries with respect to the $\mathcal{P}$ operation, respectively, and the coefficients B_{fq}^e and B_{fq}^o can be determined by the variational method. We separate the even and odd state with respect to the $\mathcal{P}$ operation in Eq. (4.73) so that the surface functions obey Eq. (4.72). The use of a mixture of these even and odd states is thus named the Mixed-Odd-Even-State (MOES) method.

In order to get the primitive basis functions $\mathcal{F}$ centered in each chemical arrangement channel we express them in the delves hyperspherical coordinate θ_{D_f} and Θ_f, where θ_{D_f} measures the ratio between two scaled Jacobi vectors in the τ_f arrangement and Θ_f is the angle between these two Jacobi vectors. In order to make sure the basis functions $\mathcal{F}$ have good parity under $\chi_i \rightarrow \chi_i + \pi$ we write

$$\mathcal{F}_f(\theta, \chi_i; \rho_n) = \cos^p(\chi_f) F_f(\theta_{D_f}, \Theta_f; \rho_n) \tag{4.74}$$

where χ_f is the kinematic angle between arrangement τ_f and τ_i and it is given as (108)

$$\chi_f = \chi_i - \chi_{fi}. \tag{4.75}$$

In this study, we choose to study the $J = 0$ and $p = 0$ case, which makes the $\cos^p(\chi_f)$ factor unity. For brevity we ignore this parity function for the following derivations.

The transformation between (θ, χ_f) and (θ_{D_f}, Θ_f) are given in Ref. (108) as

$$\tan \theta_{D_f} = \left[\frac{1 - \sin \theta \cos 2\chi_f}{1 + \sin \theta \cos 2\chi_f} \right]^{1/2}, \tag{4.76}$$

$$\cos \Theta_f = \frac{\sin \theta \sin 2\chi_f}{\left[1 - \sin^2 \theta \cos^2 2\chi_f \right]^{1/2}}, \tag{4.77}$$

and their inverse as

$$\tan \theta = \frac{\left[\cos^2 2\theta_{D_f} + \cos^2 2\theta_{D_f} \cos^2 \Theta_f \right]^{1/2}}{\sin 2\theta_{D_f} \sin \Theta_f}, \tag{4.78}$$

$$\sin 2\chi_f = \frac{\sin 2\theta_{D_f} \cos \Theta_f}{\left[\cos^2 2\theta_{D_f} + \cos^2 2\theta_{D_f} \cos^2 \Theta_f \right]^{1/2}}, \tag{4.79}$$

$$\cos 2\chi_f = \frac{\cos 2\theta_{D_f}}{\left[\cos^2 2\theta_{D_f} + \cos^2 2\theta_{D_f} \cos^2 \Theta_f \right]^{1/2}}. \tag{4.80}$$

Eq. (4.20) can be partitioned as

$$\left(T_h + \frac{15\hbar^2}{8\mu\rho^2} + V + (A_R + iA_I) \right) \phi_q = \mathcal{E}_q \phi_q. \tag{4.81}$$

Here, T_h is given as

$$
\begin{aligned}
T_h &\equiv -\frac{\hbar^2}{2\mu} \left(\frac{4}{\rho_n^2 \sin 2\theta} \frac{\partial}{\partial \theta} \sin 2\theta \frac{\partial}{\partial \theta} + \frac{1}{\rho_n^2 \sin^2 \theta} \frac{\partial^2}{\partial \chi^2} \right) \\
&= \frac{1}{2\mu} \left[\frac{-\hbar^2}{\sin^2 2\theta_{D_f}} \frac{\partial}{\partial \theta_{D_f}} \sin^2 2\theta_{D_f} \frac{\partial}{\partial \theta_{D_f}} + \left[\frac{1}{\cos^2 \theta_{D_f}} + \frac{1}{\sin^2 \theta_{D_f}} \right] \mathcal{L}^2 \right] \tag{4.82}
\end{aligned}
$$

A_R is given as

$$A_R \equiv \frac{\hbar^2}{2\mu\rho_n^2} \left[4A_\theta^2 + \frac{1}{\sin^2 \theta} A_\chi^2 \right], \tag{4.83}$$

and A_I is given as

$$A_I \equiv \frac{\hbar^2}{2\mu\rho_n^2} \left[8A_\theta \cot 2\theta + \frac{4\partial A_\theta}{\partial \theta} + 8A_\theta \frac{\partial}{\partial \theta} + \frac{1}{\sin^2 \theta} \frac{\partial A_\chi}{\partial \chi} \frac{2}{\sin^2 \theta} A_\chi \frac{\partial}{\partial \chi} \right], \tag{4.84}$$

where $\mathcal{L}^2$ is given by

$$\mathcal{L}^2 = \frac{-\hbar^2}{\sin \Theta_f} \frac{\partial}{\partial \Theta_f} \sin \Theta_f \frac{\partial}{\partial \Theta_f} \tag{4.85}$$

Following Ref. (116), we choose the analytic primitive basis function as

$$F_f(\theta_{D_f}, \Theta_f; \rho_n) = \frac{\Upsilon_f(\theta_{D_f}; \rho_n)}{\sin 2\theta_{D_f}} \hat{P}^0_{j_f}(\cos \Theta_f) \tag{4.86}$$

where $\hat{P}^0_{j_f}$ is the normalized associated Legendre polynomials. Here, $\Upsilon_f(\theta_{D_f}; \rho_n)$ is chosen to be

$$\frac{\Upsilon_f(\theta_{D_f}; \rho_n)}{\sin \theta_{D_f}} = \frac{1}{B_f(\theta_{D_f})} \Xi_{\nu_f}(z_f), \tag{4.87}$$

where Ξ is a simple harmonic oscillator function of z_f,

$$\Xi_{\nu_f}(z_f) = \frac{1}{\sqrt{\pi^{1/2} 2^{\nu_f}(\nu_f!)}} H_{\nu_f}(z_f) e^{-z_f^2/2}. \tag{4.88}$$

H_{ν_f} is a Hermite polynomial, and B_f is a factor chosen to simplify the Jacobian for Ξ normalized on z_f, where z_f is

$$z_f = a_f \tan \theta_{D_f} - \frac{b_f}{\tan \theta_{D_f}} + c_f. \tag{4.89}$$

We choose $a_f > 0$ and $b_f > 0$ so that, when θ_{D_f} runs from 0 to $\pi/2$, z_f runs from $-\infty$ to $+\infty$, and has compact support on the boundaries. Further details of the choice of these basis functions in the ABM can be found in Ref. (116).

It can be seen from Eq. (4.76,4.77,4.78,4.79,4.80) that when $\chi \to -\chi$ we have $\theta_{D_f} \to \theta_{D_f}$ and $\Theta_f \to -\Theta_f$. We can then deduce that $\hat{P}^0_{j_f}(\cos \Theta_f)$ is antisymmetric with respect to the $\mathcal{P}$ operator when j_f is even and symmetric with respect to $\mathcal{P}$ when j_f is odd. The even primitive basis functions $\mathcal{F}^e_t$ are of two kinds,

$$\mathcal{F}^e(\tau_f = 1) = \frac{\Upsilon_f(\theta_{D_f}; \rho_n)}{\sin 2\theta_{D_f}} \hat{P}^0_{j_f}(\cos \Theta_f) \tag{4.90}$$

where j_f are even, and

$$\begin{aligned} \mathcal{F}^e(\tau_f = 2, 3) &= \left[\frac{\Upsilon_f(\theta_{D_f}; \rho_n)}{\sin 2\theta_{D_f}} \hat{P}^0_{j_f}(\cos \Theta_f) \right] (\tau_f = 2) \\ &\pm \left[\frac{\Upsilon_f(\theta_{D_f}; \rho_n)}{\sin 2\theta_{D_f}} \hat{P}^0_{j_f}(\cos \Theta_f) \right] (\tau_f = 3) \end{aligned} \tag{4.91}$$

which is a linear combination of the wavefunctions in chemical arrangements 2 and 3. The $\pm$ signs are chosen to be $+$ if j_f is even and $-$ if j_f is odd. In this way, we have

$$\mathcal{F}^e_t(\theta, -\chi; \rho) = \mathcal{F}^e_t(\theta, \chi; \rho). \tag{4.92}$$

The odd primitive basis functions $i\mathcal{F}_t^o$ are of two kinds,

$$\mathcal{F}^o(\tau_f = 1) = \frac{\Upsilon_f(\theta_{D_f}; \rho_n)}{\sin 2\theta_{D_f}} \hat{P}_{j_f}^0(\cos \Theta_f) \tag{4.93}$$

where j_f are odd, and

$$
\begin{aligned}
\mathcal{F}^o(\tau_f = 2, 3) &= \left[\frac{\Upsilon_f(\theta_{D_f}; \rho_n)}{\sin 2\theta_{D_f}} \hat{P}_{j_f}^0(\cos \Theta_f) \right] (\tau_f = 2) \\
&\pm \left[\frac{\Upsilon_f(\theta_{D_f}; \rho_n)}{\sin 2\theta_{D_f}} \hat{P}_{j_f}^0(\cos \Theta_f) \right] (\tau_f = 3)
\end{aligned}
\tag{4.94}
$$

which is a linear combination of the wavefunctions in chemical arrangements 2 and 3. The $\pm$ signs are chosen to be $-$ if j_f is even and $+$ if j_f is odd. In this way, we have

$$i\mathcal{F}_t^o(\theta, -\chi; \rho) = -i\mathcal{F}_t^o(\theta, \chi; \rho). \tag{4.95}$$

Therefore, the surface functions ϕ has the correct symmetry property with respect to the $\mathcal{P}$ operation:

$$
\begin{aligned}
\mathcal{P}\phi(\theta, \chi; \rho) &= \phi(\theta, -\chi; \rho) = \sum_{f_e} \mathcal{F}_f^e(\theta, -\chi; \rho) B_{fq}^e + i \sum_{f_o} \mathcal{F}_t^o(\theta, -\chi; \rho) B_{fq}^o \\
&= \sum_{f_e} \mathcal{F}_f^e(\theta_{D_f}, -\cos \Theta_f; \rho) B_{fq}^e + i \sum_{f_o} \mathcal{F}_t^o(\theta_{D_f}, -\cos \Theta_f; \rho) B_{fq}^o \\
&= \sum_{f_e} \mathcal{F}_f^e(\theta_{D_f}, \cos \Theta_f; \rho) B_{fq}^e - i \sum_{f_o} \mathcal{F}_t^o(\theta_{D_f}, \cos \Theta_f; \rho) B_{fq}^o \\
&= \phi^*(\theta, \chi; \rho).
\end{aligned}
\tag{4.96}
$$

This condition is satisfied when the expansion coefficients B_{fq}^e and B_{fq}^o are all real.

4.6.2 Construction of the ABM Hamiltonian

Our basis functions $\mathcal{F}_f^e$ are real, but the wavefunctions $i\mathcal{F}_f^o$ are purely imaginary. Eq. (4.81) shows that the surface Hamiltonian can be partitioned into four parts, T_h, $\frac{15\hbar^2}{8\mu\rho^2} + V$, A_R and iA_I. It can be easily shown that this Hamiltonian from Eq. (4.81) is a Hermitian operator and thus its eigenvalues are real. In general the Hamiltonian matrix is complex and its solutions are complex. However, because of our unique choice of the basis functions, we can show that this Hamiltonian, in

the ABM basis set, is real and symmetric. This feature can tremendously reduce our computational effort.

The *even even* sub-block of T_h is

$$[T_h]_{m_e,n_e} = \langle \mathcal{F}^e_m | T_h | \mathcal{F}^e_n \rangle , \tag{4.97}$$

the *even odd* sub-block of T_h is

$$[T_h]_{m_e,n_o} = \langle \mathcal{F}^e_m | T_h | i\mathcal{F}^o_n \rangle , \tag{4.98}$$

the *odd even* sub-block of T_h is

$$[T_h]_{m_o,n_e} = \langle i\mathcal{F}^o_m | T_h | \mathcal{F}^e_n \rangle , \tag{4.99}$$

and the *odd odd* sub-block of T_h is

$$[T_h]_{m_o,n_o} = \langle i\mathcal{F}^o_m | T_h | i\mathcal{F}^o_n \rangle . \tag{4.100}$$

The integration is done in both θ and χ, and the T_h operator is real and symmetric with respect to the $\mathcal{P}$ operation. Because the primitive basis functions $\mathcal{F}^e_m$ are symmetric under $\mathcal{P}$ and $\mathcal{F}^o_m$ are antisymmetric under $\mathcal{P}$, we obtain $[T_h]_{m_e,n_o} = [T_h]_{m_o,n_e} = 0$. Furthermore, we realize that both $[T_h]_{m_e,n_e}$ and $[T_h]_{m_o,n_o}$ are real because

$$\begin{aligned}
[T_h]_{m_o,n_o} &= \langle i\mathcal{F}^o_m | T_h | i\mathcal{F}^o_n \rangle \\
&= \langle \mathcal{F}^o_m | T_h | \mathcal{F}^o_n \rangle .
\end{aligned} \tag{4.101}$$

Thus, the T_h matrix is shown to be block-diagonalized real symmetric.

We define

$$V_{eff} \equiv \frac{15\hbar^2}{8\mu\rho^2} + V, \tag{4.102}$$

which, in the ABM basis set, has four sub-blocks. These sub-blocks are the *even even* sub-block

$$[V_{eff}]_{m_e,n_e} = \langle \mathcal{F}^e_m | V_{eff} | \mathcal{F}^e_n \rangle , \tag{4.103}$$

the *even odd* sub-block

$$[V_{eff}]_{m_e,n_o} = \langle \mathcal{F}^e_m | V_{eff} | i\mathcal{F}^o_n \rangle , \tag{4.104}$$

the *odd even* sub-block

$$[V_{eff}]_{m_o,n_e} = \langle i\mathcal{F}_m^o | V_{eff} | \mathcal{F}_n^e \rangle, \tag{4.105}$$

and the *odd odd* sub-block

$$[V_{eff}]_{m_o,n_o} = \langle i\mathcal{F}_m^o | V_{eff} | i\mathcal{F}_n^o \rangle. \tag{4.106}$$

Likewise, the V_{eff} operator is real and symmetric with respect to the $\mathcal{P}$ operator. Thus, V_{eff} is also block-diagonal and real symmetric. With similar arguments for the A_R operator, which is symmetric with respect to the $\mathcal{P}$ operator, A_R is also block-diagonal and real symmetric.

The iA_I operator is imaginary. However, it can be shown to be antisymmetric with respect to the $\mathcal{P}$ operator:

$$iA_I(\theta, -\chi; \rho) = -iA_I(\theta, \chi; \rho) = (iA_I(\theta, \chi; \rho))^* \tag{4.107}$$

which can be deduced from Eq. (5.34) and Eq. (5.35). Therefore, the *even even* sub-block

$$[iA_I]_{m_e,n_e} = \langle \mathcal{F}_m^e | iA_I | \mathcal{F}_n^e \rangle, \tag{4.108}$$

and the *odd odd* sub-block

$$[iA_I]_{m_o,n_o} = \langle i\mathcal{F}_m^o | iA_I | i\mathcal{F}_n^o \rangle \tag{4.109}$$

are both null. The *even odd* and *odd even* sub-blocks are non-zero and are both real:

$$\begin{aligned}
[iA_I]_{m_e,n_o} &= \langle \mathcal{F}_m^e | iA_I | i\mathcal{F}_n^o \rangle \\
&= -\langle \mathcal{F}_m^e | A_I | \mathcal{F}_n^o \rangle,
\end{aligned} \tag{4.110}$$

$$\begin{aligned}
[iA_I]_{m_o,n_e} &= \langle i\mathcal{F}_m^o | iA_I | \mathcal{F}_n^e \rangle \\
&= \langle \mathcal{F}_m^o | A_I | \mathcal{F}_n^e \rangle.
\end{aligned} \tag{4.111}$$

So far, we have shown that all four parts of the surface Hamiltonian in Eq. (4.81) are real. Because it is a Hermitian operator, this Hamiltonian thus has a symmetric matrix form. Since the first three parts, T_h, V_{eff} and A_R, have

57

symmetric matrix forms, the last part, A_I, is also symmetric. We diagonalize this Hamiltonian to obtain the real expansion coefficients B_{fq}^e and B_{fq}^o, which will be used later on to construct the overlap matrices, $\mathbf{O}_{n,n-1}$ between the current ρ_n and the previous ρ_{n-1}. The overlap matrices are, in general, not real because of our complex basis functions. However, with the choice of our basis set in the MOES method, the overlap between the even and odd states are simply zero, because they are even/odd with respect to the $\chi \rightarrow -\chi$ operation. Therefore, the overlap matrices are now real and can be directly used in the propagation of the nuclear wavefunction.

4.7   DVR method

For shorter hyperradius ρ, where the potential is not dominated by the two-body potential, it is difficult for the ABM and other similar methods to calculate the adiabatic surface functions and the associated surface energies. On the contrary, the DVR method is fast, accurate, and very flexible in calculating highly excited bound states of arbitrarily shaped multi-dimensional potentials. Bačić, Light and co-workers have shown the DVR method to be exceptionally effective for calculating these large amplitude vibrational states of H+H$_2$ (117), F+H$_2$ (121), H$_3^+$ (122) and others (123; 124; 125; 126). We use the DVR method in the short hyperradius region to calculate the various matrix elements which will be used in the propagation calculations.

We adopt the approach of Whitnell and Light (117) to solve for the surface function $\phi_q(\theta, \chi; \rho_n)$ and we utilize the sequential diagonalization-truncation procedure of Bačić, Light $et~al$ (117; 121; 122; 123; 124; 125; 126). Both basis sets for the θ and χ coordinates are formed in the DVR.

4.7.1   Finite basis representation of surface Hamiltonian

We first construct the Hamiltonian in Eq.(4.20) in the finite basis representation (FBR), which is then subsequently transformed to the DVR (117). Instead of using real functions for the basis set, we adopt the MOES method. This basis set is complex and includes both even and odd states with respect to the $\chi \rightarrow$

$-\chi$ operation. The FBR employed consists of normalized Legendre polynomials in $\cos 2\theta$, $\hat{P}_l(\cos 2\theta)$ $l = 0, 1, \ldots, l_{max}$, for the θ coordinate, and of normalized symmetry adapted trigonometric functions $\Pi_m(\chi)$ $m = 1, 2, \ldots, m_{max}$, for the χ coordinate. Here, the $\Pi_m(\chi)$ functions have even and odd labels, as

$$\Pi_m^e(\chi) = \sqrt{\frac{1}{(1 + \delta_{m,1})\pi}} \cos 2(m-1)\chi, \qquad (4.112)$$

and

$$i\Pi_m^o(\chi) = i\sqrt{\frac{1}{\pi}} \sin 2n\chi, \qquad (4.113)$$

where $m, n = 1, 2, \ldots$.. The surface function ϕ_q can then be expanded in the FBR basis set

$$
\begin{aligned}
\Phi_q &= \sum_{l=0}^{l_{max}} \sum_{m=1}^{m_{max}} k_{lm}^{qe} \hat{P}_l(\cos 2\theta)\Pi_m^e(\chi) + i\sum_{l=0}^{l_{max}} \sum_{m=1}^{m_{max}} k_{lm}^{qo} \hat{P}_l(\cos 2\theta)\Pi_m^o(\chi) \\
&= \sum_{l=0}^{l_{max}} \sum_{m=1}^{m_{max}} k_{lm}^{qe} \phi^e + i\sum_{l=0}^{l_{max}} \sum_{m=1}^{m_{max}} k_{lm}^{qo} \phi^o,
\end{aligned}
\qquad (4.114)
$$

where the expansion coefficients k_{lm}^{qe} and k_{lm}^{qo} are real. This surface wavefunction still satisfies the symmetry requirement of the $\chi \to -\chi$ operation

$$\Phi_q(\theta, -\chi; \rho_n) = \Phi_q^*(\theta, \chi; \rho_n). \qquad (4.115)$$

The overlap matrices are real and block diagonal in this FBR because the integration over *odd* functions of χ in the range of $(-\pi, +\pi)$ is simply zero.

We perform a transformation $\theta' = 2\theta$ as discussed by Whitnell and Light (117), which induces a minor modification of the two-dimensional surface function partial-differential equation Eq.(4.20)

$$
\begin{aligned}
&\left\{ -\frac{\hbar^2}{2\mu}\left(\frac{16}{\rho_n^2 \sin\theta'}\frac{\partial}{\partial\theta'}\sin\theta'\frac{\partial}{\partial\theta'} + \frac{1}{\rho_n^2 \sin^2(\theta'/2)}\frac{\partial^2}{\partial\chi^2} \right) \right. \\
&+\frac{15}{8\mu\rho_n^2} + V(\theta'/2, \chi; \rho_n) + \frac{\hbar^2}{2\mu\rho_n^2}\left[4A_{\theta'}^2 + \frac{1}{\sin^2(\theta'/2)}A_\chi^2 \right. \\
&+i\left(8A_{\theta'}\cot\theta' + \frac{8\partial A_{\theta'}}{\partial\theta'} + 16A_{\theta'}\frac{\partial}{\partial\theta'} + \frac{1}{\sin^2(\theta'/2)}\frac{\partial A_\chi}{\partial\chi} \right. \\
&\left.\left.\left. +\frac{2}{\sin^2(\theta'/2)}A_\chi\frac{\partial}{\partial\chi} \right)\right]\right\} \phi_q(\theta', \chi; \rho_n) = \mathcal{E}_q(\rho_n)\phi_q(\theta', \chi; \rho_n),
\end{aligned}
\qquad (4.116)
$$

59

where $A_{\theta'} = A_\theta(\theta'/2)$ and $A_\chi = A_\chi(\theta'/2)$. Let us define

$$h_{\theta'} = -\frac{\hbar^2}{2\mu}\frac{16}{\rho_n^2 \sin\theta'}\frac{\partial}{\partial\theta'}\sin\theta'\frac{\partial}{\partial\theta'}, \tag{4.117}$$

$$h_\chi = -\frac{\hbar^2}{2\mu}\frac{1}{\rho_n^2}\frac{\partial^2}{\partial\chi^2}, \tag{4.118}$$

$$\bar{V}(\rho_n, \theta', \chi) = V(\rho_n, \theta'/2, \chi) + \frac{15}{8\mu\rho_n^2}, \tag{4.119}$$

and

$$f_{\theta'} = [\sin(\theta'/2)]^{-2}. \tag{4.120}$$

We also define the A_R and iA_I terms as

$$A_R = \frac{\hbar^2}{2\mu\rho_n^2}\left[4A_{\theta'}^2 + \frac{1}{\sin^2(\theta'/2)}A_\chi^2\right], \tag{4.121}$$

$$iA_I = iA_{I\theta'} + if_{\theta'}A_{I\chi} \tag{4.122}$$

where

$$A_{I\theta'} = \frac{\hbar^2}{2\mu\rho_n^2}\left(8A_{\theta'}\cot\theta' + \frac{8\partial A_{\theta'}}{\partial\theta'} + 16A_{\theta'}\frac{\partial}{\partial\theta'}\right) \tag{4.123}$$

and

$$A_{I\chi} = \frac{\hbar^2}{2\mu\rho_n^2}\left(\frac{\partial A_\chi}{\partial\chi} + 2A_\chi\frac{\partial}{\partial\chi}\right). \tag{4.124}$$

With the definitions above, we can express Eq.(4.116) in a much simplified form

$$\left[(h_{\theta'} + f_{\theta'}h_\chi) + \bar{V} + A_R + i(A_{I\theta'} + f_{\theta'}A_{I\chi})\right]\phi_q(\theta', \chi; \rho_n)$$
$$= \mathcal{E}_q(\rho_n)\phi_q(\theta', \chi; \rho_n). \tag{4.125}$$

Before we make the FBR-to-DVR transformation to obtain the Hamiltonian in the DVR, we need to investigate the properties of the Hamiltonian in Eq.(4.125) in the FBR. The entire surface Hamiltonian is Hermitian (105). But, the Hamiltonian in Eq.(4.125) is complex. Because the $(h_{\theta'} + f_{\theta'}h_\chi) + \bar{V} + A_R$ terms are symmetric with respect to the $\chi \to -\chi$ operation, they do not mix the even (ϕ^e) and odd (ϕ^o) states. Thus, the $(h_{\theta'} + f_{\theta'}h_\chi) + \bar{V} + A_R$ terms in FBR, using the MOES method, is block-diagonal and, more importantly, is real symmetric. The proof is similar to that of the equivalent terms in the ABM, and thus we do not list it here. The

$i(A_{I\theta'} + f_{\theta'}A_{I\chi})$ terms are in general complex and is a full matrix. However, with the choice of the FBR basis functions in the MOES method, the

$$i(A_{I\theta'} + f_{\theta'}A_{I\chi})$$

terms can be shown to be block-off-diagonal which means the *even even* and *odd odd* blocks are simply zero. The off-diagonal blocks *even odd* and *odd even* can be shown to be real. Because the entire Hamiltonian is Hermitian and real, we can deduce the total Hamiltonian in the FBR with the MOES method is then symmetric. The use of this real and symmetric representation of the Hamiltonian in the calculation can significantly reduce the computational effort as compared to that with the complex and asymmetric representation of the Hamiltonian.

4.7.2 The DVR Hamiltonian

The FBR-to-DVR transformation matrices and the DVR points for θ' and χ are obtained by diagonalizing the coordinate matrices in the corresponding FBR basis. The goal is to obtain a diagonal form of the potential matrix $\bar{V}$ with each diagonal element α, β corresponding to the point $(\theta'_\alpha, \chi_\beta)$. For the θ' coordinate, we diagonalize $\cos\theta'$ in the $\hat{P}_l(\cos\theta')$ basis. The eigenvalues are taken as the θ' DVR points, and the eigenfunctions correspond to the FBR-DVR transformation matrix $T^{\theta'}$ for the θ' coordinate. We follow Ref. (117) by using the symmetry-adapted DVR (SADVR) to form the transformation matrix and the DVR points for the χ coordinate. Note that, we do not use the C_{6v} symmetry used in Ref. (117) because it only applies to A$_3$ system. We use the C_{2v} symmetry to form the SADVR so that it can be applied to the AB$_2$ system with conical intersections in C_{2v} geometries. Therefore, the SADVR in χ are constructed from the eigenvalues of the matrix of $\cos 2\chi$ in the $\Pi_m(\chi)$ basis, where the points in χ are not necessarily the same for the *even* and the *odd* states. The FBR-DVR transformation matrix T^χ is then formed with the eigenvectors of this $[\cos 2\chi]$ matrix. The full FBR-DVR transformation matrix in (θ', χ) is the direct product of $T^{\theta'}$ and T^χ

$$T = T^{\theta'} \bigotimes T^\chi \tag{4.126}$$

It should be noted that, $\cos 2\chi$ is symmetric under the $\chi \to -\chi$ operation and, therefore, does not mix the *even* and *odd* states in the FBR. And thus the $\mathbf{T}_\chi$

transformation matrix is block diagonal. We then can show that the FBR-DVR transformation matrices are real matrices instead of complex matrices. These real transformation matrices do not conflict with Eq.(4.72). The Hamiltonian in this DVR is no longer the complex Hamiltonian in Eq.(4.20). However, because the *even* and *odd* states do not mix in the overlap matrices and the eigenvalues $\mathcal{E}_q$ are real, the overlap matrices and eigenvalues in this real DVR is equivalent to those in the complex DVR. Therefore, we do not need to solve the complex differential equation as in Eq.(4.20), as done in Ref. (105).

The DVR representation of the surface function Hamiltonian is obtained as

$$\mathbf{H}^{DVR} = \mathbf{T}^T \mathbf{H}^{FBR} \mathbf{T}, \tag{4.127}$$

where H^{FBR} is the matrix representation of the surface Hamiltonian in Eq.(4.125). H^{FBR} is formed in the FBR defined in Eq.(4.114), and T is defined in Eq.(4.126). We then can partition the Hamiltonian in Eq.(4.127) as

$$\begin{aligned}
\mathbf{H}^{DVR} &= \mathbf{h}_{\theta'}^{DVR} \bigotimes \mathbf{I}_\chi + \mathbf{f}_{\theta'}^{DVR} \bigotimes \mathbf{h}_\chi^{DVR} + \tilde{\mathbf{V}}^{DVR} \\
&+ \mathbf{f}_{\theta'}^{DVR} \bigotimes (i\mathbf{A}_{I\chi})^{DVR} + (i\mathbf{A}_{I\theta'})^{DVR}, \tag{4.128}
\end{aligned}$$

where $\mathbf{I}_\chi$ is the unit square matrix in the χ basis,

$$\mathbf{h}_y^{DVR} = \mathbf{T}^T \mathbf{h}_y^{FBR} \mathbf{T}, \quad (y = \theta, \chi) \tag{4.129}$$

$$[\tilde{\mathbf{V}}]_{\alpha'\beta',\alpha,\beta}^{DVR} = [\bar{V} + A_R](\rho_n, \theta'_\alpha, \chi_\beta) \delta_{\alpha'\alpha} \delta_{\beta'\beta}, \tag{4.130}$$

and

$$[\mathbf{f}_{\theta'}]_{\alpha'\alpha}^{DVR} = \left[\sin(\theta'_\alpha/2)\right]^{-2} \delta_{\alpha'\alpha}. \tag{4.131}$$

We defined $(i\mathbf{A}_{I\chi})^{DVR}$ and $(i\mathbf{A}_{I\theta'})^{DVR}$ as

$$(i\mathbf{A}_{I\chi})^{DVR} = \mathbf{T}_\chi^T (i\mathbf{A}_{I\chi})^{FBR} \mathbf{T}_\chi, \tag{4.132}$$

and

$$(i\mathbf{A}_{I\theta'})^{DVR} = \mathbf{T}^T (i\mathbf{A}_{I\theta'})^{FBR} \mathbf{T}. \tag{4.133}$$

The δ functions in these equations are due to the fact that the functional operators are diagonal in the DVR (117; 121; 122; 123; 124; 125; 126); and thus the $\tilde{\mathbf{V}}^{DVR}$ and $\mathbf{f}_{\theta'}^{DVR}$ terms are simply evaluated at the corresponding DVR points, $(\rho_n, \theta_\alpha, \chi_\beta)$.

We can obtain the surface functions ϕ_q by diagonalizing Eq.(4.128). We have mentioned in the previous derivation that we adopt the sequential diagonalization-truncation procedure (117; 121; 122; 123; 124; 125; 126), which is used to reduce the dimension of $\mathbf{H}^{DVR}$ and the associated computational effort required to diagonalize it. As shown in Ref. (117), the rank of the DVR matrix in the θ coordinates is $l_{max} + 1$. For each θ_α ($\alpha \in (0, 1, \ldots, l_{max})$), we construct the one-dimensional Hamiltonian in χ as

$$\mathbf{H}^{1D} \equiv \mathbf{f}_{\theta'}^{DVR} \bigotimes \mathbf{h}_\chi^{DVR} + \tilde{\mathbf{V}}^{DVR} + \mathbf{f}_{\theta'}^{DVR} \bigotimes (i\mathbf{A}_{I\chi})^{DVR} \tag{4.134}$$

and thus the matrix elements have the form as

$$
\begin{aligned}
[\mathbf{H}^{1D}]_{\alpha'\alpha,\beta'\beta} &= [\mathbf{f}_{\theta'}^{DVR}]_{\alpha'\alpha}[\mathbf{h}_\chi^{DVR}]_{\beta'\beta}\delta_{\alpha'\alpha} + [\tilde{\mathbf{V}}^{DVR}]_{\alpha'\alpha,\beta'\beta} \\
&\quad + [\mathbf{f}_{\theta'}^{DVR}]_{\alpha'\alpha}[(i\mathbf{A}_{I\chi})^{DVR}]_{\beta'\beta}\delta_{\alpha'\alpha}
\end{aligned}
\tag{4.135}
$$

We know that the $f_{\theta'}h_\chi + \tilde{V}$ terms are block-diagonal and real symmetric in the FBR. Because the transformation matrix $\mathbf{T}_\chi$ is also real block-diagonal, the first two terms in Eq.(4.134), $\mathbf{f}_{\theta'}^{DVR} \bigotimes \mathbf{h}_\chi^{DVR} + \tilde{\mathbf{V}}^{DVR}$, are real symmetric in the DVR. We also know that $f_{\theta'}(iA_{I\chi})$ is real symmetric in the FBR and the transformation matrix $\mathbf{T}_\chi$ is real block-diagonal, so the $\mathbf{f}_{\theta'}^{DVR} \bigotimes (i\mathbf{A}_{I\chi})^{DVR}$ is real symmetric but block-off-diagonal. In this way, the one-dimensional Hamiltonian in the DVR in Eq.(4.134) is real symmetric and can be solved easily

$$(\mathbf{d}^\alpha)^T \mathbf{H}^{1D} (\mathbf{d}^\alpha) =^{1D} \mathbf{E}^\alpha, \tag{4.136}$$

where $^{1D}E^\alpha$ is the real diagonal matrix containing the eigenvalues, and $\mathbf{d}^\alpha$ is the associated eigenvector. The dimension of the $\mathbf{d}^\alpha$ is N_χ, which is the number of χ points used in the DVR calculation. We truncate the eigenvectors, $\mathbf{d}^\alpha$, by retaining those 1D eigenvectors whose eigenvalues $^{1D}E_t^\alpha$ satisfy the energy cutoff condition

$$^{1D}E_t^\alpha \leq E_{cut}. \tag{4.137}$$

The truncated matrix, $\mathbf{d}^\alpha$, is now an $N_\chi \times n_\alpha$ matrix, where n_α is the number of 1D eigenvalues retained for each θ'_α point. We perform convergence study on the E_{cut} parameter until we observe no significant change in the scattering results.

We then perform the unitary transformation on the Hamiltonian in Eq.(4.128) using the 1D eigenvector $\mathbf{d}^\alpha$ so that part of the Hamiltonian is diagonalized and truncated. The new Hamiltonian can be expressed as

$$
\begin{aligned}
\tilde{\mathbf{H}}^{DVR} &\equiv (\mathbf{d})^T \mathbf{H}^{DVR}(\mathbf{d}) \\
&= \mathbf{h}_{\theta'}^{DVR} \bigotimes \mathbf{I}_\chi + ^{1D}\mathbf{E}^\alpha + (\mathbf{d})^T (i\mathbf{A}_{I\theta'})^{DVR}(\mathbf{d}).
\end{aligned}
\tag{4.138}
$$

The first two terms in Eq.(4.138) are real symmetric. The last term

$$
(\mathbf{d})^T (i\mathbf{A}_{I\theta'})^{DVR}(\mathbf{d}),
$$

needs to be analyzed carefully. We have know from the previous subsection that $(i\mathbf{A}_{I\theta'})^{FBR}$ is real symmetric but block-off-diagonal. Because the FBR-DVR transformation matrices, $\mathbf{T}$, and the 1D eigenvector, $\mathbf{d}$, are both real and unitary, the resulting $(\mathbf{d})^T (i\mathbf{A}_{I\theta'})^{DVR}(\mathbf{d})$ is then still real symmetric. Therefore, the 2D DVR surface Hamiltonian in Eq.(4.138) is still real symmetric and thus can be diagonalized easily

$$
(\mathbf{C})^T \tilde{\mathbf{H}}^{DVR}(\mathbf{C}) = \mathbf{E}^{SF}
\tag{4.139}
$$

where $[\mathbf{E}^{SF}]_{tt'} = \mathcal{E}_t \delta_{tt'}$.

4.7.3 The DVR overlap matrix

Because we use the Numerov propagator, the potential matrix to be used in the propagation is just the diagonal $\mathcal{E}$ eigenvalue matrix. The overlap matrix between surface functions belonging to the neighboring ρ_n and ρ_{n+1} sectors,

$$
[\mathbf{O}]_{tt'} = \langle \phi_t(\rho_n) \,|\, \phi_t(\rho_n) \rangle,
\tag{4.140}
$$

is needed to transform the Numerov ratio matrix from one sector to the next. The tth surface eigenvector in the 2D DVR is obtained via

$$
\phi = \mathbf{d}\mathbf{C}.
\tag{4.141}
$$

And thus the overlap matrix $\mathbf{O}$ can be expressed as

$$
\mathbf{O} = [\mathbf{d}\mathbf{C}]^T(\rho_n)\mathbf{d}\mathbf{C}(\rho_{n+1}).
\tag{4.142}
$$

Both matrices $\mathbf{d}$ and $\mathbf{C}$ are real and they lead to a real overlap matrix $\mathbf{O}$.

4.8 Conclusion

In this chapter, we have demonstrated how to solve the time-independent Schrodinger equation with the conical intersections in the C_{2v} geometries. We have shown that by using the Numerov propagator, the first derivative terms $(\partial/\partial\rho)$ and the complex terms are not included. We use the ABM and DVR method to solve for the surface two-dimensional Hamiltonian. By using the MOES method, the Hamiltonian matrix is constructed as a real symmetric matrix and the overlap matrices are real and do not need special treatment. This MOES method should greatly simplify the Hamiltonian and the overlap matrices.

Chapter 5

The $C_{\infty v}$ conical intersections

The spin-aligned lithium triatomic system has a seam of conical intersections between the lowest two electronic potential energy surfaces (PESs) in the collinear geometries. The lowest conical intersection point is energetically located at 3×10^{-4} Ha., which is slightly above the three-body dissociation limit at zero (10). However, the minimum energy required to circumscribe a seam of conical intersections is -2.11×10^{-3} Ha., which is below the lowest vibrational energy of the separate diatoms. Therefore, though the reactive scattering processes can happen at ultracold temperatures, the geometric phase should not be neglected. To properly treat the geometric phase effect, Kendrick and Pack used the vector potential method to treat H+O$_2$ (105), Na$_3$ (106) and H+D$_2$ (107). These systems either do not have collinear conical intersections or it is energetically impossible move about the lowest conical intersections. They did not treat the more difficult situation where collinear conical intersections occur. However, it has not been applied to the collinear case, which we will tackle in this study.

The conical intersections in the spin-aligned Li$_3$ system lie in the collinear geometries, which induce additional difficulties in deriving the geometric phase angle η. Unlike the cases where the conical intersections lie in the C_{2v} geometries (101; 105), to completely go around the conical intersections in the $C_{\infty v}$ geometries requires very careful derivation.

5.1 Derivation of $\eta(R)$

5.1.1 $\eta(R)$ in A_3 systems

In this section, we will derive a new geometric phase angle for collinear conical intersections. The major difficulty lies in the dependence of the geometric phase angle η on the nuclear coordinates. It has been proved that in the Jahn-Teller molecular system, where the conical intersections are in the non-linear geometries, the geometric phase angle depends solely on the internal coordinates (15). However, when the conical intersections are collinear, determining whether η depends only on the internal coordinates has been a challenging question. In a normal body-framed (BF) internal coordinates (108; 109; 110) for a triatomic system, the three nuclei are allowed only to move on half of the BF plane. For instance, the BF mass-scaled Jacobi coordinate $\vec{s}_\tau$ is chosen to have a positive component along the BF X axis in the coordinates of Ref. (108). In the BF APH coordinates, the Z axis is chosen so that it has the smallest moment of inertia I_z; the Y axis is chosen to be perpendicular to the triatomic plane. Here, the mass-scaled Jacobi coordinate is proportional to the internuclear distance between the diatom. The other half of the BF plane is defined by rotating the BF X-Y plane about the BF Z axis by an angle of π. Thus, the rotated BF coordinates can still have a positive X component of $\vec{s}_\tau$. However, this rotation results in a problem describing the loop around the seam of collinear conical intersections because this enclosed loop depends on two different γ_Q angles. We will show that the geometric phase angle, for a triatomic system with collinear conical intersections, depends on both the internal coordinates (ρ, θ, χ) and one Euler angle γ_Q. We, therefore, denote this new geometric phase angle as $\bar{\eta} = \bar{\eta}(\rho, \theta, \chi, \gamma_Q)$, to be distinguished from $\eta = \eta(\rho, \theta, \chi)$.

For simplicity, we start with the half plane in the BF coordinates where the three Euler angles are constants. In this half plane, we can define an angle η which depends only on the three internal coordinates. This angle η will describe the rotation about the conical intersections in this half plane. We will first derive an expression for this angle η in the half plane with a constant γ_Q angle, and then draw a connection between the geometric phase angle $\bar{\eta}$ and this angle η.
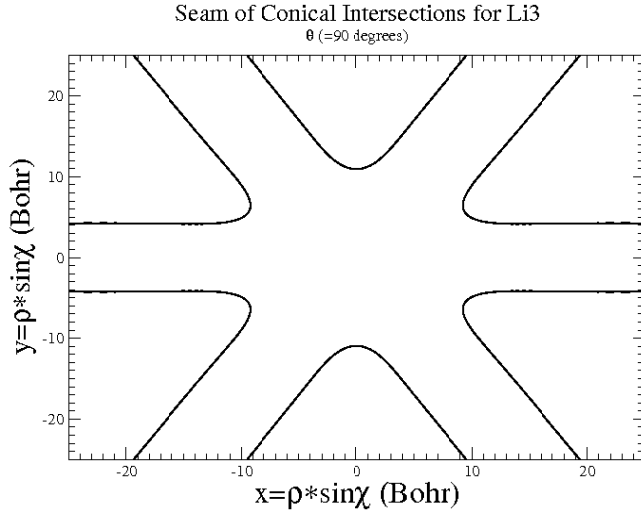
Figure 5.1: Seams of conical intersections in the $\theta = \pi/2$ plane.

An explicit functional form for $\eta(R) = \eta(\rho, \theta, \chi)$ needs to be derived very carefully because there are three seams of conical intersections in this triatomic lithium system. We now focus on the $^7\text{Li}_3$ system to illustrate this problem. A more general derivation for collinear conical intersections of an ABC system is shown in the next subsection. Because the coordinate system, which we choose from Ref. (108), covers the configuration space twice, there are six seams of conical intersections in these particular internal coordinates. We define Cartesian coordinates (x, y, z) in the upper half of the sphere in the internal coordinates via $x = \rho \sin\theta \cos\chi$, $y = \rho \sin\theta \sin\chi$ and $z = \rho \cos\theta$. It is called upper half sphere because the θ angle is defined in the range of $[0, \pi/2]$. The conical intersections are located in the collinear geometries where $(\theta = \pi/2)$. And, thus, these six seams of conical intersections are confined in the $Z = 0$ plane, which is shown in Fig. 5.1. As we have mentioned in the previous sections, a triatomic system has three internal degrees of freedom and two relations are need for the nuclear coordinates to form conical intersections. Therefore, there are, in general, several seams (lines) of conical intersections in these triatomic systems. We define the rotating angle $\eta(\rho, \theta, \chi)$

as a sum of six angles, each of which describes the rotation about one particular seam of conical intersections

$$\eta(\rho, \theta, \chi) = \sum_{i=1}^{6} B_i \eta_i(\rho, \theta, \chi), \tag{5.1}$$

where B_i are the signs for each η_i angle, as will be explained later.

Take the $i = 1$ case for example. This seam of conical intersection is confined to the $\chi \in [0, \pi/3]$ region. If we rotate the seam clockwise by $\chi = \pi/6$ and fit the functional form of this curve as $x = f(y)$, it is clear that $f(y) = f(-y)$. It is, in general, difficult to define an angle of rotation about a curve instead of a straight line. Therefore, we perform a diffeomorphism so that we can bijectively map (x, y, z) to (x', y', z') in which the $x' = f(y')$ is a straight line. A diffeomorphism is a map between manifolds which is differentiable and has a differentiable inverse. The mapping relation is given as

$$
\begin{aligned}
x' &= x - f(y) = \rho \sin \theta \cos \chi - f(\rho \sin \theta \sin \chi) \\
y' &= y = \rho \sin \theta \sin \chi \\
z' &= z = \rho \cos \theta,
\end{aligned} \tag{5.2}
$$

where the $x' = f(y')$ is given as a straight line $x' = 0$. We then need to rotate the seam of conical intersections back by rotation about the Z axis counter-clockwise through $\chi = \pi/6$. Therefore, for the first seam of the conical intersections, the new coordinate transformation is given as

$$
\begin{aligned}
x'' &= \rho \sin \theta \cos(\chi - \pi/6) - f(\rho \sin \theta \sin(\chi - \pi/6)) \\
y'' &= \rho \sin \theta \sin(\chi - \pi/6) \\
z'' &= \rho \cos \theta.
\end{aligned} \tag{5.3}
$$

Therefore, for the new coordinates (x'', y'', z''), the rotating angle $\eta_1(\rho, \theta, \chi)$ is defined as

$$\tan \eta_1(\rho, \theta, \chi) \equiv \frac{z''}{x''} = \frac{\rho \cos \theta}{\rho \sin \theta \cos(\chi - \pi/6) - f(\rho \sin \theta \sin(\chi - \pi/6))}. \tag{5.4}$$

Note that, this angle η_i is defined only in the range of $[0, \pi)$, because θ is only defined in the range of $[0, \pi/2]$ and thus $\rho \cos \theta$ is always positive. All the other

rotating angles $\eta_i(\rho, \theta, \chi)$ can be obtained in the same fashion or simply by doing a rotation by χ, because the shape of each seam of conical intersections are identical. Both procedures give the same representation of the rotating angles $\eta_i(\rho, \theta, \chi)$. Therefore, if we define

$$\eta_1(\rho, \theta, \chi) = \tan^{-1}\left[\frac{\rho \cos \theta}{\rho \sin \theta \cos(\chi - \pi/6) - f(\rho \sin \theta \sin(\chi - \pi/6))}\right] \equiv g(\rho, \theta, \chi),$$
(5.5)

all six angles can be expressed as

$$\eta_i(\rho, \theta, \chi) = g(\rho, \theta, \chi - (i-1)\frac{\pi}{3}).$$
(5.6)

The signs of the coefficients B_i in Eq. (5.1) are not always positive, which is due to the special coordinate system. As pointed by Kuppermann in Ref. (8), the geometric phase factor needs to satisfy certain initial conditions, e.g. parity. The total wavefunction has definite parity, p_{total}, because the Hamiltonian operator in Eq. (3.2) is invariant under the inversion operator. The total wavefunction can be written as

$$\begin{aligned}\Psi_{tot}(\vec{R}, \vec{r}) &= \Psi_0^{SV}(\vec{R})\varphi_0^{SV}(\vec{r}) \\ &= \Psi_0^{DV}(\vec{R})\varphi_0^{DV}(\vec{r})\end{aligned}$$
(5.7)

where "SV" denotes single-valued and "DV" denotes double-valued. Because $\varphi_0^{DV}(\vec{r})$ and $\varphi_0^{SV}(\vec{r})$ are eigenvectors of the $H_e(\vec{r}, R)$ operator, and $H_e(\vec{r}, R)$ is invariant under inversion, $\varphi_0^{DV}(\vec{r})$ and $\varphi_0^{SV}(\vec{r})$ need to have definite parity. Thus, the geometric phase angle needs to have definite symmetry under the inversion operation. The rotation of the χ angle about the z axis is completely orthogonal to the rotation of our geometric phase angle in this study. Therefore, the inversion operator in O(2), $\chi \to \chi + \pi$, should not change the geometric phase factor, $\exp[-l/2\bar{\eta}]$. In other words, the geometric phase angle, $\bar{\eta}(\rho, \theta, \chi, \gamma_Q)$, should be invariant under inversion. It should be noted that the inversion operator can also be expressed in O(3), $\alpha \to \alpha + \pi, \beta \to \pi - \beta, \gamma_Q \to \pi - \gamma_Q$. This also implies that $\bar{\eta}(\rho, \theta, \chi, \gamma_Q)$ needs to be invariant under the inversion operator in O(3), which will
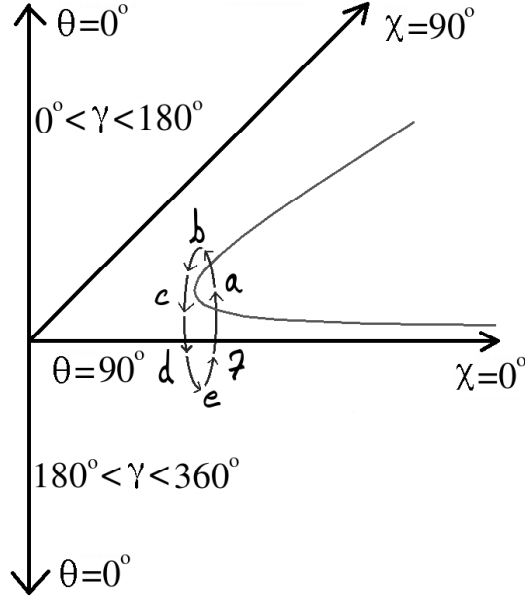
Figure 5.2: The closed loop encircles the $\chi = \pi/6$ conical intersection seam.

be used as a check of our final expression of $\bar{\eta}$. With the parity argument above, we choose $B_i = 1$ so that

$$\eta(\rho, \theta, \chi) = \sum_{i=1}^{6} \eta_i(\rho, \theta, \chi). \tag{5.8}$$

In order to relate $\bar{\eta}(\rho, \theta, \chi, \gamma_Q)$ to $\eta(\rho, \theta, \chi)$, we need to visualize the closed path which goes completely around the seam of conical intersections in the collinear geometries. One can start from a point outside the conical intersections at the collinear plane ($\theta = \pi/2$), e.g. point a in Fig. 5.2. One then goes to point b, and then point c, which is inside the conical intersection on the collinear plane. However, the internal coordinates only define the upper hemisphere where $\theta \in [0, \pi/2]$. In the body fixed frame, the internal coordinates define the angle between the two mass-scaled Jacobi coordinates $\vec{S}_\tau$ and $\vec{s}_\tau$ to be in the range of $[0, \pi]$ while these two coordinates in the range $(\pi, 2\pi]$ are not defined, because this $(\pi, 2\pi]$ range can be achieved by rotating the $X - Y$ axis about the Z axis for π while fixing all the internal coordinates the same. In order to completely go around the conical intersection, one needs to rotate the Euler angle γ_Q. Therefore, this closed path depends on the Euler angle, which means a virtual rotation of the BF $X - Y$

71
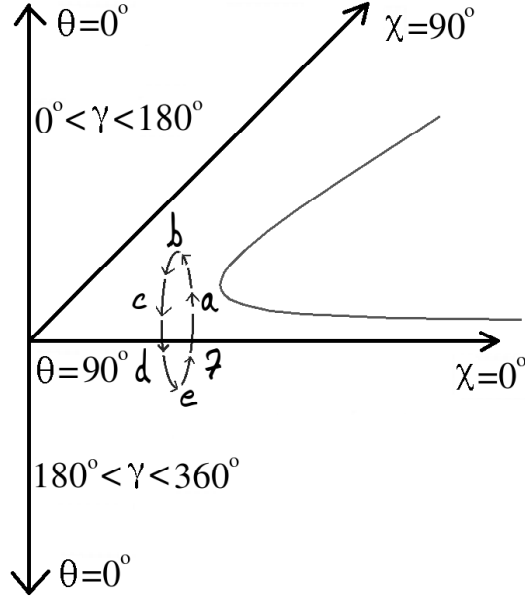
Figure 5.3: The closed loop does not encircle the $\chi = \pi/6$ conical intersection seam.

axis. This action can be express in terms of the γ_Q angle as $\gamma_Q \to \gamma_Q \pm \pi$. We then can "stitch" the upper ($\gamma_Q \in [0, \pi]$) hemisphere in the internal coordinates to the lower (($\gamma_Q + \pi$) $\in [\pi, 2\pi]$) hemisphere, which is shown in Fig. 5.2. To be simple, we express the $\bar{\eta}$ angle as $\bar{\eta}(\rho, \theta, \chi, \gamma_Q)$.

The closed path which encircles the $\chi = \pi/6$ conical intersection seam once can be shown in Fig. 5.2 as $a \to b \to c \to d \to e \to f$. The total angle $\bar{\eta}$ needs to change by a factor of 2π along this path. We know that in either hemisphere the angle γ_Q remains constant and only undergoes a rotation of a π angle when it passes the collinear plane, the stitching plane. Therefore, we can relate $\bar{\eta}$ with η in a simple form as

$$\bar{\eta}(\rho, \theta, \chi, \gamma_Q) = h_1(\gamma_Q)\eta(\rho, \theta, \chi) + h_2(\gamma_Q), \qquad (5.9)$$

where $h_1(\gamma_Q)$ and $h_2(\gamma_Q)$ depend only on γ_Q. The functional forms of $h_1(\gamma_Q)$ and $h_2(\gamma_Q)$ are not arbitrary because they need to satisfy three rules:

1. Sign change rule: $\bar{\eta}$ needs to change by a factor of 2π when it goes completely around the seam of conical intersections. This rule can be expressed as

$$\bar{\eta}(f) - \bar{\eta}(a) = 2\pi \qquad (5.10)$$

72

where a and f denotes the points on the path in Fig. 5.2.

2. Continuous rule: $\bar{\eta}$ needs to be continuous when it changes from point c to d as we rotate the γ_Q angle by π. This rule can be expressed as

$$\bar{\eta}(d) = \bar{\eta}(c). \tag{5.11}$$

Interestingly this rule can also be viewed as a special case of the sign change rule, which means that a closed loop does not change sign when it does not encircle the seam of conical intersections. This case can be seen from Fig. 5.3.

3. No bias rule: the upper hemisphere ($\gamma_Q \in (0, \pi)$) and the lower hemisphere ($(\gamma_Q + \pi) \in (\pi, 2\pi)$) should be equivalent and there should be no basic discrimination against either one of the hemispheres. This rule can be expressed as

$$\bar{\eta}(c) - \bar{\eta}(a) = \pi. \tag{5.12}$$

These rules result in a usual branch cut of the $\bar{\eta}$ angle outside of all conical intersections, due entirely to the geometric phase. However, another discontinuous plane is also introduced when $\gamma_Q = \pi$; it is also due to the conical intersections. The effect of this discontinuous plane at $\gamma_Q = \pi$ should be treated carefully, as we will discuss in the next section.

The three mathematical expressions, Eq. (5.10, 5.11,5.12), for the three rules can lead to the following conditions:

$$
\begin{aligned}
h_2(\gamma_Q + \pi) - h_2(\gamma_Q) &= 2\pi \\
h_1(\gamma_Q)\pi + h_2(\gamma_Q) &= h_1(\gamma_Q + \pi)\pi + h_2(\gamma_Q + \pi) \\
h_1(\gamma_Q)\pi &= \pi
\end{aligned}
\tag{5.13}
$$

where $\gamma_Q \in (0, \pi)$. And then we obtain

$$
\begin{aligned}
h_1(\gamma_Q)\pi &= 1 \\
h_1(\gamma_Q + \pi) &= -1 \\
h_2(\gamma_Q) &= h_2(\gamma_Q + \pi) - 2\pi
\end{aligned}
\tag{5.14}
$$

73
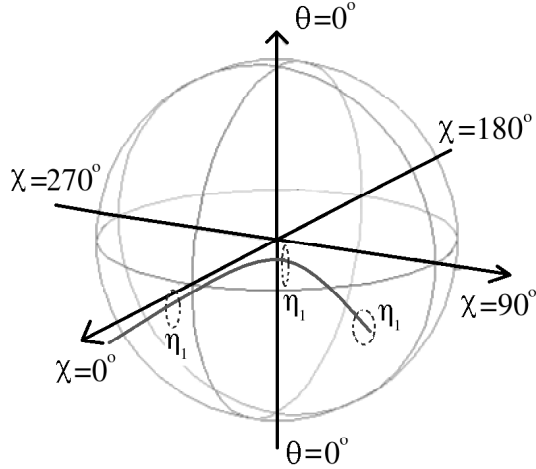
Figure 5.4: Three dimensional plot of the stitched hemispheres and the geometric phase angle to encircle the $\chi = \pi/6$ conical intersection seam.

where $\gamma_Q \in [0, \pi)$. Here, the choice of $h_2(\gamma_Q)$ is simply an initial condition of the $\bar{\eta}$ at point a. We then choose $h_2(\gamma_Q) = 0$ where $\gamma_Q \in [0, \pi)$ so that $\bar{\eta}(a) = 0$.

Therefore, the angle $\bar{\eta}$ can be expressed as

$$\bar{\eta}(\rho, \theta, \chi, \gamma_Q) = \begin{cases} \eta(\rho, \theta, \chi) & \text{if } \gamma_Q \in [0, \pi); \\ -\eta(\rho, \theta, \chi) + 2\pi & \text{if } \gamma_Q \in [\pi, 2\pi). \end{cases} \quad (5.15)$$

It can be seen from Fig. 5.2 that $\bar{\eta}$ changes by 2π from point a to f and encircles the seam of conical intersections; it can also be seen from Fig. 5.3 that $\bar{\eta}$ remains unchanged as it goes from point a to f because it does not encircle the seam of conical intersections. the three-dimensional plot of this stitching is illustrated in Fig. 5.4. We can also start with a much more general relation between $\bar{\eta}$ and η than Eq. (5.9):

$$\bar{\eta} = F(\rho, \theta, \chi, \gamma_Q). \quad (5.16)$$

Using the three rules from Eq. (5.10,5.11,5.12), one obtains the same relation between $\bar{\eta}$ and η expressed in Eq. (5.15).

One alternative way to find $\bar{\eta}$ is to start from a different set of coordinates. Here we define $\vec{\mathbf{R}}' = (\rho, \theta', \chi, \alpha_Q, \beta_Q, \gamma'_Q)$ where the new $\theta' \in [0, \pi]$ and $\gamma'_Q \in [0, \pi)$. This set of coordinates is equivalent to Pack's coordinates in Ref. (127; 128; 129),

74

in which the whole BF plane is defined by the internal coordinates. The new coordinates, $\vec{\mathbf{R}}'$, make the geometric phase angle very easy to express as

$$\eta_1(\rho, \theta', \chi) = \tan^{-1}\left[\rho\cos\theta', \rho\sin\theta'\cos(\chi - \pi/6) - f(\rho\sin\theta'\sin(\chi - \pi/6))\right].$$
(5.17)

This geometric phase angle, in the $\vec{\mathbf{R}}'$ coordinates, does not depend on γ'_Q because the internal coordinates allow the BF $\vec{s}_\tau$ to have negative values in the X direction; the geometric phase angle, in the $\vec{\mathbf{R}}$ coordinates, however, does depend on γ_Q because the BF $\vec{s}_\tau$ is chosen to be positive in the x direction while the negative part are described by a new BF frame which undergoes a virtual rotation in γ_Q by an angle of π.

The relation between $\vec{\mathbf{R}}'$ and $\vec{\mathbf{R}}$ can be obtained via the transformations to the SF coordinates $(\vec{\mathbf{S}}, \vec{s})$

$$\begin{pmatrix} \vec{S}_\tau \\ \vec{s}_\tau \end{pmatrix} = \tilde{T}(\chi_\tau)\tilde{R}(\alpha_Q, \beta_Q, \gamma_Q) \begin{pmatrix} 0 \\ 0 \\ \frac{\rho}{\sqrt{2}}\sqrt{1 + \sin\theta} \\ \frac{\rho}{\sqrt{2}}\sqrt{1 - \sin\theta} \\ 0 \\ 0 \end{pmatrix},$$
(5.18)

and

$$\begin{pmatrix} \vec{S}_\tau \\ \vec{s}_\tau \end{pmatrix} = \tilde{T}(\chi_\tau)\tilde{R}(\alpha_Q, \beta_Q, \gamma'_Q) \begin{pmatrix} 0 \\ 0 \\ \frac{\rho}{\sqrt{2}}\sqrt{1 + \sin\theta'} \\ \frac{\rho}{\sqrt{2}}(\cos\frac{\theta'}{2} - \sin\frac{\theta'}{2}) \\ 0 \\ 0 \end{pmatrix}.$$
(5.19)

Here, $\tilde{T}$ is a kinematic rotation matrix and $\tilde{R}$ is the spatial rotation matrix, both of which can be found in Appendix E.3 or Ref. (108). By setting Eq. (5.18) equal to Eq. (5.19), we obtain the relation between the $\vec{\mathbf{R}}'$ and $\vec{\mathbf{R}}$ coordinates,

$$\theta' = \begin{cases} \theta & \text{if } \gamma_Q = \gamma'_Q \text{ and } \gamma_Q \in [0, \pi) \\ \pi - \theta & \text{if } \gamma_Q = \gamma'_Q + \pi \text{ and } \gamma_Q \in [\pi, 2\pi) \end{cases}$$

or
$$\theta' = \theta = \pi/2.$$
(5.20)

Therefore, we can simplify the relation in Eq. (5.20) as

$$\theta' = 2[H(\pi - \gamma_Q) - 1/2]\theta + [1 - H(\pi - \gamma_Q)]\pi, \qquad (5.21)$$

where $H(x)$ is the Heaviside function defined as

$$H(x) = \begin{cases} 0 & \text{if } x \leq 0 \\ 1 & \text{if } x > 0 \end{cases}. \qquad (5.22)$$

Note that, the third solution in Eq. (5.20) is incorporated in Eq. (5.21) because it also complies with Eq. (5.20). The geometric phase angle $\bar{\eta}$, in the $\vec{\mathbf{R}}'$ coordinates, can be expressed in the conventional $\vec{\mathbf{R}}$ coordinates as

$$\bar{\eta}_1(\rho, \theta, \chi, \gamma_Q) = \tan^{-1}\left[\frac{\rho\cos[2[H(\pi - \gamma_Q) - 1/2]\theta + [1 - H(\pi - \gamma_Q)]\pi]}{\rho\sin\theta\cos(\chi - \pi/6) - f(\rho\sin\theta\sin(\chi - \pi/6))}\right]. \qquad (5.23)$$

We notice that Eq. (5.23) is exactly the same as Eq. (5.15).

We numerically fit the $x = f(y)$ function to the seam of conical intersections using more than 1000 data points, which depends on ρ and χ because $\theta = \pi/2$. We use a form of $x = f(y) = \sqrt{a + 3y^2} + b - \sqrt{a}$ to give the correct asymptotic behavior, where a and b are adjustable parameters. In the fitting process, we give heavier weights to the data points near the $\chi = \pi/6$ line where the energies of the conical intersections are comparatively much smaller than those at other χ angles. For example, the energy of the conical intersection at ($\rho = 16$ Bohr, $\theta = \pi/2$, $\chi = \pi/6$) is 0.02 Ha. which is much higher than the atom-diatom dissociation limit. After minimizing the room-mean-square error the fitted parameters are obtained as $a = 16.5716$ a.u.and $b = 10.9344$ a.u., and the fitted function is plotted against the data in Fig. 5.5.

It should be noted that we cannot directly follow the derivation in Ref. (105) to get the one-form components of $\mathbf{A}(R)$, because $\bar{\eta}$ now depends on the Euler angle, γ_Q. Therefore, we use $\bar{\mathbf{A}}(\vec{R})$ to denote the new one-form components and it depends on ρ, θ, χ and γ_Q. We first express $\mathbf{A}(R)$ in terms of η

$$
\begin{aligned}
A_\rho(R) &= -\frac{l}{2}\frac{\partial\eta(R)}{\partial\rho}, \\
A_\theta(R) &= -\frac{l}{2}\frac{\partial\eta(R)}{\partial\theta}, \\
A_\chi(R) &= -\frac{l}{2}\frac{\partial\eta(R)}{\partial\chi}.
\end{aligned}
\qquad (5.24)
$$

76
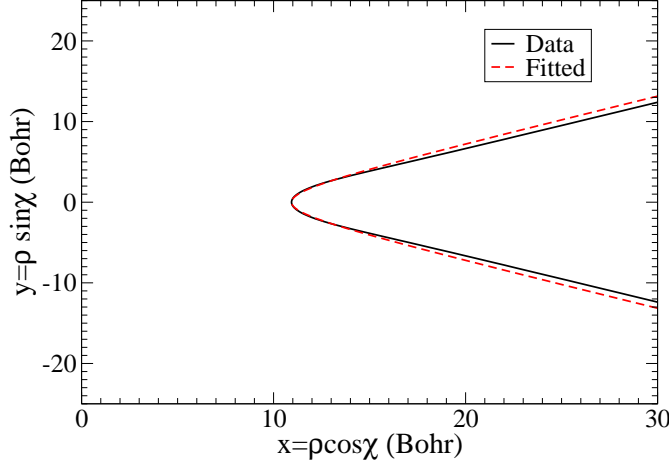
Figure 5.5: Fitting results of the $x = f(y)$ function.

Therefore, $\bar{\mathbf{A}}(\vec{R})$ can be expressed as

$$\bar{\mathbf{A}}_x(\rho, \theta, \chi, \gamma_Q) = \begin{cases} A_x(R) & \text{if } \gamma_Q \in (0, \pi); \\ -A_x(R) & \text{if } \gamma_Q \in (\pi, 2\pi). \end{cases} \tag{5.25}$$

where $x = (\rho, \theta, \chi)$. Notice, the $\bar{\mathbf{A}}_{\gamma_Q}$ is zero when $\gamma_Q \neq \pi$. The discontinuity problem of $\bar{\mathbf{A}}_{\gamma_Q}$ at $\gamma_Q = \pi$ will be addressed later on.

Using the fitted form of $f(y)$ and Eq. (5.5), we can solve the expression for

$$A_\rho^1 \equiv -\frac{l}{2} \frac{\partial \eta_1(R)}{\partial \rho} \tag{5.26}$$

as

$$\begin{aligned} A_\rho^1 &= -\frac{l}{2} \\ &\times \frac{\cos\theta}{\rho^2 \cos^2\theta + [\rho \sin\theta \cos(\chi - \pi/6) - \sqrt{a + 3\rho^2 \sin^2\theta \sin^2(\chi - \pi/6)} - b + \sqrt{a}]^2} \\ &\times \frac{-a + (b - \sqrt{a})\sqrt{a + 3\rho^2 \sin^2\theta \sin^2(\chi - \pi/6)}}{\sqrt{a + 3\rho^2 \sin^2\theta \sin^2(\chi - \pi/6)}}, \end{aligned} \tag{5.27}$$

which leads to

$$A_\rho = A_\rho^1 + A_\rho^2 + A_\rho^3 + A_\rho^4 + A_\rho^5 + A_\rho^6. \tag{5.28}$$

77

Likewise we can obtain A_θ^1

$$A_\theta^1 = -\frac{l}{2}$$

$$\times \frac{1}{\rho^2 \cos^2\theta + [\rho\sin\theta\cos(\chi - \pi/6) - \sqrt{a + 3\rho^2\sin^2\theta\sin^2(\chi - \pi/6)} - b + \sqrt{a}]^2}$$

$$\times \left[\frac{\rho\sin\theta(a + 3\rho^2\sin^2(\chi - \pi/6))}{\sqrt{a + 3\rho^2\sin^2\theta\sin^2(\chi - \pi/6)}} - \rho^2\cos(\chi - \pi/6) \right.$$

$$+ \left. (b - \sqrt{a})\rho\sin\theta \right], \tag{5.29}$$

which leads to

$$A_\theta = A_\theta^1 + A_\theta^2 + A_\theta^3 + A_\theta^4 + A_\theta^5 + A_\theta^6; \tag{5.30}$$

and we can obtain A_χ^1

$$A_\chi^1 = -\frac{l}{2}$$

$$\times \frac{\rho^2\sin\theta\cos\theta\sin(\chi - \pi/6)}{\rho^2\cos^2\theta + [\rho\sin\theta\cos(\chi - \pi/6) - \sqrt{a + 3\rho^2\sin^2\theta\sin^2(\chi - \pi/6)} - b + \sqrt{a}]^2}$$

$$\times \left[\frac{3\rho\sin\theta\cos(\chi - \pi/6)}{\sqrt{a + 3\rho^2\sin^2\theta\sin^2(\chi - \pi/6)}} + 1 \right], \tag{5.31}$$

which leads to

$$A_\chi = A_\chi^1 + A_\chi^2 + A_\chi^3 + A_\chi^4 + A_\chi^5 + A_\chi^6. \tag{5.32}$$

Before we continue our derivation of the Hamiltonian with the inclusion of this geometric phase angle, $\bar{\eta}(\rho, \theta, \chi, \gamma_Q)$, we write down certain properties of the Hamiltonian with respect to certain operations, e.g. inversion. We have tested that the $\eta(\rho, \theta, \chi)$ is invariant under inversion operator in O(2) with $\chi \to \chi \pm \pi$, and thus $\bar{\eta}(\rho, \theta, \chi, \gamma_Q)$ is also invariant under inversion in O(2). The inversion operator can also be expressed in O(3) as $\alpha \to \alpha + \pi, \beta \to \pi - \beta, \gamma_Q \to \pi - \gamma_Q$. Because it only depends on γ_Q, $\bar{\eta}(\rho, \theta, \chi, \gamma_Q)$ is also invariant under inversion in O(3). We can conclude that all the $\bar{\mathbf{A}}(\vec{R})$ terms are invariant under inversion operation.

We define $\mathcal{P}$ as $(\rho, \theta, \chi, \alpha, \beta, \gamma_Q) \to (\rho, \theta, -\chi, \alpha, \beta, \gamma_Q)$. It can be shown that

$$\mathcal{P}\eta_1 = \eta_6, \quad \mathcal{P}\eta_6 = \eta_1$$

$$\mathcal{P}\eta_2 = \eta_5, \quad \mathcal{P}\eta_5 = \eta_2$$

$$\mathcal{P}\eta_3 = \eta_4, \quad \mathcal{P}\eta_4 = \eta_3 \tag{5.33}$$

and thus $\mathcal{P}\eta = \eta$. It can be easily shown that certain symmetry properties exist for the vector potential terms, A, with respect to $\chi \to -\chi$:

$$
\begin{aligned}
A_\theta(\rho, \theta, -\chi) &= A_\theta(\rho, \theta, \chi) \\
\left(\frac{\partial A_\theta}{\partial \theta}\right)(\rho, \theta, -\chi) &= \left(\frac{\partial A_\theta}{\partial \theta}\right)(\rho, \theta, \chi)
\end{aligned}
\tag{5.34}
$$

and

$$
\begin{aligned}
A_\chi(\rho, \theta, -\chi) &= -A_\chi(\rho, \theta, \chi) \\
\left(\frac{\partial A_\chi}{\partial \chi}\right)(\rho, \theta, -\chi) &= \left(\frac{\partial A_\chi}{\partial \chi}\right)(\rho, \theta, \chi).
\end{aligned}
\tag{5.35}
$$

This property will be used in the next subsection to simplify the Hamiltonian.

5.1.2 $\eta(R)$ in ABC systems

The lithium atom has two major isotopes, ^{6}Li and ^{7}Li. Conical intersections in a ^{6}Li^{7}Li^{7}Li system should be treated differently than in a ^{7}Li^{7}Li^{7}Li system. In general, we denote a triatomic system by A_3 when three atoms are identical and by ABC when three atoms are different. We will briefly discuss how to treat the geometric phase angle of an ABC system with collinear conical intersections.

The fundamental difference is the symmetry group for an ABC system. An A_3 system's PES belongs to a D_{3h} group; and an ABC system's PES belongs to a lower symmetry group, C_S. Let us assume this ABC system still has three seams of conical intersections in the configuration space. Because the locations of conical intersections in an ABC system are different from those in an A_3 system, our expression of the η in Eq. (5.6) does not apply to the ABC system. We thus need to change Eq. (5.6) into

$$
\begin{aligned}
\eta_i(\rho, \theta, \chi) = \tan^{-1} & \left[\rho \cos\theta, \rho \sin\theta \cos(\chi - \pi/6 - (i-1)\pi/3) \right. \\
& \left. - f_i(\rho \sin\theta \sin(\chi - \pi/6 - (i-1)\pi/3))\right],
\end{aligned}
\tag{5.36}
$$

where the fitted functions f_i are different for each seam of conical intersections. The total geometric phase angle $\bar{\eta}$ is then expressed as

$$
\bar{\eta}(\rho, \theta, \chi, \gamma_Q) = \begin{cases} \eta(\rho, \theta, \chi) & \text{if } \gamma_Q \in [0, \pi); \\ -\eta(\rho, \theta, \chi) + 2\pi & \text{if } \gamma_Q \in [\pi, 2\pi), \end{cases}
\tag{5.37}
$$

where η is

$$\eta = \sum_i^6 \eta_i. \tag{5.38}$$

The associated vector potential terms can still be computed in a similar fashion, and no symmetry argument should be used to simplify those expressions. These new expressions of the vector potential terms, $\bar{A}$, can be directly applied to the Hamiltonian, as will be discussed in the next section. The molecular Hamiltonian is no longer invariant under the symmetry operation $\mathcal{P}$ and thus there is no need to discuss the even or odd states with respect to this operation.

5.2 The Hamiltonian

The double-valued nuclear wavefunction, $\Psi \exp[-l/2\bar{\eta}(\rho, \theta, \chi, \gamma_Q)]$, includes the geometric phase factor which now depends on the Euler angle γ_Q. Therefore, we need to modify Eq. (3.14) and Eq. (3.15) as

$$\bar{\mathbf{A}}_R(\vec{R}) = -\frac{l}{2} \nabla_R \, \bar{\eta}(\vec{R}), \tag{5.39}$$

$$\bar{\mathbf{A}}_{\hat{R}}(\vec{R}) \equiv i \left\langle \bar{\varphi}_0(\vec{R}) | U^{-1}(\hat{R}) \left(\nabla_{\hat{R}} U(\hat{R}) \right) | \bar{\varphi}_0(\vec{R}) \right\rangle - \frac{l}{2} \nabla_{\hat{R}} \bar{\eta}(\vec{R}) \tag{5.40}$$

where

$$\bar{\mathbf{A}}(\vec{R}) = \bar{\mathbf{A}}_R(\vec{R}) + \bar{\mathbf{A}}_{\hat{R}}(\vec{R}). \tag{5.41}$$

The first term in Eq. (5.40) has been assumed to play a very minor role and thus we ignore this factor. The additional term in Eq. (5.40) is because of the dependence of $\bar{\eta}$ on the Euler angle γ_Q, which is only true for the collinear conical intersections. More explanations can be found in previous sections.

Before we rewrite Eq. (3.17), we need to specify the approximations we have made in deriving Eq. (3.17): one-state adiabatic representation with the Born-Oppenheimer approximation and an appropriate boundary condition (8). In this one-state adiabatic representation with the Born-Oppenheimer approximation, we assume that the effect of the other electronic adiabatic PESs is negligible. We have also assumed the diagonal part of the nonadiabatic couplings are negligible. These assumptions are valid when the probability of the nuclear wavefunction near the

conical intersection is negligible, which eliminates the divergence problem of the nonadiabatic coupling terms. This approximation is, therefore, valid for scattering at the ultracold temperatures, where the nuclear wavefunction exponentially dies off in the conical intersection region. However, because the nuclear wavefunction is able to completely move around the conical intersections, an appropriate boundary condition must be applied. This boundary condition is different from the conventional Born-Oppenheimer approximation, which excludes the geometric phase effect. This boundary condition states that the use of a real double-valued adiabatic electronic function leads to the double-valued nuclear wavefunction so that the total molecular wavefunction remains single-valued; or, equivalently, that the use of a complex, single-valued, adiabatic electronic wavefunction leads to a single-valued nuclear wavefunction and additional vector potential terms in the Hamiltonian. These non-trivial vector potential terms are the major difference between this study and the previous scattering calculations (31; 32).

One major difference in the modified Hamiltonian from the derivations with nonlinear conical intersections for a Jahn-Teller system in Eq. (3.17), is the γ_Q dependence of the vector potentials. However, not only the geometric phase angle depends on γ_Q, but also the BF adiabatic double-valued electronic wavefunction depends on γ_Q. The single-valued adiabatic electronic wavefunction is defined as

$$\phi^{SV} = e^{il\bar{\eta}/2}\phi^{DV} \tag{5.42}$$

where SV denotes the single-valuedness and DV denotes the double-valuedness. The $e^{il\bar{\eta}/2}$ term in Eq. (5.42) is included to compensate for the phase accumulated by the double-valued ϕ^{DV} as it transverses the conical intersections. We then can choose the single-valued ϕ^{SV} to have a constant zero derivative with respect to the Euler angle γ_Q. This choice should not change the dynamics of this problem because the dependence on γ_Q is simply a Heaviside function and, therefore, the only non-zero derivative terms are at $\gamma_Q = \pi$. The derivative term $(\partial\bar{\eta}/\partial\gamma_Q)$ later leads to an integration of a $\delta(\gamma_Q - \pi)$ function over γ_Q and needs to be treated very carefully. However, the single-valued function ϕ^{SV} is required to be continuous and differentiable everywhere in the nuclear coordinates. Therefore, the derivative terms at $\gamma_Q = \pi$ are finite. Therefore, the subsequent integration of the derivative terms for the γ_Q dependence, multiplied by the Wigner rotational matrices over

$\gamma_Q \in [0, 2\pi)$ is zero. In other words, the singularity of the derivative terms of the $e^{il\bar{\eta}/2}$ exactly cancels the singularity of the derivative terms of ϕ^{DV}, making the singled-valued ϕ^{DV} differentiable. Therefore, the neglecting the γ_Q dependence of the single-valued ϕ^{SV} function is legitimate and does not change the dynamics of the scattering process.

We now modify Eq. (3.17) as

$$\frac{\hbar^2}{2\mu}(-i\nabla - \bar{\mathbf{A}}(\vec{R}))^2 = -\frac{\hbar^2}{2\mu}\left(\frac{\partial}{\partial\rho}\rho^5\frac{\partial}{\partial\rho} + \frac{4}{\rho^2\sin 2\theta}\frac{\partial}{\partial\theta}\sin 2\theta\frac{\partial}{\partial\theta} + \frac{1}{\rho^2\sin^2\theta}\frac{\partial^2}{\partial\chi^2}\right)$$
$$+ \frac{J_x^2}{\mu\rho^2(1+\sin\theta)} + \frac{J_y^2}{\mu\rho^2\sin^2\theta} + \frac{J_z^2}{\mu\rho^2(1-\sin\theta)}$$
$$+ i\frac{\hbar^2}{2\mu}\left[\frac{5}{\rho}\bar{A}_\rho + \frac{\partial\bar{A}_\rho}{\partial\rho} + \frac{8\cot 2\theta}{\rho^2}\bar{A}_\theta + \frac{4}{\rho^2}\frac{\partial\bar{A}_\theta}{\partial\theta}\right.$$
$$+ \frac{1}{\rho^2\sin^2\theta}\frac{\partial\bar{A}_\chi}{\partial\chi} + 2\bar{A}_\rho\frac{\partial}{\partial\rho} + \frac{8}{\rho^2}\bar{A}_\theta\frac{\partial}{\partial\theta} + \frac{2}{\rho^2\sin^2\theta}\bar{A}_\chi\frac{\partial}{\partial\chi}\Bigg]$$
$$+ \frac{\hbar^2}{2\mu}\left[\bar{A}_\rho^2 + \frac{4}{\rho^2}\bar{A}_\theta^2 + \frac{1}{\rho^2\sin^2\theta}\bar{A}_\chi^2\right] - \frac{i\hbar\cos\theta}{\mu\rho^2\sin^2\theta}J_y\frac{\partial}{\partial\chi} \quad (5.43)$$

The vector potential terms for the $\hat{J}_z$ operator are dropped because $\hat{J}_z \approx \partial/(\partial\gamma_Q)$ and we have chosen

$$\frac{\partial}{\partial\gamma_Q}\phi^{SV} = 0. \quad (5.44)$$

Note that, the $\bar{A}(\rho, \theta, \chi, \gamma_Q)$ terms are different from the conventional vector potential terms $A(\rho, \theta, \chi)$ because the $\bar{A}$ terms also depend on γ_Q.

5.2.0.1 Zero total J case

In this study, we focus on the derivation of the $J = 0$ scattering process on the $1^4A'$ surface and we can simplify Eq. (5.43) as

$$\frac{\hbar^2}{2\mu}(-i\nabla - \mathbf{A}(\vec{R}))^2 = -\frac{\hbar^2}{2\mu}\left(\frac{\partial}{\partial\rho}\rho^5\frac{\partial}{\partial\rho} + \frac{4}{\rho^2\sin 2\theta}\frac{\partial}{\partial\theta}\sin 2\theta\frac{\partial}{\partial\theta} + \frac{1}{\rho^2\sin^2\theta}\frac{\partial^2}{\partial\chi^2}\right)$$
$$+ i\frac{\hbar^2}{2\mu}\left[\frac{5}{\rho}\bar{A}_\rho + \frac{\partial\bar{A}_\rho}{\partial\rho} + \frac{8\cot 2\theta}{\rho^2}\bar{A}_\theta + \frac{4}{\rho^2}\frac{\partial\bar{A}_\theta}{\partial\theta}\right.$$
$$+ \frac{1}{\rho^2\sin^2\theta}\frac{\partial\bar{A}_\chi}{\partial\chi} + 2\bar{A}_\rho\frac{\partial}{\partial\rho} + \frac{8}{\rho^2}\bar{A}_\theta\frac{\partial}{\partial\theta} + \frac{2}{\rho^2\sin^2\theta}\bar{A}_\chi\frac{\partial}{\partial\chi}\Bigg]$$
$$+ \frac{\hbar^2}{2\mu}\left[\bar{A}_\rho^2 + \frac{4}{\rho^2}\bar{A}_\theta^2 + \frac{1}{\rho^2\sin^2\theta}\bar{A}_\chi^2\right] \quad (5.45)$$

We expand the single-valued nuclear wavefunction following Ref. (108)

$$\Psi^{JMpn} = 4 \sum_{t,\Lambda} \rho^{-5/2} \psi^{Jpn}_{t\Lambda}(\rho) \Phi^{Jp}_{t\Lambda}(\theta, \chi_i; \rho_\zeta) \hat{D}^{Jp}_{\Lambda M}(\alpha_Q, \beta_Q, \gamma_Q). \qquad (5.46)$$

Because we take $J = 0$ in this study, the Wigner rotation matrix $\hat{D}^{Jp}_{\Lambda M}$ is just a constant, $1/\sqrt{8\pi^2}$. We left-multiply the complex conjugate of the Wigner rotation matrix, and then integrate the Hamiltonian over the three Euler angles. Eq. (5.45) now becomes

$$\int_0^{2\pi} \frac{1}{2\pi} d\gamma_Q \frac{\hbar^2}{2\mu} (-i\nabla - \mathbf{A}(\vec{R}))^2$$

$$= -\frac{\hbar^2}{2\mu} \left(\frac{\partial^2}{\partial\rho^2} + + \frac{15}{8\mu\rho^2} + \frac{4}{\rho^2 \sin 2\theta} \frac{\partial}{\partial\theta} \sin 2\theta \frac{\partial}{\partial\theta} + \frac{1}{\rho^2 \sin^2\theta} \frac{\partial^2}{\partial\chi^2} \right)$$

$$+ \int_0^{2\pi} \frac{1}{2\pi} d\gamma_Q \ i\bar{A}_I + \int_0^{2\pi} \frac{1}{2\pi} d\gamma_Q \ \bar{A}_R, \qquad (5.47)$$

where $i\bar{A}_I$ is defined as the complex component

$$i\bar{A}_I \equiv \frac{\hbar^2}{2\mu} \left[\frac{5}{\rho} \bar{A}_\rho + \frac{\partial \bar{A}_\rho}{\partial\rho} + \frac{8 \cot 2\theta}{\rho^2} \bar{A}_\theta + \frac{4}{\rho^2} \frac{\partial \bar{A}_\theta}{\partial\theta} \right.$$

$$\left. + \frac{1}{\rho^2 \sin^2\theta} \frac{\partial \bar{A}_\chi}{\partial\chi} + 2\bar{A}_\rho \frac{\partial}{\partial\rho} + \frac{8}{\rho^2} \bar{A}_\theta \frac{\partial}{\partial\theta} + \frac{2}{\rho^2 \sin^2\theta} \bar{A}_\chi \frac{\partial}{\partial\chi} \right], \qquad (5.48)$$

and $\bar{A}_R$ is defined as part of the real components

$$\bar{A}_R \equiv \frac{\hbar^2}{2\mu} \left[\bar{A}_\rho^2 + \frac{4}{\rho^2} \bar{A}_\theta^2 + \frac{1}{\rho^2 \sin^2\theta} \bar{A}_\chi^2 \right]. \qquad (5.49)$$

The integral $\int_0^{2\pi} \frac{1}{2\pi} d\gamma_Q \ i\bar{A}_I$ can be done by separating the integration into $\int_0^{2\pi} = \int_0^\pi + \int_\pi^{2\pi}$. We don't have to worry about $\gamma_Q = \pi$ in this integral, because $\bar{A}_I$ is discontinuous at $\gamma_Q = \pi$ but remains finite at this point. As shown in the previous subsection, all the $\bar{A}_x$ terms have the symmetry property as $\bar{A}_x(\gamma_Q + \pi) = -\bar{A}_x(\gamma_Q)$ and thus we have

$$\int_0^{2\pi} d\gamma_Q \ i\bar{A}_I$$

$$= \int_0^\pi d\gamma_Q \ i\bar{A}_I + \int_\pi^{2\pi} d\gamma_Q \ i\bar{A}_I$$

$$= \int_0^\pi d\gamma_Q \ i\bar{A}_I + \int_0^\pi d\gamma'_Q \ i(-\bar{A}_I(\gamma'_Q))$$

$$= 0, \qquad (5.50)$$

where $\gamma_Q' = \gamma_Q - \pi$.

The integral $\int_0^{2\pi} \frac{1}{2\pi} d\gamma_Q \ \bar{A}_R$ can be simplified in the same fashion by separating the integration into $\int_0^{2\pi} = \int_0^{\pi} + \int_\pi^{2\pi}$. Because $[\bar{A}_x(\gamma_Q + \pi)]^2 = [\bar{A}_x(\gamma_Q)]^2$, we obtain

$$
\begin{aligned}
&\int_0^{2\pi} \frac{1}{2\pi} d\gamma_Q \ \bar{A}_R \\
&= \frac{1}{2\pi} [\int_0^\pi d\gamma_Q \ \bar{A}_R + \int_\pi^{2\pi} d\gamma_Q \ \bar{A}_R] \\
&= \frac{1}{2\pi} [\int_0^\pi d\gamma_Q \ \bar{A}_R + \int_0^\pi d\gamma_Q' \ (+\bar{A}_R(\gamma_Q'))] \\
&= A_R,
\end{aligned}
\tag{5.51}
$$

where $\gamma_Q' = \gamma_Q - \pi$ and A_R is defined as

$$
A_R \equiv \frac{\hbar^2}{2\mu} \left[A_\rho^2 + \frac{4}{\rho^2} A_\theta^2 + \frac{1}{\rho^2 \sin^2 \theta} A_\chi^2 \right].
\tag{5.52}
$$

It should be noted that this A_R term does not have the bar and depends only on the three internal coordinates, ρ, θ and χ.

After integration over the Euler angles, the nuclear Hamiltonian becomes

$$
\begin{aligned}
H_{tot} &= -\frac{\hbar^2}{2\mu} \left(\frac{\partial^2}{\partial \rho^2} + +\frac{15}{8\mu\rho^2} + \frac{4}{\rho^2 \sin 2\theta} \frac{\partial}{\partial \theta} \sin 2\theta \frac{\partial}{\partial \theta} + \frac{1}{\rho^2 \sin^2 \theta} \frac{\partial^2}{\partial \chi^2} \right) \\
&\quad + \frac{\hbar^2}{2\mu} \left[A_\rho^2 + \frac{4}{\rho^2} A_\theta^2 + \frac{1}{\rho^2 \sin^2 \theta} \right] + V(\rho, \theta, \chi)
\end{aligned}
\tag{5.53}
$$

We then choose the basis function $\Phi_{t\Lambda}^{Jp}$ to satisfy a two-dimensional Schrodinger equation

$$
\begin{aligned}
&\left\{ -\frac{\hbar^2}{2\mu} \left(\frac{4}{\rho^2 \sin 2\theta} \frac{\partial}{\partial \theta} \sin 2\theta \frac{\partial}{\partial \theta} + \frac{1}{\rho^2 \sin^2 \theta} \frac{\partial^2}{\partial \chi^2} \right) + \frac{15}{8\mu\rho_\zeta^2} + V(\theta, \chi; \rho_\zeta) \right. \\
&\quad \left. + \frac{\hbar^2}{2\mu\rho_\zeta^2} \left[A_\rho^2 \rho_\zeta^2 + 4A_\theta^2 + \frac{1}{\sin^2 \theta} A_\chi^2 \right] \right\} \Phi_{t\Lambda}^{Jp} = \mathcal{E}_t(\rho_\zeta) \Phi_{t\Lambda}^{Jp}
\end{aligned}
\tag{5.54}
$$

Solving this real two-dimensional Schrodinger equation leads to real eigenvalues $\mathcal{E}_t(\rho_\zeta)$ and eigenvectors $\Phi_{t\Lambda}^{Jp}$. Therefore, all overlap matrices and interaction matrices are real and can be easily generated to be used in the propagation.

Three things should be noted when we compare this study to Ref. (105):

1. The generally complex Hamiltonian, with the inclusion of the vector potential, becomes real in the internal coordinates. This information does not conflict with the gauge invariance property of the vector potentials. It needs to be noted that the inspection of gauge invariance needs to be done at Eq. (5.45), in which the generally complex terms $\vec{A} \cdot \vec{p}$ and $\vec{p} \cdot \vec{A}$ still exist. Here, $\vec{A}$ refers to the general form of the vector potential term and $\vec{p}$ refers to the momentum operator. Eq. (5.54) does not need to satisfy the gauge invariance because we have made further approximation as mentioned the previous sections.

2. The two-dimensional Hamiltonian in Eq. (5.54) now is invariant under the $\chi \to -\chi$ operation. Therefore, the even and odd symmetry states with respect to this operator do not mix. This does not conflict with Ref. (105). The reason lies in the geometric phase angle. In Ref. (101; 105), the geometric phase angle is or is proportional to the χ angle in the APH coordinates or the ϕ angle in the symmetrized spherical coordinates, and this geometric phase angle is antisymmetric with respect to the $\chi \to -\chi$ operation. Furthermore, the iA_I term does not depend on the Euler angle γ_Q, and remains nonzero after the integration over the Euler angles. In Ref. (105) $A_I(-\chi) = -A_I(\chi)$, which makes the Hamiltonian asymmetric with respect to the $\chi \to -\chi$ operation. So even and odd states for this operation do mix. However, in this study, the $\bar{A}_I$ terms are antisymmetric with respect to the $\gamma_Q \to \gamma_Q + \pi$ operation and thus the integration of this term over $(0, 2\pi)$ is zero. The rest of the geometric contribution to the Hamiltonian, A_R, is symmetric with respect to the $\chi \to -\chi$ operation and thus the Hamiltonian remains symmetric with respect to this operation. Therefore, in this study where the conical intersections are in the collinear geometries, the even and odd states for the $\chi \to -\chi$ operation are not mixed by the geometric phase. We can then just focus on either set of the symmetry states.

3. The Hamiltonian remains real and there are no first derivative terms, $\partial/\partial\rho$. Therefore, one does not need to use Numerov propagator to get rid of the first derivative terms in ρ. Also the interaction matrices and the overlap matrices

are always real and symmetric, which does not need special treatments to make them real.

5.3 Conclusion

In this chapter, we have shown how to solve the time-independent Schrodinger equation with conical intersections in the collinear geometries. We have shown that, by stitching the γ_Q and $\gamma_Q + \pi$ hemispheres together, we are able to describe the complete loop around the conical intersections in the $C_{\infty v}$ geometries. We are the first, as far as we know, to derive the general form of the geometric phase angle and the associated vector potentials for collinear conical intersections.

We then shown that, in the $J = 0$ case, the Hamiltonian in the internal coordinates (ρ, θ, χ), after the integration of the three Euler angles, is real. This real Hamiltonian is a result of the special collinear conical intersections and does not break gauge invariance. The Hamiltonian with the inclusion of the geometric phase differs from that without the inclusion of the geometric phase by only a real effective potential term. This additional potential term, which depends on the vector potential terms, diverges at the conical intersections and thus the resultant nuclear wavefunction tends to die off in these highly repulsive regions.

This additional potential term can then be included in a scattering calculation or a triatomic bound states calculation to show how much the geometric phase effect can affect these results. Because, even at ultracold temperatures, the real electronic wavefunction needs to be double-valued as nuclear coordinates completely around the conical intersections, proper treatment of the geometric phase effect needs to be included. We have confidence to state that the geometric phase effect should be non-trivial in a reactive scattering calculation for the spin-aligned triatomic lithium system.

Part IV

Other subjects

Chapter 6

Potential Construction

6.1 Motivation

Potential energy surface (PES) plays a fundamental role in understanding collisions and field-induced interactions between cold and ultracold atoms and molecules. Some of the simplest systems are alkali metal trimers, whose ground-state atoms have only one valence electron in an s orbital. Spin-aligned alkali-trimer systems have received considerable attention since the discovery of Bose-Einstein condensation in ultracold hydrogen (67), lithium (68), sodium (69), rubidium (70) and cesium (71). For lithium, the lightest of the alkalies, understanding the lowest PES's is important for dynamics of elastic and inelastic collisions as well as field-induced-interactions. Several global surfaces for low-lying $1^4A'$ have been reported (130; 32) with a seam of conical intersections between the $^4\Sigma$ and $^4\Pi$ surfaces in the $C_{\infty v}$ geometries (75; 31; 10). To the best of our knowledge, the present work is the first to calculate all four low-lying global PES's, $1^4A'$, $2^4A'$, $1^4A''$, and $2^4A''$, of the spin-aligned lithium trimer (140).

Intuitively, the pairwise-additive two-body interactions should contribute more than the three-body interaction to the PES of spin-aligned trimers. However, the three-body contribution is not generally negligible for these alkali metal trimers. Theoretical and experimental work on sodium (9) has shown that the pairwise-additive potential (PAP) accounts for only 62% of the well depth 849.37 cm^{-1} of the Na$_3$ potential, and the diatomic bond distance at the true minimum of the full PES is 1.5 Bohr smaller than the value predicted from the PAP. For Li$_3$,

the PAP predicts only 25% of the well depth of the absolute minimum in D_{3h} geometry, and a bond distance nearly 2 Bohr larger than the correct value (130). What is more, assignment of the contribution from diatomic potentials to the PAPs for excited PES's is complicated because diatomic potentials mix. Take the $2^4A''$ PES. A sum of three diatomic potentials is not accurate because the PAP can have contributions from $^3\Sigma_u^+$, $^3\Sigma_g^+$, $^3\Pi_u$, $^3\Pi_g$ states. Moreover, the three-body term should die off in the asymptotic region, but a sum of three diatomic potentials does not give the correct dissociation limit unless the symmetry of the system is broken. A DIM (diatomics in molecules) model (131; 132; 133; 134; 11), which can couple all the relevant diatomic potentials and give the correct dissociation limit, can thus represent the mixed pairwise-additive terms. The DIM terms obtained by diagonalizing the electronic Hamiltonian represent the ground and first few excited PES's. To construct the three-body terms, we perform *ab initio* calculations for the $1^4A'$, $2^4A'$, $1^4A''$, and $2^4A''$ PES's using full configuration interaction for the three valence electrons with an augmented Gaussian basis and the effective core potential of Stevens, Basch and Krauss (135) for the other electrons. We then use a global-fit method of Aguado et al. (136) to fit the result of $V_{total} - V_{DIM}$ at the points where the *ab initio* calculations are performed to obtain the three-body terms. The DIM method is quantitatively correct in the conical intersection regions (in the $C_{\infty v}$ geometries). Therefore, the DIM method gives the electronic eigenvectors in these regions, and from these the geometric phase and non-adiabatic effects can be computed.

We use a DIM (diatomics in molecules) model to fit the *ab initio* calculation of the four lowest spin-aligned potential energy surfaces of triatomic lithium. There are two advantages in using the DIM model as compared to other models (130; 32):

1. The DIM model gives an accurate potential almost everywhere. The mixings of all the diatomic energy levels gives a detailed and explicit description of the potential in both the well region and the asymptotic region of the global potential. The ability to accurately describe the ground spin-aligned potential enables us to perform accurate scattering calculations at a cold or ultracold temperature. Also, the ability to accurately describe the excited potential energy surfaces enables us to accurately describe the triatomic bound states.

The information of the bound state on this electronically excited PES can be used to compute transition dipole moments so that one can utilize laser(s) to link the continuum states on the ground PES and the bound state on the excited PES to coherently control the chemical reaction of the triatomic lithium system on the ground state.

2. The DIM method is quantitatively correct in the conical intersection regions (in the $C_{\infty v}$ geometries). Therefore, the DIM method is able to produce the electronic adiabatic eigenvectors in these regions. Also, the derivative couplings (nonadiabatic coupling) terms can be analytically computed from the DIM model, which can be used to include the geometric phase effect with either one-state or two-state adiabatic representation (8). Another way to treat the geometric phase effect is to use a diabatic representation of the electronic wavefunctions. One can use the DIM model to obtain the accurate diabatic-to-adiabatic transformation to treat these the geometric phase and non-adiabatic effects. More information on using the electronic diabatic representation to treat the geometric phase is covered in Chapter 3.

6.2 Results

The *ab initio* PES's for all four states of Li_3 were generated via three-electron full configuration interaction calculations, using the effective core potentials of Stevens, Basch and Krauss (SBK) (135) and an augmented Gaussian basis with the MOLPRO software package (137). The SBK basis set is augmented with three d-type and one f-type polarization functions. The basis is shown in Table I. Further description of this basis set can be found in refs. (135; 130). Each Li_3 PES is calculated at 2958 internuclear configurations in the C_{2v}, D_{3h}, $D_{\infty h}$ and $C_{\infty v}$ geometries.

Our global potential very accurately describes the conical intersection regions and is also quantitatively correct elsewhere. Table II. shows the RMS deviation of our global fitting for the four PES's at different regions. SET 3 tests our global potential at unfitted *ab initio* points for arbitrary C_s geometries. Figure 6.1 shows the behavior of our PES's in $D_{\infty h}$ geometries, where the solid circles are the *ab*

PES type	SET 1	SET 2	SET 3
$1A'$	1.8×10^{-4} Ha.	1.2×10^{-4} Ha.	5.3×10^{-4} Ha.
$2A'$	9.1×10^{-4} Ha.	3.4×10^{-4} Ha.	1.6×10^{-3} Ha.
$1A''$	2.5×10^{-4} Ha.	0.8×10^{-4} Ha.	1.5×10^{-4} Ha.
$2A''$	5.1×10^{-4} Ha.	1.0×10^{-3} Ha.	2.1×10^{-4} Ha.

Table 6.1: RMS deviation of all four PES's in different geometries. SET 1 stands for RMS error of global potential ($E \leq 0.01$ Ha. for the $1A'$ surface and $E \leq 0.08$ Ha. for the $2A'$, $1A''$ and $2A''$ surfaces), SET 2 stands for RMS error in the $C_{\infty v}$ geometries and SET 3 stands for RMS error only of unfitted C_s points
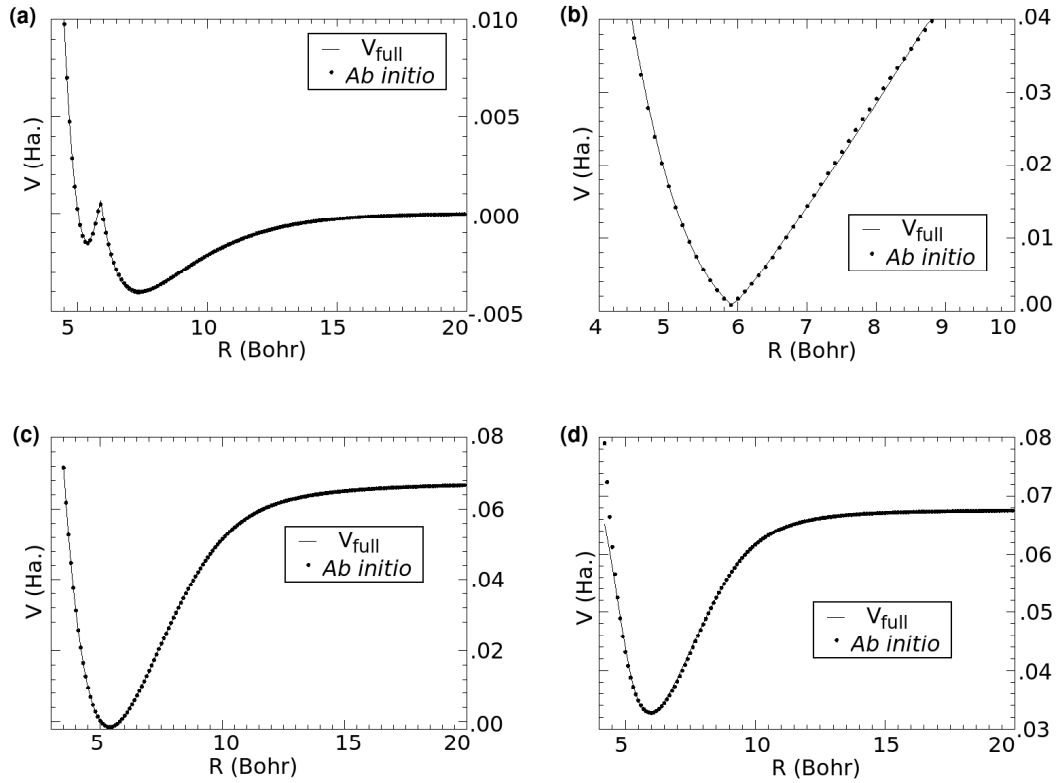
Figure 6.1: The $^4A'$ surfaces in $D_{\infty h}$ geometries. Solid curves are the fitted potential, V_{FULL}, and dark circles are the *ab initio* data for $^4A'$ surfaces:(a)-$1A'$ surface, (b)-$2A'$ surface, (c)-$1A''$ surface and (d)-$2A''$ surface.
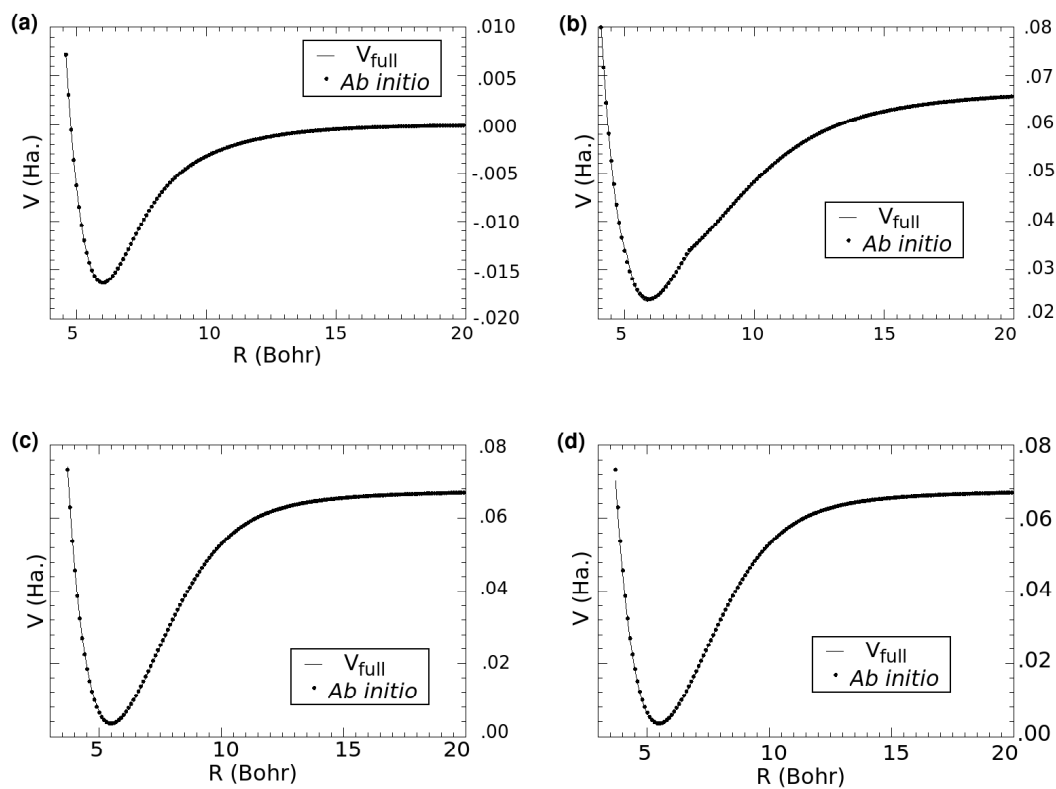
Figure 6.2: The $^4A'$ surfaces in D_{3h} geometries. Solid curves are the fitted potential, V_{FULL}, and dark circles are the *ab initio* data for $^4A'$ surfaces:(a)-$1A'$ surface, (b)-$2A'$ surface, (c)-$1A''$ surface and (d)-$2A''$ surface.
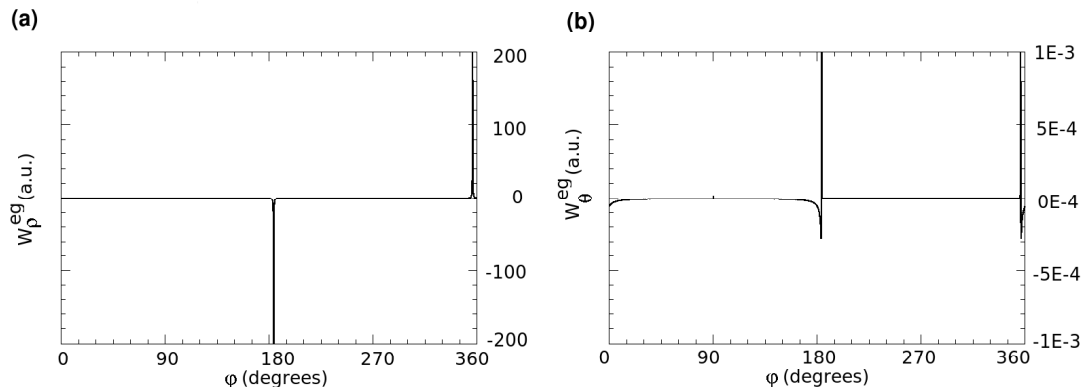
Figure 6.3: Nonadiabatic couplings around the conical intersection in the C_{2v} geometries: (a)-W_ρ^{eg} and (b)-W_θ^{eg}.

initio points, and the solid curves are our fitted PES's with $R = R_1 = R_2 = 0.5R_3$. Figure 6.2 shows the behavior of our PES's in D_{3h} geometries, where the solid circles are the *ab initio* points, and the solid curves are our fitted PES's with $R = R_1 = R_2 = R_3$.

Plots of the nonadiabatic coupling in the C_{2v} geometries are shown in Figure 6.3, where φ is defined to describe the enclosed loop around the conical intersection in $D_{\infty h}$ geometries:

$$\rho = 11 + \sin(\varphi)[\text{Bohr}], \quad \theta = 90 + \cos(\varphi)[\text{degree}]. \tag{6.1}$$

Because the ground and excited electronic wavefunctions both change signs as they follow an enclosed loop around the conical intersections, the nonadiabatic coupling terms are still single-valued.

In the *ab initio* calculation, we noticed one possible diabolic conical intersections in the C_{2v} geometries. The other known symmetry-allowed CIs have been observed and discussed elsewhere (32). The diabolic conical intersections are often referred to as accidental degeneracies. These diabolic conical intersections are a result of two PES's of the same irreducible representation crossing, when, in general, the symmetry arguments require avoided crossings. These diabolic conical intersections are not predicted by group theory. They occur only if the coupling between two degenerate PES's are zero. These unexpected diabolic conical intersections can clarify confusing branching ratios (138; 139).
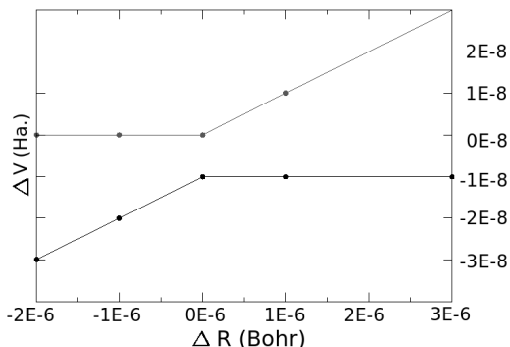
Figure 6.4: Possible diabolic conical intersection in the C_{2v} geometries for the lowest A_2 states, where $\Delta V \equiv V - 0.0419418$ Ha. and $\Delta R \equiv R - 5.952103$ Bohr.

Figure 6.4 shows a possible diabolic conical intersections of the A_2 states in the C_{2v} geometries when $\phi = 99.17525^o$ where ϕ is the angle between two diatomic separations, and $R = R_1 = R_2 = 5.952103$ Bohr, at 0.0419418 Ha. above the (2S+2S+2S) three-body dissociation limit. We calculated more than 100 *ab initio* points in the neighborhood of this diabolic conical intersection region. The two PES's are shown to be separated by 1×10^{-8}Ha.. To verify the true existence of this diabolic conical intersection, we trace the sign of the electronic wave function along a path in the nuclear configuration space which encircles this diabolic conical intersection in the C_{2v} geometries. Figure 6.5 shows the coefficients of the configuration interaction vectors of two electronic wavefunctions at C_{2v} geometries in a loop defined as:

$$\begin{aligned} R &= 5.952103 + 0.0001 \sin(\varphi)[\text{Bohr}] \\ \phi &= 99.17525 + 0.001 \cos(\varphi)[\text{degree}]. \end{aligned} \tag{6.2}$$

This diabolic conical intersection, which indicates a seam of diabolic conical intersections in C_s geometries, may cause unexpected behavior in calculations using these excited PES's.
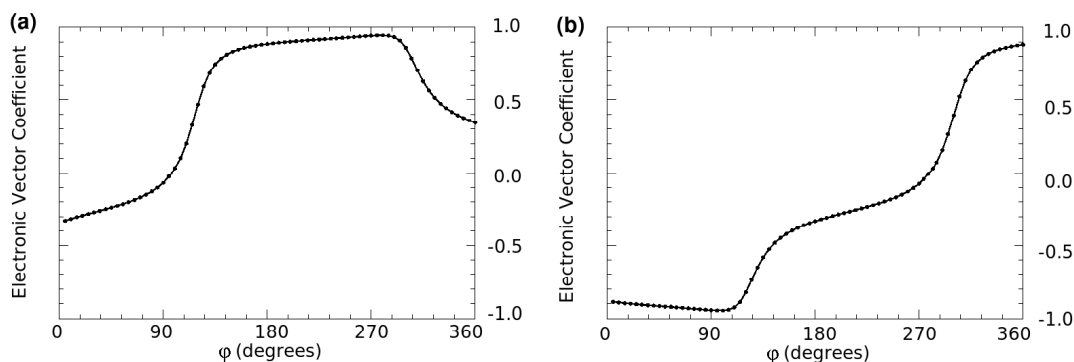
Figure 6.5: Coefficients of the configuration interaction vectors of two electronic wavefunctions along the loop which encircles the diabolic conical intersction in the C_{2v} geometries: (a)-the ground state and (b)-the excited state.

6.3 Conclusions

We have constructed all four low-lying spin-aligned electronic PES's, $1^4A'$, $2^4A'$, $1^4A''$ and $2^4A''$, for Li$_3$. The resulting fit accurately describes $D_{\infty h}$ conical intersection for both the $1^4A'$ and $2^4A'$ surfaces. It is a global fit with an RMS deviation of 1.8×10^{-4} Ha. for $1^4A'$, 9.2×10^{-4} Ha. for $2^4A'$, 2.5×10^{-4} Ha. for $1^4A''$, and 5.1×10^{-4} Ha. for $2^4A''$. The DIM terms can be used to compute the non-adiabatic terms to describe the conical intersection beyond the Born-Oppenheimer approximation. We have found a possible diabolic conical intersection in A_2 *ab initio* calculations in the C_{2v} geometries, which indicates a seam of conical intersections in C_s geometries.

More information on how to use the DIM model to fit the *ab initio* calculation of all four low-lying spin-aligned potential energy surfaces, fitting results, and the possible seam of diabolic conical intersection on the excited potential energy surface, can be found in Appendix F or equivalently Ref. (140).

Chapter 7

Bound states calculation of Li$_3$

7.1 Motivation

In this study, we present the most comprehensive calculation of the bound states of the spin-aligned lithium trimer to date. We also present a new method for calculating these bound states, which is noteworthy because of a tremendous increase in efficiency of these normally very expensive calculations.

Calculation of accurate bound states for the Li$_3$ system is motivated by several applications. One of the most prominent is Bose-Einstein condensation, which has driven ultracold reactive molecular collisions to become one of the key interests in chemical reaction dynamics. The simplest, non-trivial systems to study are the alkali metals, and as such many physicists and chemists are interested in ultracold chemical reactions of Li$_3$. The formation of ultracold molecules (T $\leq$ 100 μK) from laser-cooled alkali atoms has been observed by several groups (141; 142; 143; 144). Photoassociation and radiative stabilization processes are necessary in the formation of ultra-cold molecules, and both require knowledge of the quartet bound states. One of the most important factors in these process is the Frank-Condon (FC) factor between the ground continuum atom-diatom state and the excited bound triatomic state. With the knowledge of all bound states on the excited electronic PES, one has more freedom to choose a good candidate which has large FC overlaps with the initial continuum state to maximize the photoassociation rate and further steps. Also, the spin-aligned states are of particular interest for such ultracold studies because the large magnetic moment of the quartet states

makes the molecules easier to contain in a magneto optical trap (MOT). Studies of three-body recombination, a primary vehicle of trap loss, are also performed on the quartet potential surface because of the relatively shallow energy wells. Another possible application is the formation of Feshbach molecules. Feshbach molecules can be produced by using a ramped magnetic field (5). The Feshbach molecules then can be used to produce the low-lying rovibrational molecules by using STIRAP (stimulated Raman adiabatic passage) with two-frequency laser irradiation (6). The key to this technique is the accurate knowledge of the weakly bound excited rovibrational Feshbach molecules. Accurate calculation of the highly excited bound state on the ground electronic PES can lead to the first formation of a triatomic molecule at ultracold temperature. Another possible application of highly excited bound state of this kind is the photoassociation process.

Another reason the bound states of this specific system are interesting is the opportunity to study the effects of non-adiabatic couplings. This system exhibits a conical intersection between the two lowest spin-aligned ($^4A'$) states when the atoms are collinear ($C_{\infty v}$ geometries). Our group (10) and others (31; 75; 32) have made reference to this conical intersection before. The effect of the conical intersection is to couple the states of these two surfaces, as well as introduce geometric or Berry phase effects. This conical intersection is an interesting example because of its proximity to the three-body dissociation limit. Geometric phase effects are introduced to the system because a real electronic wavefunction is double-valued as the nuclear coordinates moves about the conical intersection in a closed loop. In this system, it is possible to circumscribe the conical intersection at energies below the three-body dissociation limit! The lowest point of intersection is at the symmetric-stretch collinear ($D_{\infty h}$) geometry at an energy of 0.0952eV above the dissociation limit. However, in order to traverse a path around the conical intersection, the maximum energy needed is -0.057eV, *below* the dissociation limit. More information about this structure can be found in reference (10). Because of its proximity to the ranges of energies studied in ultracold collisions, many are interested to see what effects the conical intersection will have on both bound state and scattering calculations. This present study will provide a comparison of the

bound states with a future calculation including the non-adiabatic effects of the conical intersection.

Yet another application of accurate bound states is the study of floppy molecules, that is, those with large amplitude vibrational motions. Bačić and Light (145) have noted these states and their importance:

> 'The LAM (large amplitude motion) vibrational states, because of the delocalized nature of their wave functions, contain detailed information about large regions of the potential surface beyond the global minimum. Moreover, while executing LAM vibrations, molecules can populate high-energy local minima inaccessible at lower energies, thus permitting detection of new isomers with strange structures and dynamics.'

The study of LAM states is very difficult as it requires knowledge of large regions of the potential energy surfaces, and also the coupling between the LAM vibrational states and the other vibrational modes. These calculations are difficult and become increasingly so for the highly excited vibrational states. Successful calculations of LAM states have been performed by Bačić et al. (146; 147; 148; 149; 150; 151; 152), Tennyson et al. (153; 154; 155) and other groups (156; 157; 158; 159; 160; 161; 162; 163; 164; 165; 166; 167; 168; 169; 170; 171). The calculation for many-bound-states system is extremely difficult especially for the most highly excited states, and no comprehensive study on Li_3 bound states has been published. Rather than using a Lanczos type method to find the eigenvalue of the Hamiltonian, our new subspace method utilizes the ray diagonalization of Bačić et al. (172) to generate adiabatic potential energy surfaces and the associated surface functions in the one-dimensional(1D) hyperradius. We then obtain reasonable subspace vectors by solving the 1D Schrödinger equation on each adiabatic surface without non-adiabatic couplings. Finally, we include the non-adiabatic couplings and use the subspace vectors to form the Hamiltonian matrix to solve for the eigenvalues and eigenvectors. We estimate the number of Li_3 bound states at 601 for the A1 symmetry. We hope that the new, more efficient calculation method described in Appendix G will enable studies of the LAM states of more complicated systems.

7.2 Novelty of the Method

In this study, we present a calculation of the bound states of A_1 symmetry on the spin-aligned $Li_3(1\ ^4A')$ potential energy surface. We apply a mixture of the discrete variable representation (DVR) and distributed approximating functional (DAF) methods to discretize the Hamiltonian. We also introduce a new method that significantly reduces the computational effort needed to determine the lowest eigenvalues and eigenvectors (bound state energies and wavefunctions of the full Hamiltonian) (171). More detailed information of the derivation of the subspace method can be found in Ref. (171) or equivalently Appendix G.

The subspace basis method is necessary to reduce computational effort. The full construction and direct diagonalization of the Hamiltonian would require storage for an $N_{points} \times N_{points}$ matrix where $N_{points} = N_\rho \times N_\theta \times N_\chi$. The subspace basis method requires only memory for an $N_{points} \times N_G$ matrix. In this study, the memory required for the largest calculation was reduced from 14 TB to 30 GB, and the time from months to days. (Calculations were performed on a single computer with 32 GB of RAM and Xeon Intel EM64T processors.)

We also compared Implicitly Restarted Arnoldi Method (IRAM) and the subspace method on the same computer. When the matrix to be diagonalized is symmetric, IRAM reduces to a variant of the Lanczos process called the Implicitly Restarted Lanczos Method (IRLM). Many groups have used IRLM method with parallel processing and obtained excellent results (163; 153; 154; 155; 158). But most aspects of our subspace method can be parallelized as well. We performed calculations using both methods to illustrate their time difference. Table 1 lists the CPU time for each method with different numbers of points. "Direct diagonalization" means directly diagonalizing the fully constructed Hamiltonian matrix $\bar{H}$. As the number of points increases, the time difference between IRAM and the subspace method increases greatly.

The present theory is for $J = 0$. When $J = 1$ and parity p is even, for instance, the Hamiltonian matrix doubles in size with respect to the $J = 0$ case. The treatment of the $J = 1$ Hamiltonian would be similar to that for $J = 0$. First diagonalize the subblock matrices $\mathbf{H}_o + \mathbf{H}_r$ to form a subspace basis. Then use

Method	# of Points	# of eigenvalues	CPU Time(hour)
IRAM	$40 \times 30 \times 6$	100	0.30
IRAM	$40 \times 30 \times 6$	600	5.58
DD	$40 \times 30 \times 6$	600	0.24
$NM(N_G = 2000)$	$40 \times 30 \times 6$	600	0.18
IRAM	$50 \times 40 \times 8$	600	18.52
DM	$50 \times 40 \times 8$	600	2.37
$NM(N_G = 2000)$	$50 \times 40 \times 8$	600	0.42
IRAM	$60 \times 40 \times 11$	600	> 150
DD	$60 \times 40 \times 11$	600	9.96
$NM(N_G = 2000)$	$60 \times 40 \times 11$	600	0.73

Table 7.1: Time comparison of different methods with different number of points; DD stands for Direct Diagonalization and NM stands for our new subspace method.

a carefully truncated subspace basis to construct the Hamiltonian matrix . This matrix will have dimensions of $N_G(\Lambda = 0) + N'_G(\Lambda = 1)$ by $N_G(\Lambda = 0) + N'_G(\Lambda = 1)$ for $J = 1$. The memory required is the same as for $J = 0$, because we construct each subblock one at a time. However, the time required is four times larger than for $J = 0$, because there are four nonzero submatrices for $J = 1$. Other $J \neq 0$ cases can be treated similarly. The time required for matrix operations compared to the time T for $J = 0$ is estimated to be $(14 + (J - 3) \times 5) \times T$, because of the banded structure of the total Hamiltonian.

7.3 Results

In table III, we show convergence of the A_1 bound state energies with respect to N_G. We list the extrapolated energies from the data in the last column. We perform the extrapolation for the ith bound state in the form of

$$E_i(N_G) = E_i(\infty) + \frac{A}{(N_G)^B}, \tag{7.1}$$

State	$N_G = 800$	$N_G = 900$	$E_i(\infty)$
E_1	-0.4721655833	-0.4721655834	-0.4721655839
E_{50}	-0.2652297	-0.2652297	-0.2652343
E_{100}	-0.2035117	-0.2035118	-0.2035163
E_{150}	-0.168091	-0.168092	-0.168126
E_{200}	-0.139570	-0.139581	-0.139847
E_{300}	-0.0997	-0.0998	-0.1018
E_{400}	-0.06840	-0.06870	$Failed$
E_{500}	-0.04340	-0.04424	-0.51239
E_{600}	-0.03430	-0.03476	-0.03754
State	$N_G = 2800$	$N_G = 2900$	$E_i(\infty)$
E_1	-0.4721655839	-0.4721655839	-0.4721655839
E_{50}	-0.2652343	-0.2652343	-0.2652343
E_{100}	-0.2035155	-0.2035155	-0.2035163
E_{150}	-0.168119	-0.168120	-0.168126
E_{200}	-0.139776	-0.139777	-0.139847
E_{300}	-0.1009	-0.1009	-0.1018
E_{400}	-0.07164	-0.07207	$Failed$
E_{500}	-0.04899	-0.04939	-0.51239
E_{600}	-0.03678	-0.03680	-0.03754

Table 7.2: Convergence of the A_1 bound state energies in eV; N_G is the number of subspace basis functions

where A and B are constants and $E_i(\infty)$ is the extrapolated energy. The lowest 150 energies are converged to be less than 0.005%, those between the 200th and 350th energies are obtained to 0.05% to 1%, while most of the excited energy states are converged with less than 2.0% error. Some of the extrapolated energies are not available, because the extrapolation failed. (See section IIIC. in Appendix G or Ref. (171)) The minimum energy needed to circumscribe the conical intersection is $-0.0574eV$. Any state with an energy greater than $-0.0574eV$ may be affected by the conical intersection.

As expected, convergence of the most highly excited states is not as good as that of low-lying states. The highly excited states are notoriously difficult to obtain accurately and our stated accuracies are as good as those of other researchers on similar systems. Lack of better convergence may be due to the strong nonadiabatic coupling between surface energy curves. We are using subspace bases associated with the ith adiabatic surface energy curve. Strong nonadiabatic couplings between curves would make the adiabatic surface energy curves rough at high energy. Convergence in N_θ and N_χ for the 100 highest bound states is better than 0.05%, but the rough feature for $\rho \in [10a_o, 13a_o]$ is troublesome for the calculation of the subspace basis. This rough feature has been confirmed by our independent DVR study in θ and χ without a symmetry-adapted transformation. One possible explanation for this rough behavior is the influence from the seam of the conical intersection for $\rho \in [11a_o, 15a_o]$ Bohr that is accessible by the bound states (10). The potential is not differentiable at the conical intersection, which may cause strong nonadiabatic couplings between surface energy curves here.

Despite the imperfect convergence of some of the most highly excited energies, states with less than $1\% - 2\%$ error would provide us a good comparison when we move on to the nonadiabatic case to investigate the effect of the conical intersection. Moreover, based on the convergence of the A_1 bound states, the extrapolated energy for the 600th state is $-0.03754eV$, that of the 601th state is $-0.03746eV$, and that of the 602th state is $-0.03731eV$. The dissociation limit for Li and ground state Li_2 is at $-0.03742eV$. So the number of the A_1 bound states should be no larger than 601. We also calculated energies for LI_3 without the three-body potential term, where we assume the interaction potential is a sum of pairwise

additive potential and three-body potential. Excluding the three-body potential term makes the potential much shallower and we estimate the number of A_1 bound states to be no larger than 183.

More detailed information can be found in Appendix G and equivalently in Ref. (171)

Part V

Epilogue

Chapter 8

Conclusion

To summarize, we have shown different ways to control chemical reactions at different temperatures and in different cases. We show that, at very low collision energies and for energetically narrow (~ 0.01 cm^{-1}) initial reactant wave packets, it is possible to tune the yield of the exchange reaction from 0 to near-unity. Controllability is somewhat reduced at collisions involving energetically wider (~ 1 cm^{-1}) initial reactant wave packets. At these energetic bandwidths the radiative reactive control, though still impressive, is limited to the $0 - 76\%$ reactive-probability range, in which case we use interferences of two intermediate bound states to boost the final reaction yield. We developed the population transfer by adiabatic passage theory. This theory relates laser catalysis to adiabatic passage, enhancing chemical reactions with the freedom to choose the translational energies of the reactants and products separately. We showed the ability to use pulsed lasers to form homonuclear and heteronuclear molecules at ultracold temperatures. The production rate is estimated to be 4×10^5 /s. This technique should be an alternative way of producing ultracold molecules.

We have also shown the treatment of the geometric phase in two different cases. When the conical intersection occurs in the C_{2v} geometries, we developed the Mixed-Odd-Even-States method to expand the nuclear wavefunctions, so the general complex problems can be treated in a simple fashion where all the matrices are real and symmetric. The Hamiltonian does not need to give additional treatment, e.g. permutation symmetry treatment, to produce real overlap matrices which are used in the propagation stage. When the conical intersection occurs in

the $C_{\infty v}$ geometries, we carefully derived the geometric phase angle $\bar{\eta}$, and, as far as we know, this is the first derivation of treating conical intersections in collinear geometries. We show that the geometric phase angle not only on the internal coordinates but also depends on the Euler angles. This additional dependence caused the Hamiltonian, with the inclusion of the vector potential terms, to be different from the Hamiltonian with vector potentials of a Jahn-Teller system. After integration over three Euler angles, the resultant Hamiltonian is real and can be directly applied to the reactive scattering calculations.

In addition to the coherent control and the geometric phase, we have also done other important studies. We use a MOLPRO software package to calculate the *ab initio* electronic PES's for the spin-aligned triatomic lithium system. We then use a DIM model to fit the four low-lying PES's and obtain a very accurate description of both the global potential and the conical intersections. The DIM model can be used to produce the adiabatic electronic wavefunction, which can be used to compute the non-adiabatic coupling terms; the DIM model can also be used to produce the adiabatic-to-diabatic transformation matrix at any point, which can be used in the two-state diabatic representation to treat the geometric phase.

Bibliography

[1] *Principles of the Quantum Control of Molecular Processes* by M. Shapiro and P. Brumer (Wiley, New Jersey, 2003).

[2] H. L. Bethlem *et al.*, Nature **406** 491, (2000)

[3] J. D. Weinstein *et al.*, Nature **395** 148, (1998)

[4] S. Kotochigova, E. Tiesinga, P.S. Julienne, Eur. Phys. J. D **31** 189 (2004).

[5] T. Kohler, K. Goral and P. S. Julienne, Rev. Mod. Phys. **78**, 1311 (2006)

[6] K.-K. Ni, *et al*, Science, **322**, 5899 (2008)

[7] M. Born and J. Oppenheimer, Ann. Phys. **84** 457 (1927)

[8] *Dynamics of Molecules and Chemical Reactions*, edited by R. E. Wyatt and J. Z. H. Zhang (Dkker, New York, 1996).

[9] J. Higgins, T. Hollebeek, J. Reho, T.-S. Ho, K. K. Lehmann, H. Rabitz, and G. Scoles, J. Chem. Phys. **112**, 5751 (2000), and reference therein.

[10] D. A. Brue, X. Li and G. A. Parker, J. Chem. Phys., **123** 091101 (2005)

[11] B. Kendrick and R. T Pack, J. Chem. Phys. **102**, 1994 (1995)

[12] G. Hirsch, R. J. Buenker and C. Petrongolo, Mol. Phys, **70**, 835 (1990)

[13] M. V. Berry, Proc. R. Soc. London, Ser. A, **392**, 45 (1984)

[14] C. A. Mead and D. G. Truhlar, J. Chem. Phys., **70** 2284 (1979)

[15] *The Geometric Phase in Quantum Systems: Foundations, Mathematical Concepts, and Applications in Molecular and Condensed Matter Physics* by A. Bohm, A. Mostafazadeh, H. Koizumi, Q. Niu, and J. Zwanziger, (Springer, Berlin, 2003).

[16] Y. Aharonov and D. Bohm, Phys. Rev. , **115** 485 (1959)

[17] G. Herzberg and H. C. Loguet-Higgins, Discuss. Faraday Soc. **35**, 77(1963)

[18] H. C. Loguet-Higgins, U. Opik, M. H. L. Pryce, R .A. Sack, Proc. R. Soc. London, Ser. A, **244**, 1 (1958)

[19] H. A. Jahn and E. Teller, Proc. R. Soc. A **161** 220 (1937)

[20] B. Lepetit, Z. Peng and A. Kuppermannn, Chem. Phys. Lett, **166** 572 (1990)

[21] B. Lepetit and A. Kuppermannn, Chem. Phys. Lett, **166** 581 (1990)

[22] L. Schnieder *et al*, Science, **269** 207 (1995)

[23] Y.-S. M. Wu, A. Kuppermannn and B. Lepetit, Chem. Phys. Lett, **186** 319 (1991)

[24] Y.-S. M. Wu and A. Kuppermannn, Chem. Phys. Lett, **201** 178 (1993)

[25] A. Kuppermannn and Y.-S. M. Wu, Chem. Phys. Lett, **205** 577 (1993)

[26] Y.-S. M. Wu and A. Kuppermannn, Chem. Phys. Lett, **235** 105 (1993)

[27] A. Kuppermannn and Y.-S. M. Wu, Chem. Phys. Lett, **241** 229 (1993)

[28] D. A. V. Kliner, K. D. Rinen, and R. N. Zare,Chem. Phys. Lett **166** 107 (1990)

[29] D. A. V. Kliner, D. E. Adelman, and R. N. Zare, J. Chem. Phys. **95** 1648 (1991)

[30] D. Neuhauser, R. S. Judson, D. J. Kouri, D. E. Adelman, N. E. Shafer, and D. A. V. Kliner, Science, **257** 519 (1992)

[31] M.T. Cvitaš, P. Soldán, J.M. Hutson, P. Honvault, and J-M. Launay, Phys. Rev. Lett. **94**, 033201 (2005)

[32] M. T. Cvitaš, P. Soldán, J. M. Hutson, P. Honvault, and J.-M. Launay, J. Chem. Phys. **127**, 074302 (2007).

[33] For reviews, see *"Molecules in Laser Fields"*, A.D. Bandrauk editor (Marcel Dekker, New York, 1994); M. Shapiro and P. Brumer, *"Principles of the Quantum Control of Molecular Processes"* (Wiley, New York, 2003)

[34] M.V. Fedorov, O.V. Kudrevatova, V.P. Makarov, and A.A. Samokhin, Opt. Commun. **13**, 299 (1975)

[35] N.M. Kroll and K.M. Watson, Phys. Rev. A **8**, 804 (1973); **13**, 1018 (1976)

[36] J.I. Gerstein and M.H. Mittleman, J. Phys. B **9**, 383 (1976)

[37] J.M. Yuan, T.F. George, and F.J. McLafferty, Chem. Phys. Lett. **40**, 163 (1976); J. M. Yuan, J.R. Laing, and T.F. George, J. Chem. Phys. **66**, 1107 (1977); T.F. George, J.M. Yuan, and I.H. Zimmermann, Faraday Discuss. Chem. Soc. **62**, 246 (1977); P.L. DeVries and T.F. George, ibid. **67**, 129 (1979); T.F. George, J. Phys. Chem. **86**, 10 (1982)

[38] A.M.F. Lau and C.K. Rhodes, Phys. Rev. A **16**, 2392 (1977); A.M.F. Lau, ibid. **13**, 139 (1976); **25**, 363 (1981)

[39] V.S. Dubov, L.I. Gudzenko, L.V. Gurvich, and S.I. Iakovlenko, Chem. Phys. Lett. **45**, 351 (1977)

[40] A.D. Bandrauk and M.L. Sink, Chem. Phys. Lett. **57**, 569 (1978); J. Chem. Phys. **74**, 1110 (1981)

[41] A.E. Orel and W.H. Miller, Chem. Phys. Lett. **57**, 362 (1978); **70**, 4393 (1979); **73**, 241 (1980)

[42] J.C. Light and A. Altenberger-Siczek, J. Chem. Phys. **70**, 4108 (1979)

[43] K.C. Kulander and A.E. Orel, J. Chem. Phys. **74**, 6529 (1981)

[44] H.J. Foth, J.C. Polanyi, and H.H. Telle, J. Phys. Chem. **86**, 5027 (1982)

[45] T. Ho, C. Laughlin, and S.I. Chu, Phys. Rev. A **32**, 122 (1985)

[46] M. Shapiro and Y. Zeiri, J. Chem. Phys. **85**, 6449 (1986)

[47] T. Seideman and M. Shapiro, J. Chem. Phys. **88**, 5525 (1988); **92**, 2328 (1990); **94**, 7910 (1991)

[48] T. Seideman, J.L. Krause, and M. Shapiro, Chem. Phys. Lett. **173**, 169 (1990); Faraday Discuss. Chem. Soc. **91**, 271 (1991)

[49] A. Zavriyev, P.H. Bucksbaum, H.G. Muller, and D.W. Schumacher, Phys. Rev. A **42**, 5500 (1990)

[50] A. Guisti-Suzor and F.H. Mies, Phys. Rev. Lett. **68**, 3869 (1992)

[51] G. Yao and S.-I. Chu, Chem. Phys. Lett. **197**, 413 (1992)

[52] E.E. Aubanel and A.D. Bandrauk, Chem. Phys. Lett. **197**, 419 (1992); A.D. Bandrauk, E.E. Aubanel, and J.M. Gauthier, Laser Phys. **3**, 381 (1993)

[53] D.R. Matusek, M.Yu. Ivanov, and J.S. Wright, Chem. Phys. Lett. **258**, 255 (1996)

[54] J. Herbig, T. Kraemer, M. Mark, T. Weber, C. Chin, H.-C. Nägerl, and R. Grimm, Science **301**, 1510 (2003)

[55] T. Kraemer, M. Mark, P. Waldburger, J.G. Danzl, C. Chin, B. Engeser, A.D. Lange, K. Pilch, A. Jaakkola, H.-C. Nägerl and R. Grimm, Nature **440**, 315 (2006)

[56] C. Chin, T. Kraemer, M. Mark, J. Herbig, P. Waldburger, H.-C. ägerl, and R. Grimm, Phys.Rev. Lett. **94** , 123201 (2005)

[57] D. J. Heinzen and R. Wynar, P. D. Drummond and K. V. Kheruntsyan, Phys. Rev. Lett. **84**, 5029 (2000)

[58] R. Wynar, R.S. Freeland, D.J. Han, C. Ryu, and D.J. Heinzen, Science **287**, 1016,(2000)

[59] M. Bartenstein, A. Altmeyer, S. Riedl, R. Geursen, S. Jochim, C. Chin, J. Hecker Denschlag, and R. Grimm, A. Simoni, E. Tiesinga, C.J. Williams, and P. S. Julienne, Phys. Rev. Lett. **94**, 103201 (2005)

[60] A. Vardi and M. Shapiro, Phys. Rev. A **58**, 1352 (1998).

[61] A. Vardi and M. Shapiro, J. Chem. Phys. **111**, 7713 (1999).

[62] I. Thanopulos and M. Shapiro, J. Chem. Phys. **117**, 8404 (2002).

[63] X. Li, G. A. Parker, P. Brumer, I. Thanopulos I and M. Shapiro, Phys. Rev. Lett., **101** 043003 (2008)

[64] J.G. Underwood, M. Spanner, M.Yu. Ivanov, J. Mottershead, B.J. Sussman, and A. Stolow, Phys. Rev. Lett. **90**, 223001 (2003)

[65] K. Bergmann, H. Theuer, and B.W. Shore", Rev. Mod. Phys., **70**, 1003 (1998)

[66] P. Král, I. Thanopulos, and M. Shapiro, Rev. Mod. Phys., **79**, 53 (2007)

[67] D. G. Fried, T. C. Killan, L. Willmann, D. Landhuis, S. C. Moss, D. Kleppner, and T. S. Greytak, Phys. Rev. Lett. **81**, 3811 (1998).

[68] C. C. Bradley, C. A. Sackett, J. J. Tollett, and R. G. Hulet, Phys. Rev. Lett. **75**, 1687 (1995).

[69] K. B. Davis, M. -O. Mewes, M. R. Andrews, N. J. van Druten, D. S. Durfee, D. M. Kurn, and W. Ketterle, Phys. Rev. Lett. **75**, 3969 (1995).

[70] M. H. Anderson, J. R. Ensher, M. R. Mathews, C. E. Wieman, and E. A. Cornell, Science **269**, 198 (1995).

[71] M. Weber, J. Herbig, M. Mark, H.-C. Nägerl and R. Grimm , Science **299**, 232(2003).

[72] A.G. Truscott, K.E. Strecker, W.I. McAlexander, G.B. Partridge, and R. G. Hulet, Science **291**, 198 (2001).

[73] F. Schreck, G. Ferrari, K. L. Corwin, J. Cubizolles, L. Khaykovich, M. -O. Mewes, and C. Salomon, Phys. Rev. A **64**, 011402(R) (2001).

[74] L. Khaykovich, F. Schreck, J. Cubizolles, T. Bourdel, K.L. Corwin, G. Ferrari, and C. Salomon, Physica B **329**, 13 (2003).

[75] M.T. Cvitaš, P. Soldán, and J.M. Hutson, Mol. Phys. **104**,23 (2006)

[76] X. Li, G. A. Parker, P. Brumer, I. Thanopulos I and M. Shapiro, J. Chem. Phys., **128** 124314 (2008)

[77] D. Grischkowski, M. M. T. Loy, and P. F. Liao, Phys. Rev. A **12** 2514, 1975

[78] J. Oreg, F. T. Hioe and J. H. Eberly, Phys. Rev. A **29** 690, 1984

[79] A. Vardi, D. Abrashkevich, E. Frishman and M. Shapiro, J. Chem. Physics. **107**, 6166 (1997)

[80] P. Kral, I. Thanopulos and M. Shapiro, Rev. Mod. Phys. **79** 53 (2007)

[81] X. Li and G. A. Parker, J. Chem. Phys., **128** 184113 (2008)

[82] M. Grether, M. de Llano, and G. A. Baker, Jr., Phys. Rev. Lett. **99**, 200406 (2007), and references therein.

[83] J. Doyle, B. Friedrich, R. V. Krems, F. Masnou-Seeuws, European Physical Journal D **31**, 149 (2004), and references therein.

[84] A. Micheli, G.K. Brennen, P. Zoller, Nature Physics **2**, 341 (2006).

[85] A. Vardi, D. Abrashkevich, E. Frishman and M. Shapiro, J. Chem Phys. **107**(16) 6166 (1997)

[86] R. Dumke, J.D. Weinstein, M. Johanning, K.M. Jones, P.D. Lett, Phys. Rev. A **72**, 041801(R) (2005).

[87] K. Winkler, G. Thalhammer, M. Theis, H. Ritsch, R. Grimm and J. H. Denschlag, Phys. Rev. Lett. **95**, 063202 (2005).

[88] I. Thanopulos and M. Shapiro, to be published.

[89] D. DeMille, Phys. Rev. Lett. **88** 067901 (2002)

[90] J. J. Hudson *et al.*, Phys. Rev. Lett. **89** 023003 (2002)

[91] B. Damski *et al.*, Phys. Rev. Lett. **90** 110401 (2003)

[92] A. J. Kerman *et al.*, Phys. Rev. Lett. **92** 153001 (2004)

[93] M. W. Mancini *et al.*, Phys. Rev. Lett. **92** 133203 (2004)

[94] J. P. Shaffer, W. Chalupczak and N. P. Bigelow, Phys. Rev. Lett. **82** 1124 (1999)

[95] P. L. DeVries and T. F. George, Mol. Phys. **36**, 151 (1978).

[96] P. L. DeVries and T. F. George, Phys. Rev. A **18**, 1751 (1978).

[97] P. L. DeVries and T. F. George, J. Chem. Phys. **71**, 1543 (1979).

[98] J. L. Krause, M. Shapiro, and P. Brumer, J. Chem. Phys. **92**, 1126 (1990).

[99] D. H. Kobe, Phys. Rev. Lett. **40**, 538 (1978)

[100] D. H. Kobe, Phys. Rev. A. **19**, 205 (1979)

[101] R. Abrol, A. Shaw, A. Kuppermann and D. Yarkony, J. Chem. Phys., **115** 4640 (2001)

[102] D. W. Schwenke *el al.*, Chem. Phys. Lett.,**203** 565(1993)

[103] M. Baer, Chem. Phys. Lett.,**35** 112 (1975)

[104] P. Halvick and D. G. Truhlar, J. Chem. Phys., **96** 2895 (1992)

[105] B. Kendrick and R. T Pack, J. Chem. Phys., **104** 7475 (1996)

[106] B. Kendrick, Phys. Rev. Lett., **79** 2431 (1997)

[107] B. Kendrick, J. Chem. Phys., **118** 10502 (2000)

[108] R. T Pack and G. A. Parker, J. Chem. Phys. **87**, 3888 (1987)

[109] F. T. Smith, J. Math. Phys., **3**, 735 (1962)

[110] B. R. Johnson, J. Chem. Phys., **73**, 5051 (1980)

[111] *Elementary Theory of Angular Momentum*, B. R. Rose (Wiley, New York, 1957); *Quantum Mechanics*, A. S. Davydov (Pergamon, New York, 1985)

[112] M. V. Berry and R. Lim, J. Phys. A, **23**, L655 (1990)

[113] B. R. Johnson, J. Comput. Phys., **13**, 445 (1973)

[114] B. R. Johnson, J. Chem. Phys., **79**, 1906 (1983);**79**, 1916 (1983)

[115] F. D. Colavecchia, M. Mrugala, G. A. Parker and R. T Pack, J. Chem. Phys., **118**, 10387 (2003)

[116] G. A. Parker and R. T Pack, J. Chem. Phys. **98**, 6883 (1993)

[117] R. M. Whitenell and J. C. Light, J. Chem. Phys., **89**, 3674 (1988)

[118] G. C. Schatz, Chem. Phys. Lett., **150**, 92 (1988)

[119] A. Kupperman and P. G. Hipes, J. Chem. Phys., **84**, 5962 (1986)

[120] B. Kenderick, J. Chem. Phys., **117**, 6083 (2002)

[121] Z. Bačić, J. D. Kress, G. A. Parker and J. C. Light, J. Chem. Phys., **92**, 2344 (1990)

[122] R. M. Whitenell and J. C. Light, J. Chem. Phys., **90**, 1774 (1989)

[123] Z. Bačić and J. C. Light, J. Chem. Phys., **85**, 4594 (1986)

[124] J. C. Light and Z. Bačić, J. Chem. Phys., **87**, 4008 (1987)

[125] Z. Bačić and J. C. Light, J. Chem. Phys., **86**, 3065 (1987)

[126] Z. Bačić, D. Watt and J. C. Light, J. Chem. Phys., **89**, 974 (1988)

[127] R. T Pack and J. O. Hirschfelder, J. Chem. Phys., **49**, 4009 (1968)

[128] R. T Pack and J. O. Hirschfelder, J. Chem. Phys., **52**, 521 (1970)

[129] R. T Pack, J. Chem. Phys., **60**, 633 (1974)

[130] F.D Colavecchia, J. P. Burke, Jr., W. J. Stevens, M. R. Salazar, G. A. Parker and R. T Pack, J. Chem. Phys. **118**, 5484 (2003)

[131] F. O. Ellison, J. Amer. Chem. Soc. **85**, 3540. (1963)

[132] J.C. Tully, J. Chem. Phys. **58**, 1396 (1973)

[133] E. Steiner, P.R. Certain, and P.J. Kuntz, J. Chem. Phys. **59**, 47 (1973)

[134] C.W. Eaker and C.A. Parr, J. Chem. Phys. **64**, 1322 (1976).

[135] W.J.Stevens, H. Basch and M. Krauss, J. Chem. Phys. **81**, 6026 (1984)

[136] A. Aguado, C. Tablero and M.Paniagua, Comput. Phys. Comm., **108**, 259-266 (1998)

[137] H.-J. Werner, P. J. Knowles, R. Lindh, M. Schütz. P. Celani, T. Korana, F. R. Manby, G. Rauhut, R. D. Amos, A Bernhardsson, et al., *Molpro, version 2006.1, a package of ab initio programs (2006)*, see http://www.molpro.net

[138] D. R. Yarkony, J. Chem. Phys., **100** 3639, (1994)

[139] D. R. Yarkony, Rev. Mod. Phys., **68** 985, (1996)

[140] X. Li, D. A. Brue and G. A. Parker, J. Chem. Phys. **129**, 124305 (2008)

[141] A. Fioretti, D. Comparat, A. Crubellier, O.Dulieu, F. Masnou-Seeuws, and P. Pillet, Phys. Rev. Lett, **80**, 4402, (1998)

[142] T. Takekoshi, B. M. Patterson, and R. J. Knize, Phys. Rev. Lett, **81**, 5105, (1999)

[143] N. Nikolov, E. E. Eyler, X. Wang, J. Li, H. Wang, W. C. Stwalley and P. Gould, Phys. Rev. Lett, **82**, 703, (1999)

[144] C. Gabbanini, A. Fioretti, A. Lucchesini, S. Gozzini, and M. Mazzoni, **84**, 2814, (2000)

[145] Z. Bačić, and J. C. Light, Annu. Rev. Phys. Chem.,**40**, 469, (1989)

[146] Z. Bačić and J. Z. H. Zhang, J. Chem. Phys. **96**, 3707 (1992)

[147] Z. Bačić, J. Chem. Phys. **95**, 3456 (1991)

[148] M. Mladenovic and Z. Bačić, J. Chem. Phys. **93**, 3039 (1990)

[149] Z. Bačić, D. Watt, and J. C. Light, J. Chem. Phys. **89**, 947 (1988)

[150] J. C. Light and Z. Bačić, J. Chem. Phys. **87**, 4008 (1987)

[151] Z. Bačić and J. C. Light, J. Chem. Phys. **86**, 3065 (1987)

[152] Z. Bačić and J. C. Light, J. Chem. Phys. **85**, 4594 (1986)

[153] J. R. Henderson and J. Tennyson, Chem. Phys. Lett. **173**, 133 (1990)

[154] S. V. Shirin, O. L. Polyansky, N. F. Zobov, P. Barletta, and J. Tennyson, J. Chem. Phys. **118**, 2124 (2002)

[155] M. A. Kostin, O. L. Polyansky, J. Tennyson,and H. Y. Mussa, J. Chem. Phys. **118**, 3538 (2002)

[156] S. Carter, I. M. Mills and N. C. Handy, J. Chem. Phys. **99**, 4379 (1993)

[157] T. González-Lezana, J. Rubayo-Soneira, S. Miret-Artés, F. A. Gianturco, G. Delgado-Barrio, and P. Villarreal, J. Chem. Phys. **110**, 9000 (1999)

[158] N. J. Wright and J. M. Hutson, J. Chem. Phys. **112**, 3214 (2000)

[159] F. A. Gianturco, F. Paesani, I. Baccarelli, G. Delgado-Barrio, T. Gonzalez-Lezana, S. Miret-Artés, P. Villarreal, G. B. Bendazzoli, and S. Evangelisti, J. Chem. Phys. **114**, 5520 (2001)

[160] N. V. Blinov, P.-N. Roy, and Gregory A. Voth, J. Chem. Phys. **115**, 4484 (2001)

[161] S. Y. Grebenshchikov, R. Schinke, P. Fleurat-Lessard, and M. Joyeux, J. Chem. Phys. **119**, 6512 (2003)

[162] D. Babikov, J. Chem. Phys. **119**, 6554 (2003)

[163] H. Lee and J. C. Light, J. Chem. Phys. **120**, 5859 (2004)

[164] I. Baccarelli, F. A. Gianturco, T. González-Lezana, G. Delgado-Barrio, S. Miret-Artés, and P. Villarreal, J. Chem. Phys. **122**, 144319 (2005)

[165] I.V. Boychenko and H. Huber, J. Chem. Phys. **124**, 014305 (2006)

[166] J. E. Cuervo and P.-N. Roy, J. Chem. Phys. **125**, 124314 (2006)

[167] E. Scifoni, F. A. Gianturco, S. Yu. Grebenshchikov, and R. Schinke, J. Chem. Phys. **125**, 164304 (2006)

[168] S. Orlandini, I. Baccarelli, and F. A. Gianturco, J. Chem. Phys. **125**, 234307 (2006)

[169] I. Sioutis, V. L. Stakhursky, R. M. Pitzer, and T. A. Miller, J. Chem. Phys. **126**, 124308 (2007)

[170] I. Sioutis, V. L. Stakhursky, R. M. Pitzer, and T. A. Miller, J. Chem. Phys. **126**, 124309 (2007)

[171] X. Li, D. A. Brue and G. A. Parker, J. Chem. Phys. **127**, 014108 (2007)

[172] Z. Bačić, J.D. Kress, G. A. Parker, and R. T Pack, J. Chem. Phys. **92**, 2344 (1990)

[173] A. Griesmaier, J. Werner, S. Hensler, J. Stuhler and T. Pfau, Phys. Rev. Lett. **94**, 160401 (2005).

[174] M. Shapiro, J. Chem. Phys. **101**, 3884 (1994).

[175] E. Frishman and M. Shapiro, Phys. Rev. A. **54**, 3310 (1996).

[176] A. Vardi and M. Shapiro, J. Chem. Phys. **104**, 5490 (1996).

[177] A. G. Abrashkevich and M. Shapiro, Phys. Rev. A. **50**, 1205 (1994).

[178] M. Shapiro, J. Chem. Phys. **56**, 2582 (1972).

[179] M. Shapiro and R. Bersohn, Ann. Rev. Phys. Chem. **33**, 409 (1982).

[180] F. Smith, J. Chem. Phys. **31**, 1352 (1959).

[181] J. O. Hirschfelder and J. S. Dahler, Proc. Natl. Acad. Sci. **42**, 363 (1956).

[182] L. M. Delves, Nucl. Phys. **9**, 391 (1959).

Appendix A

Laser enhancement of cold reactions

Theory of laser enhancement and suppression of cold reactions: The fermion-boson $^6Li+{}^7Li_2 \overset{\hbar\omega_0}{\leftrightarrow} {}^6Li^7Li+{}^7Li$ radiative collision

Xuan Li,[1,a] Gregory A. Parker,[1] Paul Brumer,[2] Ioannis Thanopulos,[3] and Moshe Shapiro[3,4]

[1]*Homer L. Dodge Department of Physics and Astronomy, University of Oklahoma, Oklahoma 73019, USA*
[2]*Department of Chemistry and Center for Quantum Information and Quantum Control, University of Toronto, Toronto, Canada*
[3]*Department of Chemistry, The University of British Columbia, Vancouver, Canada*
[4]*Department of Chemical Physics, The Weizmann Institute, Rehovot, Israel*

We present a nonperturbative time-dependent quantum mechanical theory of the laser catalysis and control of a bifurcating $A+BC \overset{\hbar\omega_0}{\leftrightarrow} ABC^*(v) \overset{\hbar\omega_0}{\leftrightarrow} AB+C$ reaction, with $ABC^*(v)$ denoting an intermediate, electronically excited, complex of ABC in the vth vibrational state. We apply this theory to the low collision energy fermion-boson light-induced exchange reaction, $^6Li(^2S) + {}^7Li_2(^3\Sigma_u^+) \overset{\hbar\omega_0}{\leftrightarrow} (^6Li^7Li^7Li)^* \overset{\hbar\omega_0}{\leftrightarrow} {}^6Li^7Li(^3\Sigma^+) + {}^7Li(^2S)$. We show that at very low collision energies and energetically narrow (~ 0.01 cm^{-1}) initial reactant wave packets, it is possible to tune the yield of the exchange reaction from 0 to near-unity (yield $\geqslant 99\%$) values. Controllability is somewhat reduced at collisions involving energetically wider (~ 1 cm^{-1}) initial reactant wave packets. At these energetic bandwidths, the radiative reactive control, although still impressive, is limited to the 0%–76% reactive-probabilities range. © 2008 American Institute of Physics.
[DOI: 10.1063/1.2899666]

I. INTRODUCTION

The possibility of enhancing or suppressing atomic and bimolecular reactions by lasers has attracted the attention of many researchers over the years.[1–27] Some of the most studied scenarios involve the modification of the potential surfaces of the colliding systems by light, thereby creating "light-induced potentials" (LIPs). The laser parameters are tuned so as to produce LIPs that possess lower reaction barriers along the reaction pathways leading to the desired products. The main stumbling block in realizing these scenarios is the requirement for high laser powers (in the TW/cm^2 range). These high powers are needed because of the relative weakness of *continuum-continuum* transition dipoles which are at the heart of the mechanism leading to the formation of LIP.

The necessity of strong laser fields can be reduced when (quasi-) bound states are involved. Here, the presence of the much stronger *bound-continuum* transition dipoles is expected to lower the power requirements to the MW/cm^2 to GW/cm^2 regime.[14,15,28–30] This is the situation in the "laser catalysis" (LC) scenario,[14,15,28–30] called such because it involves no net absorption of photons. Rather, colliding partners, which cannot react due to the existence of a high potential barrier, are made to "hop" over this barrier by first absorbing a photon to an excited bound state which straddles both sides of the barrier. The system is then de-excited, by stimulated emission of a photon identical to the

one just absorbed, to the products' side of the original reaction barrier. The process can occur on resonance or off resonance[31] with respect to the continuum-bound transition frequencies. It has also been shown[28] that for a coherent process, as the laser power goes up, the population of the intermediate bound state goes down. Eventually, the intermediate state becomes unpopulated, in great similarity to the simple three-state adiabatic passage process.[32,33]

The use of ultracold reactants,[34] e.g., hydrogen,[35] lithium,[36] sodium,[37] rubidium,[38] and cesium,[39] is expected to greatly enhance the ability to quantum mechanically control reactive scattering. Of special interest are reactions between spin-aligned atoms and molecules. This is so because spin-aligned states have relatively large magnetic moments, which make them easier to be captured in magnetic traps. Using this technique one may consider reactions between cold bosons and fermions, resulting in a large variety of bimolecular interactions. For example, isotopic mixtures of fermionic ^6Li and bosonic ^7Li give rise to the formation of either heteronuclear or homonuclear diatomic molecules.[40–43]

Thus, it is of great interest to examine the use of laser fields to coherently control the reactive scattering process in cold and ultracold mixtures of spin-aligned $^6Li+{}^7Li_2$. In addition to the light-induced interaction between the two lowest spin-aligned ($^4A'$) states, this system displays a variety of interesting features, including conical intersections between the two surfaces in the collinear ($C_{\infty v}$) configurations.[43–46]

In what follows, we consider a strong-field laser-assisted reactive scattering process of the type

a)Electronic mail: li@nhn.ou.edu.

128, 124314-1

$$A + BC \xrightarrow{\hbar\omega_0} (ABC)^* \xrightarrow{\hbar\omega_0} \begin{cases} A + BC & (q=1) \\ AB + C & (q=2). \end{cases} \quad (1)$$

As indicated above, the coupling between the electronic surfaces is induced by a laser pulse of carrier frequency ω_0. Conducting the above reaction constitutes the joining together of two radiatively induced "half-collisions"[15,47,48] in which the first half-collision constitutes a photoassociation process, and the second constitutes a photodissociation process.

Extensive work on photoassociation has been conducted in recent years in the context of ultracold collisions, as this process appears to be an efficient way of producing ultracold molecules.[49–52] For example, one may consider[49,53] the anti-Stokes stimulated Raman process,

$$Na + Na \xrightarrow{\hbar\omega_1} Na_2(A\ ^1\Sigma_u/b^3\Pi_u)$$
$$\times(v') \xrightarrow{\hbar\omega_2} Na_2(X\ ^1\Sigma_g)(v=0) \quad (2)$$
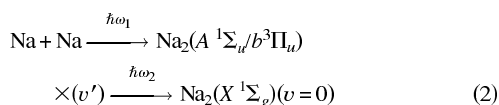
as a way of forming ultracold ground state Na_2 molecules. The same process was considered for Rb+Rb (Ref. 53) and for Rb+K. Possibly the most efficient way of executing such a process is to use a train of coherent pulses (optical frequency comb).[54] In that scheme, transfer is implemented in a piecewise fashion using sequences of ultrashort small-area pulses with pulse-to-pulse amplitude and phase variation.[54,55] Equivalently viewed in the frequency perspective, these techniques exploit interferences between many quantum pathways leading to the same final state.

In the present paper, we capitalize on all the above features: Laser catalysis, cold collisions, and the joining together of two light-induced half-collisions. As explained in Sec. II, it is possible to develop a nonperturbative time-dependent theory for treating the general process of Eq. (1) in a rather complete fashion. In Sec. III, we apply this theory to the collinear $^6Li + ^7Li_2$ system coupled to one or more bound states in the excited state complex. We show that for cold collisions with a very narrow distribution of initial reactant energies, the inclusion of one bound state is enough to obtain an essentially complete transfer to the reactive channel of interest. We also show that with a comparatively energetically wide initial reactant wave packet, the involvement of at least two bound states is necessary in order to significantly affect the reaction yield. The excitation of several intermediate states introduces *time* to the excited state dynamics, thereby utilizing the interference between these states in addition to the interference between the radiative and nonradiative scattering processes.

II. THEORY

The dynamics of all light-induced processes is governed by the total (matter+radiation) Hamiltonian $H_{\text{tot}} = H - \boldsymbol{\mu} \cdot \boldsymbol{\varepsilon}(t)$, where H is the material Hamiltonian, and $\boldsymbol{\varepsilon}(t) = \hat{\varepsilon}\varepsilon(t)$ is the laser's electric field, with $\hat{\varepsilon}$ being the polarization direction and $\varepsilon(t)$—the (scalar) electric field amplitude. In order to solve the time-dependent Schrödinger equation,

$$i\hbar\frac{\partial\Psi}{\partial t} = H_{\text{tot}}\Psi, \quad (3)$$

we expand $\Psi(t)$ in a complete basis, composed of $|E_i\rangle$, the bound and $|E,q,n^-\rangle$, the continuum, eigenstates of H,

$$(E_i - H)|E_i\rangle = 0,$$
$$(E - H)|E,q,n^-\rangle = 0, \quad q = 1,2. \quad (4)$$

In the above, E_i are the bound energies in the excited electronic state and E are the continuum energies of the ground electronic state, with n being asymptotic internal quantum numbers associated with each arrangement channel q. The—notation in the above signifies that each $|E,q,n^-\rangle$ state approaches as $t\to\infty$, a *single* asymptotic eigenstate, $|E,q,n;0\rangle$, of H_q^0—the q-arrangement material Hamiltonian for well separated reactants (or products). These states satisfy the energy eigenvalue relations,

$$(E - H_q^0)|E,q,n;0\rangle = 0, \quad q = 1,2. \quad (5)$$

The expansion of $\Psi(t)$ thus assume the form,

$$|\Psi(t)\rangle = \sum_{q,n}\int dE b_{E,q,n}(t)|E,q,n^-\rangle\exp(-iEt/\hbar)$$
$$+ \sum_j b_j(t)|E_j\rangle\exp(-iE_jt/\hbar), \quad (6)$$

where $b_{E,q,n}(t)$ and $b_j(t)$ are the expansion coefficients of the continuum and bound states, respectively.

Substitution of Eq. (6) into Eq. (3) results in the following set of differential equations for the expansion coefficients:

$$\dot{b}_i = \frac{i}{\hbar}\varepsilon(t)\left\{\sum_j b_j(t)\mu(i,j)e^{-i\omega_{ji}t}\right.$$
$$\left. + \sum_{q,n}\int dE b_{E,q,n}^-(t)\mu^-(E;i,q,n)e^{-i\omega_{E,i}t}\right\} \quad (7)$$

$$\dot{b}_{E,q,n} = \frac{i}{\hbar}\varepsilon^*(t)\sum_j b_j(t)\mu^-(E;q,n,j)e^{-i\omega_{E,j}t} + \frac{i}{\hbar}\varepsilon(t)$$
$$\times\sum_{q',m}\int dE' b_{E',q',m}(t)\mu(E,E';q,q',n,m)e^{-i\omega_{E',E}t}, \quad (8)$$

where

$$\omega_{j,i} \equiv (E_j - E_i)/\hbar, \quad \omega_{E,i} = (E - E_i)/\hbar,$$
$$\omega_{E',E} \equiv (E' - E)/\hbar \quad (9)$$

$$\mu(i,j) \equiv \langle E_i | \boldsymbol{\mu} \cdot \hat{\varepsilon} | E_j \rangle,$$

$$\mu^-(E;i,q,n) \equiv \langle E_i | \boldsymbol{\mu} \cdot \hat{\varepsilon} | E,q,n^- \rangle, \qquad (10)$$

$$\mu(E,E';q,q',n,m) \equiv \langle E,q,n^- | \boldsymbol{\mu} \cdot \hat{\varepsilon} | E',q',m^- \rangle.$$

Here, $\omega_{j,i}$, $\omega_{E,i}$, and $\omega_{E',E}$ are the transition frequencies between the bound-bound, bound-free, and free-free states, respectively; $\mu(i,j)$, $\mu^-(E;i,q,n)$ and $\mu(E,E';q,q',n,m)$ are the bound-bound, bound-free, and free-free dipole moment coupling terms, respectively. Assuming that $\mu(E,E';q,q',n,m) \approx 0$, i.e., there is no radiative coupling between different continuum states on the ground electronic surface, which allows us to eliminate the continuum couplings in Eq. (8) and enables us to solve for $b_{E,q,n}(t)$ to yield,

$$b_{E,q,n}(t) = b_{E,q,n}(-\infty)$$
$$+ (i/\hbar) \sum_j \int_{-\infty}^{t} dt' \, b_j(t') \mu^-(E;q,n,j) \varepsilon^*(t') e^{i\omega_{E,j}t'}. \qquad (11)$$

The initial wave packet has been assumed to belong to the $(q_s=1)$ $^6\text{Li}+^7\text{Li}_2$ reactant channel with the initial bound state coefficients $b_j(-\infty)=0$. The continuum coefficients, $b_{E,q,n}(-\infty)$, are determined from the form of the incoming wave packet, assumed to belong to the $q_s=1$ arrangement with the $^7\text{Li}_2$ vibrational quantum number $n_s=0$,

$$\Psi_{in} = \int dE \, b^+_{E,q_s=1,n_s=0}(t) | E, q_s=1, n_s=0^+ \rangle e^{-iEt/\hbar}. \qquad (12)$$

The $b^+_{E,q_s,n_s}(t)$ coefficients, specifying the shape of the incoming wave packet, are chosen, as specified below, as Gaussian functions in energy.

Using the well known relations between the *incoming* and *outgoing* scattering solutions, we have

$$| E, q_s, n_s^+ \rangle = \sum_{q,n} | E,q,n^- \rangle \langle E,q,n^- | E,q_s,n_s^+ \rangle$$
$$= \sum_{q,n} | E,q,n^- \rangle S_{q,n;q_s,n_s}. \qquad (13)$$

Hence,

$$b_{E,q,n}(-\infty) = S_{q,n;1,n_s} b^+_{E,1,n_s}(-\infty), \qquad (14)$$

where as mentioned above, q_s is assigned the value 1 and $S_{q,n;1,n_s}$ is the nonradiative S-matrix. Substituting the solution of $b_{E,q,n}(t)$ into Eq. (7), we obtain a (smaller) set of integro-differential equations for $b_i(t)$

$$\dot{b}_i(t) = \frac{i\varepsilon(t)}{\hbar} \mu^s_i(t) + \frac{i\varepsilon(t)}{\hbar} \sum_j \left\{ b_j(t) \mu(i,j) e^{-i\omega_{j,i}t} \right.$$
$$\left. + e^{-i\omega_{j,i}t} \int_{-\infty}^{t} dt' \, b_j(t') F_{i,j}(t-t') \varepsilon^*(t') \right\} \qquad (15)$$

where $\mu^s_i(t)$ are known source terms, given as,

$$\mu^s_i(t) \equiv \sum_{q,n} \int dE \, b_{E,q,n}(-\infty) \mu^-(E;i,q,n) e^{-i\omega_{E,i}t}, \qquad (16)$$

and

$$F_{i,j}(\tau) = \frac{i}{\hbar} \int dE \sum_{q,n} \mu^-(E;i,q,n) \mu^-(E;q,n,j) e^{-i\omega_{E,j}\tau} \qquad (17)$$

are the spectral *cross-correlation functions*. When $i=j$, $F_{i,j}$ become the spectral *autocorrelation functions*, i.e., the Fourier transform of $A_i(\omega)$, the photoabsorption spectrum from bound levels i,

$$F_i(\tau) \equiv i \int d\omega A_i(\omega) e^{-i\omega\tau}, \qquad (18)$$

where

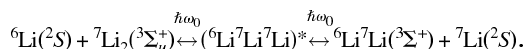$$A_i(\omega) = \sum_{q,n} |\mu^-(E_i + \hbar\omega; i,q,n)|^2. \qquad (19)$$

Using, e.g., the artificial channel method[56–58] to calculate $\mu^-(E;i,q,n)$, as customarily done to obtain the weak field photodissociation cross sections, we can construct, based on Eq. (17), the $F_{i,j}(\tau)$ spectral cross-correlation functions. Having $F_{i,j}(\tau)$ constructed, one can obtain $b_i(t)$ in the strong laser field domain by solving the integro-differential equations [Eq. (15)]. The continuum coefficients $b_{E,q,n}(t)$ are then directly obtained from Eq. (11). This gives the entire wave packet $\Psi(t)$, from which we can obtain the reactive yield at any time t. Varying the experimentally controllable functions $\varepsilon(t)$ and the initial condition $\Psi(t=-\infty)$, allows one to coherently control the reactive scattering process.

In the above, we have used two approximations, the dipole approximation and the rotating wave approximation (RWA). For the comparatively long IR and visible wavelengths, the dipole approximation is quite accurate, even for strong fields. In the present system, the validity of the RWA is more questionable for short <100 fs pulses at high >10¹³ W/cm² intensities. It turns out that since all the transitions we consider are nearly *on resonance*, if the pulse is longer than ~100 fs and the power weaker than ~10¹³ W/cm², the assumption of the RWA in our system, as confirmed by our calculations, is completely justified.

III. RESULTS

A. The spin-aligned Li₃ system

In this section, we report on computations based on the formulation presented above of the laser enhancement and suppression of the

$$^6\text{Li}(^2S) + ^7\text{Li}_2(^3\Sigma_u^+) \overset{\hbar\omega_0}{\leftrightarrow} (^6\text{Li}^7\text{Li}^7\text{Li})^* \overset{\hbar\omega_0}{\leftrightarrow} {}^6\text{Li}^7\text{Li}(^3\Sigma^+) + {}^7\text{Li}(^2S).$$

reaction. Both the $^7\text{Li}_2$ and $^6\text{Li}^7\text{Li}$ diatomic molecules are in their lowest $(^3\Sigma^+)$ spin-aligned electronic states. The triatomic states of interest are the lowest $^4A'$ states for the reactants and products, and the $^4A''$ states for the $(^6\text{Li}^7\text{Li}^7\text{Li})^*$ complex.

In order to control this reaction, we apply a light pulse given as,
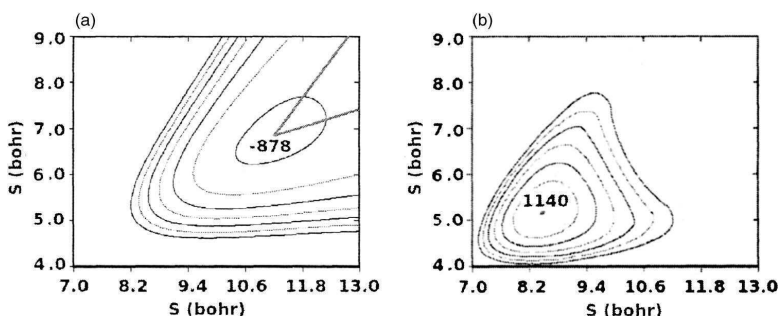
120

FIG. 1. (a) Ground potential energy surface (PES). Contour lines are spaced by 440 cm^{-1}, increasing outward from the indicated minimum. Reaction path is shown as a thick line that connects the ^{6}Li+^{7}Li$_2$ and the ^{6}Li ^{7}Li+^{7}Li products. (b) Excited PES. Contour lines are spaced by 330 cm^{-1}, increasing outward from the indicated minimum. The coordinates S and s are the *mass-scaled* Jacobi coordinates.

$$\varepsilon(t) = \varepsilon_0 e^{-(t/\delta_t)^2} \exp(-i\omega_0 t), \qquad (20)$$

where ω_0 is the carrier laser frequency, chosen to induce the transition between the intermediate states and the reactant/product states.

The potential barrier along the reaction path leading from reactants to products on the lower $^4A'$ potential surface of the ^{6}Li^{7}Li^{7}Li system is essentially zero. The ground vibrational energy of ^{7}Li^{7}Li is calculated to be -301.78 cm^{-1}, whereas the ground vibrational energy of ^{6}Li^{7}Li is calculated to be -300.50 cm^{-1}, so that reaction from the ground state ^{7}Li$_2$ to the ground state ^{6}Li^{7}Li is possible nonradiatively. This means that at cold temperatures in our study, which corresponds to kinetic energies in the range of $17-30$ cm^{-1}, the energy of the system is below the first excited vibrational energy level of the ^{7}Li^{7}Li at -243.78 cm^{-1}. Thus, the formation of ^{6}Li^{7}Li in the first excited state is energetically impossible in the absence of the laser field.

Based on the small energy separation and the comparatively large dipole moments, we have chosen the $|E_1\rangle$ and $|E_2\rangle$ intermediate states to be the 15th and 16th bound vibrational states of the ^{6}Li^{7}Li^{7}Li ($^4A''$) complex. These states are separated by 1.4 cm^{-1} from one another. Figure 1(a) shows the two electronic potential energy surfaces (PES) and the reaction path on the ground PES. The Frank–Condon region is best represented by the 2460 cm^{-1} contour line (the 4th line outward from the minimum) of part (b) in Fig. 1(a). For reference, the energy of the 14th state is 87.79 cm^{-1} below the 15th state, and that of the 17th state is 109.7 cm^{-1} above the 16th state. Thus, the 14th and 17th bound states need not be included in the calculation, provided that the laser power is lower than 1 TW/cm^2 and its carrier frequency is not too close to the 14th or the 17th states.

B. Narrow initial wave packet case

We consider a narrow initial wave packet whose energy bandwidth is 0.01 cm^{-1}, and in this case, we use a laser whose bandwidth is 3.5×10^{-3} cm^{-1}, i.e., ~3 ns in duration. At this bandwidth, when the laser's carrier frequency is on resonance with transition to the $|E_1\rangle$ bound state, the maximum population of the $|E_2\rangle$ bound state is 10^{-7} that of the $|E_1\rangle$ state. Thus, for the above laser and wave packet parameters there is no need to include the $|E_2\rangle$ state in the calculation.

We control the laser assisted scattering into the ^{7}Li $+^6$Li^{7}Li product channel by varying the laser power (P), the temporal width of the laser (δ_t), the carrier frequency of the laser (ω_0), the energy bandwidth of initial wave packet (δ_E), and the center of the initial wave packet (E_0). The range of control obtained is truly impressive: Figure 2 shows that one can maximize the reaction probability to near unity values. By varying the above parameters we are, in fact, able to change the reaction probability from 0% to 99.9%. Thus, we are able to suppress the naturally occurring reaction, as well as enhance it.

Of the above parameters, the reaction probability appears to be especially sensitive to P and E_0. Specifically, an increase in P while leaving all other parameters unchanged causes the population of the $|E_1\rangle$ intermediate state to go down and the reaction yield to increase. Thus, as in other reactions,[28] at high laser powers one approaches the three-state adiabatic passage[32] limit.

As shown in Table I, the wave packet average energy E_0 can also greatly affect the reaction probability. Figure 3 depicts the energy-dependent dipole moments $|\mu^-(E_0; i =1,q,n=0)|$ as a function of energy E_0 for the two arrangement channels. Figure 4 describes the behavior of the opti-
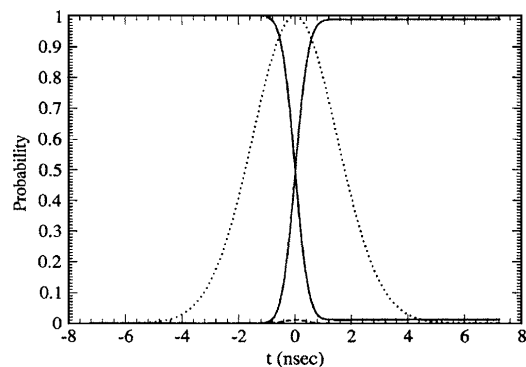
FIG. 2. The integrated populations of the continuum states and the population of the intermediate state $|E_1\rangle$. The dashed line is the intensity profile of the Gaussian pulse whose maximum intensity is 20 GW/cm^{-1}, the temporal width is $\delta_t=3$ ns. The carrier frequency ω_0 is chosen such that the laser is on resonance with the $|E_1\rangle$ state. The initial wave packet has a center energy of $E_0=-270.7$ cm^{-1} and a width of $\delta_E=0.01$ cm^{-1}.

TABLE I. The reactive yield vs the position of the center of initial wave packet E_0. All other parameters have been optimized. The 15th vibrational state is used as the intermediate state.

E_0 (cm^{-1})	Reaction yield (%)	$|\mu(E_0; i=1, q=1, n=0)|$	$|\mu(E_0; i=1, q=2, n=0)|$
−277.46	99.9	8.3×10^{-2}	8.1×10^{-2}
−272.6	94.1	0.62	0.80
−273.9	27.1	0.28	0.99

mized reactive yield versus the ratio of different dipole moments. It is clear that the ratio $|\mu(E_0; i=1, q=1, n=0)/\mu(E_0; i=1, q=2, n=0)|$ should be near unity in order to maximize the reactive yield. This phenomenon is analogous to Young's two slits experiment for which the highest fringe contrast is obtained when the slits widths are the same.

When the transition dipole moments do not vary appreciably within the bandwidth of the laser or the initial wave packet, it is possible to use the (Markovian-like) slowly varying Continuum Approximation (SVCA).[49] This is the case when both the initial wave packet and the laser have energy bandwidths of a few wavenumbers or less, since within this narrow bandwidth the continuum-bound dipole moments are essentially constant. When the SVCA is valid, the spectral cross-correlation functions of Eq. (17) become essentially proportional to a $\delta(\tau)$ function, and the integro-differential equations of Eq. (15) become simple differential equations.

C. Wide initial wave packet case

In the wide initial wave packet case, the initial wave packet assumes a wider bandwidth, e.g., $\delta_E \sim 1$ cm^{-1}. The laser power must now be higher and the laser duration made shorter in order to maintain a high reaction yield. When the laser bandwidth is sufficiently high, both $|E_1\rangle$ and $|E_2\rangle$ intermediate states are excited. The coherent motion of the two bound states now becomes an important knob in controlling the total reactive yield.
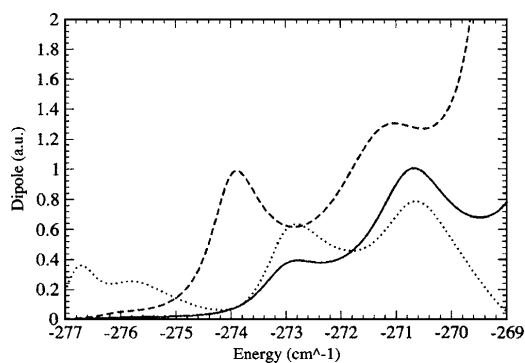
FIG. 3. Dipole moment $|\mu^-(E_0; i=1, q, n=0)|$ as a function of the wave packet center energy E_0. Solid line, $|\mu^-(E_0; i=1, q=1, n=0)|$; dashed line, $|\mu^-(E_0; i=1, q=2, n=0)|$; dotted line, $|\mu^-(E_0; i=1, n=0)/\mu^-(E_0; i=1, q=1, n=0)|$.
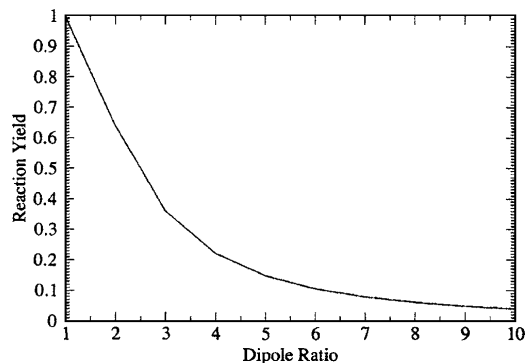
FIG. 4. The reactive yield vs the ratio of two dipole moments in different channels. All experimental parameters have been optimized and the 15th state is used as the intermediate state.

We find that the results are insensitive to δ_t as long as $\delta_t \geq 2/\delta_E$. Hence, calculations are performed with a fixed laser temporal width, $\delta_t = 16.1$ ps. We also fix the initial wave packet's parameters, δ_E and E_0, in order to focus on the effect of the external laser field and on the interference between the two intermediate states. Specifically, we vary the laser power P and $\Delta \equiv E_0 + \hbar\omega_0 - (E_1 + E_2)/2$, the difference between the average energy of the system after absorbing a laser photon and the average value of the intermediate states energies $(E_1 + E_2)/2$.

Figure 5 shows the nonreactive and reactive yields' dependence on P and Δ at $t = 50$ ps. The maxima and minima are not shown on the plot because the maxima may occur at a very high powers where the present calculation may be invalid. The initial wave packet has a center energy of $E_0 = -272.87$ cm^{-1}, and bandwidth $\delta_E = 1.097$ cm^{-1} and laser time duration $\delta_t = 16.1$ ps. At energy E_0, the nonradiative reactive probability is calculated to be 4.2%. We see that the reactive yield can be controlled from 0% to 76% with this range of parameters.

To illustrate the importance of the interference between the two intermediate states as an additional control mechanism, we perform a calculation in which only one bound state is included. With equivalent range of experimental parameters, the reactive yield is found to vary over a much smaller range. For example, at $P = 450$ GW/cm^2, the reactive yield with two bound states ranges from 1% to 71%, while the reactive yield obtained with only one bound intermediate state can be varied from 7% to 56% only.

In the present study, we refrained from increasing the laser power beyond 1 TW/cm^2 to avoid complicating the dynamics, as at these intensities the involvement of excited reactant and product states on the ground electronic surface is unavoidable.

It should be noted that this calculation is performed on the collinear reactive scattering process which has no hyperfine structures and, thus, the effect of different hyperfine states do not contribute to this case. In general, cold atoms and molecules in different hyperfine states have been shown to have very different interaction properties, especially dif-
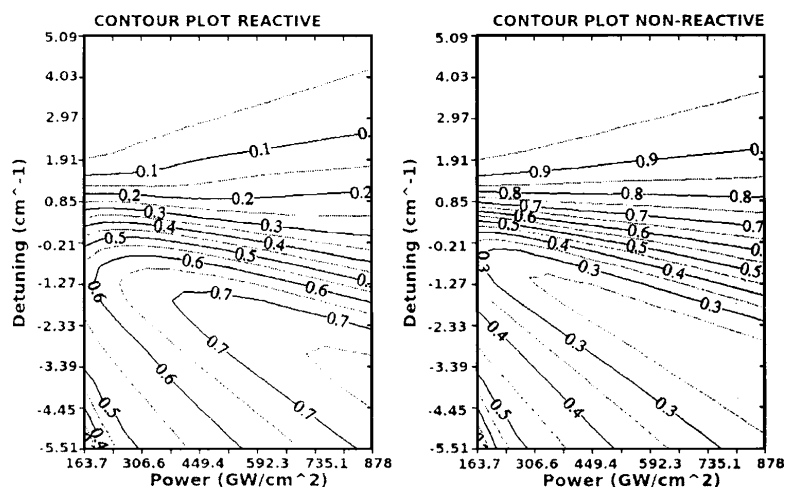
FIG. 5. A contour plot of the reactive and nonreactive yields vs power and detuning with respect to the transition frequency to the intermediate states $|E_1\rangle$ and $|E_2\rangle$. The initial wave packet has a center energy of $E_0 = -272.9$ cm^{-1} and a bandwidth of $\delta_E = 1.097$ cm^{-1}. The temporal width of the laser is $\delta_t = 16.1$ ps.

ferent (in magnitude and sign) coupling matrix elements between the intermediate states and the continua. Therefore, when the hyperfine splittings are smaller than the pulse width multiple intermediate, the reactant and product quantum states are coupled and these effects should not be neglected. Thus, two possible effects should be addressed: The inclusion of more intermediate states and the inclusion of more reactant and product states. We know from stimulated Raman adiabatic passage (and laser catalysis has the main features of an adiabatic passage) under what conditions it works when multiple intermediate states are involved, and more details on how to maximize the reaction yield for multiple intermediate states under different conditions can be found in the work Vitanov and Stenholm.[59] In principle, the scheme should still work with the inclusion of more intermediate states, one should expect probably less efficiency compared to the single intermediate state case, but promising reaction yields are possible. The inclusion of different reactant and product states, at a cold temperature, might decrease the control ability. However, one can consider systems with only one reactant and product hyperfine state, i.e., systems with total angular momentum **F** (including the nuclear spin) equal to zero, in which case high reaction yield ($\geqslant 99\%$) can be achieved.

IV. CONCLUSIONS

In this paper, we have derived a nonperturbative time-dependent theory of laser enhancement and suppression of reactive scattering. The theory has been applied to a system of bosons (^{7}Li) and fermions (^{6}Li) on the spin-aligned electronic PES. We have shown that for an initially prepared reactant wave packet with a narrow bandwidth (~ 0.01 cm^{-1}), the reactive yield can be varied from 0% (complete suppression of the reactive scattering) to 99.9% (complete population transfer to the products). In this case, one intermediate bound state, which utilizes the coherence between the radiative process and the nonradiative process suffices for control. Studies using a wider initial reactant

wave packet (~ 1 cm^{-1}) are found to require several intermediate bound states to enhance the control. In this case, control of the reactive yield extends from 0% to 76%, with interference between the intermediate bound states playing an important role in enhancing or suppressing the reaction.

The current theory and calculation can be applied to systems with a relatively small number of atoms which involves continuum states and bound states on different electronic PES to achieve quantum control of a reactive scattering process. The control is more significant in a system with negligible reactive probability into the product arrangement either with a barrier in the reaction path leading from reactants to products or in a similar system like the current one. To optimize the controllability one should look for an intermediate bound state which has a pair of not only relatively large but also close dipole couplings with the reactant and product arrangements, respectively. Also, the number of internal quantum modes should be chosen to be as few as possible for the reactant and product states so that the calculation does not have to include many states to wash out the perfect interferences.[14,15]

ACKNOWLEDGMENTS

[1] For reviews, see *Molecules in Laser Fields*, edited by A. D. Bandrauk (Dekker, New York, 1994); M. Shapiro and P. Brumer, *Principles of the Quantum Control of Molecular Processes* (Wiley, New York, 2003).
[2] M. V. Fedorov, O. V. Kudrevatova, V. P. Makarov, and A. A. Samokhin, Opt. Commun. **13**, 299 (1975).
[3] N. M. Kroll and K. M. Watson, Phys. Rev. A **8**, 804 (1973); **13**, 1018 (1976).

[4] J. I. Gerstein and M. H. Mittleman, J. Phys. B **9**, 383 (1976).

[5] J. M. Yuan, T. F. George, and F. J. McLafferty, Chem. Phys. Lett. **40**, 163 (1976); J. M. Yuan, J. R. Laing, and T. F. George, J. Chem. Phys. **66**, 1107 (1977); T. F. George, J. M. Yuan, and I. H. Zimmermann, Faraday Discuss. Chem. Soc. **62**, 246 (1977); P. L. DeVries and T. F. George, *ibid.* **67**, 129 (1979); T. F. George, J. Phys. Chem. **86**, 10 (1982).

[6] A. M. F. Lau and C. K. Rhodes, Phys. Rev. A **16**, 2392 (1977); A. M. F. Lau, *ibid.* **13**, 139 (1976); **25**, 363 (1981).

[7] V. S. Dubov, L. I. Gudzenko, L. V. Gurvich, and S. I. Iakovlenko, Chem. Phys. Lett. **45**, 351 (1977).

[8] A. D. Bandrauk and M. L. Sink, Chem. Phys. Lett. **57**, 569 (1978); J. Chem. Phys. **74**, 1110 (1981).

[9] A. E. Orel and W. H. Miller, Chem. Phys. Lett. **57**, 362 (1978); **70**, 4393 (1979); **73**, 241 (1980).

[10] J. C. Light and A. Altenberger-Siczek, J. Chem. Phys. **70**, 4108 (1979).

[11] K. C. Kulander and A. E. Orel, J. Chem. Phys. **74**, 6529 (1981).

[12] H. J. Foth, J. C. Polanyi, and H. H. Telle, J. Chem. Phys. **86**, 5027 (1982).

[13] T. Ho, C. Laughlin, and S. I. Chu, Phys. Rev. A **32**, 122 (1985).

[14] M. Shapiro and Y. Zeiri, J. Chem. Phys. **85**, 6449 (1986).

[15] T. Seideman and M. Shapiro, J. Chem. Phys. **88**, 5525 (1988); **92**, 2328 (1990); **94**, 7910 (1991).

[16] T. Seideman, J. L. Krause, and M. Shapiro, Chem. Phys. Lett. **173**, 169 (1990); Faraday Discuss. Chem. Soc. **91**, 271 (1991).

[17] A. Zavriyev, P. H. Bucksbaum, H. G. Muller, and D. W. Schumacher, Phys. Rev. A **42**, 5500 (1990).

[18] A. Guisti-Suzor and F. H. Mies, Phys. Rev. Lett. **68**, 3869 (1992).

[19] G. Yao and S.-I. Chu, Chem. Phys. Lett. **197**, 413 (1992).

[20] E. E. Aubanel and A. D. Bandrauk, Chem. Phys. Lett. **197**, 419 (1992); A. D. Bandrauk, E. E. Aubanel, and J. M. Gauthier, Laser Phys. **3**, 381 (1993).

[21] D. R. Matusek, M. Yu. Ivanov, and J. S. Wright, Chem. Phys. Lett. **258**, 255 (1996).

[22] J. Herbig, T. Kraemer, M. Mark, T. Weber, C. Chin, H.-C. Nägerl, and R. Grimm, Science **301**, 1510 (2003).

[23] T. Kraemer, M. Mark, P. Waldburger, J. G. Danzl, C. Chin, B. Engeser, A. D. Lange, K. Pilch, A. Jaakkola, H.-C. Nägerl, and R. Grimm, Nature (London) **440**, 315 (2006).

[24] C. Chin, T. Kraemer, M. Mark, J. Herbig, P. Waldburger, H.-C. Ägerl, and R. Grimm, Phys. Rev. Lett. **94**, 123201 (2005).

[25] D. J. Heinzen, R. Wynar, P. D. Drummond, and K. V. Kheruntsyan, Phys. Rev. Lett. **84**, 5029 (2000).

[26] R. Wynar, R. S. Freeland, D. J. Han, C. Ryu, and D. J. Heinzen, Science **287**, 1016 (2000).

[27] M. Bartenstein, A. Altmeyer, S. Riedl *et al.*, Phys. Rev. Lett. **94**, 103201 (2005).

[28] A. Vardi and M. Shapiro, Phys. Rev. A **58**, 1352 (1998).

[29] A. Vardi and M. Shapiro, J. Chem. Phys. **111**, 7713 (1999).

[30] I. Thanopulos and M. Shapiro, J. Chem. Phys. **117**, 8404 (2002).

[31] J. G. Underwood, M. Spanner, M. Yu. Ivanov, J. Mottershead, B. J. Sussman, and A. Stolow, Phys. Rev. Lett. **90**, 223001 (2003).

[32] K. Bergmann, H. Theuer, and B. W. Shore, Rev. Mod. Phys. **70**, 1003 (1998).

[33] P. Král, I. Thanopulos, and M. Shapiro, Rev. Mod. Phys. **79**, 53 (2007).

[34] K. Winkler, G. Thalhammer, M. Theis, H. Ritsch, R. Grimm, and J. Hecker Denschlag, Phys. Rev. Lett. **95**, 063202 (2005).

[35] D. G. Fried, T. C. Killan, L. Willmann, D. Landhuis, S. C. Moss, D. Kleppner, and T. S. Greytak, Phys. Rev. Lett. **81**, 3811 (1998).

[36] C. C. Bradley, C. A. Sackett, J. J. Tollett, and R. G. Hulet, Phys. Rev. Lett. **75**, 1687 (1995).

[37] K. B. Davis, M.-O. Mewes, M. R. Andrews, N. J. van Druten, D. S. Durfee, D. M. Kurn, and W. Ketterle, Phys. Rev. Lett. **75**, 3969 (1995).

[38] M. H. Anderson, J. R. Ensher, M. R. Mathews, C. E. Wieman, and E. A. Cornell, Science **269**, 198 (1995).

[39] T. Weber, J. Herbig, M. Mark, H.-C. Nägerl, and R. Grimm, Science **299**, 232 (2003).

[40] A. G. Truscott, K. E. Strecker, W. I. McAlexander, G. B. Partridge, and R. G. Hulet, Science **291**, 198 (2001).

[41] F. Schreck, G. Ferrari, K. L. Corwin, J. Cubizolles, L. Khaykovich, M.-O. Mewes, and C. Salomon, Phys. Rev. A **6401**, 011402 (2001).

[42] L. Khaykovich, F. Schreck, J. Cubizolles, T. Bourdel, K. L. Corwin, G. Ferrari, and C. Salomon, Physica B **329**, 13 (2003).

[43] M. T. Cvitaš, P. Soldán, J. M. Hutson, P. Honvault, and J.-M. Launay, J. Chem. Phys. **127**, 074302 (2007).

[44] D. A. Brue, X. Li, and G. A. Parker, J. Chem. Phys. **123**, 091101 (2005).

[45] M. T. Cvitaš, P. Soldán, J. M. Hutson, P. Honvault, and J.-M. Launay, Phys. Rev. Lett. **94**, 033201 (2005).

[46] M. T. Cvitaš, P. Soldán, and J. M. Hutson, Mol. Phys. **104**, 23 (2006).

[47] M. Shapiro and R. D. Levine, Chem. Phys. Lett. **5**, 499 (1970).

[48] H. Shyldkrot and M. Shapiro, J. Chem. Phys. **79**, 5927 (1983).

[49] A. Vardi, D. G. Abrashkevich, E. Frishman, and M. Shapiro, J. Chem. Phys. **107**, 6166 (1997).

[50] H. R. Thorsheim, J. Weiner, and P. S. Julienne, Phys. Rev. Lett. **58**, 2420 (1987).

[51] W. C. Stwalley and H. Wang, J. Mol. Spectrosc. **195**, 194 (1999), and references therein.

[52] C. M. Dion, C. Drag, O. Dulieu, B. Laburthe Tolra, F. Masnou-Seeuws, and P. Pillet, Phys. Rev. Lett. **86**, 2253 (2001).

[53] E. A. Shapiro, M. Shapiro, A. Pe'er, and J. Ye, Phys. Rev. A **75**, 013405 (2007); A. Pe'er, E. A. Shapiro, M. C. Stowe, M. Shapiro, and J. Ye, Phys. Rev. Lett. **98**, 113004 (2007).

[54] E. A. Shapiro, V. Milner, C. Menzel-Jones, and M. Shapiro, Phys. Rev. Lett. **99**, 033002 (2007).

[55] S. Zhdanovich, E. A. Shapiro, M. Shapiro, J. W. Hepburn, and V. Milner, "Population transfer between two quantum states with piecewise chirped pulses: Theory and experiment," Phys. Rev. Lett. (submitted).

[56] M. Shapiro, J. Chem. Phys. **56**, 2582 (1972).

[57] M. Shapiro and R. Bersohn, Annu. Rev. Phys. Chem. **33**, 409 (1982).

[58] A. G. Abrashkevich and M. Shapiro, Phys. Rev. A **50**, 1205 (1994).

[59] N. V. Vitanov and S. Stenholm, Phys. Rev. A **60**, 3820 (1999).

Appendix B

Population transfer by adiabatic passage

Theory of laser enhancement of ultracold reactions: The fermion-boson population transfer by adiabatic passage of $^6\text{Li}+^6\text{Li}^7\text{Li}(T_r=1\text{ mK})\rightarrow ^6\text{Li}^6\text{Li}+^7\text{Li}(T_p=1\text{ mK})$

Xuan Li[a] and Gregory A. Parker
Homer L. Dodge Department of Physics and Astronomy, University of Oklahoma,
Norman, Oklahoma 73019, USA

We present a new theory of population transfer by adiabatic passage. This theory relates laser catalysis to adiabatic passage, enhancing chemical reactions with the freedom to choose the translational energies of the reactants and products separately. The process, $A+BC\overset{\hbar\omega_p}{\longleftrightarrow}ABC^*(v)\overset{\hbar\omega_s}{\longleftrightarrow}AB+C$, involves two laser fields that are slowly varying so the process is adiabatic, and sufficiently intense so the population of the intermediate bound complex (ABC) is minimized. We apply this theory to the collinear exchange reaction $^6\text{Li}+^7\text{Li}_2(T_r)\overset{\hbar\omega_p}{\longleftrightarrow}(^6\text{Li}^7\text{Li}^7\text{Li})^*\overset{\hbar\omega_s}{\longleftrightarrow}{}^6\text{Li}^7\text{Li}(T_p)+^7\text{Li}$. We show that at translational energies $T_p=T_r=1$ mK with a narrow energy bandwidth of $\delta_E=0.01$ mK, we can obtain nearly total ($\geq98\%$) population transfer from the reactant to the product states. This can be done with a pump laser and a Stokes laser in an "intuitive" sequence ($t_p<t_s$) at a low intensity ($I_p\leq600$ MW/cm^2) and a "coincident" sequence ($t_p=t_s$) at a higher intensity. © *2008 American Institute of Physics.*
[DOI: 10.1063/1.2920186]

I. INTRODUCTION

The ability to transfer population from one chemical arrangement to another is very attractive to physicists and chemists. However, the need to use high laser intensities, up to TW/cm^2, has been a major obstacle. Two possible procedures that require lower intensities are laser catalysis and adiabatic passage (AP).

Laser catalysis involves no net absorption of photons and usually requires a laser intensity of MW/cm^2.[1–3] It enables colliding partners, which cannot react due to a high potential barrier, to "hop" over this barrier by absorbing a photon to an excited bound state which straddles both sides of the barrier. The conventional laser catalysis scenario uses a single laser pulse and predicts different translational energies for the reactants and products when the diatoms have distinct energy levels. When a system consists of different atoms or isotopes, a single laser does not allow much freedom to tune the product's temperature for a fixed reactants' temperature. Such tuning would also change the system's overall temperature because the conservation of the total energy of the molecular system enforces a relationship between the translational energies of the reactants and of the products when no net photon is absorbed. Freedom to choose the reactants and products' translational energies requires a new theory. Reactions between cold or ultracold boson and fermion isotopes can cause a variety of bimolecular interac-

tions. For example, in isotopic mixtures of fermionic ^6Li and bosonic ^7Li, either heteronuclear or homonuclear diatomic molecules may form.[4–7]

Conventional AP,[8,9] on the other hand, involves three bound states and two slowly varying laser fields. The population is transferred from the initial bound state to the final bound state without populating the intermediate bound state. Vardi *et al.*[10] extends conventional AP theory to the photoassociation AP (PAP), which involves one initial continuum state, one intermediate bound state, and one final bound state. In this process, the population in the intermediate state is minimized, and the process is adiabatic. Both conventional AP and the PAP require a pump laser and a Stokes laser in a "counterintuitive" sequence, i.e., the Stokes pulse comes before the pump pulse ($t_p>t_s$). For conventional AP, this mechanism can be understood in terms of *dark states*.[11] However, dark states do not formally exist in the PAP mechanism, and total suppression of the population of the intermediate state may be difficult.[10]

Our goal is to relate laser catalysis and AP theories involving two slowly varying laser pulses so as to keep the process adiabatic, to allow for two sets of continuum reactant and product states, and to minimize the population in the intermediate bound state. Figure 1 shows a schematic of population transfer by AP (PTAP) from the reactant channel to the product channel using two pulsed lasers. This PTAP theory can be applied to control the exchange process, in which one wishes to replace an atom attached to a molecule with another atom without adding heat to the system. PTAP can also be applied to control tuning of a vibrational mode,

[a]Electronic mail: li@nhn.ou.edu.

Intermediate bound state

Δ_p Δ_s

ω_p ω_s
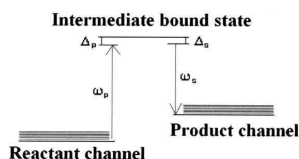
Product channel

Reactant channel

FIG. 1. Schematic plot of population transfer by adiabatic passage with two pulsed lasers.

which uses two lasers to change the vibrational quantum number of the diatoms in an ensemble of cold or ultracold atom-diatom mixtures without heating the ensemble. PTAP does not necessarily keep the temperatures of the reactants and the products the same but it can tune the products' temperature.

We study ultracold PTAP of the ^{6}Li+^{6}Li^{7}Li (T_r=1 mK) arrangement channel into the ^{6}Li^{6}Li+^{7}Li (T_p=1 mK) arrangement channel. In Sec. II, we present a nonperturbative theory of PTAP using two laser pulses. In Sec. III, we use this theory for the time-dependent ultracold mixtures of the ^{6}Li^{6}Li^{7}Li system. We show that to obtain the maximum reaction yield ($\geq$98%), one should apply the pump laser and the Stokes laser either in an "intuitive" sequence with a low laser intensity, or in a coincident sequence with a higher laser intensity.

II. THEORY

The dynamics of all light induced processes are governed by the total (matter+radiation) Hamiltonian $H_{\text{tot}}=H-\vec{\mu}\cdot\vec{\varepsilon}(t)$ where H is the material Hamiltonian, $\vec{\mu}$ is the dipole moment, and $\vec{\varepsilon}(t)=\hat{\varepsilon}\varepsilon(t)$ is the laser's electric field, with $\hat{\varepsilon}$ as the polarization direction and $\varepsilon(t)$ as the (scalar) electric field amplitude. We consider two lasers, with $\varepsilon_p(t)$ as the pump pulse and $\varepsilon_s(t)$ as the Stokes pulse. Both pulses are assumed to be Gaussian,

$$\varepsilon_p(t) = \varepsilon_{\text{op}} \exp\left[-\left(\frac{t-t_p}{\Delta_{t_s}}\right)^2\right]\exp(-i\omega_p t) \qquad (1)$$

and

$$\varepsilon_s(t) = \varepsilon_{\text{os}} \exp\left[-\left(\frac{t-t_s}{\Delta_{t_s}}\right)^2\right]\exp(-i\omega_s t), \qquad (2)$$

where ε_{op} and ε_{os} are the field strengths, Δ_{tp} and Δ_{ts} are the temporal pulse widths, and ω_p and ω_s are the carrier frequencies. To solve the time-dependent Schrödinger equation,

$$i\hbar\frac{\partial\Psi}{\partial t} = H_{\text{tot}}\Psi, \qquad (3)$$

we expand $\Psi(t)$ in a complete basis that consists of all bound

eigenstates $|E_i\rangle$, and all continuum eigenstates $|E,q,n^-\rangle$ of H,

$$(E_i - H)|E_i\rangle = 0,$$

$$(E - H)|E,q,n^-\rangle = 0, \quad q = 1,2. \qquad (4)$$

In the above equations, E_i are the bound state energies in the excited electronic state, and E is the continuum energy of the ground electronic state, with n as the asymptotic internal quantum numbers associated with the arrangement channel q. The minus superscript on n^- signifies that as $t\rightarrow\infty$, each $|E,q,n^-\rangle$ approaches a *single* asymptotic eigenstate, $|E,q,n;0\rangle$, of H_q^0—the q-arrangement channel material Hamiltonian for well separated reactants (or products). These states satisfy the energy eigenvalue relations,

$$(E - H_q^0)|E,q,n;0\rangle = 0, \quad q = 1,2. \qquad (5)$$

The expansion of $\Psi(t)$ in Eq. (3) thus assumes the form,

$$|\Psi(t)\rangle = \sum_{q,n}\int dE b_{E,q,n}(t)|E,q,n^-\rangle\exp(-iEt/\hbar)$$
$$+ \sum_j b_j(t)|E_j\rangle\exp(-iE_j t/\hbar), \qquad (6)$$

where $b_{E,q,n}(t)$ and $b_j(t)$ are the expansion coefficients of the continuum and bound states, respectively. We limit the number of intermediate bound states to one (A study of including two intermediate states in order to use the phase evolution to *coherently control* PTAP is underway.)

Substitution of Eq. (6) into Eq. (3) results in the following set of differential equations for the expansion coefficients:

$$b_j = \frac{i}{\hbar}\varepsilon(t)\sum_{q,n}\int dE b_{E,q,n}^-(t)\mu^-(E;j,q,n)e^{-i\omega_{E,j}t}, \qquad (7)$$

$$\dot{b}_{E,q,n} = \frac{i}{\hbar}\varepsilon^*(t)b_j(t)\mu^-(E;q,j,n)e^{i\omega_{E,j}t} + \frac{i}{\hbar}\varepsilon(t)$$
$$\times \sum_{q',m}\int dE' b_{E',q',m}(t),\mu(E,E';q,q',n,m)e^{-i\omega_{E',E}t}, \qquad (8)$$

where

$$\omega_{j,i} \equiv (E_j - E_i)/\hbar, \quad \omega_{E,i} = (E = E_i)/\hbar,$$

$$\omega_{E',E} \equiv (E' - E)/\hbar, \qquad (9)$$

$$\mu(i,j) \equiv \langle E_i|\vec{\mu}\cdot\hat{\varepsilon}|E_j\rangle, \quad \mu^-(E;i,q,n) \equiv \langle E_i|\vec{\mu}\cdot\hat{\varepsilon}|E,q,n^-\rangle,$$

$$\mu(E,E';q,q',n,m) \equiv \langle E,q,n^-|\vec{\mu}\cdot\hat{\varepsilon}|E',q',m^-\rangle. \qquad (10)$$

Here, $\omega_{j,i}$, $\omega_{E,i}$, and $\omega_{E',E}$ are the transition frequencies between the bound-bound, bound-free, and free-free states, respectively. The quantities $\mu(i,j)$, $\mu^-(E;i,q,n)$, and $\mu(E,E';q,q',n,m)$ are the bound-bound, bound-free, and free-free dipole-moment coupling matrix elements, respectively. Assuming that $\mu(E,E';q,q',n,m)\approx 0$, i.e., that there is no radiative coupling between different continuum states of the ground electronic surface, we can eliminate the continuum couplings in Eq. (8) and solve for $b_{E,q,n}(t)$,

$$b_{E,q,n}(t) = b_{E,q,n}(-\infty)$$
$$+ (i/\hbar)\int_{-\infty}^{t} dt' b_j(t')\mu^-(E;q,n,j)\varepsilon^*(t')e^{i\omega_{E,j}t'}. \qquad (11)$$

We have assumed that the initial wave packet belongs to the ($q_s=1$) reactant channel with initial bound state coefficients $b_j(-\infty)=0$. The continuum coefficients, $b_{E,q,n}(-\infty)$, are determined from the form of the incoming wave packet, which we assume belongs to the $q_s=1$ arrangement with vibrational quantum number $n_s=0$,

$$\Psi_{in} = \int dE b^+_{E,q_s=1,n_s=0}(t)|E,q_s=1,n_s=0^+\rangle e^{-iEt/\hbar}. \qquad (12)$$

The $b^+_{E,q_s,n_s}(t)$ coefficients, which specify the shape of the incoming wave packet, are chosen, as specified below, to be Gaussian functions in energy.

Using the well-known relationship between the *incoming* and *outgoing* scattering solutions, we have

$$|E,q_s,n_s^+\rangle = \sum_{q,n}|E,q,n^-\rangle\langle E,q,n^-|E,q_s,n_s^+\rangle$$
$$= \sum_{q,n}|E,q,n^-\rangle S_{q,n;q_s n_s}. \qquad (13)$$

Hence,

$$b_{E,q,n}(-\infty) = S_{q,n;1,n_s}b^+_{E,1,n_s}(-\infty), \qquad (14)$$

where as mentioned above, $q_s=1$, and $S_{q,n;1,n_s}$ is the nonradiative S-matrix. Substituting the solution $b_{E,q,n}(t)$ into Eq.

(7), we obtain a (smaller) set of integrodifferential equations for $b_i(t)$,

$$\dot{b}_j(t) = \frac{i\varepsilon(t)}{\hbar}\mu_j^s(t) + \frac{i\varepsilon(t)}{\hbar}\int_{-\infty}^{t} dt' b_j(t')F_j(t-t')\varepsilon^*(t'), \qquad (15)$$

where $\mu_j^s(t)$ are the known source terms

$$\mu_j^s(t) \equiv \sum_{q,n}\int dE b_{E,q,n}(-\infty)\mu^-(E;j,q,n)e^{-i\omega_{E,j}t}, \qquad (16)$$

and

$$F_j(\tau) = \frac{i}{\hbar}\int dE\sum_{q,n}|\mu^-(E;j,q,n)|^2 e^{-i\omega_{E,j}\tau} \qquad (17)$$

are the spectral *autocorrelation functions*. The function F_j is the Fourier transform of $A_i(\omega)$, the photoabsorption spectrum from bound levels j,

$$F_j(\tau) \equiv i\int d\omega A_j(\omega)e^{-i\omega\tau}, \qquad (18)$$

where

$$A_j(\omega) = \sum_{q,n}|\mu^-(E_j+\hbar\omega;j,q,n)|^2. \qquad (19)$$

We will ignore the summation over n because in an ultracold system, $n=0$ for all arrangements.

To investigate the second term on the right-hand side of Eq. (15), we explicitly write out $\varepsilon_p(t)$ and $\varepsilon_s(t)$ and define

$$\Upsilon(t) \equiv -\frac{1}{\hbar^2}\int_{-\infty}^{t} dt' b_j(t')$$
$$\times \sum_q \int dE|\mu^-(E_j+\hbar\omega;j,q,n)|^2\hat{E}(t,t'), \qquad (20)$$

where

$$\hat{E}(t,t') \equiv [\varepsilon_p(t)+\varepsilon_s(t)][\varepsilon_p^*(t')+\varepsilon_s^*(t')]e^{-i\omega(t-t')}. \qquad (21)$$

The operator $E(t,t')$ can be written as the sum of the four terms

$$E(t,t') = |\varepsilon_{op}|^2 e^{-(t-t_p/\Delta_{t_p})^2}e^{-(t'-t_p/\Delta_{t_p})^2}e^{-it(\omega_p+(E-E_j/\hbar))}e^{it'(\omega_p+(E-E_j/\hbar))}$$

$$+ \varepsilon_{op}\varepsilon_{os}^* e^{-(t-t_p/\Delta_{t_p})^2}e^{-(t'-t_s/\Delta_{t_s})^2}e^{-it(\omega_p+(E-E_j/\hbar))}e^{it'(\omega_s+(E-E_j/\hbar))}$$

$$+ \varepsilon_{op}^*\varepsilon_{os} e^{-(t-t_s/\Delta_{t_s})^2}e^{-(t'-t_p/\Delta_{t_p})^2}e^{-it(\omega_s+(E-E_j/\hbar))}e^{it'(\omega_p+(E-E_j/\hbar))}$$

$$+ |\varepsilon_{os}|^2 e^{-(t-t_s/\Delta_{t_s})^2}e^{-(t'-t_s/\Delta_{t_s})^2}e^{-it(\omega_s+(E-E_j/\hbar))}e^{it'(\omega_s+(E-E_j/\hbar))}. \qquad (22)$$

The first and third terms correspond to coupling between the intermediate state and the states $|E_j - \hbar\omega_p, q, n^-\rangle$ with respect to integration over t' and E; the second and fourth terms correspond to coupling between the intermediate state and the states $|E_j - \hbar\omega_s, q, n^-\rangle$ with respect to the integration over t' and E. Therefore, the states $|E_j - \hbar\omega_p, q=2, n^-\rangle$ do not exist, and we can ignore the contribution from the first and third terms when $q=2$. If we write $\Upsilon(t) \equiv \Upsilon_{q=1}(t) + \Upsilon_{q=2}(t)$, we can use the slowly varying continuum approximation[12–15] (SVCA) to express

$$\Upsilon_{q=2}(t) = -\frac{\pi}{\hbar} b_j(t)|\mu^-(E_j - \hbar\omega_s; j, q=2, n)|^2 \varepsilon_{os}^* e^{-(t-t_s/\Delta_{t_s})^2}$$
$$\times \left[\varepsilon_{op} e^{-(t-t_p/\Delta_{t_p})^2} e^{-it(\omega_p - \omega_s)} + \varepsilon_{os} e^{-(t-t_s/\Delta_{t_s})^2} \right] \quad (23)$$

and

$$\Upsilon_{q=1}(t) = -\frac{\pi}{\hbar} b_j(t)|\mu^-(E_j - \hbar\omega_s; j, q=1, n)|^2 \varepsilon_{os}^* e^{-(t-t_s/\Delta_{t_s})^2}$$
$$\times \left[\varepsilon_{op} e^{-(t-t_p/\Delta_{t_p})^2} e^{-it(\omega_p - \omega_s)} + \varepsilon_{os} e^{-(t-t_s/\Delta_{t_s})^2} \right]$$
$$-\frac{\pi}{\hbar} b_j(t)|\mu^-(E_j - \hbar\omega_p; j, q=1, n)|^2 \varepsilon_{op}^* e^{-(t-t_p/\Delta_{t_p})^2}$$
$$\times \left[\varepsilon_{os} e^{-(t-t_s/\Delta_{t_s})^2} e^{+it(\omega_p - \omega_s)} + \varepsilon_{op} e^{-(t-t_p/\Delta_{t_p})^2} \right]. \quad (24)$$

In Eqs. (23) and (24), we can identify three rapidly oscillating terms $e^{\pm it(\omega_p - \omega_s)}$. If these terms oscillate much faster than the slowly varying $\varepsilon_s(t)$ and ε_p terms, we can eliminate them. Making this adiabatic approximation, which ignores the three rapidly oscillating terms, we can express $\Upsilon(t)$ as

$$\Upsilon(t) = -\Omega(t) b_j(t), \quad (25)$$

$$\Omega(t) \equiv +\frac{\pi}{\hbar}|\mu^-(E_j - \hbar\omega_s; j, q=2, n)|^2 |\varepsilon_{os}|^2 e^{-2(t-t_s/\Delta_{t_s})^2}$$
$$+\frac{\pi}{\hbar}|\mu^-(E_j - \hbar\omega_s; j, q=1, n)|^2 |\varepsilon_{os}|^2 e^{-2(t-t_s/\Delta_{t_s})^2}$$
$$+\frac{\pi}{\hbar}|\mu^-(E_j - \hbar\omega_p; j, q=1, n)|^2 |\varepsilon_{op}|^2 e^{-2(t-t_p/\Delta_{t_p})^2}. \quad (26)$$

Equation (26) implies an approximate ratio between I_p and I_s for an optimized reaction yield,

$$\frac{I_s}{I_p} \approx \frac{|\mu_{1p}|^2}{|\mu_{1s}|^2 + |\mu_{2s}|^2}, \quad (27)$$

where $\mu_{1p} \equiv \mu^-(E_j - \hbar\omega_p; j, q=1, n)$, $\mu_{1s} \equiv \mu^-(E_j - \hbar\omega_s; j, q=1, n)$ and $\mu_{2s} \equiv \mu^-(E_j - \hbar\omega_s; j, q=2, n)$. Equation (27) balances the pump and dump processes to achieve perfect interferences.

Using the artificial channel method[16–18] (ACM) to calculate $\mu^-(E; i, q, n)$, we can calculate the $\Upsilon(t)$ absorbing term in Eq. (15) from Eq. (25). Having constructed $\Upsilon(t)$, we can calculate $b_j(t)$ by solving the first-order differential equations [Eq. (15)].

To obtain an analytical solution of Eq. (15), we write this equation as

$$\dot{b}_j(t) = iG(t) - \Omega(t) b_j(t), \quad (28)$$

where

$$G(t) = \frac{\varepsilon(t)}{\hbar} \mu_j^s(t). \quad (29)$$

Therefore, the analytical solution of $b_j(t)$ is

$$b_j(t) = \upsilon(t)\phi(t) + \upsilon(t) b_j(t_0), \quad (30)$$

where

$$\upsilon(t) = \exp\left[-\int_{t_0}^t \Omega(t')dt' \right] \quad (31)$$

and

$$\phi(t) = i\int_{t_0}^t \frac{G(t')}{\upsilon(t')} dt'. \quad (32)$$

Implying the initial condition $b_j(t_0) = 0$, we obtain

$$b_j(t) = i\int_{t_0}^t G(t') \exp\left[-\int_{t'}^t \Omega(t'')dt'' \right] dt'. \quad (33)$$

From $b_j(t)$, we can calculate the continuum coefficients $b_{E,q,n}(t)$ from Eq. (11).

III. RESULTS

The theory in Sec. II enables one to easily study laser-assisted population transfer. We apply the theory to population transfer between reactant and product states of a coherent wave packet of the collinear ultracold triatomic $^6\text{Li}^6\text{Li}^7\text{Li}$ system. We describe the coherent wave packet of the initial reactant wave packet by a normalized Gaussian wave packet

$$b_{E,q_s,n_s}^+(-\infty) = (\delta_E^2 \pi)^{-1/4} \exp[-(E - E_0)^2/(2\delta_E^2)], \quad (34)$$

where δ_E is the narrow energy bandwidth, and E_0 is the energy center of the initial reactant wave packet. In our simulations, we have chosen the mean initial kinetic energies of the reactants to be $E_0 = E(q=1, n=0, T_r=1 \text{ mK})$ and the wave packet width to be $\delta_E = 0.01 - 0.1 \text{ mK}$.

As depicted in Fig. 1, the combined effect of the two laser pulses with carrier frequencies ω_p and ω_s is to transfer population from the ultracold initial reactant ($q=1$, $n=0$, $T_r=1 \text{ mK}$) to the ultracold product ($q=2$, $n=0$, $T_r=1 \text{ mK}$) on the $^4A'$ electronic potential energy surface, with the bound ($v=31, J=0$) state acting as an intermediate resonance on the $^4A''$ electronic potential energy surface. The energy level of this intermediate state lies 2693.04 cm^{-1} above the three-body dissociation limit of the ground $^4A'$ surface.

For a narrow initial reactant wave packet, with $\delta_E = 0.01 - 0.1 \text{ mK}$, and a long temporal pulse, with $\Delta_{p,s} \sim 2/\delta_E$, the $\mu^-(E; j, q=1, n)$ bound-continuum coupling does not vary appreciably with kinetic energy over the spectral bandwidth of the pulse. Therefore, we can apply the SVCA to Eq. (29) to form the simplified $G(t)$ function

$$G(t) \approx \left(\frac{4\delta_E^2 \pi}{\hbar} \right)^{1/4} \mu^-(E_0; j, q = 1, n)\varepsilon_{op}$$
$$\times \exp\left\{ -\left(\frac{t-t_p}{\Delta_{t_p}}\right)^2 - i\frac{\Delta_p}{\hbar}t - \frac{\delta_E^2 t^2}{2\hbar^2} \right\}, \quad (35)$$

where the detuning Δ_p is

$$\Delta_p \equiv \omega_p - [E_j - E(q = 1, n = 0, T_r = 1 \text{ mK})]. \quad (36)$$

We have neglected a rapidly oscillating term which is proportional to $\exp\{-i(E_0 - E_j + \omega_s)t/\hbar\}$, because we assume that the two carrier frequencies ω_s and ω_p are significantly different compared to the energy bandwidth of the pulses.

To maximize the reaction yield, one can vary the experimental parameters $\Delta_{t_s}, \Delta_{t_p}, t_p, t_s, \Delta_s, \Delta_p$ along with the laser intensities I_p and I_s, where the detuning Δ_s is

$$\Delta_s = \omega_s - [E_j - E(q = 2, n = 0, T_p = 1 \text{ mK})]. \quad (37)$$

There exists an exact scaling relation between these parameters. According to Eq. (28), this relation is obtained when the initial wave packet's width and the pulse intensities are scaled down as

$$\delta_E \rightarrow \frac{\delta_E}{w}, \quad I_{p,s} \rightarrow \frac{I_{p,s}}{w}, \quad (38)$$

and the duration of both pulses and $t_{p,s}$ are scaled up as

$$\Delta_{p,s} \rightarrow \Delta_{p,s}w, \quad t_{p,s} = t_{p,s}w. \quad (39)$$

It follows from Eqs. (35) and (26) that under these transformations

$$G(t) \rightarrow \bar{G}(t) = \frac{G(t/w)}{w}, \quad \Omega(t) \rightarrow \bar{\Omega}(t) = \frac{\Omega(t/w)}{w}, \quad (40)$$

so Eq. (28) becomes

$$\frac{d}{d(t/w)}b_j = iG(t/w) - \Omega(t/w)b_j. \quad (41)$$

In all cases studied, we obtained optimized results by choosing Δ_s and Δ_p to be zero which implies the on-resonance case, and the laser temporal widths Δ_{t_s} and Δ_{t_p} to be equal. We choose δ_E to be smaller than 0.15 mK so the SVCA is valid.

In this case, the ability to execute AP is limited because the initial and the final states are continuum states. However, it would be interesting to check how close to AP we can be in PTAP so as to minimize the population of the intermediate state. The PTAP scheme does not take into account losses due to spontaneous emission from the intermediate bound state, which may be significant if there is appreciable population in this state. In the laser catalysis scenario,[1-3] this problem can be effectively eliminated by increasing the laser intensities, as can be done in PTAP. For $T_r = T_p = 1$ mK and $\delta_E = 0.1$ mK, the populations transferred into the bound states are less than 1% provided the laser intensity I_p is greater than 2.4 GW/cm^2 and the two pulses have significant overlaps. The process described here, though not a perfect AP, is nevertheless adiabatic, since the solution of Eqs. (11) and (15), with or without the fast oscillating terms in Eq. (23) and

Eq. (24), agree to within a 0.5% error with $6 \times 10^3 \leq (\omega_p - \omega_s)\Delta_{t_s,t_p}$ and a 0.05% error with $6 \times 10^4 \leq (\omega_p - \omega_s)\Delta_{t_s,t_p}$.

More interesting is the relationship between t_p and t_s. When the pump laser's intensity is smaller than 6 GW/cm^2, the maximum reaction yield occurs with an intuitive sequence, in which the pump pulse proceeds the Stokes pulse ($t_p < t_s$). With an intensity of $I_p \geq 2.45$ GW/cm^2, the optimum reaction yield with an intuitive sequence is almost exactly equal to the reaction yield for a coincident sequence, and $|t_p - t_s|$ for the optimum reaction yield with an intuitive sequence goes to zero which indicates the coincident sequence. However, PTAP with the intuitive and coincident sequences depends differently on the laser intensities. Additionally, for the counterintuitive sequence ($t_p > t_s$), the reaction yield is smaller than that with the intuitive and coincident sequences. Moreover the dependence on the laser intensities are similar for the counterintuitive sequence and the coincident sequence. Therefore, we only present the coincident sequence and the intuitive sequence cases herein.

A. Coincident sequence

Setting t_p and t_s to be zero maximizes overlaps in time for the pulses with the initial reactant wave packet. To optimize population transfer into the product channel, one should be aware of four possible resultant states: Wave packets centered at $|E = E_j - \omega_p, q = 1, n = 0\rangle$, $|E = E_j - \omega_s, q = 1, n = 0\rangle$, and $|E = E_j - \omega_s, q = 2, n = 0\rangle$, and the intermediate bound state $|E_j\rangle$. (The wave packet centered at $|E = E_j - \omega_p, q = 2, n = 0\rangle$ does not exist because these energies are not allowed in this case.) The population of the intermediate bound state may decrease with increasing laser intensities. The population of the wavepacket centered at $|E = E_j - \omega_p, q = 1, n = 0\rangle$ can be optimized to nearly zero using the destructive interference between the optical route and the nonradiative scattering route. However, the product wave packet centered at $|E = E_j - \omega_s, q = 2, n = 0\rangle$ must compete with the reactant wave packet centered at $|E = E_j - \omega_s, q = 1, n = 0\rangle$ because the probability that the system will stay in the final reactant wave packet at $|E = E_j - \omega_s, q = 1, n = 0\rangle$ cannot be coherently controlled by interference between the optical route and the nonradiative scattering route because the latter does not exist in this case. Therefore, to minimize the effect of the "satellite state" $|E = E_j - \omega_s, q = 1, n = 0\rangle$, one should use an intermediate bound state that preferentially couples to the $|E = E_j - \omega_s, q = 2, n = 0\rangle$ state rather than the $|E = E_j - \omega_s, q = 1, n = 0\rangle$ state. We need not to worry about the ratio between $\mu^-(E_j - \hbar\omega_p; j, q = 1, n)$ and $\mu^-(E_j - \hbar\omega_s; j, q = 2, n)$ because the intensities of pump and Stokes lasers can be scaled according to Eq. (27).

At $T_r = T_p = 1$ mK, we choose $\Delta_{t_s} = \Delta_{t_p} = 431$ ns and $\delta_E = 0.1$ mK. For the intermediate bound state we choose the 32nd bound state of the excited state complex, ^{6}Li^{6}Li^{7}Li in the collinear geometry. By using two lasers with intensities $I_p = 2.45$ GW/cm^2 and $I_s = 1$ MW/cm^2, we obtain a population transfer into the ^{6}Li^{6}Li+^{7}Li chemical arrangement with a probability of 98.44%. Figure 2 shows the time dependence of the probabilities of the reactant, product, and intermediate states. Wave packets centered at $|E = E_j - \omega_p, q = 1, n = 0\rangle$ and
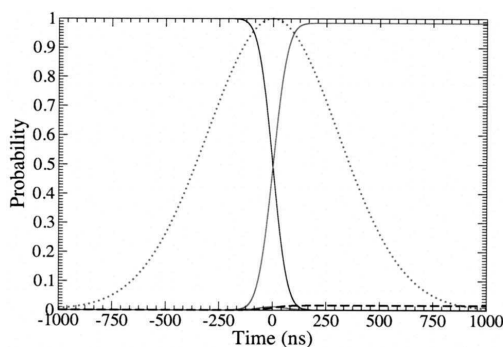
FIG. 2. Integrated population of the reactant wave packet centered at $|E=E_j-\omega_p,\ q=1,\ n=0\rangle$, product wave packet centered at $|E=E_j-\omega_s,\ q=2,\ n=0\rangle$ (solid lines), and reactant wave packet centered at $|E=E_j-\omega_s,\ q=q,\ n=0\rangle$ (dashed lines) vs time; laser profile (dotted line) vs time; $T_p=T_r=1$ mK, $\delta_E=0.1$ mK, $\Delta_{t_s}=\Delta_{t_p}=431$ ns, $t_p=t_s=0$ and $I_p=2.45$ GW/cm^2 and $I_s=1$ MW/cm^2.

$|E=E_j-\omega_s,\ q=1,\ n=0\rangle$ contribute to the reactant probabilities, which are both minimized. The total probability of the reactant wave packet centered at $|E=E_j-\omega_s,\ q=1,\ n=0\rangle$ is 1.55%, and the probability that the system will stay in the initial reactant wave packet centered at $|E=E_j-\omega_p,\ q=1,\ n=0\rangle$ is 0.01%.

One way to decrease the laser intensities without changing the reaction yield is to use the exact scaling relation in Eqs. (38) and (39). Setting $w=10$, we can control population transfer using laser intensities ten times smaller than that with $w=1$, as shown in Fig. 3. The large ratio of I_p/I_s, which requires a large I_p, results from the small dipole moment $\mu^-(E_j-\hbar\omega_p;j,q=1,n)$, and a possible solution for this problem is to perform a full three-dimensional (3D) calculation where more intermediate bound states can be found in the Frank–Condon region.

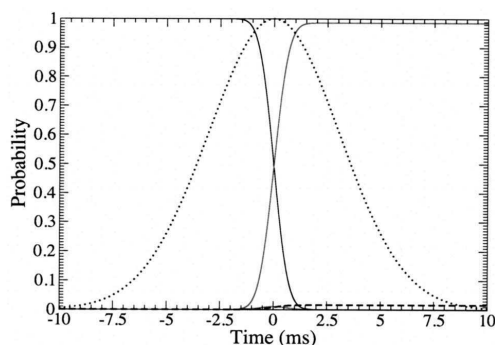When $t_p=t_s=0$, the two-pulse PTAP theory is very simi-

FIG. 3. Integrated population of the reactant wave packet centered at $|E=E_j-\omega_p,\ q=1,\ n=0\rangle$, product wave packet centered at $|E=E_j-\omega_s,\ q=2,\ n=0\rangle$ (solid lines), and reactant wavepacket centered at $|E=E_j-\omega_s,\ q=q,\ n=0\rangle$ (dashed lines) vs time; laser profile (dotted line) vs time; $T_p=T_r=1$ mK, $\delta_E=0.01$ mK, $\Delta_{t_s}=\Delta_{t_p}=4.31$ μs, $t_p=t_s=0$ and $I_p=245$ MW/cm^2 and $I_s=1$ MW/cm^2.

lar to the laser catalysis theory, which use only one pulsed laser. For population transfer, the bimolecular system absorbs a photon from the pump laser and, simultaneously, the Stoke laser stimulates a photon emission while minimizing the population of the intermediate state; in laser catalysis, the system absorbs a photon and simultaneously emits the same photon into the field. The reaction yield of PTAP monotonically increases with increasing laser intensity, as shown in Fig. 4, which is very similar to Fig. 9 of Vardi and Shapiro's laser catalysis paper.[2]

B. Intuitive sequence

When $t_p < t_s$, the pump pulse proceeds the Stokes pulse, and the maximum reaction yield requires the pulses to overlap appreciably. Because the optimized reaction yield with an intuitive sequence is very close to the reaction yield obtained with a coincident sequence, we do not show the time-dependent probabilities of all possible states. However, the relationship between laser intensities and the reaction yield with the intuitive sequence with the ratio I_s/I_p fixed, as shown in Fig. 5, differs from that with the coincident sequence. The reaction yield has a clear maximum with respect
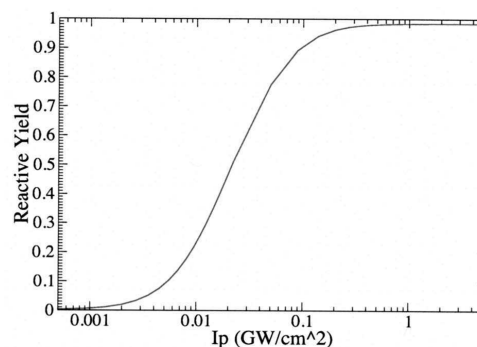

FIG. 4. Reaction yield vs laser intensity I_p. Here, $T=1$ mK, $\delta_E=0.1$ mK, $t_p=t_s=0$, $\Delta_{t_s}=\Delta_{t_p}=431$ ns, and I_s/I_p satisfies the relation in Eq. (27).
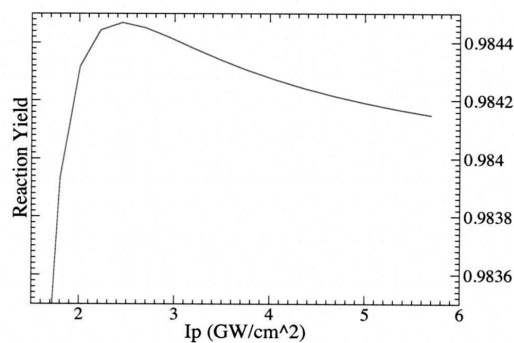

FIG. 5. Reaction yield vs laser intensity I_p. Here, $T=1$ mK, $\delta_E=0.1$ mK, $t_p=-t_s=12$ ns, $\Delta_{t_s}=\Delta_{t_p}=431$ ns, and I_s/I_p satisfies the relation in Eq. (27).

to laser intensities; merely increasing the pulse intensity does not improve the transfer yield. This feature is similar to the radiative recombination studies by Vardi *et al.*,[10] where the system has two bound states and one continuum state. In the PTAP, if one decreases $|t_p-t_s|$, thereby increasing the overlap of the pulses, then the maxima occurs at a higher intensity. In the $t_p-t_s=0$ limit, the location of the maximum approaches positive infinity, where a PTAP with the intuitive sequence becomes one with the coincident sequence and the reaction yield monotonically increases with increasing laser intensity.

In the PTAP, the optimum reaction yield occurs with the intuitive sequence or the coincident sequence; but in both conventional AP and PAP, the optimum reaction yield occurs with the counterintuitive sequence. In the conventional AP, the counterintuitive sequence enables a *dark state* to connect the initial and final states without populating the intermediate state. Both optimum reaction yields occur with the intuitive and counterintuitive sequence in PAP, but only the latter does not populate the intermediate state appreciably. It is not clear why the intuitive sequence gives a higher yield when both the initial and the final are in the continuum. This is currently under investigation.

IV. CONCLUSION

We have developed a nonperturbative theory of two-photon pulsed PTAP for triatomic reactions. This is the first theory that shows the connection between the laser catalysis and adiabatic passage. We have demonstrated control of population transfer of ultracold molecules with the freedom to choose the translational energies for the reactants and the products separately. We have presented results for the ^{6}Li $+ ^6$Li^{7}Li$(T_r=1$ mK$) \rightarrow ^6$Li^{6}Li$+ ^7$Li$(T_p=1$ mK$)$ process, and found that 98.4% of the population of the reactants is transferred to the products. We further found that, PTAP with the intuitive sequence at a low laser intensity, and with the coincident sequence at a high laser intensity give the optimum reaction yields. PTAP with a coincident sequence with two pulsed lasers acts like the laser catalysis scheme with a single laser pulse.

The system in this study is collinear. The 3D calculations are currently in progress. Moving to 3D greatly increases the number and density of states. The 3D calculation will include a plethora of rotational angular momentum states but the increase in the number of states on the ground electronic surface is not overwhelming at ultracold temperatures. The increase in the number and the density of states on the excited electronic potential surface is not as problematic because the narrow-band laser pulse is very selective. When the laser detuning is several magnitude larger than the energy bandwidth of the lasers, one can totally suppress the reaction process. The calculations presented here are model calculations designed to describe the physical process and the ability of PTAP to control the process at cold and ultracold temperatures.

[1] A. Vardi and M. Shapiro, Phys. Rev. A **58**, 1352 (1998).
[2] A. Vardi and M. Shapiro, J. Chem. Phys. **111**, 7713 (1999).
[3] I. Thanopulos and M. Shapiro, J. Chem. Phys. **117**, 8404 (2002).
[4] A. G. Truscott, K. E. Strecker, W. I. McAlexander, G. B. Partridge, and R. G. Hulet, Science **291**, 198 (2001).
[5] F. Schreck, G. Ferrari, K. L. Corwin, J. Cubizolles, L. Khaykovich, M.-O. Mewes, and C. Salomon, Phys. Rev. A **64**, 011402 (2001).
[6] L. Khaykovich, F. Schreck, J. Cubizolles, T. Bourdel, K. L. Corwin, G. Ferrari, and C. Salomon, Physica B **329**, 13 (2003).
[7] M. T. Cvitaš, P. Soldán, J. M. Hutson, P. Honvault, and J.-M. Launay, J. Chem. Phys. **127**, 074302 (2007).
[8] D. Grischkowski, M. M. T. Loy, and P. F. Liao, Phys. Rev. A **12**, 2514 (1975).
[9] J. Oreg, F. T. Hioe, and J. H. Eberly, Phys. Rev. A **29**, 690 (1984).
[10] A. Vardi, D. Abrashkevich, E. Frishman, and M. Shapiro, J. Chem. Phys. **107**, 6166 (1997).
[11] P. Kral, I. Thanopulos, and M. Shapiro, Rev. Mod. Phys. **79**, 53 (2007).
[12] M. Shapiro, J. Chem. Phys. **101**, 3884 (1994).
[13] E. Frishman and M. Shapiro, Phys. Rev. A **54**, 3310 (1996).
[14] A. Vardi and M. Shapiro, J. Chem. Phys. **104**, 5490 (1996).
[15] A. Vardi, D. Abrashkevich, E. Frishman, and M. Shapiro, J. Chem. Phys. **107**, 6166 (1997).
[16] M. Shapiro, J. Chem. Phys. **56**, 2582 (1972).
[17] M. Shapiro and R. Bersohn, Annu. Rev. Phys. Chem. **33**, 409 (1982).
[18] A. G. Abrashkevich and M. Shapiro, Phys. Rev. A **50**, 1205 (1994).

Appendix C

Formation ultracold heteronuclear molecules

PHYSICAL REVIEW LETTERS

Laser-Catalyzed Production of Ultracold Molecules:
The ^{6}Li + ^{6}Li^{7}Li $\overset{\hbar\omega}{\rightarrow}$ ^{6}Li − ^{6}Li + ^{7}Li Reaction

Xuan Li* and Gregory A. Parker

Homer L. Dodge Department of Physics and Astronomy, University of Oklahoma, USA

Paul Brumer

Chemical Physics Theory Group, Department of Chemistry, University of Toronto, Canada

Ioannis Thanopulos[1] and Moshe Shapiro[1,2]

[1]*Department of Chemistry, The University of British Columbia, Vancouver, Canada*
[2]*Department of Chemical Physics, The Weizmann Institute, Rehovot, Israel*
(Received 15 February 2008; published 25 July 2008)

We show that by using laser catalysis, we can employ translationally cold ($T_r \approx 1.75$ K) collisions to produce *ultracold* (0.01 mK $< T_p <$ 1 mK) (homonuclear) molecules. We illustrate this approach by studying the laser catalysis of the ^{6}Li + ^{6}Li^{7}Li $\overset{\hbar\omega}{\rightarrow}$ (^{6}Li^{6}Li^{7}Li)*($1^4A''$) $\overset{\hbar\omega}{\rightarrow}$ ^{6}Li^{6}Li + ^{7}Li reaction in the collinear approximation. Ultracold ^{6}Li^{6}Li product molecules are shown to be produced at an extraordinary yield of up to 99.97%, using moderate laser intensities of $I = 100$ kW/cm^2 − 10 MW/cm^2.

The existence of Bose-Einstein Condensates (BEC) of various atoms [1] and the possibility of the production of their molecular analogues [2–7] has spurred great interest in reactions between ultracold, bosonic, or fermionic (spin-aligned), molecules. For the lightest alkali, Li, isotopic mixtures of the fermionic ^{6}Li and the bosonic ^{7}Li are of great interest because they lead to the creation of either heteronuclear or homonuclear diatomic molecules [3,7–11].

In this Letter, we show that the involvement of pulsed lasers of moderate intensities in the reactions between *cold* reactants can lead to the production of *ultracold* diatomic molecules. We propose achieving this goal via the "laser catalysis" scenario [12–16], according to which, a laser assists a chemical reaction in a process involving no net absorption of photons. According to this scenario, the laser assists the $A + BC \rightarrow AB + C$ reaction by first forcing a (virtual) transition of the $A + BC$ reactants to the $(ABC)^*$ excited state complex (ESC). The ESC then undergoes a stimulated emission process to the $AB + C$ ground state products, releasing a photon identical to the photon just absorbed. Thus, no net photons are absorbed, justifying the name "laser catalysis." When the process is done coherently and the intensity of the laser is high enough, the prediction is that the system would transit smoothly from reactants to products, with the ESC "stepping stone" remaining unpopulated even in a transient way [12], thus rendering the ESC an authentic "virtual state."

As an illustration of this concept, we consider in detail the $A = {}^6$Li(^2S), $B = {}^6$Li(^2S), and $C = {}^6$Li(^2S) triatomic system. The diatomic molecules $AB = {}^6$Li$_2(3\Sigma_u^+)$ and $BC = {}^7$Li^{6}Li($3\Sigma^+$) are taken to be in their lowest spin-aligned electronic states. The triatomic states are the $1^4A'$ states for the reactants and products, and the $1^4A''$ states for

the ESC $(ABC)^*$. The zero energy is chosen to be at the three-body break up limit ($^2S + {}^2S + {}^2S$). There is no natural barrier in the reaction path between chemical arrangements of the quartet ^{6}Li^{6}Li^{7}Li system. We note, however, that the lowest vibrational energy of the triplet ^{6}Li^{7}Li state is calculated to be $E(q = 1, v = 0) = -300.51194$ cm^{-1}, while the lowest vibrational energy of the triplet ^{6}Li^{6}Li state is calculated to be slightly higher, at $E(q = 2, v = 0) = -299.29412$ cm^{-1}. Figure 1 shows the schematic energy levels of the current ^{6}Li^{6}Li^{7}Li in a laser catalysis scenario.

We thus envision a collinear collision between counter-propagating ^{6}Li and ^{6}Li^{7}Li beams, having zero center of mass velocity, each prepared with translational tempera-

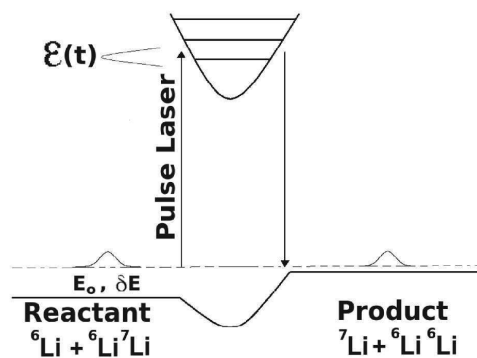
FIG. 1. Schematic energy levels of ^{6}Li^{6}Li^{7}Li system in the laser catalysis scheme.

134

tures of $T_r \approx 1.75$ K. By tuning the laser center frequency to be in exact resonance with a transition to one of the bound states of the ESC, we can make use of the energetic difference between the reactant and product diatoms to produce the ^{6}Li^{6}Li at *ultracold* temperatures. These temperatures range between 0.01 mK $< T_p <$ 1 mK, depending on the bandwidth of the laser used. The intervention of the laser is necessary because at translational temperatures of 1.75 K, the nonradiative reaction probability is negligible (< 1%).

We proceed now to outline the theoretical basis of our calculations. The total matter + radiation Hamiltonian is given in the dipole approximation as $H_{\text{tot}} = H - \vec{\mu} \cdot \vec{\varepsilon}(t)$, where H is the material Hamiltonian and $\vec{\varepsilon}(t) = \hat{\varepsilon}\varepsilon(t)$, with $\hat{\varepsilon}$ being the laser's polarization direction and $\varepsilon(t)$, its electric field strength. We expand the wave function, $\Psi(t)$, which solves the time-dependent Schrödinger equation, $i\hbar\partial\Psi/\partial t = H_{\text{tot}}\Psi$, in a complete basis composed of $|E_j\rangle$, the bound ESC, and $|E, q, n^-\rangle$, the ground-electronic or nuclear-continuum, eigenstates of H,

$$(E_j - H)|E_j\rangle = (E - i\epsilon - H)|E, q, n^-\rangle = 0. \quad q = 1, 2. \quad (1)$$

In the above, q denotes the asymptotic chemical arrangements and n, the internal quantum numbers associated with them, in the $t \to \infty$ limit. For narrow laser bandwidths it is usually sufficient to consider a single excited $|E_j\rangle$ bound state since in that case, the effect of other bound states is negligible [14,16]. Thus, the laser pulse creates a superposition of ground continuum states and one excited bound state of the form

$$|\Psi(t)\rangle = \sum_{q,n} \int dE b_{E,q,n}^-(t) |E, q, n^-\rangle \exp(-iEt/\hbar)$$
$$+ b_j(t)|E_j\rangle \exp(-iE_j t/\hbar). \quad (2)$$

We assume that initially there is no population in the ESC bound states, i.e., that $b_j(t = -\infty) = 0$. The system that starts in the ^{6}Li $+ ^6$Li^{7}Li reactants ($q_s = 1$) channel at the ground vibrational state ($n_s = 0$) is composed of a translational wave packet given as $\int dE b_{E,q_s,n_s}^+ |E, q_s, n_s^+\rangle \exp(-iEt/\hbar)$ whose energetic dependence is determined by b_{E,q_s,n_s}^+. Using the connection between the $|E, q, n^-\rangle$ and the $|E, q_s, n_s^+\rangle$ states, we have that

$$b_{E,q,n}^-(t = -\infty) = S_{q,n;q_s,n_s}(E) b_{E,q_s,n_s}^+,$$

where

$$S_{q,n;q_s,n_s}(E) \equiv \langle E', q, n^- | E, q_s, n_s^+\rangle \delta(E - E')$$

is the nonradiative scattering matrix element.

Substituting Eq. (2) into the time-dependent Schrödinger equation, and using the rotating wave approximation (RWA) [17], we obtain a set of integro-differential equations for the expansion coefficients, $b_j(t)$ and $b_{E,q,n}^-(t)$,

$$\dot{b}_j = \frac{i\varepsilon(t)}{\hbar} \mu_j^s(t) + \sum_{q,n} \int dE b_{E,q,n}^-(t) \mu^-(E; j, q, n)$$
$$\times e^{-i\omega_{E,j}t},$$

$$b_{E,q,n}^-(t) = b_{E,q,n}^-(-\infty) + \frac{i}{\hbar} \int_{-\infty}^t dt' b_j(t') \varepsilon^*(t') \langle E, q, n^- | \vec{\mu}$$
$$\cdot \hat{\varepsilon} |E_j\rangle e^{i\omega_{E,j}t'}, \quad (3)$$

where $\mu_j^s(t)$ is the "source" term

$$\mu_j^s(t) \equiv \sum_{q,n} \int dE b_{E,q,n}^-(-\infty)\langle E_j|\vec{\mu} \cdot \hat{\varepsilon}|E, q, n^-\rangle e^{-i\omega_{E,j}t}. \quad (4)$$

Assuming the Markov-like "slowly varying continuum approximation" (SVCA) [4,18], which can be fully justified for this case [12], we obtain after some manipulations a simple differential equation for b_j,

$$\frac{d}{dt} b_j(t) = \frac{i\varepsilon(t)}{\hbar} \mu_j^s(t) - \frac{\pi}{\hbar} |\langle E_j|\vec{\mu} \cdot \hat{\varepsilon}|E_o, q, n^-\rangle \varepsilon(t)|^2 b_j(t) \quad (5)$$

where E_o is the energy center of the initial reactant wave packet.

The solution of Eq. (5) and its substitution into Eq. (3) yields the time-dependent probabilities to observe the intermediate state, the reactants, and the products. One can vary the experimentally controllable function $\varepsilon(t)$ and the initial wave packet, $\Psi(t = -\infty)$, to optimize the reactive scattering process, using, as the case may be, the constructive or destructive interferences between the nonradiative scattering route and the radiatively assisted route.

Computational results.— We have chosen the light pulse that induces transitions between the intermediate states and the reactant/product states to have a Gaussian envelope function,

$$\varepsilon(t) = 2R_e \varepsilon_0 \exp(-t^2/\Delta_t^2) \exp(-i\omega_0 t), \quad (6)$$

where ε_0 is the field strength, Δ_t (often $= 431$ ns) is the temporal pulse width, and ω_0 is the carrier frequency chosen to be in resonance with the $|E_{j=21}\rangle$ state. We have also chosen the initial reactant wave packet to have a Gaussian shape,

$$b_{E,q_s,n_s}^+ = (\delta_E^2 \pi)^{-1/4} \exp[-(E - E_o)^2/(2\delta_E^2)], \quad (7)$$

where δ_E is the energy bandwidth, determined by the initial temperature, and E_o is the center of the initial reactant wave packet. The energy-dependent dipole coupling terms, $\langle E_j|\vec{\mu} \cdot \hat{\varepsilon}|E, q, n^-\rangle$, are then calculated using the reactive version of the Artificial Channel Method [19].

In order to achieve the desired ultracold product temperature, we choose the detuning parameter defined as $\Delta \equiv \omega_0 - E_j + E_o$ to be equal to 0. In this way, a narrow (e.g., $\Delta_t = 431$ ns $- 43.1$ μs) transform-limited laser pulse

135

carves out of the $T_r = 1.75$ K initial reactant distribution a narrow energetic component whose width is ~ 0.01 mK $-$ 1 mK and transforms it into products of roughly ~ 0.01 mK $-$ 1 mK. Therefore, the molecular reactants, ^{6}Li^{7}Li, can be prepared with a Maxwell-Boltzmann distribution at $T_r \approx 1.75$ K. With the typical experimental error in preparing the translational energies of the initial atomic species, the narrow energy bandwidth (δ_E) of the atomic species ^{6}Li and a narrow laser pulse will filter out the ultracold portion of the initial molecular beam of ^{6}Li^{7}Li reacting with ^{6}Li to form an ultracold cloud of ^{6}Li^{6}Li and ^{7}Li. Depending on the experimental error in beam preparation, the product cloud will then move uniformly in one direction with a known center of mass (c.m.) velocity which will be at least three to 4 times slower than the reactants and thus can be removed by a molecular optical lattice.

Figure 2 shows the time dependence of the probabilities in each state using a laser with an intensity of $I = 13.7$ MW/cm^2 with a $\Delta_t = 431$ ns. The reaction yield of the ultracold ($T_p = 1$ mK) product is shown to be 99.3% when the nonradiative reaction probability at this temperature is negligible ($<1\%$). The probability of the intermediate state $|E_{j=27}\rangle$ (dashed line in Fig. 2) remains very small compared to that of the reactant or product so that spontaneous emission is essentially nonexistent.

To illustrate the effect of the laser intensity, Fig. 3 shows the reaction yield as a function of the laser intensity with other parameters being fixed as they are in Fig. 2. Before reaching saturation at $I \sim 2$ MW/cm^2, the reaction yield increases monotonically with increasing laser intensity. However, in order to avoid spontaneous emission, losses from the population of the intermediate bound state necessitate a much higher intensity of $I \geq 10$ MW/cm^2. The intense laser pulse couples the material state with the field state to form two dress states that the population follows

adiabatically from the reactants to the products on the ground dress state without populating the intermediate state significantly [12].

Total suppression of the reaction scattering process can also be achieved. For instance, if we use a detuning of $\Delta = 3 \times 10^{-3}$ cm^{-1} with the other parameters assuming the values of Fig. 2, total suppression, due to destructive interference with the nonradiative reactive process, results. The effect (not shown in detail here) is more significant in the cold regime ($T_p = 10$–100 K) where the nonradiative tunneling probability is non-negligible [16].

We also performed calculations for radiatively assisted reactions yielding other product temperatures, $T_p = 0.1$ and 0.01 mK. Here, we define a scaling variable, s, to describe the change of product temperatures as $T_p \rightarrow T_p/s$. And thus, for $T_p = 1$, 0.1, and 0.01 mK, we choose the following scaling relation for the experimental parameters

$$\Delta \rightarrow \Delta/s, \qquad \Delta_T \rightarrow \Delta_T \times s \qquad (8)$$

and a laser intensity, I, large enough to saturate the reaction yield. These experimental parameters at $T_p = 0.1$, 0.01 mK with such scaling relation are suggested values to make sure the SVCA is still valid when the dipole moments vary faster for lower temperatures than they do for $T_p = 1$ mK. Though the SVCA is not necessary for the entire scheme to work, it requires more computations when the SVCA is not valid. The intermediate bound states are $E_{j=37}$ for $T_p = 0.1$ mK and $E_{j=32}$ for $T_p = 0.01$ mK to maximize the reaction yield.

For $T_p = 0.1$ mK, Δ_t and Δ are related to those in the $T_p = 1$ mK case by a scaling relation ($s = 10$) in Eq. (8), and the carrier frequency, ω_0, is changed to have a temperature of $T_p = 0.1$ mK. With $I = 1.37$ MW/cm^2, the reaction yield is saturated at 99.97%. For $T_p = 0.01$ mK, Δ_t and Δ are related to those in the $T_p = 1$ mK case by a
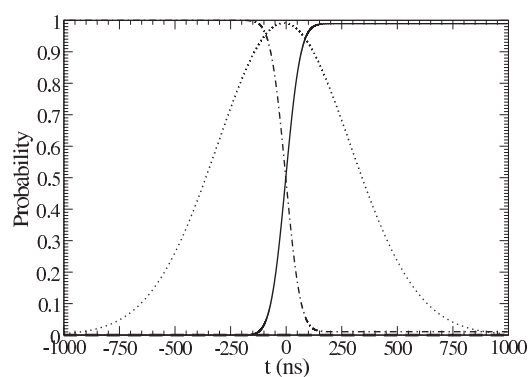
FIG. 2. Population of the reactant (dashed-dot line), product (solid line), and intermediate (dashed line of near zero value) states, and laser profile (dotted line) vs time; $T_p = 1$ mK.
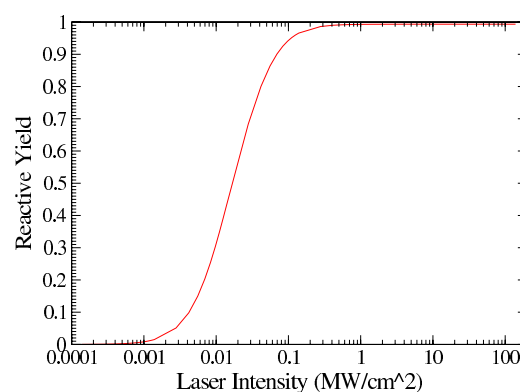
FIG. 3 (color online). Reaction yield vs laser intensity; $T_p = 1$ mK.

scaling relation ($s = 100$) in Eq. (8), the laser intensity is $I = 137$ kW/cm^2, and the reaction yield is 99.2%. For brevity, we do not show the plot of the $T_p = 0.1$ mK and $T_p = 0.01$ mK cases which is almost identical to Fig. 2 except for a scaling factor in Eq. (8).

The trap loss process in the above simulations is not appreciable. Since the product diatomic states are in the ground vibrational level and they correspond to nonrotational motion ($n = 0$), the inelastic collision in the reaction channel is zero. Though the reaction channel ^{7}Li + ^{6}Li^{6}Li is exoenergetic, the reactive scattering probability of the reaction channel is calculated to be small ($\approx 1\%$) at $T_p \sim 1$ mK. This does not conflict with the previous scattering calculations [11,20] on this system because Cvitaš *et al.* focused on the rotationally excited ^{7}Li + ^{6}Li^{6}Li ($v = 0$, $n = 1$) state. The production rate of the ultracold ^{6}Li^{6}Li diatoms, for the $T_p = 1$ mK case, is estimated to be 4×10^5/s. This estimate is based on the temporal width of the pulse, the percentage of the carved portion of the broadly distributed initial molecular beam, and a typical molecular beam density of 10^{12} cm^{-3}.

The electronic potential energy surface (PES) used in this calculation is based on a full configuration interaction *ab initio* computation. Though a better PES with inclusion of future experimental spectra can be constructed, we see no reason why this should alter the qualitative features of this scheme. This is because laser catalysis only requires that the intermediate state is properly chosen so that the population transfer from the intermediate state to the reactants and the products are balanced [16]. Thus, one can tune the laser intensity and the laser detuning, respectively, to compensate the quantitative difference in Franck-Condon overlap and the transition energies. The same argument applies when one wishes to move to the three-dimension (3D) case. This simulation uses a collinear approximation which specifies all the rotational motions are absent, and in a 3D calculation only an additional ^{6}Li + ^{6}Li^{7}Li($v = 0, n = 1$) level would be opened on the ground-electronic PES. As long as the intermediate state is properly chosen to have a small Franck-Condon overlap with this additional state, the final reaction yield would remain optimum. One needs to perform a careful scattering calculation to make sure the reverse reactive scattering process is suppressed at the desired product temperature.

In summary, we have pointed out the possibility of producing mK ^{6}Li^{6}Li molecules, which according to our calculation may be performed at a yield as high as 99.97%, as a result of a laser-catalyzed reaction between counterpropagating 1.75 K cold ^{6}Li and ^{6}Li^{7}Li beams. This scheme is not restricted to the production of homonuclear molecules, and we can also apply this scenario to hetero-nuclear molecules which is of interest for applications like quantum computations.

*li@nhn.ou.edu

[1] M. Grether, M. de Llano, and G. A. Baker, Jr., Phys. Rev. Lett. **99**, 200406 (2007), and references therein.
[2] J. Doyle, B. Friedrich, R. V. Krems, F. Masnou-Seeuws, Eur. Phys. J. D **31**, 149 (2004), and references therein.
[3] A. Micheli, G. K. Brennen, P. Zoller, Nature Phys. **2**, 341 (2006).
[4] A. Vardi, D. Abrashkevich, E. Frishman, and M. Shapiro, J. Chem. Phys. **107**, 6166 (1997).
[5] R. Dumke, J. D. Weinstein, M. Johanning, K. M. Jones, P. D. Lett, Phys. Rev. A **72**, 041801(R) (2005).
[6] K. Winkler, G. Thalhammer, M. Theis, H. Ritsch, R. Grimm, and J. H. Denschlag, Phys. Rev. Lett. **95**, 063202 (2005).
[7] S. Kotochigova, E. Tiesinga, P. S. Julienne, Eur. Phys. J. D **31**, 189 (2004).
[8] A. G. Truscott, K. E. Strecker, W. I. McAlexander, G. B. Partridge, and R. G. Hulet, Science **291**, 2570 (2001).
[9] F. Schreck, G. Ferrari, K. L. Corwin, J. Cubizolles, L. Khaykovich, M. -O. Mewes, and C. Salomon, Phys. Rev. A **64**, 011402(R) (2001).
[10] L. Khaykovich, F. Schreck, J. Cubizolles, T. Bourdel, K. L. Corwin, G. Ferrari, and C. Salomon, Physica B (Amsterdam) **329**, 13 (2003).
[11] M. T. Cvitaš, P. Soldán, J. M. Hutson, P. Honvault, and J.-M. Launay, J. Chem. Phys. **127**, 074302 (2007).
[12] A. Vardi and M. Shapiro, Phys. Rev. A **58**, 1352 (1998).
[13] A. Vardi and M. Shapiro, J. Chem. Phys. **111**, 7713 (1999).
[14] I. Thanopulos and M. Shapiro, J. Chem. Phys. **117**, 8404 (2002).
[15] I. Thanopulos and M. Shapiro (to be published).
[16] X. Li, G. A. Parker, P. Brumer, I. Thanopulos, and M. Shapiro, J. Chem. Phys. **128**, 124314 (2008).
[17] *Optical Resonance and Two-level Atoms*, edited by L. Allen and J. H. Eberly (Wiely, New York, 1975).
[18] M. Shapiro, J. Chem. Phys. **101**, 3844 (1994).
[19] A. G. Abrashkevich and M. Shapiro, Phys. Rev. A **50**, 1205 (1994).
[20] M. T. Cvitaš, P. Soldán, J. M. Hutson, P. Honvault, and J.-M. Launay, Phys. Rev. Lett. **94**, 200402 (2005).

Appendix D

Formation of ultracold heteronuclear molecules

Laser-catalyzed production of ultracold heteronuclear molecules:
The ^{6}Li + ^{7}Li^{7}Li $\xrightarrow{\hbar\omega}$ ^{6}Li^{7}Li+ ^{7}Li reaction.
by X. Li, G. A. Parker, P. Brumer, I. Thanopulos I and M. Shapiro
to be submitted to Chem. Phys. Lett.

Quantum control of molecular dynamics by lasers has been applied to a wide variety of processes, and one of the most studied scenarios which requires a moderate laser intensity of MW/cm^2 is the "laser catalysis" (LC) scenario (60; 61; 88). In the laser catalysis scenario, a pulsed laser is used to alter a chemical reaction, but returns to its initial photon state with no net photons absorbed in the process: $A + BC \xleftrightarrow{\hbar\omega_0} ABC^*(v) \xleftrightarrow{\hbar\omega_0} AB + C$, with $ABC^*(v)$ denoting an intermediate, electronically-excited, complex state (ESC) of ABC in the v-th vibrational state. With the recent discovery of Bose-Einstein condensation in ultracold hydrogen (67), lithium (68), sodium (69), rubidium (70), cesium (71) and chromium (173), quantum control of the spin-aligned systems is of great interest. This is so because spin-aligned states have relatively large magnetic moments, making them easier to capture in magnetic traps. With the laser catalysis theory one may consider the reaction between mixed cold or ultracold bosons and fermions which leads to a great variety of triatomic interactions. For example, isotopic mixtures of ^{6}Li (fermion) and ^{7}Li (boson) are of great interest because one can create either heteronuclear or homonuclear ultracold diatoms (72; 73; 74; 32). In this Letter we consider the theory of laser catalysis to control the reactive scattering process of this mixture on two spin-aligned electronic potential energy surfaces to either enhance or suppress the reation of forming the ultracold dimer, ^{6}Li^{7}Li.

We consider quantum control of the reactive scattering process where the atoms are A=^{6}Li(^2S), B=^{7}Li(^2S) and C=^{7}Li(^2S) in the ultracold regime. The diatomic molecules AB=^{6}Li^{7}Li($^3\Sigma^+$) and BC=^{7}Li$_2$($^3\Sigma_u^+$) are taken to be in their lowest spin-aligned electronic states. The triatomic states are the $1^4A'$ states for the reactants and products, and the $1^4A''$ states for the ESC (A-B-C)*. The zero energy is chosen to be at the three-body break up limit ($^2S +^2 S +^2 S$). There

Intermediate Complex (^{6}Li$_i^7$Li$_i^7$Li$_i$)*
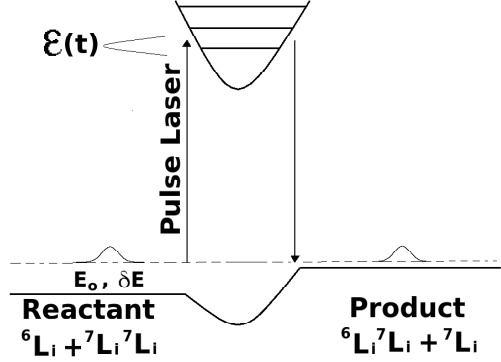
Figure D.1: Schematic energy levels of ^{6}Li^{7}Li^{7}Li system in the laser catalysis scenario

is no natural barrier in the reaction path between chemical arrangements of the quartet ^{6}Li^{7}Li^{7}Li system. However, the lowest vibrational energy of the triplet ^{7}Li^{7}Li state is calculated to be $E(q=1, v=0) = -1.37501101 \times 10^{-3}$ Hartree, while the lowest vibrational energy of the triplet ^{6}Li^{7}Li state is calculated to be $E(q=2, v=0) = -1.36923315 \times 10^{-3}$ Hartree. Therefore, the initial reactant ^{6}Li$+^7$Li^{7}Li is prepared at a cold temperature of $T_r \approx 1.8$ K, then is subjected to a moderate laser field ($I = 1 \sim 100$ MW/cm^2) and transferred to the product arrangement ^{6}Li$+^7$Li^{7}Li with an ultracold temperature of 0.01 mK $\leq T_p \leq 1$ mK. Here, T_r and T_p denote the temperatures in the reactant arrangement and the product arrangement respectively, and thus defined as $T_r = [E - E(q=1, v=0)]/K_B$ and $T_r = [E - E(q=2, v=0)]/K_B$ where K_B is the Boltzmann constant. Fig. D.1 shows schematic energy levels of the current ^{6}Li^{7}Li^{7}Li in a laser catalysis scenario. At the ultracold temperature, T_p, the non-radiative tunneling probability is negligible ($< 1\%$) and thus a laser catalysis scenario is useful to achieve the optimum controllability.

The matter+radiation interaction is described by the Hamiltonian $H_{tot} = H - \vec{\mu} \cdot \vec{\varepsilon}(t)$ with the dipole approximation, where H is the material Hamiltonian and $\vec{\varepsilon}(t) = \hat{\varepsilon}\varepsilon(t)$, where $\hat{\varepsilon}$ is the polarization of the laser field and $\varepsilon(t)$ is its electric field strength. We expand the wave function, $\Psi(t)$, which solves the time dependent Schrödinger equation,

$$i\hbar\frac{\partial \Psi}{\partial t} = H_{tot}\Psi, \tag{D.1}$$

in a complete basis that is composed of the sets of bound, $|E_j\rangle$, and continuum, $|E, q, n^-\rangle$, eigenstates of H, defined as,

$$
\begin{aligned}
(E_j - H)|E_j\rangle &= 0 \\
(E - H)|E, q, n^-\rangle &= 0, \quad q = 1, 2.
\end{aligned}
\tag{D.2}
$$

E_j are the bound-state energies on the excited electronic potential energy surface (PES); E are the continuum energies on the ground electronic PES; and n are the $t \to \infty$ asymptotic internal quantum numbers associated with each arrangement channel q. In this study, we choose to use a single intermediate bound state because the effect from other bound states is negligible when the energy bandwidth of the pulse laser is narrow compared the energy separation between the discrete intermediate states (60; 61) for this ultracold case.

The laser pulse excites the system into a superposition of continuum states of the ground electronic PES and bound states of the excited electronic PES. The resulting wavepacket is

$$
\begin{aligned}
\Psi(t) \ &= \ \sum_{q,n} \int dE \, b^-_{E,q,n}(t) \, |E,q,n^-\rangle \exp(-iEt/\hbar) \\
&+ \ b_j(t) \, |E_j\rangle \exp(-iE_j t/\hbar)
\end{aligned}
\tag{D.3}
$$

where $q = 1, 2$ represent the reactant and product chemical arrangement channels respectively. We have assumed that the initial wavepacket starts in channel $q_s = 1$(reactant channel A+BC=^{6}Li+^{7}Li^{7}Li) with the following initial conditions:

$$
\begin{aligned}
b^-_{E,q,n}(-\infty) \ &= \ S_{q,n;q_s,n_s} b^+_{E,q_s,n_s}(-\infty) \\
b_j(-\infty) \ &= \ 0.
\end{aligned}
\tag{D.4}
$$

where $b^+_{E,q_s,n_s}(-\infty)$ is chosen so as to give the initial wavepacket the desired (Gaussian) shape in state n_s of the reactant arrangement q_s. Here, $S_{q,n;q_s,n_s}$ is the scattering matrix element between the $|E,q,n^-\rangle$ state and the $|E,q_s,n_s^+\rangle$ state.

Substituting the wavepacket in Eq. (D.3) into the time-dependent Schrödinger equation, Eq. (D.1), and using the rotating wave approximation (RWA) we then obtain an ordinary differential equation to solve for the expansion coefficients, $b_j(t)$ and $b^-_{E,q,n}(t)$. The solution of the coefficients $b_j(t)$ is subjected to the simplified ordinary differential equation:

$$
\begin{aligned}
\dot{b}_j(t) \ &= \ (i\varepsilon(t)/\hbar)\,\mu_i^s(t) \\
&- \ (\pi/\hbar)\left|\langle E_j|\vec{\mu}\cdot\hat{\varepsilon}|E_o,q,n^-\rangle\varepsilon(t)\right|^2 b_j(t)
\end{aligned}
\tag{D.5}
$$

where E_o is the center energy of the initial reactant wavepacket and $\mu_i^s(t)$ is the source term for the reactant channel $q_s = 1$

$$
\begin{aligned}
\mu_i^s(t) \ &\equiv \ \sum_{q,n} \int dE b^-_{E,q,n}(-\infty) \\
&\times \ \langle E_j|\vec{\mu}\cdot\hat{\varepsilon}|E,q,n^-\rangle . \exp(-i\omega_{E,i}t)
\end{aligned}
\tag{D.6}
$$

And, the solution of the coefficients $b_{E,q,n}^-(t)$ are subjected to the relation:

$$\begin{aligned}
b_{E,q,n}^-(t) &= b_{E,q,n}^-(-\infty) \\
&+ (i/\hbar) \int_{-\infty}^{t} dt' b_j(t') \varepsilon^*(t') \\
&\times \langle E, q, n^- | \vec{\mu} \cdot \hat{\varepsilon} | E_j \rangle \exp(i\omega_{E,j} t').
\end{aligned} \tag{D.7}$$

It should be noted that in deriving these solutions we have used SVCA (slowing varying continuum approximation) (174; 175; 176; 85) which assumes the molecular continua are unstructured. A detailed derivation subjected to reasonable approximations can be found in reference (60).

The solution of the expansion coefficients, $b_j(t)$ and $b_{E,q,n}^-(t)$, determines the wavepacket $\Psi(t)$ from which we can obtain the intermediate state, reactant and product probabilities at any time. To obtain the optinum controllability of the reactive scattering process, we consider differernt initial conditions, $\Psi(t = -\infty)$, and vary the electric field strength scalar $\varepsilon(t)$. We use constructive or destructive interferences between the non-radiative scattering route and the radiative route to achieve near-complete ($\geq 99\%$) population transfer or near-complete ($\leq 1\%$) reactive suppresion.

The light pulse is chosen as a Gaussian,

$$\varepsilon(t) = \varepsilon_o \exp(-t^2/\Delta_t^2) \exp(-i\omega_o t), \tag{D.8}$$

where ε_o is the field strength, Δ_t is the temporal pulse width, and ω_o is the carrier frequency of the laser pulse which induces the transition between the intermediate, reactant and product states. The initial reactant wavepacket is,

$$b_{E,q_s,n_s}^+(-\infty) = (\delta_E^2 \pi)^{-1/4} \exp\left[-(E - E_o)^2/\left(2\delta_E^2\right)\right], \tag{D.9}$$

where δ_E is the energy bandwidth and E_o is the center of the initial reactant wavepacket. The energy dependent dipole coupling terms, $\langle E_j | \vec{\mu} \cdot \hat{\varepsilon} | E, q, n^- \rangle$, are obtained using the artificial channel method (177; 178; 179).

Different ultracold temperatures are studied, and therefore, we define a scaling variable, s, to describe the change of product temperatures as $t_p \rightarrow t_p/s$. And thus, for $T_p = 1$ mK, 0.1 mK and 0.01 mK we choose the following scaling relation for the experimental parameters

$$\Delta \rightarrow \Delta/s, \qquad \delta_E \rightarrow \delta_E/s, \qquad \Delta_T \rightarrow \Delta_T \times s \tag{D.10}$$

and a laser intensity, I, large enough to saturate the reactive yield. It should be noted that this scaling relation is not the same scaling relation in reference (60), and these experimental parameters at $T_p = 0.1, 0.01$ mK are only changed to make sure the SVCA is still valid since the dipole moments varies faster for lower temperatures than that for $T_p = 1$ mK.

Figure D.2: Integrated population of the reactant, product (solid lines) and intermediate state (dashed lines) vs time; laser profile (dotted line) vs time; $T_p = 0.01$ mK

For the $T_p = 1$ mK case, the center of the initial reactant wavepacket is prepared to be $E_o = -1.3692300 \times 10^{-3}$ Hartree with an energy bandwidth of $\delta_E = 0.1$ mK. The cold reactant ($T_r = 1.825491$ K) is then under the influence of a strong laser field with a temporal width of $\Delta_t = 431$ ns and a detuning of $\Delta = 0$. The detuning parameter, Δ, is defined as $\Delta = \omega_o - (E_j - E_o)$, which in this case is optimized to be zero so that carrier frequency ω_o is on resonance with the 21st bound state to obtain the maximum reactive yield. Different intermediate bound states, E_j, were tested and we choose to use the 21st bound state because we obtain the best reactive yield results with it for $T_p = 1$ mK. Reactive yield is optimized to be 97.4% with a laser intensity of $I = 137$ MW/cm^2. Total suppression of the reactive scattering process can also be achieved, for instance, if we use a detuning of $\Delta = 4 \times 10^{-7}$ Hartree with the other parameters the same as in Fig. D.2. The total suppresion is more significant in the cold regime ($T_p = 1 \sim 100$ K) when the non-radiative reactive probability is not negligible and therefore we do not show plots here for brevity.

For the $T_p = 0.01$ mK case, shown in Fig. D.2, the reactive yield is optimized to be 99.8% with an intensity of $I = 1.37$ MW/cm^2. The experimental parameters are chosen according to the scaling relation in Eq. (D.10) and the 29th intermediate bound state is used. The probability of the intermediate state $|E_j >$ (dashed line in Fig. D.2) is very small compared to that of the reactant or product so that spontaneous emission is essentially nonexistent. To illustrate the effect of the laser intensity, Fig. D.3 shows the reactive yield as a function of the laser intensity with other parameters fixed at their optimized values as in Fig. D.2 at

142
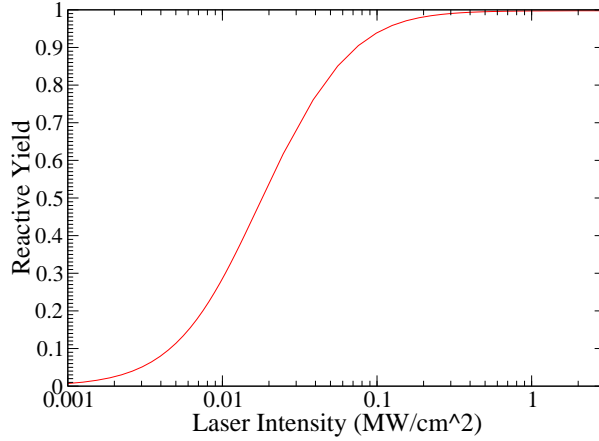
Figure D.3: Reactive yield vs laser intensity; $T_p = 0.01$ mK

$T_p = 0.01$ mK. Before reaching saturation at $I \sim 1$ MW/cm^2, the reactive yield increases monotonically with increasing laser intensity. However, in order to avoid the spontaneous emission losses from the population of the intermediate bound state we suggest the use of intensity $I \geq 2.5$ MW/cm^2.

Results for the $T_p = 0.1$ mK is shown Fig. D.4 with a decreased optimum reactive yield. With the scaled experimental parameters in Eq. (D.10), we use the 29th intermediate bound state and an optimized laser intensity of $I = 13.7 MW/cm^2$. The reactive yield is optimized to be 76.6%, though the total suppression is achieved with a detuning of $\Delta = 4 \times 10^{-8}$ at the same intensity. The reason for decreased control ability at $T_p = 0.1$ mK, compared to that at $T_p = 1$ mK and 0.01 mK, is due to the large difference between $\langle E_j | \vec{\mu} \cdot \hat{\varepsilon} | E, q = 1, n^- \rangle$ and $\langle E_j | \vec{\mu} \cdot \hat{\varepsilon} | E, q = 2, n^- \rangle$. With a specific intermediate state, e.g. the 29th bound state, the ratio of these two dipole moments changes as the ultracold temperature T_p varies, as shown in Fig. D.5, and this large ratio causes the inbalance between the population transfers into the reactant and into the product arrangements. As it is shown elsewhere (76) the optimized reactive yield decreases as the ratio deviates from unity. This phenomenon is analogous to Young's two slits experiment for which the highest fringe contrast is obtained when the slits widths are the same. In order to achieve the optimum controllability, we look for an intermediate bound state with the near-unity ratio of the two dipole couplings, however, the 29th bound state is the best candidate for the intermediate state in the current system.

In summary, we have presented the possible quantum control of ultracold reactive scattering process in collinear ^{6}Li^{7}Li^{7}Li system using laser catalysis theory.
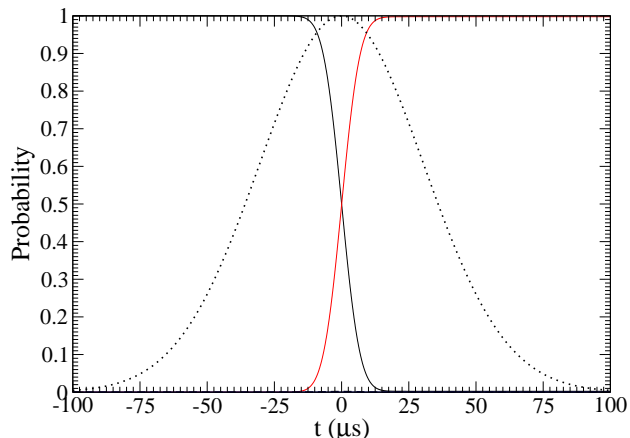
143
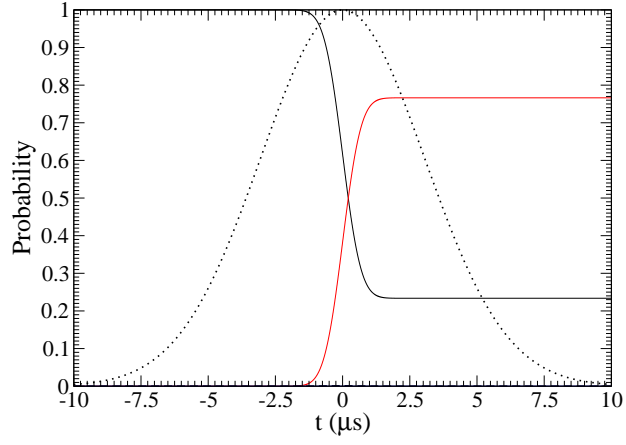
Figure D.4: Integrated population of the reactant, product (solid lines) and intermediate state (dashed lines) vs time; laser profile (dotted line) vs time; $T_p = 0.1$ mK
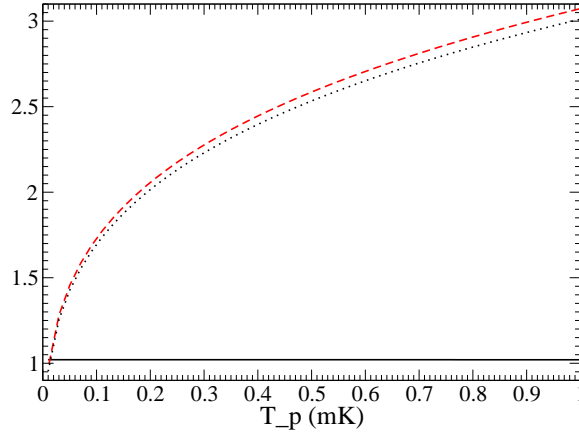
Figure D.5: Dipole moments $\langle E_j | \vec{\mu} \cdot \hat{\varepsilon} | E, q = 1, n^- \rangle$ (solid line) and $\langle E_j | \vec{\mu} \cdot \hat{\varepsilon} | E, q = 2, n^- \rangle$ (dashed line) vs temperature T_p; ratio (dotted line) vs T_p; $|E_j\rangle$ as the 29th bound state

Our results show a control ability of up to 99.8% reactive yield to form the ultra-cold dimer ^{6}Li^{7}Li and total suppresion of the reactive scattering process with a 0% yield.

Appendix E

Jacobi, Delves and APH coordinates

E.1   Jacobi coordinates

For a triatomic system we use A, B and C to label three atoms. We denote masses m_τ (τ = A,B,C) and use $\vec{x}_\tau$ as the column vectors of the atoms' coordinates relative to an fixed origin. Here, we use τ to denote each chemical arrangements. After separation of the center of mass motion, we define Jacobi coordinates for relative motion in this triatomic system as

$$\vec{R}_\tau = \vec{x}_\tau - \frac{m_{\tau+1}\vec{x}_{\tau+1} + m_{\tau+2}\vec{x}_{\tau+2}}{m_{\tau+1} + m_{\tau+2}}, \tag{E.1}$$

$$\vec{r}_\tau = \vec{x}_{\tau+2} - \vec{x}_{\tau+1}, \tag{E.2}$$

where $\tau, \tau+1$,and $\tau+2$ are any cyclic permutation of A, B and C. We define the corresponding mass-scaled Jacobi coordinates for arrangement τ as (180; 181)

$$\vec{S}_\tau = d_\tau \vec{R}_\tau, \quad \vec{s}_\tau = d_\tau^{-1}\vec{r}_\tau, \tag{E.3}$$

where d_τ are the dimensionles mass-scaling factors as

$$d_\tau = \left[\frac{m_\tau}{\mu}\left(1 - \frac{m_\tau}{M}\right)\right]. \tag{E.4}$$

Here, μ is the three-body reduced mass

$$\mu = \left[\frac{m_A m_B m_C}{M}\right], \tag{E.5}$$

and M is the total mass of the triatomic system

$$M = m_A + m_B + m_C. \tag{E.6}$$

E.2   Delves coordinates

We can express the well-known Delves coordinates (182) of arrangement τ in terms of the mass-scaled Jacobi coordinates

$$\rho = \sqrt{S_\tau^2 + s_\tau^2} \tag{E.7}$$

and

$$\theta_{D_\tau} = \tan^{-1}(s_\tau/S_\tau). \tag{E.8}$$

Here, ρ is referred as the hyperradius and it does not depend on arrangement channel τ. We define the Θ_τ as the angle between two Jacobi vectors, $\vec{S}_\tau$ and $\vec{s}_\tau$, for arrangement τ:

$$\Theta_\tau = \frac{\vec{S}_\tau \cdot \vec{s}_\tau}{S_\tau s_\tau}. \tag{E.9}$$

E.3   APH coordinates

The adiabatically adjusting, principal axes hyperspherical (APH) coordinates (108) can be related to the mass-scaled Jacobi coordinates as

$$\rho = \sqrt{S_\tau^2 + s_\tau^2}, \tag{E.10}$$

$$\tan\theta = \frac{\sqrt{(S_\tau^2 - s_\tau^2)^2 + (2\vec{S}_\tau \cdot \vec{s}_\tau)^2}}{2 S_\tau s_\tau \sin\Theta_\tau}, \tag{E.11}$$

$$\sin(2\chi_\tau) = \frac{2\vec{S}_\tau \cdot \vec{s}_\tau}{\sqrt{(S_\tau^2 - s_\tau^2)^2 + (2\vec{S}_\tau \cdot \vec{s}_\tau)^2}}, \tag{E.12}$$

and

$$\cos(2\chi_\tau) = \frac{(S_\tau^2 - s_\tau^2)}{\sqrt{(S_\tau^2 - s_\tau^2)^2 + (2\vec{S}_\tau \cdot \vec{s}_\tau)^2}}. \tag{E.13}$$

Here, the hyperradius ρ is defined the same as in the Delves coordinate; and θ and χ_τ angles describe the shape of the three atoms. $\theta = 0$ cooresponds to an oblate top triangular configuration; $\theta = \pi/2$ cooresponds to a collinear configuration.

The three Euler angles in the APH coordinates, α_Q, β_Q, and γ_Q, are defined to describe the rotation of a rigid body:

$$\begin{pmatrix} \vec{S}_\tau \\ \vec{s}_\tau \end{pmatrix} = \tilde{T}(\chi_\tau)\tilde{R}(\alpha_Q, \beta_Q, \gamma_Q) \begin{pmatrix} 0 \\ 0 \\ \frac{\rho}{\sqrt{2}}\sqrt{1 + \sin\theta} \\ \frac{\rho}{\sqrt{2}}\sqrt{1 - \sin\theta} \\ 0 \\ 0 \end{pmatrix}. \tag{E.14}$$

Here, $\tilde{T}(\chi_\tau) = T^{-1}(\chi_\tau)$ is a kinematic rotation matrix, and $\tilde{R}(\alpha_Q, \beta_Q, \gamma_Q) = R^{-1}(\alpha_Q, \beta_Q, \gamma_Q)$ is the spatial rotation matrix. We define the $T(\chi_\tau)$ matrix as

$$T(\chi_\tau) = \begin{pmatrix} \cos\chi_\tau\mathbf{I} & \sin\chi_\tau\mathbf{I} \\ -\sin\chi_\tau\mathbf{I} & \cos\chi_\tau\mathbf{I} \end{pmatrix}, \tag{E.15}$$

where $\mathbf{I}$ is a 3×3 identity matrix. And we define $R(\alpha_Q, \beta_Q, \gamma_Q)$ as

$$R(\alpha_Q, \beta_Q, \gamma_Q) = \begin{pmatrix} \mathbf{R} & \mathbf{0} \\ \mathbf{0} & \mathbf{R} \end{pmatrix} \tag{E.16}$$

where $\mathbf{0}$ is a 3×3 null matrix and R is a 3×3 matrix of Euler angles

$$\mathbf{R} = \begin{pmatrix} \cos\alpha\cos\beta\cos\gamma - \sin\alpha\sin\gamma & \sin\alpha\cos\beta\cos\gamma + \cos\alpha\sin\gamma & -\sin\beta\cos\gamma \\ \cos\alpha\cos\beta\sin\gamma - \sin\alpha\cos\gamma & -\sin\alpha\cos\beta\sin\gamma + \cos\alpha\cos\gamma & +\sin\beta\sin\gamma \\ \cos\alpha\sin\beta & \sin\alpha\sin\beta & \cos\beta \end{pmatrix}. \tag{E.17}$$

More details of the APH coordinates can be found in Ref.(108).

Appendix F

Potential Construction

Potential energy surfaces for the $1^4A'$, $2^4A'$ $1^4A''$ and $2^4A''$ States of Li$_3$
by X. Li, D. A. Brue and G. A. Parker
J. Chem. Phys. Volume **129**, Page 124305 (2008)

Potential energy surfaces for the 1 $^4A'$, 2 $^4A'$ 1 $^4A''$ and 2 $^4A''$ states of Li$_3$

Xuan Li,[a] Daniel A. Brue, and Gregory A. Parker
Homer L. Dodge Department of Physics and Astronomy, University of Oklahoma,
Norman, Oklahoma 73072, USA

Global potential energy surfaces for the 1 $^4A'$, 2 $^4A'$, 1 $^4A''$, and 2 $^4A''$ spin-aligned states of Li$_3$ are constructed as sums of a diatomics-in-molecules (DIM) term plus a three-body term. The DIM model, using a large basis set of 15 $^4A''$ and 22 $^4A'$ states, is used to obtain a "mixed-pairwise additive" contribution to the potential. A global fit of the three-body terms conserves the accuracy of the *ab initio* points of a full configuration-interaction calculation. The resulting fit accurately describes conical intersections for both the 1 $^4A'$ and 2 $^4A'$ surfaces with a root-mean-square (rms) deviation of 5.4×10^{-5} hartree in $D_{\infty h}$ geometries and 1.2×10^{-4} hartree in $C_{\infty v}$ geometries. The global fit appears to be quantitatively correct with a rms deviation of 1.8×10^{-4} hartree for 1 $^4A'$, 9.2×10^{-4} hartree for 2 $^4A'$, 2.5×10^{-4} hartree for 1 $^4A''$, and 5.1×10^{-4} hartree for 2 $^4A''$. A possible diabolic conical intersection, also called an accidental degeneracy, in C_{2v} geometries, indicating a seam of conical intersections in C_s geometries, is also found in *ab initio* calculations for A_2 states. As shown in this example, the DIM procedure can be optimized to describe the geometric phase and nonadiabatic effects in multisurface potentials. © *2008 American Institute of Physics.*
[DOI: 10.1063/1.2985857]

I. INTRODUCTION

Potential energy surfaces (PESs) play a fundamental role in understanding collisions and field-induced interactions between cold and ultracold atoms and molecules. Some of the simplest systems are alkali metal trimers, whose ground-state atoms have only one valence electron in an *s* orbital. Spin-aligned alkali-trimer systems have received considerable attention since the discovery of Bose–Einstein condensation in ultracold hydrogen,[1] lithium,[2] sodium,[3] rubidium,[4] and cesium.[5] For lithium, the lightest of the alkalies, understanding the lowest PESs is important for dynamics of elastic and inelastic collisions as well as field-induced interactions. Several global surfaces for low-lying 1 $^4A'$ have been reported[6,7] with a seam of conical intersections (CIs) between the $^4\Sigma$ and $^4\Pi$ surfaces in $C_{\infty v}$ geometries.[8–10] To the best of our knowledge, the present work is the first on all four low-lying global PESs, 1 $^4A'$, 2 $^4A'$, 1 $^4A''$, and 2 $^4A''$, of the spin-aligned lithium trimer.

Intuitively, the pairwise-additive two-body interactions should contribute more than the three-body interaction to the PES of spin-aligned trimers. However, the three-body contribution is not generally negligible for these alkali metal trimers. Theoretical and experimental work on sodium[11] has shown that the pairwise-additive potential (PAP) accounts for only 62% of the well depth 849.37 cm^{-1} of the Na$_3$ potential, and the diatomic bond distance at the true minimum of the full PES is 1.5 bohr smaller than the value predicted from the PAP. For Li$_3$, the PAP predicts only 25% of the well depth of the absolute minimum in D_{3h} geometry, and a bond distance nearly 2 bohr larger than the correct value.[6] What is

more, assignment of the contribution from diatomic potentials to the PAPs for excited PESs is complicated because diatomic potentials mix. Take the 2 $^4A''$ PES. A sum of three diatomic potentials is no longer accurate because the PAP can have contributions from $^3\Sigma_u^+$, $^3\Sigma_g^+$, $^3\Pi_u$, and $^3\Pi_g$ states. Moreover, the three-body term should die off in the asymptotic region, but a sum of three diatomic potentials does not give the correct dissociation limit unless the symmetry of the system is broken. A diatomics-in-molecules (DIM) model,[12–16] which can couple all the relevant diatomic potentials and give the correct dissociation limit, can thus represent the mixed-pairwise-additive terms. The DIM terms obtained by diagonalizing the electronic Hamiltonian represent the ground and first few excited PESs. To construct the three-body terms, we perform *ab initio* calculations for the 1 $^4A'$, 2 $^4A'$, 1 $^4A''$, and 2 $^4A''$ PESs using full configuration interaction for the three valence electrons with an augmented Gaussian basis and the effective core potential of Stevens *et al.*[17] for the other electrons. We then use a global-fit method of Aguado *et al.*[18] to fit the result of $V_{total} - V_{DIM}$ at the points where the *ab initio* calculations are performed to obtain the three-body terms. The DIM method is quantitatively correct in the CI regions (in $C_{\infty v}$ geometries). Therefore, the DIM method gives the electronic eigenvectors in these regions, and from these, the geometric phase and nonadiabatic effects can be computed.

We begin in Sec. II with a review of the DIM method and the global three-body-fit theory. In Sec. III, we present the basis set and the fitting procedure for each PES. A brief description of how to compute the nonadiabatic coupling terms is included. One possible seam of diabolic intersections in C_s geometries is also reported.

[a] Electronic mail: li@nhn.ou.edu.

II. THEORY

A. The DIM method

We begin with a brief review of the DIM method for triatomic molecules. Detailed explanations can be found in the works of Tully[13] and Steiner *et al.*[14] The DIM method computes adiabatic solutions of the electronic Hamiltonian in the nonrelativistic Born–Oppenheimer method. The nuclei of a triatomic system have nine degrees of freedom: three for the center-of-mass motion, three for the angular orientation of the body-fixed reference frame with respect to the space-fixed frame, and three for internal motions of the nuclei in the body-fixed frame. We ignore spin-orbit interactions and only consider Coulomb interactions. Our potential, obtained from eigenenergies of the electronic Hamiltonian, depends only on three internal coordinates, e.g., three diatomic distances. Thus, the electronic Hamiltonian defines the eigenvalue problem

$$\hat{h}(\vec{r};\vec{R})|\phi_t(\vec{r};\vec{R})\rangle = \mathcal{E}_t(\vec{R})|\phi_t(\vec{r};\vec{R})\rangle, \tag{1}$$

where $\hat{h}$ is the electronic Hamiltonian and $|\phi_t(\vec{r};\vec{R})\rangle$ is the tth eigenvector, and both of which depend parametrically on the three internal coordinates $\vec{R}$, and $\mathcal{E}_t(\vec{R})$ is the associated lth electronic energy. An arbitrary nuclear configuration has a C_s symmetry, and the electronic PESs are labeled by the irreducible representations A' (even under reflection of the electronic wave function) and A'' (odd under reflection of the electronic wave function). The electronic Hamiltonian operator for the triatomic system ABC can be partitioned as

$$\hat{h} = \hat{h}^{AB} + \hat{h}^{BC} + \hat{h}^{AC} - \hat{h}^A - \hat{h}^B - \hat{h}^C, \tag{2}$$

where $\hat{h}^{AB}$, $\hat{h}^{BC}$, and $\hat{h}^{AC}$ are diatomic Hamiltonians and $\hat{h}^A$, $\hat{h}^B$, and $\hat{h}^C$ are atomic Hamiltonians. Equation (2) is an *exact* expression,[12] and it is used as the fundamental principal of the DIM method.

The eigenvectors $|\phi_t\rangle$ can be expanded in a complete basis as $|\Phi_m\rangle$,

$$|\phi_t\rangle = \sum_m |\Phi_m\rangle\Gamma_{mt}, \tag{3}$$

where $\Gamma_{mt}(\vec{R})$ are expansion coefficients and the basis vectors $|\Phi_m\rangle$ are independent of $\vec{R}$. Substituting Eq. (3) into Eq. (1), we obtain the matrix equation

$$\mathbf{h}\Gamma = \mathbf{S}\Gamma\mathbf{E}, \tag{4}$$

where the matrix $\mathbf{E}$ is the diagonal eigenvalue matrix, the matrix $\mathbf{h}$ is defined by its elements as

$$h_{mm'} \equiv \langle\Phi_m|\hat{h}|\Phi_{m'}\rangle, \tag{5}$$

and the overlap matrix $\mathbf{S}$ is

$$S_{mm'} \equiv \langle\Phi_m|\Phi_{m'}\rangle. \tag{6}$$

Equation (4) depends only on the three internal nuclear coordinates and does not depend on the electronic coordinate $\vec{r}$.

Each $|\Phi_m\rangle$ is an antisymmetrized product of atomic basis vectors,

$$|\Phi_m\rangle = \mathcal{A}_n|A_i\rangle|B_j\rangle|C_k\rangle \equiv \mathcal{A}_3|\Phi_m^0\rangle, \tag{7}$$

where $\mathcal{A}_n$ is the n-electron antisymmetrizer, $|A_i\rangle$, $|B_j\rangle$, and $|C_k\rangle$ are atomic eigenvectors with quantum numbers i, j, and k, e.g., $i \equiv (E,l,m_l,S,m_s)$, and m denotes the composite quantum number (i,j,k). Using the fact that $\mathcal{A}_n$ commutes with $\hat{h}$, we can substitute Eq. (7) into Eq. (5) to get

$$h_{mm'} = \langle\Phi_m|\mathcal{A}_n\hat{h}|\Phi_{m'}^0\rangle. \tag{8}$$

The diatomic and atomic elements of the matrix are

$$h_{mm'}^{KL} = \langle\Phi_m|\mathcal{A}_n\hat{h}^{KL}|\Phi_{m'}^0\rangle \tag{9}$$

and

$$h_{mm'}^{K} = \langle\Phi_m|\mathcal{A}_n\hat{h}^{K}|\Phi_{m'}^0\rangle, \tag{10}$$

where K and L represent atomic indices A, B, and C. Inserting the identity operator

$$\hat{I} = \sum_{m''} |\Phi_{m''}^0\rangle\langle\Phi_{m''}^0| \tag{11}$$

into Eqs. (9) and (10), we obtain

$$\mathbf{h}^{KL} = \mathbf{S}\mathbf{h}'^{KL} \tag{12}$$

and

$$\mathbf{h}^{K} = \mathbf{S}\mathbf{h}'^{K}, \tag{13}$$

where $\mathbf{h}^{KL}$ and $\mathbf{h}^{K}$ are

$$h_{mm'}'^{KL} \equiv \langle\Phi_m^0|\hat{h}^{KL}|\Phi_{m'}^0\rangle \tag{14}$$

and

$$h_{mm'}'^{K} \equiv \langle\Phi_m^0|\hat{h}^{K}|\Phi_{m'}^0\rangle. \tag{15}$$

The atomic Hamiltonian matrix $\mathbf{h}'^{K}$ can be easily evaluated because the basis $|\Phi_{m'}^0\rangle$ is a direct product of atomic states that are eigenvectors of $\hat{h}^K$. Therefore $h_{mm'}'^{K}$ can be expressed as

$$h_{mm'}'^{K} = \langle\Phi_m^0|\Phi_{m'}^0\rangle\mathcal{E}_i^{K}, \tag{16}$$

where K specifies the atom, i represents atomic quantum numbers, and $\mathcal{E}_i^{K}$ is the measured atomic energy.

To evaluate diatomic Hamiltonian matrix $\mathbf{h}'^{KL}$, we insert the identity operator

$$\hat{I} = \sum_{\eta} |KL_{\eta}(\mathbf{R}_{KL})\rangle\langle KL_{\eta}(\mathbf{R}_{KL})| \tag{17}$$

into Eq. (14), where $|KL_{\eta}\rangle$ is the diatomic eigenvector of $\hat{h}^{KL}$, η denotes the diatomic quantum number, and $\mathbf{R}_{KL}$ is the bond length between atoms K and L. We then obtain

$$h'^{KL}_{mm'}(\mathbf{R}_{KL}) = \sum_{\eta} \langle \Phi^0_m | KL_{\eta}(\mathbf{R}_{KL}) \rangle \langle KL_{\eta}(\mathbf{R}_{KL}) | \hat{h}^{KL}(\mathbf{R}_{KL}) | \Phi^0_{m'} \rangle$$

$$= \sum_{\eta} \langle \Phi^0_m | KL_{\eta}(\mathbf{R}_{KL}) \rangle \mathcal{E}^{KL}_{\eta}(\mathbf{R}_{KL}) \langle KL_{\eta}(\mathbf{R}_{KL}) | \Phi^0_{m'} \rangle.$$

$$(18)$$

We can expand the diatomic eigenvectors in a complete set of atomic eigenvectors. For $KL=AB$,

$$|AB_{\eta}\rangle = \sum_{i,j} \mathcal{A}_{AB} |A_i\rangle |B_j\rangle U^{AB}_{ij,\eta}(\mathbf{R}_{AB}),$$

$$(19)$$

where $\mathcal{A}_{AB}$ is the $n_A + n_B$ electron antisymmetrizer and

$$U^{AB}_{ij,\eta}(\mathbf{R}_{AB}) = \langle B_j | \langle A_i | \mathcal{A}^T_{AB} | AB_{\eta} \rangle.$$

$$(20)$$

Substituting this expansion into Eq. (18), we find

$$h'^{AB}_{mm'}(\mathbf{R}_{AB}) = \sum_{\eta, st, s't'} O^{AB}_{ij,st} U^{AB}_{st,\eta}(\mathbf{R}_{AB}) \mathcal{E}^{AB}_{\eta}(\mathbf{R}_{AB})$$

$$\times U^{AB}_{s't',\eta}{}^T(\mathbf{R}_{AB}) O^{AB}_{s't',i'j'}{}^T \langle C_k | C_{k'} \rangle,$$

$$(21)$$

where the diatomic overlap matrix $O^{AB}_{ij,i'j'}(\mathbf{R}_{AB})$ is

$$O^{AB}_{ij,i'j'}(\mathbf{R}_{AB}) \equiv \langle B_j | \langle A_i | \mathcal{A}_{AB} | A_{i'} \rangle | B_{j'} \rangle.$$

$$(22)$$

We now make two simplifying approximations.

(1) We use a large but finite basis set in Eqs. (7) and (19) for the solution of the Hamiltonian in Eq. (4) so as to minimize effects from highly excited, less relevant states.

(2) All overlap matrices **S**, $\langle \Phi^0_m | \Phi^0_{m'} \rangle$, and **O** are approximated to be identity matrices. The off-diagonal couplings are indicated to have little effect on the results by previous calculations.[13,14,16]

We can rewrite Eqs. (12) and (13) for $K=A$ and $KL=AB$ as

$$h^A_{mm'} \approx h'^A_{mm'} \approx \mathcal{E}^A \delta_{ii'} \delta_{jj'} \delta_{kk'}$$

$$(23)$$

and

$$h^{AB}_{mm'}(\mathbf{R}_{AB}) \approx h'^{AB}_{mm'}(\mathbf{R}_{AB})$$

$$\approx \sum_{\eta} U^{AB}_{ijt,\eta}(\mathbf{R}_{AB}) \mathcal{E}^{AB}_{\eta}(\mathbf{R}_{AB}) U^{AB}_{i'j',\eta}{}^T(\mathbf{R}_{AB}) \delta_{kk'}. \quad (24)$$

The matrix elements $h^B_{mm'}$, $h^C_{mm'}$, $h^{BC}_{mm'}$, and $h^{AC}_{mm'}$, which are generated in a similar fashion, are used to construct the total DIM Hamiltonian $h^{mm'}$. Ignoring the overlap matrix **S**, the $U^{AB}_{ijt,\eta}(\mathbf{R}_{AB})$ transformation matrix is real and orthogonal, and the Hamiltonian **h** is real and symmetric. We write the general eigenvalue equation [Eq. (4)] as

$$\mathbf{h}\Gamma = \Gamma\mathbf{E},$$

$$(25)$$

and diagonalize **h** to obtain the DIM terms of the potential. The transformation matrix, $U^{KL}_{ij,\eta}(\mathbf{R}_{KL}) = \langle L_j | \langle K_i | \mathcal{A}^T_{KL} | KL_{\eta} \rangle$, is the form of Kenderick and Pack.[16]

B. Three-body fit

After obtaining the DIM term of the potential, which accounts for the mixed-pairwise-additive interaction, we subtract V_{DIM} from V_{total} at the points where the *ab initio* calculations are performed to get the three-body terms. We also incorporate the Axilrod–Teller–Muto term[19,20] for the 1 $^4A'$ surface for the long-range interaction region. Further description of this term can be found in Ref. 6. We then use a global-fit procedure of Aguado *et al.*[18] to obtain an analytic form for the three-body terms. For triatomic systems composed of atoms of the same species, the three-body term has the form

$$V_{3b} = \sum_{i,j,k}^{M} C_{ijk} \rho^i_{AB} \rho^j_{BC} \rho^k_{AC},$$

$$(26)$$

where ρ^i_{AB} is defined as

$$\rho^i_{AB} \equiv R_{AB} \exp(-\beta R_{AB}).$$

$$(27)$$

In Eq. (26), M is the largest power of the polynomials and C_{ijk} are expansion coefficients. These coefficients satisfy the required symmetry of the trimer. The global fit obtained then preserves all the symmetry properties of the system, including permutational symmetry.

III. RESULTS AND DISCUSSION

A. DIM basis set and *ab initio* basis set

We require PESs of 1 $^4A'$, 2 $^4A'$, 1 $^4A''$, and 2 $^4A''$ of Li$_3$. We first consider 2 ^2S, 2 ^2P atomic states of Li and from which states we form all possible states of Li$_3$. Though the total number of these possible states is $[(1+3)\times 2]^3 = 512$, the DIM Hamiltonian matrix can be partitioned into subblocks via certain approximations. We ignore contributions to the low-lying PESs from highly excited states ($PPP \equiv |A, ^2P\rangle |B, ^2P\rangle |C, ^2P\rangle$) which do not affect the computational results for the low-lying PESs appreciably. Since we neglect the spin-orbit interaction, we consider only the spin-aligned states ($M_s = m_{s_A} + m_{s_B} + m_{s_C} = 3/2$). This reduces the total number of states to 37, which includes 1 SSS state, 9 SSP states, and 27 SPP states. Among these, there are 15 $^4A''$ and 22 $^4A'$ states.

We take the Li$_3$ molecule to lie in the XZ plane with two atoms on the Z axis. The C_s symmetry has a reflection operator through the XZ plane ($y \to -y$). We construct the total Hamiltonian from Eq. (2), using the expressions for $h^K_{mm'}$ and $h^{KL}_{mm'}$ in Eqs. (23) and (24), as do Kenderick and Pack.[16] Using the symmetries of the basis, we can partition the DIM Hamiltonian into A' (22×22) and A'' (15×15) subblocks. Diagonalizing each subblock, we obtain the lowest few electronic PESs in A' and A'' irreducible representations at each internuclear configuration.

The *ab initio* PESs for all four states of Li$_3$ were generated via three-electron full configuration interaction calculations, using the effective core potentials of Stevens, Basch, and Krauss (SBK) (Ref. 17) and an augmented Gaussian basis with the MOLPRO software package.[21] The SBK basis set is augmented with three d-type and one f-type polarization functions. The basis is shown in Table I. Further descrip-

TABLE I. Lithium atom Gaussian basis set used with the effective core potentials of SBK (Ref. 17).

Orbital type	Exponents	Contraction coefficients
S	0.6177	1.0
S	0.1434	0.126 43
	0.050 48	0.761 79
S	0.0192 3	1.0
P	0.6177	1.0
P	0.1434	0.247 19
	0.050 48	0.521 40
P	0.019 23	1.0
D	0.06	1.0
D	0.02	1.0
D	0.01	1.0
D	0.007	1.0

tion of this basis set can be found in Refs. 6 and 17. Each Li_3 PES is calculated at 2958 internuclear configurations in the C_{2v}, D_{3h}, $D_{\infty h}$, and $C_{\infty v}$ geometries.

We calculate an additional 38 (39) points in A' (A'') symmetry for arbitrary C_s geometries. These points are not included in the fitting procedure, but are used to assess the accuracy of the fitted potential in these regions, as discussed in the next subsection. We also calculated 51 *ab initio* points, with the same basis set, for each of the 15 diatomic potentials, except for the $1\ ^3\Sigma_u^+$ state, to be used in the construction of the DIM term. We use the $1\ ^3\Sigma_u^+$ diatomic potential from the work of Colavecchia *et al.*[6] This diatomic potential combines the most recent Rydberg–Klein–Rees potential available[22] with the well known short and long range expansions and accurately reproduces all known experimental data, further description of which can be found in Ref. 6.

B. Fitting

Using the transformation matrix from Ref. 16, we now diagonalize each subblock of the DIM Hamiltonian and take the lowest two eigenenergies of each subblock to be fitted to the *ab initio* calculations.

For the $1\ ^4A'$ and $2\ ^4A'$ surfaces, the potential is decomposed into two potentials

$$V = V_{CI}(\phi, R_1, R_2)S(\phi) + [1 - S(\phi)]V_{ELSE}(\phi, R_1, R_2),$$
(28)

where ϕ is the angle between the two diatomic bond R_1 and R_2 and $S(\phi)$ is a switching function. The switching function is

$$S(\phi) = 0.5 * \{1 + \tanh[(\phi - \phi_o)/(\phi_o * d_\phi)]\}$$
(29)

and has two adjustable parameters ϕ_o and d_ϕ, which are optimized in the fitting. This switching function is 1 when $\phi = 180°$ ($C_{\infty v}$ geometries) but switches smoothly to zero in C_s geometries. The potential V_{CI} describes the $C_{\infty v}$ geometries and V_{ELSE} describes other geometries. For V_{CI}, we optimize the coupling parameters between diatomic potentials corresponding to the same irreducible representation so that the surface is quantitatively correct in $D_{\infty h}$ and $C_{\infty v}$ geometries and qualitatively correct elsewhere. This gives the PES

the quantitatively correct behavior in $D_{\infty h}$ and $C_{\infty v}$ geometries where the CIs occur. The CIs are very sensitive to mixing of the $1\ ^3\Sigma_u$ and $2\ ^3\Sigma_u$ states, the $1\ ^3\Pi_u$ and $1\ ^3\Pi_u$ states, and the $1\ ^3\Pi_g$ and $2\ ^3\Pi_g$ states. Each mixing matrix, $M^{AB}(R_{AB})$, between the states with the same irreducible representations is defined by

$$M^{AB}(R_{AB}) = \begin{pmatrix} \cos\theta & \sin\theta \\ -\sin\theta & \cos\theta \end{pmatrix}$$
(30)

and the mixing angle θ has a functional form of

$$\cos^2\theta = \frac{\phi^2}{1 + \phi^2}, \quad \sin^2\theta = \frac{1}{1 + \phi^2},$$

$$\cos\theta\sin\theta = \frac{\phi}{1 + \phi^2},$$
(31)

where

$$\phi^{-1}(R_{AB}) = aR_{AB}^2 \exp(-bR_{AB})$$
(32)

with a and b adjustable parameters. Other variations of these mixing functions were tried and the resulting fits were not as good. We vary these 16 mixing parameters (eight pairs of diatomic states) to fit the *ab initio* points, and this many degrees of freedom give quantitatively correct descriptions of the PES in collinear geometries while also minimizing the rms deviation of the global potential. Take the $1\ ^4A'$ surface. After optimization of the mixing parameters, we obtain an rms deviation of 5.0×10^{-5} hartree for 155 $D_{\infty h}$ points, and an rms deviation of 1.2×10^{-4} hartree for 320 $C_{\infty v}$ points. For V_{ELSE}, the couplings between diatomic potentials corresponding to the same irreducible representation are necessary to avoid incorrect CIs in the D_{3h} geometries. Therefore, the coupling parameters are optimized so those false CIs do not occur and the rms error is minimized as well. Though a numerical fitting can be done for the $1\ ^4A''$ and $2\ ^4A''$ surfaces as well, one has to sometimes manually tune the parameters to give the correct behavior. Often the higher PES interferes with the lower PES, resulting in a qualitatively poor fit. Other people tend to have similar problems in DIM studies of triatomic systems.[16] In our case, for the $^4A''$ surfaces, we need to tune these mixing parameters by hand to force the excited PESs to stay above the lower PES and behave reasonably. Once this condition is satisfied, varying these mixing parameters does not appreciably change the fitting results of the $^4A''$ surfaces.

We fit only 2640 points out of 2958 *ab initio* points. We

TABLE II. rms deviation of all four PESs in different geometries. Set 1 stands for rms error of global potential ($E \leq 0.01$ hartree for the $1A'$ surface and $E \leq 0.08$ hartree for the $2A'$, $1A''$ and $2A''$ surfaces), Set 2 stands for rms error in $C_{\infty v}$ geometries, and Set 3 stands for rms error only of unfitted C_s points.

PES type	Set 1	Set 2	Set 3
1A'	1.8×10^{-4} hartree	1.2×10^{-4} hartree	5.3×10^{-4} hartree
2A'	9.1×10^{-4} hartree	3.4×10^{-4} hartree	1.6×10^{-3} hartree
1A''	2.5×10^{-4} hartree	0.8×10^{-4} hartree	1.5×10^{-4} hartree
2A''	5.1×10^{-4} hartree	1.0×10^{-3} hartree	2.1×10^{-4} hartree

FIG. 1. The $^4A'$ surfaces in $D_{\infty h}$ geometries. Solid curves are fitted potential, V_{FULL}, and dark circles are *ab initio* data for $^4A'$ surfaces. (a) $1A'$ surface, (b) $2A'$ surface, (c) $1A''$ surface. and (d) $2A''$ surface.

excluded the highly repulsive parts ($E \geq 0.01$ Ha.) for the $1\ ^4A'$ surface and highly repulsive parts ($E \geq 0.08$ hartree) for the $2\ ^4A'$, $1\ ^4A''$, and $2\ ^4A''$ surfaces. The first fitting step shows that the mixed-pairwise-additive term from the DIM model for the $1\ ^4A'$ surface has complicated, configuration-dependent contributions from different diatomic potential en-

ergy curves. It helps explain the large deviation of the simple PAP, in the form $(^3\Sigma_u^+ + ^3\Sigma_u^+ + ^3\Sigma_u^+)$, from the global potential. The DIM model also gives the correct two-body and three-body breakup dissociation limits for these excited PESs.

These coupling parameters can be used to construct the nonadiabatic coupling terms between the $1\ ^4A'$ and $2\ ^4A'$
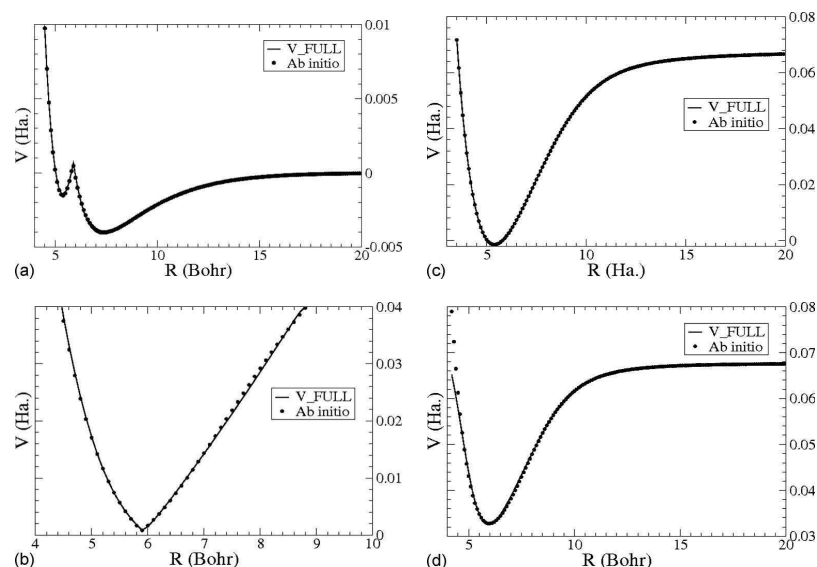

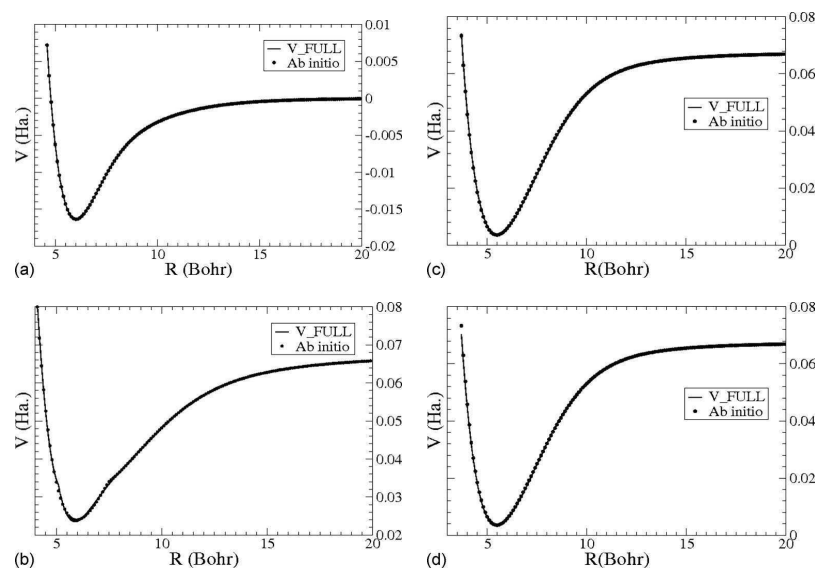FIG. 2. The $^4A'$ surfaces in D_{3h} geometries. Solid curves are fitted potential, V_{FULL}, and dark circles are *ab initio* data for $^4A'$ surfaces. (a) $1A'$ surface, (b) $2A'$ surface, (c) $1A''$ surface, and (d) $2A''$ surface.
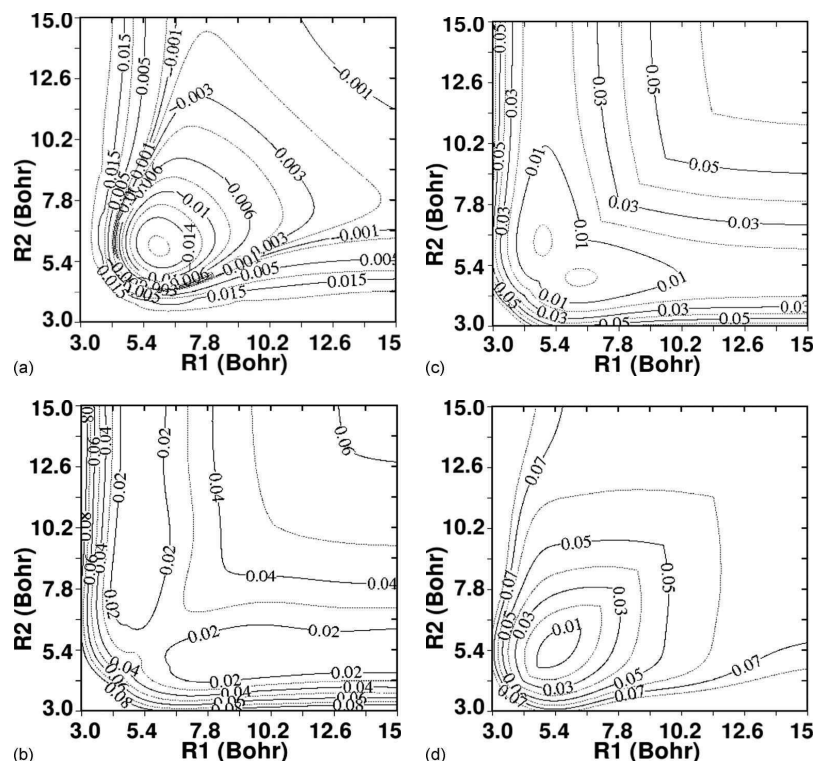
154

FIG. 3. The fitted $^4A'$ surfaces of lithium trimer for a bond angle of 60°. (a) $1A'$ surface, (b) $2A'$ surface, (c) $1A''$ surface, and (d) $2A''$ surface. Contours are labeled in hartree.

surfaces. We use an approximation in calculating these nonadiabatic couplings, which assumes the eigenvectors of the DIM potential represent the true eigenvectors of the electronic Hamiltonian. This approximation is valid in the CI region because DIM terms can very accurately describe the potential and the three-body terms are negligible. This approximation is questionable in other geometries, but the nonadiabatic couplings at other geometries are several orders of magnitude smaller than those in the CI region and thus this approximation should not deteriorate the results. The nonadiabatic coupling matrix $\mathbf{W}_{12}^{(1)ad}(\vec{R})$ between two surfaces is defined as

$$\mathbf{W}_{12}^{(1)ad}(\vec{R}) \equiv \langle \phi_1^{ad}(\vec{r};\vec{R}) | \nabla_{\vec{R}} | \phi_2^{ad}(\vec{r};\vec{R}) \rangle, \qquad (33)$$

where $\phi_t^{ad}(\vec{r};\vec{R})$ are eigenvectors of the electronic Hamiltonian in Eq. (1). By using Eq. (3) and ignoring $\langle \Phi_m(\vec{r}) | \Phi_{m'}(\vec{r}) \rangle$, we obtain

$$\mathbf{W}_{12}^{(1)ad}(\vec{R}) = \sum_M \Gamma_{m1}(\vec{R}) \nabla_{\vec{R}} \Gamma_{m2}(\vec{R}). \qquad (34)$$

We then construct the nonadiabatic coupling terms to study the CIs.

We subtract the optimized DIM term from the full *ab initio* potential to get the three-body term. We use the

global fit for the three-body term described in the previous section. We vary the maximum power of the polynomials M from 3 to 10. Our results indicate that $M=9$ is big enough to minimize the rms deviation of the global potential from the *ab initio* points.

C. Results

Our global potential very accurately describes the CI regions and is also quantitatively correct elsewhere. Table II shows the rms deviation of our global fitting for the four PESs at different regions. Set 3 tests our global potential at unfitted *ab initio* points for arbitrary C_s geometries. Figure 1 shows the behavior of our PESs in $D_{\infty h}$ geometries, where the solid circles are the *ab initio* points, and the solid curves are our fitted PESs with $R=R_1=R_2=0.5R_3$. Figure 2 shows the behavior of our PESs in D_{3h} geometries, where the solid circles are the *ab initio* points, and the solid curves are our fitted PESs with $R=R_1=R_2=R_3$.

Contour plots of the final potential for two different interbond angles ϕ are shown in Figs. 3 and 4. The sharp angles in Fig. 3 panels (c) and (d) are due to the energy splittings of two degenerate states in D_{3h} geometries to non-
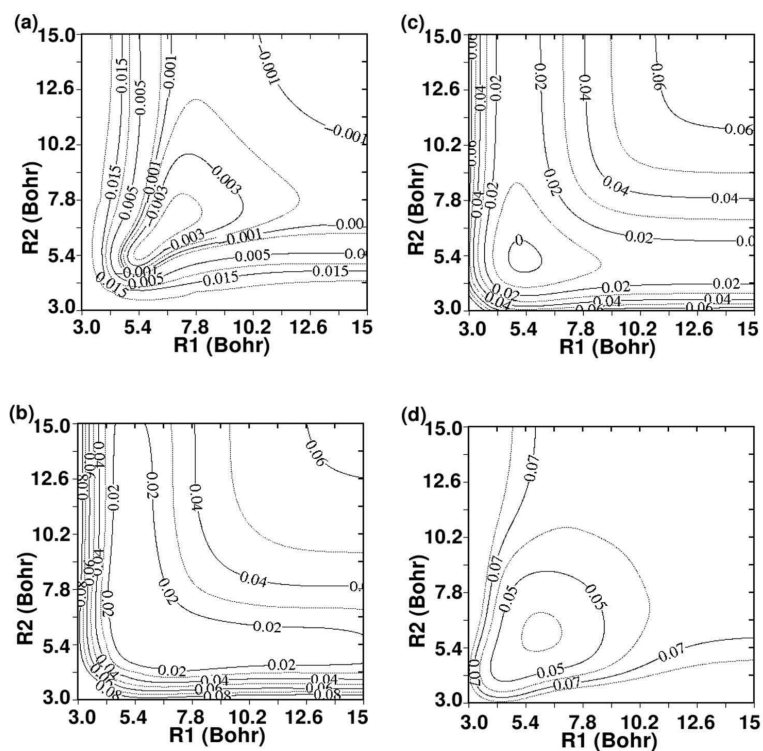
155

FIG. 4. The fitted $^4A'$ surfaces of lithium trimer for a bond angle of 120°. (a) $1A'$ surface, (b) $2A'$ surface, (c) $1A''$ surface, and (d) $2A''$ surface. Contours are labeled in hartree.

degenerate states in C_s geometries. Contour plots of the three-body contribution of the $1\,^4A'$ for two different interbond angles ϕ are shown in Fig. 5.

Plots of the nonadiabatic coupling in Eq. (33) in C_{2v} geometries are shown in Fig. 6, where φ is defined to describe the enclosed loop around the CI in $D_{\infty h}$ geometries,

$$\rho = 11 + \sin(\varphi)[\text{a.u.}], \quad \theta = 90 + \cos(\varphi)[^o]. \tag{35}$$

Because the ground and excited electronic wave functions both change signs as they follow an enclosed loop around the CIs, the nonadiabatic coupling terms are still single valued.

The Fortran routines to construct all four electronic PESs, $1\,^4A'$, $2\,^4A'$, $1\,^4A''$, and $2\,^4A''$, and *ab initio* data can be downloaded at http://nhn.ou.edu/~li/research.html.

D. Diabolic conical intersections

In the *ab initio* calculation, we noticed one possible diabolic CI in C_{2v} geometries. The other known symmetry-allowed CIs have been observed and discussed elsewhere.[7] The diabolic intersections, often referred as accidental degeneracies, are two PESs of the same irreducible representation that cross, though in general the symmetry arguments require avoided crossings. These diabolic intersections are not predicted by group theory. They occur only if the cou-

pling between two degenerate PESs are zero. These unexpected diabolic intersections can clarify confusing branching ratios.[23,24]

Figure 7 shows a possible diabolic CI of the A_2 states in C_{2v} geometries when $\phi = 99.175\,25°$, where ϕ is the angle between two diatomic separations, and $R = R_1 = R_2$ $= 5.952\,103$ bohr, at 0.041 9418 hartree above the (2S+2S +2S) three-body dissociation limit. We calculated more than 100 *ab initio* points in the neighborhood of this diabolic CI region. The two PESs are shown to be separated by 1×10^{-8} hartree. To verify the true existence of this diabolic CI, we trace the sign of the electronic wave function along a path in the nuclear configuration space, which encircles this diabolic CI in C_{2v} geometries. Figure 8 shows the coefficients of the configuration interaction vectors of two electronic wave functions at C_{2v} geometries in a loop defined as

$$R = 5.952103 + 0.0001 \sin(\varphi)[\text{a.u.}],$$
$$\phi = 99.17525 + 0.001 \cos(\varphi)[^o]. \tag{36}$$

This diabolic intersection, which indicates a seam of diabolic CIs in C_s geometries, may cause unexpected behavior in calculations using these excited PESs.

(a)

(b)
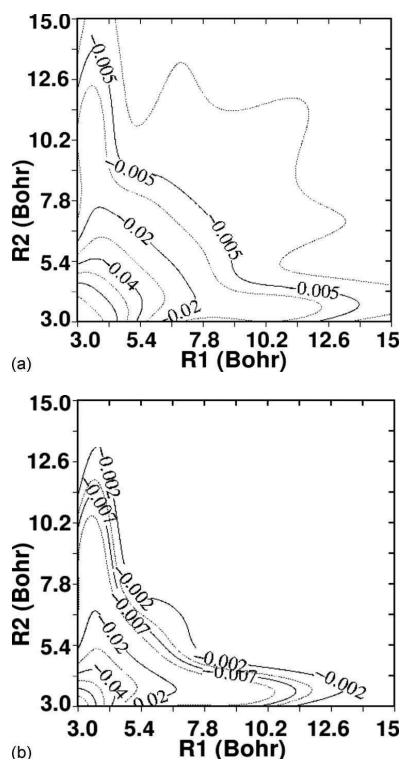
FIG. 5. Contour plots of the three-body contribution of the $1A'$ surface for a bond angle of (a) $60°$ and (b) $120°$. Contours are labeled in hartree.

FIG. 7. Possible diabolic CI in C_{2v} geometries for the lowest A_2 states, where $\Delta V \equiv V - 0.041\,941\,8$ hartree and $\Delta R \equiv R - 5.952\,103$ bohr.

IV. CONCLUSIONS

We have constructed all four low-lying spin-aligned electronic PESs, $1\,^4A'$, $2\,^4A'$, $1\,^4A''$, and $2\,^4A''$, for Li_3. The resulting fit accurately describes $D_{\infty h}$ CI for both the $1\,^4A'$ and $2\,^4A'$ surfaces. It is a global fit with an rms deviation of 1.8×10^{-4} hartree for $1\,^4A'$, 9.2×10^{-4} hartree for $2\,^4A'$, 2.5×10^{-4} hartree for $1\,^4A''$, and 5.1×10^{-4} hartree for $2\,^4A''$. The DIM terms can be used to compute the nonadiabatic terms to describe the CI beyond the Born–Oppenheimer approximation. We have found a possible diabolic CI A_2 *ab initio* calculations in C_{2v} geometries, which indicates a seam of CIs in C_s geometries.

ACKNOWLEDGMENTS

(a)

(b)

FIG. 6. Nonadiabatic couplings around the CI in C_{2v} geometries. (a) W_ρ^{eg} and (b) W_θ^{eg}.

(a)

(b)

FIG. 8. Coefficients of the configuration interaction vectors of two electronic wave functions along the loop which encircles the diabolic CI in C_{2v} geometries. (a) The ground state and (b) the excited state.

157

[1] D. G. Fried, T. C. Killan, L. Willmann, D. Landhuis, S. C. Moss, D. Kleppner, and T. S. Greytak, Phys. Rev. Lett. **81**, 3811 (1998).

[2] C. C. Bradley, C. A. Sackett, J. J. Tollett, and R. G. Hulet, Phys. Rev. Lett. **75**, 1687 (1995).
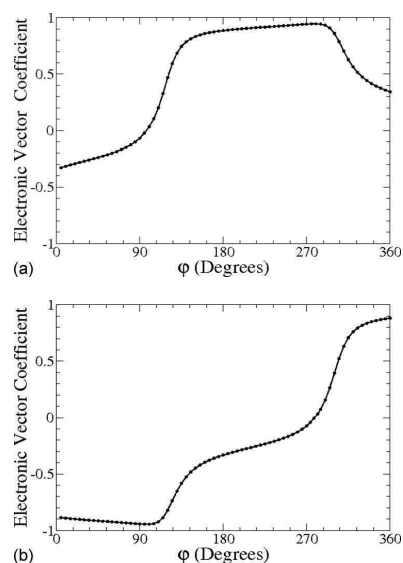
[3] K. B. Davis, M.-O. Mewes, M. R. Andrews, N. J. van Druten, D. S. Durfee, D. M. Kurn, and W. Ketterle, Phys. Rev. Lett. **75**, 3969 (1995).

[4] M. H. Anderson, J. R. Ensher, M. R. Mathews, C. E. Wieman, and E. A. Cornell, Science **269**, 198 (1995).

[5] M. Weber, J. Herbig, M. Mark, H.-C. Nägerl, and R. Grimm, Science **299**, 232 (2003).

[6] F. D. Colavecchia, J. P. Burke, Jr., W. J. Stevens, M. R. Salazar, G. A. Parker, and R. T. Pack, J. Chem. Phys. **118**, 5484 (2003).

[7] M. T. Cvitaš, P. Soldán, J. M. Hutson, P. Honvault, and J.-M. Launay, J. Chem. Phys. **127**, 074302 (2007).

[8] M. T. Cvitaš, P. Soldán, J. M. Hutson, P. Honvault, and J.-M. Launay, Phys. Rev. Lett. **94**, 033201 (2005).

[9] M. T. Cvitaš, P. Soldán, and J. M. Hutson, Mol. Phys. **104**, 23 (2006).

[10] D. A. Brue, X. Li, and G. A. Parker, J. Chem. Phys. **123**, 091101 (2005).

[11] J. Higgins, T. Hollebeek, J. Reho, T.-S. Ho, K. K. Lehmann, H. Rabitz, and G. Scoles, J. Chem. Phys. **112**, 5751 (2000), and reference therein.

[12] F. O. Ellison, J. Am. Chem. Soc. **85**, 3540 (1963).

[13] J. C. Tully, J. Chem. Phys. **58**, 1396 (1973).

[14] E. Steiner, P. R. Certain, and P. J. Kuntz, J. Chem. Phys. **59**, 47 (1973).

[15] C. W. Eaker and C. A. Parr, J. Chem. Phys. **64**, 1322 (1976).

[16] B. Kendrick and R. T. Pack, J. Chem. Phys. **102**, 1994 (1995).

[17] W. J. Stevens, H. Basch, and M. Krauss, J. Chem. Phys. **81**, 6026 (1984).

[18] A. Aguado, C. Tablero, and M. Paniagua, Comput. Phys. Commun. **108**, 259 (1998).

[19] B. M. Axilrod and E. Teller, J. Chem. Phys. **11**, 299 (1943).

[20] Y. Muto, Proc. Phys. Math. Soc. Jpn. **17**, 629 (1943).

[21] MOLPRO, a package of *ab initio* programs designed by H.-J. Werner, and P. J. Knowles, version 2006.1, R. Lindh, M. Schütz, P. Celani, T. Korana, F. R. Manby, G. Rauhut, R. D. Amos, A. Bernhardsson *et al.*, 2006.

[22] A. Ross, personal communication (May 15, 2002).

[23] D. R. Yarkony, J. Chem. Phys. **100**, 3639 (1994).

[24] D. R. Yarkony, Rev. Mod. Phys. **68**, 985 (1996).

158

Appendix G

Bound states calculation of Li$_3$

A New Method for Calculating Bound States: the A_1 States of Li$_3$ on the Spin-Aligned Li$_3$(1 ^{4}A$'$) Potential Energy Surface
by X. Li, D. A. Brue and G. A. Parker
J. Chem. Phys. Volume **127**, Page 014108 (2007)

New method for calculating bound states: The A_1 states of Li$_3$ on the spin-aligned Li$_3$(1 $^4A'$) potential energy surface

Xuan Li, Daniel A. Brue, and Gregory A. Parker
Homer L. Dodge Department of Physics and Astronomy, University of Oklahoma, Oklahoma 73019

In this paper, we present a calculation for the bound states of A_1 symmetry on the spin-aligned Li$_3$(1 $^4A'$) potential energy surface. We apply a mixture of discrete variable representation and distributed approximating functional methods to discretize the Hamiltonian. We also introduce a new method that significantly reduces the computational effort needed to determine the lowest eigenvalues and eigenvectors (bound state energies and wave functions of the full Hamiltonian). In our study, we have found the lowest 150 energy bound states converged to less than 0.005% error, and most of the excited energy bound states converged to less than 2.0% error. Furthermore, we have estimated the total number of the A_1 bound states of Li$_3$ on the spin-aligned Li$_3$(1 $^4A'$) potential surface to be 601. © *2007 American Institute of Physics*. [DOI: 10.1063/1.2753157]

I. INTRODUCTION

In this paper, we present the most comprehensive calculation of the bound states of the spin-aligned lithium trimer to date. We also present a new method for calculating these bound states, which is noteworthy because of a tremendous increase in efficiency of these normally very expensive calculations.

The impetus to calculate accurate bound states for the Li$_3$ system is motivated by several applications. One of the most prominent is the Bose-Einstein condensation, which has driven ultracold reactive molecular collisions to become one of the key interests in chemical reaction dynamics. The simplest, nontrivial systems to study are the alkali metals, and as such many physicists and chemists are interested in ultracold chemical reactions of Li$_3$. The formation of ultracold molecules ($T \leq 100$ μK) from laser-cooled alkali atoms has been observed by several groups.[1–4] Photoassociation and radiative stabilization processes are necessary in the formation of ultracold molecules, and both require knowledge of the quartet bound states. Also, the spin-aligned states are of particular interest for such ultracold studies because the large magnetic moment of the quartet states makes the molecules easier to contain in a magneto-optical trap. Studies of three-body recombination, a primary vehicle of trap loss, are also performed on the quartet potential surface because of the relatively shallow energy wells.

Another reason why the bound states of this specific system are interesting is the opportunity to study the effects of nonadiabatic couplings. This system exhibits a conical intersection between the two lowest spin-aligned ($^4A'$) states when the atoms are collinear ($C_{\infty v}$ geometries). Our group[5] and others[6–8] have made reference to this conical intersection before. The effect of the conical intersection is to couple the states of these two surfaces, as well as introduce geometric or Berry phase effects. This conical intersection is an interesting example because of its proximity to the three-body dissociation limit. Geometric phase effects are introduced to the system if the evolution of the nuclear motion of the mol-

ecule traces a path around the conical intersection. In this system, it is possible to circumscribe the conical intersection at energies below the three-body dissociation limit! The lowest point of intersection is at the symmetric-stretch collinear ($D_{\infty h}$) geometry at an energy of 0.0952 eV above the dissociation limit. However, in order to transverse a path around the conical intersection, the maximum energy needed is −0.057 eV, *below* the dissociation limit. More information about this structure can be found in Ref. 5. Because of its proximity to the ranges of energies studied in ultracold collisions, many are interested to see what effects the conical intersection will have on both bound state and scattering calculations. This present study will provide a comparison of the bound states with a future calculation including the nonadiabatic effects of the conical intersection.

Yet another application of accurate bound states is the study of floppy molecules, that is, those with large amplitude vibrational motions. Bačić and Light[9] have noted these states and their importance: "The large amplitude motion (LAM) vibrational states, because of the delocalized nature of their wave functions, contain detailed information about large regions of the potential surface beyond the global minimum. Moreover, while executing LAM vibrations, molecules can populate high-energy local minima inaccessible at lower energies, thus permitting detection of new isomers with strange structures and dynamics."

The study of LAM states is very difficult as it requires knowledge of large regions of the potential energy surfaces, and also the coupling between the LAM vibrational states and the other vibrational modes. These calculations are difficult and become increasingly more so for the highly excited vibrational states. Successful calculations of LAM states have been performed by Bačić and co-workers,[10–16] Henderson and Tennyson,[17] Shirin *et al.*,[18] Kostin,[19] and other groups.[20–34] The calculation for many-bound-states system is extremely difficult especially for the most highly excited states, and no comprehensive study on Li$_3$ bound states has been published. Rather than using a Lanczos-type method to

TABLE I. Time comparison of different methods with different number of points.

Method	Number of points	Number of eigenvalues	CPU time (hour)
IRAM	$40\times30\times6$	100	0.30
IRAM	$40\times30\times6$	600	5.58
Direct diagonalization	$40\times30\times6$	600	0.24
New method ($N_G=2000$)	$40\times30\times6$	600	0.18
IRAM	$50\times40\times8$	600	18.52
Direct diagonalization	$50\times40\times8$	600	2.37
New method ($N_G=2000$)	$50\times40\times8$	600	0.42
IRAM	$60\times40\times11$	600	>150
Direct diagonalization	$60\times40\times11$	600	9.96
New method ($N_G=2000$)	$60\times40\times11$	600	0.73

find the eigenvalue of the Hamiltonian, our new subspace method utilizes the ray diagonalization of Bačić *et al.*[35] to generate adiabatic potential energy surfaces and the associated surface functions in the one dimensional (1D) hyperradius. We then obtain reasonable subspace vectors by solving the 1D Schrödinger equation on each adiabatic surface without nonadiabatic couplings. Finally, we include the nonadiabatic couplings and use the subspace vectors to form the Hamiltonian matrix to solve for the eigenvalues and eigenvectors. We estimate the number of Li$_3$ bound states at 601 for the A1 symmetry. It is our hope that the new, more efficient calculation method described herein will enable studies of the LAM states of more complicated systems.

Potential energy surfaces for the lithium trimer are very hard to calculate, even though each lithium atom has only one valence electron. However, several groups have produced reasonably accurate potential surfaces for some of the lower states of the Li$_3$ system,[6–8,36] and a full calculation of the bound states is now possible. We perform our calculation on the surface provided by Colavecchia *et al.*[36] with new parameters updated at Ref. 37.

The details of the calculation are presented in the adiabatically adjusting principle axes hyperspherical (APH) coordinates of T Pack and Parker,[38] so in Sec. II A we review the formation of the APH Hamiltonian. In Sec. II B we introduce a new calculation method to numerically solve for the eigenvalues and eigenfunctions of the APH Hamiltonian. In Sec. III we present the results for the bound state calculation of the $^4A'$ potential energy surface. Also in Sec. III we present the convergence study of these results. The accuracy of the states is determined by the study of their convergence.

II. METHODS OF CALCULATION

A. APH wave function and Hamiltonian

In this study, we use the hyperspherical coordinates and the total wave function Ψ^{JMpn} formulated in work of T Pack and Parker,[38]

$$\Psi^{JMpn} = 4\sum_{t,\Lambda} \rho^{-5/2}\psi_{t\Lambda}^{Jpn}(\rho)\phi_{t\Lambda}^{Jp}(\theta,\chi_i;\rho_\xi)\hat{D}_{\Lambda M}^{Jp}(\alpha_Q,\beta_Q,\gamma_Q)$$

$$\equiv 4\sum_{\Lambda} \rho^{-5/2}\Phi_{\Lambda}^{Jpn}(\rho,\theta,\chi_i)\hat{D}_{\Lambda M}^{Jp}(\alpha_Q,\beta_Q,\gamma_Q), \qquad (1)$$

where J is the total angular momentum quantum number, M

is the quantum number for the projection of J along the space frame z axis, Λ is the quantum number for the projection of J along the body frame z axis, p is the parity, t indicates the tth solution for surface function $\phi_{t\Lambda}^{Jp}(\theta,\chi_i;\rho_\xi)$ in terms of θ and χ coordinates, and n indicates the nth solution for Ψ^{JMpn} functions. Further, ρ is the APH hyper-radius, θ and χ are the APH hyperangles, and ρ_ξ is the center of a ρ sector in which the nonadiabatic surface basis $\phi_{t\Lambda}^{Jp}$ is expanded. The hyperradius ρ is related to the Jacobi coordinates by $\rho = \sqrt{S^2 + s^2}$, where S and s are the corresponding mass-scaled radial distances in Jacobi coordinates. The angle θ is a bending angle of the trimer, where $\theta = \pi/2$ corresponds to the collinear arrangements, and $\theta = 0$ to equilateral arrangements. The angle χ is a kinematic rotation angle related to the permutation of three lithium atoms. Adjacent chemical arrangement channels are separated by $\chi = \pi/3$ for three identical atoms. More details and several figures of APH coordinates can be found in the work of T Pack and Parker.[38] The $\hat{D}_{\Lambda M}^{Jp}(\alpha_Q,\beta_Q,\gamma_Q)$, normalized Wigner rotation matrix elements of good parity p,[38] are functions of the APH Euler angles $\alpha_Q,\beta_Q,\gamma_Q$. The expansion coefficients $\psi_{t\Lambda}^{Jpn}(\rho)$ are functions of ρ labeled by the good quantum numbers J and p. The wave functions $\Phi_{\Lambda}^{Jpn}(\rho,\theta,\chi_i)$ are defined as

$$\Phi_{\Lambda}^{Jpn}(\rho,\theta,\chi_i) = \sum_{t} \psi_{t\Lambda}^{Jpn}(\rho)\phi_{t\Lambda}^{Jp}(\theta,\chi_i;\rho_\xi), \qquad (2)$$

and $\hat{D}_{\Lambda M}^{Jp}(\alpha_Q,\beta_Q,\gamma_Q)$ constitute the basis set we use to expand the total Hamiltonian for each Λ value, in Eq. (5) more information would be offered.

The total Hamiltonian for the three APH coordinates is given by

$$\hat{H}(\rho,\theta,\chi) = -\frac{\hbar^2}{2\mu}\left(\frac{\partial^2}{\partial\rho^2} - \frac{15}{4\rho^2} + \frac{4}{\rho^2\sin 2\theta}\frac{\partial}{\partial\theta}\sin 2\theta\frac{\partial}{\partial\theta}\right.$$
$$\left. + \frac{1}{\rho^2\sin^2\theta}\frac{\partial^2}{\partial\chi^2}\right) + \frac{J_x^2}{\mu\rho^2(1+\sin\theta)}$$
$$+ \frac{J_y^2}{\mu\rho^2\sin^2\theta} + \frac{J_x^2}{\mu\rho^2(1-\sin\theta)}$$
$$- \frac{i\hbar\cos\theta}{\mu\rho^2\sin^2\theta}J_y\frac{\partial}{\partial\chi} + \hat{V}(\rho,\theta,\chi), \qquad (3)$$

where μ is the triatomic reduced mass $\sqrt{(m_A m_B m_C/m_A + m_B + m_C)}$, and $\hat{V}$ is the Born-Oppenheimer

161

interaction potential. It is convenient to write Eq. (3) as

$$\hat{H}(J) = \hat{H}_o + \hat{H}_r + \hat{H}_c, \tag{4}$$

where $\hat{H}_o$ stands for $\hat{H}(J=0)$, r stands for rotational, and c for Coriolis. Here, $\hat{H}_r$ is the asymmetric top coupling term,

$$\frac{J_x^2}{\mu\rho^2(1+\sin\theta)} + \frac{J_y^2}{\mu\rho^2\sin^2\theta} + \frac{J_x^2}{\mu\rho^2(1-\sin\theta)},$$

and $\hat{H}_c$ is the Coriolis coupling term,

$$-\frac{ih\cos\theta}{\mu\rho^2\sin^2\theta}J_y\frac{\partial}{\partial\chi}.$$

Therefore the Hamiltonian matrix has a banded structure when total $J \geq 1$:

$$\mathbf{H}(J) = \begin{pmatrix} \mathbf{H}_o + \mathbf{H}_r & \mathbf{H}_c & \mathbf{H}_r & \mathbf{0} & \cdots & \mathbf{0} \\ \mathbf{H}_c & \mathbf{H}_o + \mathbf{H}_r & \mathbf{H}_c & \mathbf{H}_r & \cdots & \mathbf{0} \\ \mathbf{H}_r & \mathbf{H}_c & \mathbf{H}_o + \mathbf{H}_r & \mathbf{H}_c & \cdots & \mathbf{0} \\ \mathbf{0} & \mathbf{H}_r & \mathbf{H}_c & \mathbf{H}_o + \mathbf{H}_r & \cdots & \mathbf{H}_r \\ \cdots & \cdots & \cdots & \cdots & \cdots & \mathbf{H}_c \\ \mathbf{0} & \mathbf{0} & \mathbf{0} & \mathbf{H}_r & \mathbf{H}_c & \mathbf{H}_o + \mathbf{H}_r \end{pmatrix}, \tag{5}$$

where each block matrix will be labeled as $[\Lambda, \Lambda']$, where Λ corresponds to quantum number of the wave function $\psi_{t\Lambda}^{Jpn}(\rho)$ in Eq. (1). More discussion about asymmetric top coupling term and the Coriolis coupling term can be found in the work of T Pack and Parker.[38]

We are interested only in ultracold temperature reactions, for which $J=0$ is the most relevant angular momentum. Therefore, the total J is set to zero, so $p=0$, $\Lambda=0$, though the theory and our code are applicable to the nonzero total J case. Matrix $\mathbf{H}(J)$ reduces to $\mathbf{H}_o$ when $J=0$. A short explanation will be offered in Sec. II B 3 on how to calculate eigenfunctions and eigenenergies for nonzero total J cases. Note that our body-frame (BF) z axis is defined as the axis with the smallest moment of inertia. Johnson[44,45] defined his BF z axis perpendicular to the triatomic plane, which would have the largest moment of inertia. Either body frame can be used, and a unitary transformation using Clebsch-Gordan coefficients transforms the Hamiltonian in APH coordinates into Johnson's BF Hamiltonian. If no further approximations are used, the two coordinate systems must give identical energy levels. For $J=0$, there is not much difference between these two definitions.

B. Solution of the APH Hamiltonian

In the present work, the Hamiltonian matrix is formulated as a discretized direct product of different bases for three coordinates (ρ, θ, χ). In a discrete variable representation (DVR) or distributed approximating functional (DAF) formalism, elements of the eigenvectors of Eq. (5) are values of the wave function at the quadrature points, and $\Phi_\Lambda^{Jpn}(\rho_\alpha, \theta_\beta, \chi_\gamma)$ are not expansion coefficients of a basis set, though a DVR-to-FBR (FBR denotes finite basis representation) transformation exists for the DVR method.[39] More details on how to discretize a Hamiltonian using DVR can be found in Ref. 40. See Ref. 41 for a description of the DAF

method as applied to an inelastic scattering problem. We choose to use the DAF method[42] for the hyper-radius ρ, because the DAF method is not basis dependent. Therefore, the convergence for the highly excited states is very efficient for the DAF method to achieve in the ρ direction.

Because θ is not periodic and it has a finite range where the basis functions do not have compact support, it is difficult to use the DAF method unless one uses it with extreme care.[46] The best local approximation for the bounded angle θ appears to be the DVR method, which offers the simple evaluation of the matrix element. Therefore we choose to use DVR method[43] which is easy to implement and does not require compact support. Bačić and co-workers have published successful DVR calculations for APH surface functions.[13–16,35]

For χ both DVR and DAF methods are efficient (because χ is periodic), and work almost equally well. We choose the DAF method because the kinetic energy matrix of the χ coordinate has a banded, Toeplitz structure that reduces the computation time spent in matrix operations; whereas for DVR method it is full matrix. In the χ coordinate, we also apply the symmetry projection operator.[46,47] In APH coordinates, the Li_3 potential has C_{6v} symmetry instead of C_{3v} symmetry, and the χ coordinate runs through the three reactive channels twice. The C_{6v} group has four nondegenerate irreducible representations, A_1, A_2, B_1, and B_2, and two twofold degenerate irreducible representations, E_1 and E_2. Here we study the $J=0$, $p=0$ cases; so the B_1, B_2, and E_1 representations are not included in the calculation because they have the wrong parity. We apply the symmetry-adapted transformation to the χ coordinates to block diagonalize the kinetic energy matrix of the χ coordinate. There are six vertical mirror planes for the C_{6v} group. The A_1 symmetry vibrational states are totally symmetric, and the A_2 symmetry vibrational states are antisymmetric with respect to these

planes. Because of this symmetry, only a portion of the range of χ is needed: A_1 and A_2 vibrational states must be calculated only for $\chi \in [0, \pi/6]$. The E_2 symmetry vibrational states must be calculated for $\chi \in [0, \pi/3]$, which doubles the dimension of the matrix of χ. We have calculated the bound states for A_2 and E_2 symmetries but, for simplicity, we only present the A_1 vibrational states in this paper.

The total Hamiltonian matrix $\bar{H}(\rho, \theta, \chi)$ for $J=0$ can be partitioned as

$$\bar{H}(\rho, \theta, \chi) = \bar{H}_\rho(\rho) + \bar{H}_{2d}(\rho, \theta, \chi), \tag{6}$$

where $\bar{H}_\rho(\rho)$ is defined in terms of a direct product of matrices,

$$\bar{H}_\rho(\rho) = \bar{h}_\rho^{\mathrm{DAF}} \otimes \bar{I}_{\theta\chi}, \tag{7}$$

and

$$\begin{aligned}
\bar{H}_{2d}(\rho, \theta, \chi) &= \bar{f}_\rho \otimes \bar{h}_\theta^{\mathrm{DVR}} \otimes \bar{I}_\chi + \bar{H}^{\mathrm{OD}} \\
&= \bar{f}_\rho \otimes \bar{h}_\theta^{\mathrm{DVR}} \otimes \bar{I}_\chi + \bar{f}_\rho \otimes \bar{f}_\theta \otimes \bar{h}_\chi^{\mathrm{DAF}} \\
&\quad + \bar{V}(\rho, \theta, \chi).
\end{aligned} \tag{8}$$

A bar over the operator indicates a matrix. Thus $\bar{h}_\rho^{\mathrm{DAF}}$ is the Hamiltonian matrix for the $-(\hbar^2/2\mu)(\partial^2/\partial\rho^2) - (15/4\rho^2)$ operator in the DAF basis in ρ, and $\bar{f}_\rho = (1/\rho^2)$ and $\bar{f}_\theta = 1/\sin^2\theta$. Likewise, $\bar{h}_\theta^{\mathrm{DVR}}$ is the Hamiltonian matrix for $-(\hbar^2/2\mu)(4/\sin 2\theta)(\partial/\partial\theta)\sin 2\theta(\partial/\partial\theta)$ in the DVR basis in θ, and the $\bar{h}_\chi^{\mathrm{DAF}}$ is the Hamiltonian matrix for $-(\hbar^2/2\mu) \times (\partial^2/\partial\chi^2)$ in the DAF basis in χ. The $\bar{I}$ terms are identity matrices, and the subscripts indicate the dimensions of these matrices (e.g., $\bar{I}_\chi$ is an $N_\chi \times N_\chi$ matrix). Likewise, $\bar{f}$ are all diagonal, and subscripts indicate their dimensions. Note that the $J=0$ Hamiltonian corresponds to the $[\Lambda=0, \Lambda=0]$ block in Eq. (5).

The Hamiltonian is diagonalized in a novel way so that the calculation can be performed on a small computer. This approach significantly reduces the required memory and time. This diagonalization consists of two steps: surface ray diagonalization, and a subspace basis method which will be introduced in Sec. II B 2. We use the ray diagonalization technique to generate the adiabatic surface functions and potential energy curves in the ρ coordinate, and then solve the 1D Schrödinger equation to form the physically reasonable subspace basis set. The subspace basis is then used to construct the full Hamiltonian matrix with the nonadiabatic couplings between the surface functions to solve for the eigenenergies and associated eigenvectors.

1. Surface ray diagonalization

The first step is a sequential diagonalization-truncation technique as discussed by Bačić *et al.*[35] Here we review this two dimensional (2D) ray diagonalization used in the first step of the diagonalization.

The $\bar{H}^{1D}$ matrix is block diagonal, with each block corresponding to a particular value of ρ and θ. We first diagonalize $\bar{H}^{1D}$ at each ρ_α and θ_β,

$$\bar{H}^{1D}(\rho_\alpha, \theta_\beta) = f_{\rho_\alpha} \otimes f_{\theta_\beta} \otimes \bar{h}_\chi^{\mathrm{DAF}} + \bar{V}(\rho_\alpha, \theta_\beta, \chi). \tag{9}$$

Prior to diagonalization, the 1D ray Hamiltonian is truncated by retaining only those DAF points that satisfy

$$\bar{V}(\rho_\alpha, \theta_\beta, \chi_\gamma) \leq V_{\mathrm{cut}}, \tag{10}$$

where the parameter V_{cut} is chosen according to convergence study. Diagonalization of the truncated 1D ray Hamiltonian,

$$\bar{d}^T \hat{H}^{1D} \bar{d} = \mathbf{E}^{1D}, \tag{11}$$

yields the 1D ray eigenvectors $\bar{d}$ and the ray eigenvalues $\mathbf{E}^{1D}$. Because the set of eigenvectors $\{\bar{d}(\alpha, \beta)\}$ diagonalizes $\hat{H}^{1D}$, it is a good basis set for expanding the full solution of Ψ^{JMpn}, as it enables $\hat{H}^{1D}$ in the Hamiltonian matrix to be replaced with the corresponding eigenvalues $\mathbf{E}^{1D}$ at each ρ_α and θ_β. Then we use $\mathbf{E}_{\mathrm{cut}}^{1D}$ to truncate the $\bar{d}$ matrix,

$$\mathbf{E}^{1D} \leq \mathbf{E}_{\mathrm{cut}}^{1D}. \tag{12}$$

Here, for θ_β ($\beta = 1, 2, \ldots, N_\theta$) at ρ_α, the $\bar{d}(\beta)$ submatrix has dimension N_χ by n_β, where $n_\beta \leq N_\chi$ due to truncation, with N_χ the number of DAF points in χ.

After obtaining the truncated eigenvalues $\mathbf{E}^{1D}$ and the associated eigenvectors $\bar{d}$ at each ρ_α and θ_β, the 2D Hamiltonian matrix $\bar{H}_{2d}(\rho, \theta, \chi)$ is transformed as

$$\begin{aligned}
\tilde{H}_{2d}(\rho, \theta, \chi) &= \bar{d}^T \hat{H}_{2d}(\rho, \theta, \chi) \bar{d} \\
&= \bar{d}^T [\bar{f}_\rho \otimes \bar{h}_\theta^{\mathrm{DVR}} \otimes \bar{I}_\chi] \bar{d} + \bar{d}^T \hat{H}^{1D} \bar{d} \\
&= \bar{d}^T [\bar{f}_\rho \otimes \bar{h}_\theta^{\mathrm{DVR}} \otimes \bar{I}_\chi] \bar{d} + \mathbf{E}^{1D}. \tag{13}
\end{aligned}$$

Diagonalization of the 2D transformed Hamiltonian,

$$\bar{C}^T(\alpha) \tilde{H}_{2d}(\rho_\alpha, \theta, \chi) \bar{C}(\alpha) = \mathbf{E}^{2D}(\rho_\alpha), \tag{14}$$

gives the 2D ray eigenvectors $\bar{C}$ and the 2D eigenvalues $\mathbf{E}^{2D}$. These eigenvalues are the adiabatic surface energies. They depend only on ρ. The adiabatic surface energy curves (energy correlation diagram) will be presented in the next section. The eigenvectors $\bar{C}$ are a good basis set for diagonalizing the 2D transformed Hamiltonian. The total diagonalization of the 2D Hamiltonian is

$$\bar{C}^T \bar{d}^T \hat{H}_{2d} \bar{d} \bar{C} = \mathbf{E}^{2D}. \tag{15}$$

Further details of the 2D ray diagonalization can be found in the work of Bačić *et al.*[35]

2. Subspace basis method

Instead of diagonalizing the full Hamiltonian via ray diagonalization, we diagonalize the Hamiltonian on each adiabatic surface curve to reduce the memory required. The ith adiabatic surface curve is defined in terms of the ith value of $\mathbf{E}^{2D}$ at each ρ. We then obtain the subspace basis which ignores the nonadiabatic couplings between different surface curves, and we use this subspace basis set to construct the full Hamiltonian matrix including the nonadiabatic couplings to solve for the associated eigenenergies.

163

TABLE II. Converged parameters of the first group.

Parameter	Result	Definition
N_ρ	1200	Number of ρ points
N_θ	40	Number of θ points
N_χ	29	Number of χ points
V_{cut}	8 eV	Potential cutoff
$\mathbf{E}_{\text{cut}}^{1D}$	5 eV	1D energy cutoff
$\mathbf{E}_{\text{cut}}^{2D}$	0.008 eV	2D energy cutoff
$\rho_{\min}$	4 bohr	Minimum ρ value
$\rho_{\max}$	52 bohr	Maximum ρ value

Before applying the subspace basis method to be described here, we use $\mathbf{E}_{\text{cut}}^{2D}$ to truncate the matrix $\mathbf{\bar{d}C}$. We keep eigenvectors that correspond to $\mathbf{E}^{2D}$ such that

$$\mathbf{E}^{2D} \leqslant \mathbf{E}_{\text{cut}}^{2D}, \tag{16}$$

where the parameter $\mathbf{E}_{\text{cut}}^{2D}$ is chosen from the convergence study. On the ith adiabatic surface in ρ, we use the adiabatic surface eigenvector $\phi(i)$ and surface energy $\mathbf{E}^{2D}(i)$ to construct the Hamiltonian matrix. The expansion of $\phi(i)$ is

$$\phi_m^\beta(i) = \sum_{p=1}^{n_\beta} d_{mp}^\beta C_{pi}^\beta, \tag{17}$$

where i denotes the ith surface eigenvector, β denotes the βth value in θ, n_β denotes the number of functions in the truncated basis in χ, $\beta = 1, 2, \ldots, N_\theta$, $m = 1, 2, \ldots, N_\chi$, and $p = 1, 2, \ldots, n_\beta$. The truncated surface basis matrix $\bar{D}$ that diagonalizes the 2D Hamiltonian is

$$\mathbf{\bar{D}} = \mathbf{\bar{d}C}. \tag{18}$$

Therefore, the new $\widetilde{H}^i$ on the ith surface after the $\mathbf{\bar{D}}(i)([N_\rho \times N_\theta \times N_\chi, N_\rho])$ transformation is

$$\begin{aligned}
\widetilde{H}^i &= [\mathbf{\bar{D}}^T]^i \bar{H}[\mathbf{\bar{D}}]^i \\
&= [\mathbf{\bar{D}}^T]^i \bar{H}_\rho[\mathbf{\bar{D}}]^i + [\mathbf{\bar{D}}^T]^i \bar{H}_{2d}[\mathbf{\bar{D}}]^i \\
&= [\mathbf{\bar{D}}^T]^i [\bar{h}_\rho^{\text{DAF}} \otimes \bar{I}_{\theta\chi}][\mathbf{\bar{D}}]^i + \mathbf{E}^{2D}(i). \tag{19}
\end{aligned}$$

Note that $\widetilde{H}^i$ is not the exact Hamiltonian, because we are using adiabatic surface bases for expansion and ignoring the couplings between these adiabatic surfaces. By diagonalizing $\widetilde{H}^i$ (dimension of $N_\rho \times N_\rho$), we get the 1D eigenvectors $\mathbf{\bar{T}}(i)$ and the associated eigenvalues $\mathbf{E}^G(i)$. Subsequently we can obtain a subspace basis set $\mathbf{G}(i)$ on the ith adiabatic surface,

$$\mathbf{\bar{G}}(i) = \mathbf{\bar{D}}(i)\mathbf{\bar{T}}(i). \tag{20}$$

The subspace matrix $\mathbf{\bar{G}}$ does not correspond to the eigenvectors of the exact Hamiltonian, and the eigenvalues $\mathbf{E}^G$ are not the exact energies. However, the $\mathbf{G}$ subspace bases are physically motivated and constitute an efficient subspace for computation. For the ith column vector of the $\mathbf{G}(i)$ matrix, there is an associated subspace energy $\mathbf{E}_i^G(i)$. To eliminate the unnecessary high-energy states and to save sorting time for subspace energies, we truncate the number of the bases so that

$$\mathbf{E}_t^G(i) \leqslant \mathbf{E}_{\text{cut}}^{2D}. \tag{21}$$

After we sort all the subspace energies $\mathbf{E}^G$ for each adiabatic surface, we pick out the lowest N_G states to construct the Hamiltonian matrix. The $\mathbf{G}$ subspace bases are related to the adiabatic surface functions, which ignore couplings between the surfaces. These nonadiabatic couplings are then included to give accurate bound state energies of the full Hamiltonian. By diagonalizing this N_G by N_G Hamiltonian $\widetilde{H}^G$,

$$\widetilde{H}^G = [\mathbf{\bar{G}}^T]\bar{H}[\mathbf{\bar{G}}], \tag{22}$$

we get both the energies and the eigenvectors for the bound states. The eigenvectors are used to calculate the wave functions of the bound states, which we use to investigate the features of each bound state and the possible effects of the conical intersection in the next section.

3. Novelty of the subspace method and theory extension

The subspace basis method is necessary to reduce computational effort. The full construction and direct diagonalization of the Hamiltonian would require the storage for an $N_{\text{points}} \times N_{\text{points}}$ matrix, where $N_{\text{points}} = N_\rho \times N_\theta \times N_\chi$. The subspace basis method requires only memory for an $N_{\text{points}} \times N_G$ matrix. In this study, the memory required for the largest calculation was reduced from 14 Tbytes to 30 Gbytes, and the time from months to days. (Calculations were performed on a single computer with 32 Gbytes of random access memory and Xeon Intel EM64T processors.)

We also compared implicitly restarted Arnoldi method (IRAM) and the subspace method on the same computer. When the matrix to be diagonalized is symmetric, IRAM reduces to a variant of the Lanczos process called the implicitly restarted lanczos method (IRLM). Many groups have used IRLM method with parallel processing and obtained excellent results.[17–19,22,27] But most aspects of the subspace method can be parallelized as well. We performed calculations using both methods to illustrate their time difference. Table I lists the CPU time for each method with different numbers of points. "Direct diagonalization" means directly diagonalizing the fully constructed Hamiltonian matrix $\bar{H}$. As the number of points increases, the time difference between IRAM and the subspace method increases greatly.

The present theory is for $J = 0$. When $J = 1$, for instance, the Hamiltonian matrix corresponding to Eq. (5) doubles in size with respect to the $J = 0$ case. The treatment of the $J = 1$ Hamiltonian would be similar to that for $J = 0$. First diagonalize the subblock matrices $\mathbf{H}_o + \mathbf{H}_r$ to form a subspace basis. Then use a carefully truncated subspace basis to construct the Hamiltonian matrix. This matrix will have dimensions of $N_G(\Lambda = 0) + N_G'(\Lambda = 1)$ by $N_G(\Lambda = 0) + N_G'(\Lambda = 1)$ for $J = 1$. The memory required is the same as for $J = 0$, because we construct each subblock one at a time. However, the time required is four times larger than for $J = 0$, because there are four nonzero submatrices for $J = 1$. Other $J \neq 0$ cases can be treated similarly. The time required for matrix operations

164

TABLE III. Convergence of the A_1 bound state energies in eV.

State	$N_G=800$	$N_G=900$	$\cdots$	$N_G=2800$	$N_G=2900$	$E_i(\infty)$
E_1	−0.472 165 583 3	−0.472 165 583 4	$\cdots$	−0.472 165 583 9	−0.472 165 583 9	−0.472 165 583 9
E_{50}	−0.265 229 7	−0.265 229 7	$\cdots$	−0.265 234 3	−0.265 234 3	−0.265 234 3
E_{100}	−0.203 511 7	−0.203 511 8	$\cdots$	−0.203 515 5	−0.203 515 5	−0.203 516 3
E_{150}	−0.168 091	−0.168 092	$\cdots$	−0.168 119	−0.168 120	−0.168 126
E_{200}	−0.139 570	−0.139 581	$\cdots$	−0.139 776	−0.139 777	−0.139 847
E_{300}	−0.0997	−0.0998	$\cdots$	−0.1009	−0.1009	−0.1018
E_{400}	−0.068 40	−0.068 70	$\cdots$	−0.071 64	−0.072 07	Failed
E_{500}	−0.043 40	−0.044 24	$\cdots$	−0.048 99	−0.049 39	−0.512 39
E_{600}	−0.034 30	−0.034 76	$\cdots$	−0.036 78	−0.036 80	−0.037 54

compared to the time T for $J=0$ is estimated to be $(14+(J-3)\times 5)\times T$, because of the banded structure of the total Hamiltonian.

III. RESULTS AND DISCUSSION

A. Parameters convergence

We use the two-body dissociation limit (an atom and a diatom in the ground vibrational state) to determine the bound states for each irreducible representation. Colavecchia *et al.* calculated this limit to be −0.037 42 eV.[36] We restrain $\theta \in [0,\pi/2]$, $\chi \in [0,\pi/6]$ for the A_1 irreducible representation, and $\rho \in [\rho_{min},\rho_{max}]$. The main parameters in this study, N_ρ, N_θ, N_χ, V_{cut}, $\mathbf{E}_{cut}^{1D}$, $\mathbf{E}_{cut}^{2D}$, ρ_{min}, ρ_{max}, and N_G are defined in Table II.

We study convergence by splitting the parameters into two groups:

- convergence of N_ρ, N_θ, N_χ, V_{cut}, $\mathbf{E}_{cut}^{1D}$, $\mathbf{E}_{cut}^{2D}$, ρ_{min}, and ρ_{max};

- convergence of N_G.

We converge the parameters in the first group by initially converging each parameter sequentially, and then repeating until convergence for the whole group is obtained. Then we converge N_G. Finally, we study both groups together to ensure that all the bound states are converged within 0.05% error. In Table II, we present converged parameters of the first group. Converging ρ_{max} parameter is fairly hard, because the flat tail of adiabatic 1D energy curve at large ρ makes it hard for the most excited energy states to converge. With these converged parameters in the first group, we perform the convergence study of the N_G parameter alone.

B. Convergence of the results

In Table III, we show convergence of the A_1 bound state energies with respect to N_G. We list the extrapolated energies from the data in the last column. We perform the extrapolation for the ith bound state in the form of

$$E_i(N_G) = E_i(\infty) + \frac{A}{(N_G)^B}, \quad (23)$$

where A and B are constants and $E_i(\infty)$ is the extrapolated energy. The lowest 150 energies are converged to be less than 0.005%, those between the 200th and 350th energies are

obtained to 0.05%–1%, while most of the excited energy states are converged with less than 2.0% error. Some of the extrapolated energies are not available, because the extrapolation failed. (See Sec. III C.) The minimum energy needed to circumscribe the conical intersection is −0.0574 eV. Any state with an energy greater than −0.0574 eV may be affected by the conical intersection.

In the present convergence study, the lowest states are converged very well according to the extrapolated energy. The energies of the lowest 150 states are accurate to at least five significant figures. In Fig. 1 we show the spectrum of states around the 100th (bold line) with respect to N_G. Most of the energy lines remain almost straight as we increase N_G.

In Figs. 2 and 3, we show the spectrum of states around the 200th and 300th (bold lines) with respect to N_G. The energies start to decrease as we increase the N_G parameter and approach the extrapolated energy lines quickly. The energies of states between the 200th and 350th states have an error of 0.05%–1%.

In Figs. 4 and 5, we show the spectrum of states around the 400th and 500th (bold lines) with respect to N_G. These energies converge slowly. Most are converged to within 2%. However, some of the most highly excited states are converged to within 3%–6% of the extrapolated energies. We will discuss a procedure to enhance convergence in the next section.

In Table IV, we list integrated probabilities for bound states in $D_{\infty h}$ and $C_{\infty v}$ geometries as follow:
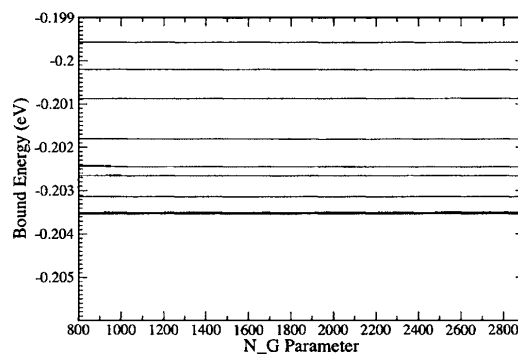

FIG. 1. The spectrum of the vibrational states around the 100th A_1 state vs N_G. The 100th state is indicated in bold.
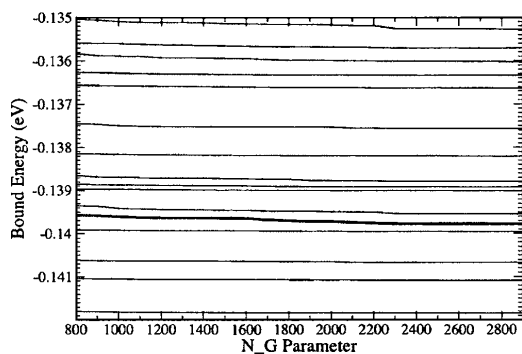
FIG. 2. The spectrum of the vibrational states around the 200th A_1 state vs N_G. The 200th state is indicated in bold.

$$P(D_{\infty h}) = \int_{\rho=0}^{\rho=\infty} \int_{\theta=88.3°}^{\theta=90.0°} \int_{\chi=29.5°}^{\chi=30.0°} \Psi^*\Psi d\tau, \qquad (24)$$

$$P(C_{\infty v}) = \int_{\rho=0}^{\rho=\infty} \int_{\theta=88.3°}^{\theta=90.0°} \int_{\chi=0.0°}^{\chi=30.0°} \Psi^*\Psi d\tau. \qquad (25)$$

As the energy increases, the probability in the two collinear symmetries increases. The conical intersection occurs in the $D_{\infty h}$ geometry, so states with large $D_{\infty h}$ probabilities may be significantly affected by the conical intersection. In Table V, we list probabilities for larger than 1% in $D_{\infty h}$ geometry and the converging energies. Convergences of the energies for some of these important states are obtained up to 1%, which assures us that these well converged states are ready for future comparison with nonadiabatic calculations.

C. Analysis and discussion

As expected, convergences of the most highly excited states are not as good as that of low-lying states. The highly excited states are notoriously difficult to obtain accurately and our stated accuracies are as good as those of other researchers on similar systems. Lack of better convergence may be due to the strong nonadiabatic coupling between sur-
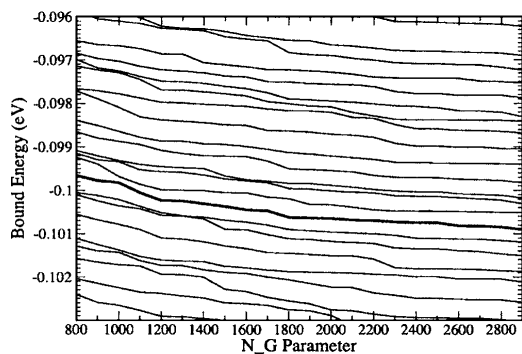

FIG. 3. The spectrum of the vibrational states around the 300th A_1 state vs N_G. The 300th state is indicated in bold.
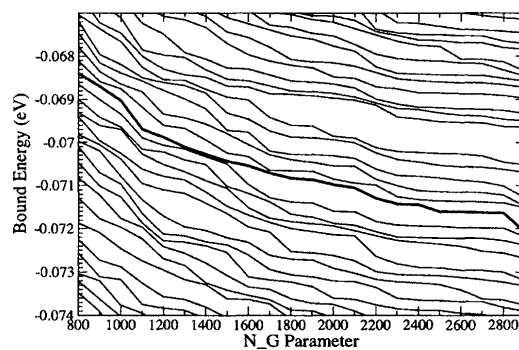

FIG. 4. The spectrum of the vibrational states around the 400th A_1 state vs N_G. The 400th state is indicated in bold.

face energy curves. We are using subspace bases associated with the ith adiabatic surface energy curve. Strong nonadiabatic couplings between curves would make the adiabatic surface energy curves rough at high energy. Figure 6, which plots 1D energy correlation diagrams as a function of the hyper-radius ρ, shows the upper region of the adiabatic 1D energy curves from the 2D ray diagonalization. Convergences in N_θ and N_χ for the 100 highest bound states are better than 0.05%, but the rough feature for $\rho \in [10a_o, 13a_o]$ is troublesome for the calculation of the subspace basis. This rough feature has been confirmed by our independent DVR study in θ and χ without a symmetry-adapted transformation. One possible explanation for this rough behavior is the influence from the seam of the conical intersection for $\rho \in [11a_o, 15a_o]$ bohr that is accessible by the bound states.[5] The potential is not differentiable at the conical intersection, which may cause strong nonadiabatic couplings between surface energy curves here.

To improve the convergence without using a larger basis, one can use diabatic surface energy curves instead of the adiabatic curves. Though it is difficult to construct accurate diabatic surface energy curves, one can minimize nonzero couplings to improve the accuracy of subspace bases. We
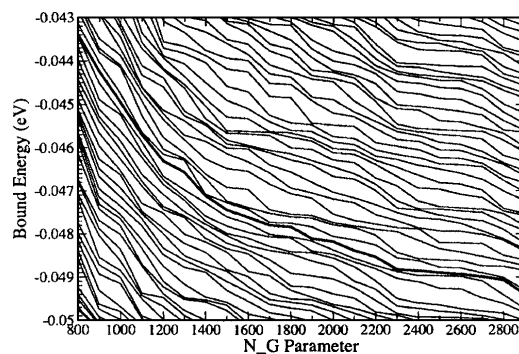

FIG. 5. The spectrum of the vibrational states around the 500th A_1 state vs N_G. The 500th state is indicated in bold.

166

TABLE IV. Probabilities of the wave functions in $D_{\infty h}$ and $C_{\infty v}$ geometries.

State	$P(D_{\infty h})$	$P(C_{\infty v})$
1	1.0×10^{-13}	3.5×10^{-13}
50	2.0×10^{-11}	6.2×10^{-11}
100	1.0×10^{-10}	4.8×10^{-10}
200	1.3×10^{-7}	4.4×10^{-7}
300	7.1×10^{-4}	2.4×10^{-3}
400	2.0×10^{-3}	9.3×10^{-3}
500	4.2×10^{-3}	2.0×10^{-2}
600	3.9×10^{-3}	3.4×10^{-2}

believe that convergence will be greatly improved with a better described adiabatic-to-diabatic transformation of the surface energy curves.

Despite the imperfect convergence of some of the most highly excited energies, states with less than 1%–2% error would provide us a good comparison when we move on to the nonadiabatic case to investigate the effect of the conical intersection. Moreover, based on the convergence of the A_1 bound states, the extrapolated energy for the 600th state is $-0.037\,64$ eV, that of the 601th state is $-0.037\,46$ eV, and that of the 602th state is $-0.037\,81$ eV. The dissociation limit for Li and ground state Li_2 is at $-0.037\,42$ eV. So the number of the A_1 bound states should be no larger than 601. We also calculated energies for Li_3 without the three-body potential term, where we assume that the interaction potential is a sum of pairwise additive potential and three-body potential. Excluding the three-body potential term makes the potential much shallower and we estimate the number of A_1 bound states to be no larger than 183.

TABLE V. Convergence for A_1 bound state with high probabilities in the $D_{\infty h}$ geometry.

State	Probability in $D_{\infty h}$	Energy (eV) ($N_G=2800$)	Energy (eV) ($N_G=2900$)
302	1.0%	$-0.100\,23$	$-0.100\,31$
333	1.2%	$-0.091\,50$	$-0.091\,64$
432	1.3%	$-0.062\,24$	$-0.062\,28$
433	1.0%	$-0.062\,18$	$-0.062\,20$
439	1.0%	$-0.060\,56$	$-0.060\,59$
442	1.4%	$-0.060\,16$	$-0.060\,22$
451	2.5%	$-0.058\,41$	$-0.058\,42$
460	1.5%	$-0.056\,95$	$-0.057\,00$
462	1.5%	$-0.056\,80$	$-0.056\,83$
472	1.3%	$-0.054\,54$	$-0.054\,86$
478	1.8%	$-0.053\,07$	$-0.053\,19$
480	1.2%	$-0.052\,61$	$-0.052\,88$
511	1.4%	$-0.047\,41$	$-0.047\,53$
526	1.1%	$-0.044\,40$	$-0.044\,58$
527	1.1%	$-0.044\,31$	$-0.044\,44$
535	1.2%	$-0.042\,89$	$-0.043\,02$
545	1.1%	$-0.041\,76$	$-0.041\,77$
550	1.0%	$-0.040\,88$	$-0.041\,12$
564	1.3%	$-0.039\,27$	$-0.039\,29$
572	1.0%	$-0.038\,30$	$-0.038\,46$
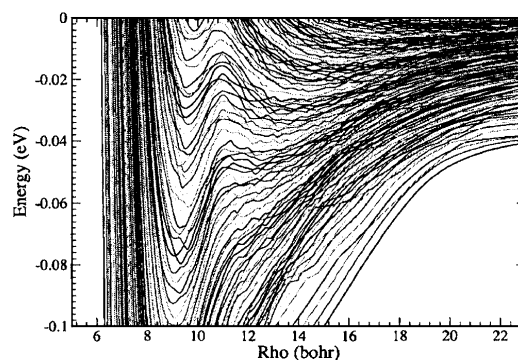
FIG. 6. Adiabatic 1D energy curves (1D energy correlation diagram) as a function of hyper-radius ρ.

IV. CONCLUSION

Here we have presented the results of our calculation of the Li_3 bound states for the $1\,{}^4A'$ potential energy surface, and we estimate the number of bound states at 601. Our calculation shows that the most highly excited vibrational states are within the energy range of the conical intersection and are likely to be affected by it. We believe this calculation to be the most comprehensive and most accurate results for this system to date. This data will be very useful in any study of the Li_3 system.

We also present a new method of calculating these states. It is only by this method that this calculation was possible. Other methods can produce similar or perhaps better results, but only with much greater computing power or much more time. A comparison of the expended CPU time used by our subspace calculation method with the time used by the IRAM method shows the subspace method to be significantly faster: up to 200 times faster when a large number of points are needed for the calculation.

[1] A. Fioretti, D. Comparat, A. Crubellier, O. Dulieu, F. Masnou-Seeuws, and P. Pillet, Phys. Rev. Lett. **80**, 4402 (1998).
[2] T. Takekoshi, B. M. Patterson, and R. J. Knize, Phys. Rev. Lett. **81**, 5105 (1999).
[3] N. Nikolov, E. E. Eyler, X. Wang, J. Li, H. Wang, W. C. Stwalley, and P. Gould, Phys. Rev. Lett. **82**, 703 (1999).
[4] C. Gabbanini, A. Fioretti, A. Lucchesini, S. Gozzini, and M. Mazzoni, Phys. Rev. Lett. **84**, 2814 (2000).
[5] D. A. Brue, X. Li, and G. A. Parker, J. Chem. Phys. **123**, 091101 (2005).
[6] M. T. Cvitaš, P. Soldán, J. M. Hutson, P. Honvault, and J.-M. Launay, Phys. Rev. Lett. **94**, 033201 (2005).
[7] M. T. Cvitaš, P. Soldán, and J. M. Hutson, Mol. Phys. **104**, 23 (2006).
[8] M. T. Cvitaš, P. Soldán, J. M. Hutson, P. Honvault, and J.-M. Launay, J. Chem. Phys. (accepted).
[9] Z. Bačić and J. C. Light, Annu. Rev. Phys. Chem. **40**, 469 (1989).
[10] Z. Bačić and J. Z. H. Zhang, J. Chem. Phys. **96**, 3707 (1992).
[11] Z. Bačić, J. Chem. Phys. **95**, 3456 (1991).

[12] M. Mladenovic and Z. Bačić, J. Chem. Phys. **93**, 3039 (1990).
[13] Z. Bačić, D. Watt, and J. C. Light, J. Chem. Phys. **89**, 947 (1988).
[14] J. C. Light and Z. Bačić, J. Chem. Phys. **87**, 4008 (1987).
[15] Z. Bačić and J. C. Light, J. Chem. Phys. **86**, 3065 (1987).
[16] Z. Bačić and J. C. Light, J. Chem. Phys. **85**, 4594 (1986).
[17] J. R. Henderson and J. Tennyson, Chem. Phys. Lett. **173**, 133 (1990).
[18] S. V. Shirin, O. L. Polyansky, N. F. Zobov, P. Barletta, and J. Tennyson, J. Chem. Phys. **118**, 2124 (2002).
[19] M. A. Kostin, O. L. Polyansky, J. Tennyson, and H. Y. Mussa, J. Chem. Phys. **118**, 3538 (2002).
[20] S. Carter, I. M. Mills, and N. C. Handy, J. Chem. Phys. **99**, 4379 (1993).
[21] T. González-Lezana, J. Rubayo-Soneira, S. Miret-Artés, F. A. Gianturco, G. Delgado-Barrio, and P. Villarreal, J. Chem. Phys. **110**, 9000 (1999).
[22] N. J. Wright and J. M. Hutson, J. Chem. Phys. **112**, 3214 (2000).
[23] F. A. Gianturco, F. Paesani, I. Baccarelli, G. Delgado-Barrio, T. Gonzalez-Lezana, S. Miret-Artés, P. Villarreal, G. B. Bendazzoli, and S. Evangelisti, J. Chem. Phys. **114**, 5520 (2001).
[24] N. V. Blinov, P.-N. Roy, and G. A. Voth, J. Chem. Phys. **115**, 4484 (2001).
[25] S. Y. Grebenshchikov, R. Schinke, P. Fleurat-Lessard, and M. Joyeux, J. Chem. Phys. **119**, 6512 (2003).
[26] D. Babikov, J. Chem. Phys. **119**, 6554 (2003).
[27] H. Lee and J. C. Light, J. Chem. Phys. **120**, 5859 (2004).
[28] I. Baccarelli, F. A. Gianturco, T. González-Lezana, G. Delgado-Barrio, S. Miret-Artés, and P. Villarreal, J. Chem. Phys. **122**, 144319 (2005).
[29] I. V. Boychenko and H. Huber, J. Chem. Phys. **124**, 014305 (2006).
[30] J. E. Cuervo and P.-N. Roy, J. Chem. Phys. **125**, 124314 (2006).
[31] E. Scifoni, F. A. Gianturco, S. Yu. Grebenshchikov, and R. Schinke, J.

Chem. Phys. **125**, 164304 (2006).
[32] S. Orlandini, I. Baccarelli, and F. A. Gianturco, J. Chem. Phys. **125**, 234307 (2006).
[33] I. Sioutis, V. L. Stakhursky, R. M. Pitzer, and T. A. Miller, J. Chem. Phys. **126**, 124308 (2007).
[34] I. Sioutis, V. L. Stakhursky, R. M. Pitzer, and T. A. Miller, J. Chem. Phys. **126**, 124309 (2007).
[35] Z. Bačić, J. D. Kress, G. A. Parker, and R. T. Pack, J. Chem. Phys. **92**, 2344 (1990).
[36] F. D. Colavecchia, J. P. Burke, Jr., W. J. Stevens, M. R. Salazar, G. A. Parker, and R. T. Pack, J. Chem. Phys. **118**, 5484 (2003).
[37] http://nhn.ou.edu/~parker/research/PubPotentials.htm
[38] R. T. Pack and G. A. Parker, J. Chem. Phys. **87**, 3888 (1987).
[39] J. V. Lill, G. A. Parker, and J. C. Light, Chem. Phys. Lett. **89**, 483 (1982).
[40] J. V. Lill, G. A. Parker, and J. C. Light, J. Phys. Chem. **85**, 900 (1986).
[41] W. Zhu, Y. Huang, G. A. Parker, D. J. Kouri, and D. K. Hoffman, J. Phys. Chem. **98**, 12516 (1994).
[42] D. K. Hoffman, M. Arnold, and D. J. Kouri, J. Phys. Chem. **96**, 6539 (1992).
[43] J. C. Light, I. P. Hamilton, and J. V. Lill, J. Chem. Phys. **82**, 1400 (1985).
[44] B. R. Johnson, J. Chem. Phys. **73**, 5051 (1980).
[45] B. R. Johnson, J. Chem. Phys. **79**, 1906 (1983).
[46] K. Zhang, G. A. Parker, D. J. Kouri, D. K. Hoffman, and S. S. Iyengar, J. Chem. Phys. **118**, 569 (2003).
[47] S. S. Iyengar, G. A. Parker, D. J. Kouri, and D. K. Hoffman, J. Chem. Phys. **110**, 10283 (1999).

168